Unraveling the Seismic History of the Himalayas: Paleoseismological
Insights from a Surface Rupture in Eastern Bhutan

by

Yuqiu Zhao

Submitted in partial fulfilment of the requirements
for the degree of Master of Science

at

Dalhousie University
Halifax, Nova Scotia
April 2024

TABLE OF CONTENTS

LIST OF TABLES

LIST OF FIGURES

ABSTRACT

The Himalayas are known for large, destructive earthquakes, and their foreland is among the most densely populated regions. For such areas, it is imperative to build a statistically relevant database of large earthquakes, establish long-term seismic history, and estimate the recurrence interval of large earthquakes for each identified fault. However, little is known about the Himalayan earthquakes in the 18th century and before. The return periods of large earthquakes and the largest possible magnitudes are poorly constrained in the Himalayas. Therefore, the paleoseismic investigation of the newly identified surface rupture is critical to improving the catalog of the Himalayan earthquakes.

A surface rupture along the Main Frontal Thrust (MFT) was recently identified in eastern Bhutan, where a putative seismic gap in the Himalayas was inferred until now. Paleoseismological investigations were conducted at the Dungsam Chu exposure to identify and characterize paleoseismic events. A retro-deformation analysis and OxCal chronostratigraphic model reveal the occurrence of at least three paleo-earthquakes along the same simple trace of the MFT in eastern Bhutan for over 10,000 years. The two earlier paleoseismic events (E2–E3) were dated to occur before medieval times. The most recent surface-rupturing event (E1) was determined as the 1714 Bhutan earthquake, with a surface rupture length of 175 to ~290 km and the maximum observed coseismic surface displacement of ~10.5 m. Computations using empirical scaling relationships, historical intensity data, and paleoseismologically determined surface ruptures in the Bhutan Himalaya yielded plausible magnitudes of 7.7–8.5 (8.1 ± 0.4). The recurrence interval of ~570 ± 270 years in eastern Bhutan was determined by calculating the stress released during the 1714 M8.1 Bhutan earthquake. It implies that the previous earthquake before 1714 was a medieval event between A.D. 894 and A.D. 1434 if we assume that the stress accumulated along the Main Himalayan Thrust (MHT) had been released completely during the event.

Based on the paleoseismological evidence recorded near our study site, at least one medieval great earthquake is inferred to most likely have occurred in the Bhutan Himalayas: the A.D. ~1100 event of $M_w > ~8.7$ or the A.D. 1255 earthquake of $M_w > 8$. The evidence for surface rupture might have been overprinted by event E1 or eroded by surface processes if the great medieval events had affected the frontal segment of the MHT. Alternatively, the slip caused by medieval events may not have reached the surface or has propagated further south into the foreland basin. The segmentation of the MHT, rather than an absence of evidence, reduces the likeliness of one mega-event rupturing the whole front and puts more weight on the scenario of multiple events.

Calculations of Coulomb stress transfer indicate that great earthquakes along the leading part of the MHT would cause surface rupture. In contrast, distal earthquakes may not immediately trigger surface rupture, although they would increase the stresses in the leading part of the MHT, facilitating future surface-rupturing earthquakes. Frontal earthquakes would also transfer stress into the modern foreland basin, facilitating southward propagation of the MHT as a blind basal décollement. It is implied that field-based paleoseismic studies alone likely underestimate the seismic slip along the Himalayan megathrust.

LIST OF ABBREVIATIONS USED

General Abbreviations

CIESIN   Center for International Earth Science Information Network

NEIC   National Earthquake Information Center

NIST   National Institute of Standards and Technology

NSC   NOIRLab Source Catalog

GPS   Global Positioning System

dGPS   differential Global Positioning System

V_p P-wave velocity

InSAR   Interferometric Synthetic Aperture Radar

DTM   Digital Terrain Model

WSW   west-southwest

Geological Structure Term Abbreviations

MHT   Main Himalayan Thrust

MCT   Main Central Thrust

MBT   Main Boundary Thrust

MFT   Main Frontal Thrust

TFT   Topographic Frontal Thrust

STD   South Tibetan Detachment

oSTD   outer South Tibetan Detachment system

iSTD   inner South Tibetan Detachment system

KT   Kakhtang Thrust

ST   Shumar Thrust

ITSZ   Indus-Tsangpo Suture Zone

TSS   Tethyan Sedimentary Sequence

GHS   Greater Himalayan Sequence

LHS   Lesser Himalayan Sequence

Sw   Siwalik

DCF   Dhubri-Chungthang Fault

DF   Dauki Fault

OF   Oldham Fault

T1   a cut-in-fill terrace

T2   a fill terrace

E1-E5   Paleoseismic Events

EH1   Event Horizon 1

Age Dating Techniques Term Abbreviations

^{14}C Radiocarbon

$^{14}CO_2$ Carbon dioxide

ABA   acid-base-acid treatment

AMS   Accelerator Mass Spectrometry

BP   before present

AD/BC   calibrated or calendar ages

OSL   Optically Stimulated Luminescence

IRSL   Infrared stimulated luminescence

TL   Thermoluminescence

VB   valence band

CB   conduction band

FB   forbidden band

D_e equivalent dose (in Grays (Gy), where 1 Gy = 1 Joule/kg)

$\dot{D}$ environmental dose rate (in Gy/year)

$\dot{D}_\alpha$ alpha dose rate

$\dot{D}_\beta$ beta dose rate

$\dot{D}_c$ cosmic dose rate

MET   multi-elevated-temperature

SAR   Single aliquot regenerative-dose

L_x signal measurement

T_x signal sensitivity assessment

α   alpha particles

β   beta particles

γ   gamma rays

U   uranium

Th   thorium

K   potassium

a-value   alpha efficiency

ICP-MS   Inductively Coupled Plasma Mass Spectrometry

PMT   photomultiplier tube

LEDs   light emitting diodes

LMT   Lithium Metatungstate

HCl   Hydrochloric acid

H_2O_2 Hydrogen peroxide

HF   Hydrogen fluoride

CAM   Central age model

MAM   Minimum age model

δ the mean of the true paleodoses in the relevant population of grains

σ Standard deviation of log paleodoses

σ_b overdispersion value

OD   overdispersion value

DRAC   Dose Rate and Age Calculator

T_c closure temperature

Magnitude-related Term Abbreviations

M_w Magnitude

M_0 Seismic Moment

IPE   Intensity prediction equations

RLD   subsurface rupture length

RW   downdip rupture width

SRL   surface rupture length

CST   Coulomb stress transfer

Location Abbreviations

Pi   Piping

Sa   Sarpang

Ge   Gelephu

Du   Dungsam

WP   Wangdue Phodrang

Ga   Gangteng

Ba   Bahgara

Ch   Charaideo Hill

Ti   Tinkhong

Th   Thimphu

Sh   Shillong

ACKNOWLEDGMENTS

I would like to direct my gratitude to everybody in the Department of Earth and Environmental Sciences at Dalhousie for their work and support.

Lastly, I am truly grateful to my family for their unconditional long-term support and understanding. Their care and encouragement are the driving force for me to move forward.

CHAPTER 1: INTRODUCTION

The Himalayan orogen is the youngest and tectonically most active large mountain belt in the world. Since ca. 50 Ma (Najman et al., 2010), it was formed due to the collision and ongoing convergence of the Indian and Eurasian continental plates (Figure 1.1a). A mid-crustal décollement termed the Main Himalayan Thrust (MHT) was produced along the plate boundary, where the Indian plate was being underthrusted beneath the Eurasian plate (Nelson et al., 1996), and it was continuously traced through the entire orogen (Figure 1.1b). Its movement caused the formation of a sequence of ductile shear zones in the orogenic metamorphic core and brittle thrust faults in the upper crust. From north to south, these crustal-scale south-verging thrust faults include the Main Central Thrust (MCT), the Main Boundary Thrust (MBT), and the Main Frontal Thrust (MFT) (Hodges, 2000; Grujic and Coutand, 2023) (Figure 1.1b). The development of these thrusts extending along the whole orogen and propagating from north to south accommodated at least 1400 km of the north-south crustal shortening caused by the plate convergence (Yin and Harrison, 2000). About half of the convergence between India and Eurasia is partitioned into the slip along the MHT (Nelson et al., 1996). Since ca. 11 Ma, the convergence rates have been steady: ~34 mm/yr in the northwest and ~44 mm/yr in the northeast of India (Molnar and Stock, 2009) (Figure 1.2). Since ca. 2 Ma, the MHT emerged along the Himalayan front as the MFT (Mugnier et al., 2004). An approximately 100 km-wide area north of the MFT accumulates the potential slip entirely as elastic strain (Stevens and Avouac, 2016). This creates a huge seismic hazard posed on the Himalayan foreland, which is one of the most densely populated areas in the world (CIESIN, 2020) (Figure 1.3).

1.1 Paleoseismology of Himalaya

Large earthquakes in the Himalayas have been recorded in three ways: a) historical records that are the main basis of Himalayan historic seismicity studies in the 19th century and before, b) instrumental data using standardized seismic recorders, space-based geodetic techniques like GPS (Global Positioning System) and InSAR (Interferometric Synthetic Aperture Radar), and c) paleoseismic evidence obtained by

field investigations of earthquake phenomena including surface faulting, injections of liquefied sand, broken speleothems, and induced landslides.
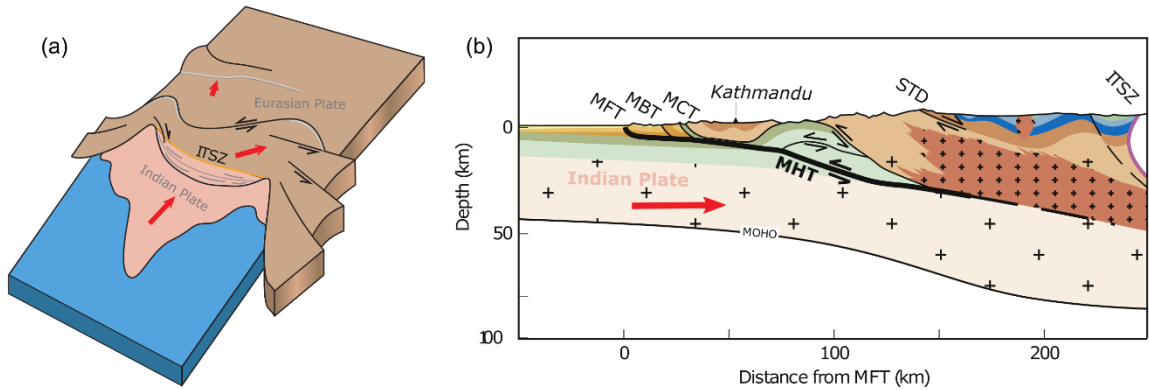
Figure 1.1 Sketch and geological cross-section of the collision and ongoing convergence of the Indian and Eurasian continental plates. Adapted from Avouac (2015). (a) Sketch showing how the Indian indentation into Eurasia has been absorbed by a combination of crustal thickening and lateral escape since the onset of the collision. ITSZ—the Indus-Tsangpo suture zone, well north of the Himalayan summits, along which relics of the Tethys Sea can now be traced. (b) Geological cross-section across central Nepal at the longitude of Kathmandu. The thick line shows the Main Himalayan Thrust fault, MHT, produced along the plate Indian-Eurasian boundary, reaching the surface at the Himalayan front and emerging as the Main Frontal Thrust, MFT. STD—South Tibetan detachment, MHT—Main Himalayan thrust, MCT—Main Central thrust, MBT—Main Boundary Thrust, and MFT—Main Frontal Thrust.
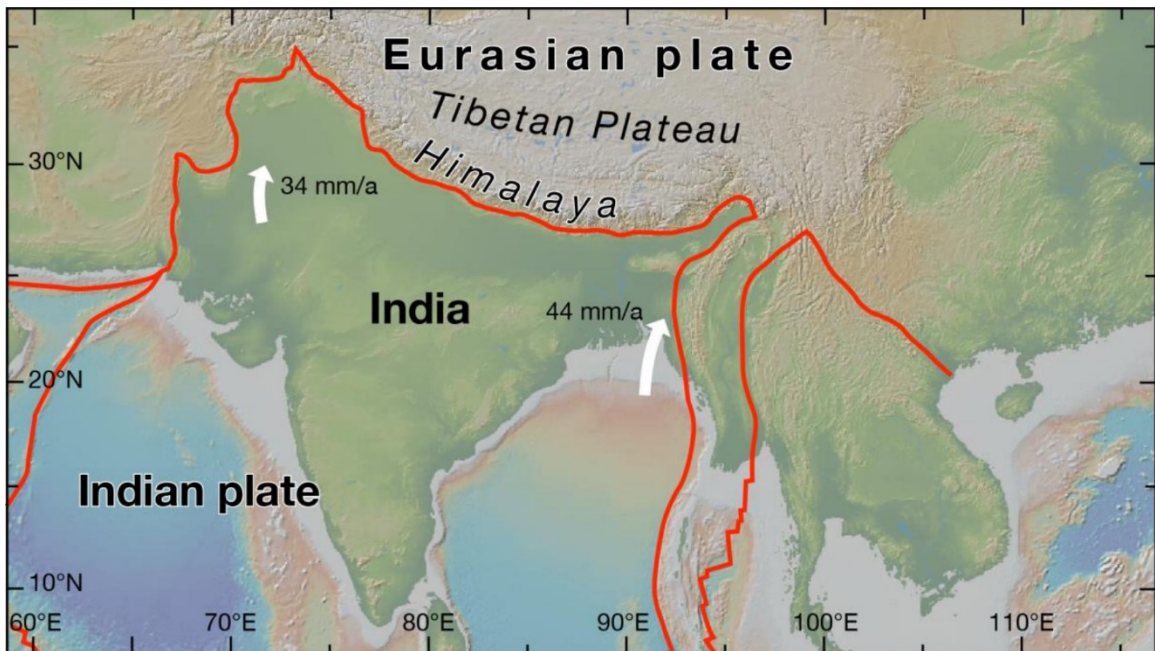
Figure 1.2 Map showing the Himalayan-Tibetan orogenic system with gradually steady convergence rates since ~11 Ma (i.e., ~34 mm/yr in the northwest and ~44 mm/yr in the northeast of India). Plate boundaries based on Bird (2003). Indian plate velocities from Molnar and Stock (2009).

2
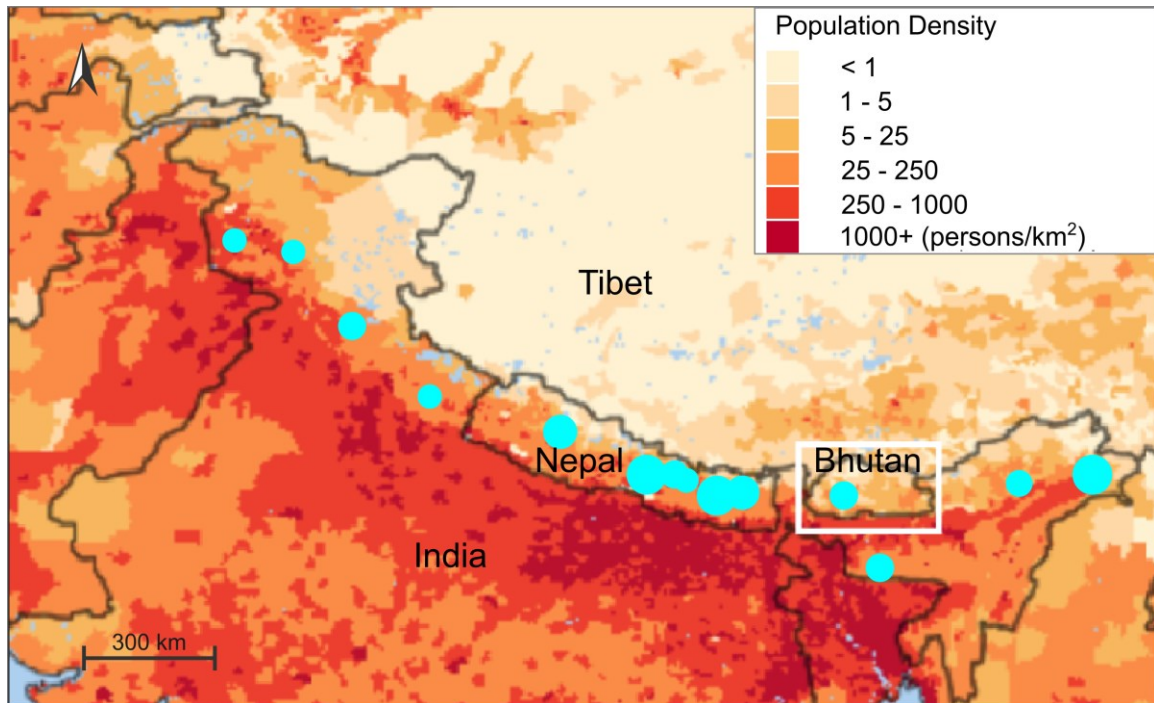
Figure 1.3 Map of population density (persons/km^2) by the Center for International Earth Science Information Network (CIESIN). Solid light blue circles indicate major or great earthquakes ($M_w > \sim7.5$) occurred along the frontal Himalaya during the last millennium. The white rectangle highlights the area of Bhutan.

Over a dozen, known major or great earthquakes (i.e., magnitude $M_w > \sim7.5$) occurred along the Himalayan arc in the last 1000 years (Figure 1.4; Table 1). Most are attributed to slip on the basal detachment, MHT. The latest major earthquake in the Himalaya was the April 2015 Gorkha earthquake (Nepal) rooted at 15 km depth along the MHT, with M_w 7.8. It induced landslides and caused over 9000 casualties (Grandin et al., 2015; Elliott et al., 2016). Since 1905, five major earthquakes with $M_w > 7.5$ have occurred in the Himalayan region. Together with great earthquakes in the 1800s, they have ruptured almost half of the MHT (Hodges, 2000; Bilham et al., 2001). Consequently, a slip potential of 1 to 10 meters has been accumulated since 1800 (Bilham et al., 2001; Bilham et al., 2019). The 1905 M_w ~7.8 Kangra earthquake (Ambraseys and Bilham, 2000; Kumar et al., 2001; Kumar et al., 2006; Bilham and Wallace, 2005; Malik et al., 2015) is nearly the first instrumentally recorded event along the arc. However, no surface rupture along the MFT was discovered to be related to this event, like the 2015 event. The 2005 M_w 7.6 Kashmir earthquake, which claimed more than 80,000 lives, occurred in the core of the tectonically complex northwestern corner of

3

the arc and produced a surface rupture of more than 75 km along the Balakot-Bagh fault parallel to the MBT (Avouac et al., 2006). This event has not released all the strain accumulated after the 1555 Kashmir event occurred ~100 km southeast of the 2005 epicentral area (Kondo et al., 2008; Kaneda et al., 2008). The largest 20th century earthquakes well documented are the 1934 M_w ~8.4 Bihar-Nepal (Chen and Molnar, 1977; Ambraseys and Douglas, 2004; Sapkota et al., 2013; Bollinger et al., 2014; Wesnousky et al., 2018; Rizza et al., 2019) and the 1950 M_w ~8.6 Assam (Ben-Menahem et al., 1974; Chen and Molnar, 1977; Kumar et al., 2010; Priyanka et al., 2017; Coudurier-Curveur et al., 2020; Singh et al. 2021). Both earthquakes produced at least ~11 m coseismic slip (Bollinger et al., 2014; Coudurier-Curveur et al., 2020), but the 1934 event is controversial as to the occurrence and extent of surface rupture (Sapkota et al., 2013; Bollinger et al., 2014; Wesnousky et al., 2018; Rizza et al., 2019) while the 1950 event ruptured the surface along at least 200 km (Coudurier-Curveur et al., 2020). The two 19th century earthquakes, 1803 Kumaon-Garhwal (M_w ~7.5) and 1833 (M_w ~7.6), were not recorded instrumentally, and no paleoseismic evidence was found along the MFT for these two events, thus their epicenters are uncertain (Ambraseys and Jackson, 2003; Ambraseys and Douglas, 2004; Kumar et al., 2006; Bilham, 1995; Mugnier et al., 2011).

Only six major or great Himalayan earthquakes are certainly known prior to 1800 (Table 1): from west to east, A.D. 1555 Kashmir (M_w ~7.6), A.D. 1505 Central (M_w ~8.2), A.D. 1255 (M_w > ~8.0), A.D. 1714 (M_w ~8.0), A.D. ~1100 (M_w > ~8.7) , and A.D. 1697 Sadiya (M_w ~7.9) (Ambraseys and Jackson, 2003; Berthet et al., 2014; Bollinger et al., 2014; Hetényi et al., 2016b; Kumar et al., 2006; Kumar et al., 2010; Lavé et al., 2005; Le Roux-Mallouf et al., 2016; Le Roux-Mallouf et al., 2020; Malik et al., 2010; Malik et al., 2017; Mugnier et al., 2011; Pant, 2002; Sapkota et al., 2013; Upreti et al., 2000; Wesnousky et al., 2017a; Wesnousky et al., 2017b; Wesnousky et al., 2019). All of them have breached the MFT zone, and the surface rupture length for each seismic event is estimated according to the distance between the two farthest paleoseismological sites where a corresponding coseismic surface rupture was identified (Figure 1.4; Table 1). Except for the A.D. ~1100 event, which was inferred exclusively from paleoseismic

4

investigations, all the others were confirmed by both historical records and paleoseismic studies. The 1555 Kashmir event caused ground fissures and a surface rupture extending up to 100 km (Ambraseys and Jackson, 2003; Malik et al., 2010). The A.D. 1505 event occurred within the area between the 1905 Kangra and 1934 Bihar-Nepal events, and it produced at least 700 km long rupture (Kumar et al., 2010). The two great earthquakes that occurred in A.D. 1255 and A.D. ~1100 brought great damage to Kathmandu (Nepal) (Kumar et al., 2010; Mugnier et al., 2011; Sapkota et al., 2013; Bollinger et al., 2014; Wesnousky et al., 2017a; Wesnousky et al., 2017b; Wesnousky et al., 2019). The A.D. 1255 event has ruptured the MFT almost along the entire Nepal and caused fatalities of one third of the population in Kathmandu while the A.D. ~1100 affected the eastern Himayala. The A.D. 1714 event is the only known historic one in Bhutan, with a rupture length of 200–300 km (Hetényi et al., 2016b; Berthet et al., 2014; Le Roux-Mallouf et al., 2016; Le Roux-Mallouf et al., 2020). Additionally, with rare historical records, the A.D. 1697 Sadiya earthquake (M_w ~7.9) was potentially identified dating liquefaction features at the sites Kaliya Nala and Kalolwa, and sand vents near Chedrang (Iyengar et al., 1999; Rajendran et al., 2004; Reddy et al., 2009) (Table 1). Recent paleoseismic study of fault scarp at Himebasti (27.54°N, 94.36°E) is likely related to this earthquake with the implication of M_w 7.4–8.1 and an estimated 100 km-long surface rupture (Pandey et al., 2021). Based on the limited historical records, instrumental data, and paleoseismic evidence in the Himalayas, it is indicated that major earthquakes ($M_w > 7$) usually produce partial ruptures of the MHT at depth, only great earthquakes ($M_w > 8$) have the potential to rupture up to the megathrust front (Dal Zilio et al., 2021).

Paleoseismology in the Himalayas is limited by a lack of historical earthquake records and insufficient paleoseismic evidence. There are only three areas where more than one major or great Himalayan earthquakes have been observed: the 1833/2015 (central Nepal), 1255/1934 (eastern Nepal), and ~1100/1714 (central Bhutan) sequences (Grandin et al., 2015; Sapkota et al., 2013; Berthet et al., 2014; Le Roux-Mallouf et al., 2016; Le Roux-Mallouf et al., 2020). In several segments along the Himalayan arc, seismic information is lacking or missing. Current understanding is that the large Himalayan earthquakes occur every 500–800 years (Bollinger et al., 2014), based on the

Table 1.1 Major or great Himalayan earthquake chronology during the last millennium. Surface rupture length was investigated along the MFT.

Event	Epicenter Location	Estimated Magnitude	Surface Rupture Length	References
~ 1100 [P]	Eastern Nepal	> ~8.7 if a single great earthquake	700–800 km	Lavé et al., 2005; Kumar et al., 2010 Mugnier et al., 2011 Le Roux-Mallouf et al., 2016, 2020 Wesnousky et al., 2017a & 2017b & 2019
1255 [H, P]	Western Nepal	> 8.0	> 450 km	Pant, 2002; Upreti et al., 2000; Mugnier et al., 2011 Sapkota et al., 2013; Bollinger et al., 2014 Wesnousky et al., 2017a & 2017b
1505 [H, P] Central	29.5°N 83.0°E	~8.2 if a single great earthquake	> 700 km	Ambraseys and Jackson, 2003; Ambraseys and Douglas, 2004; Bilham and Wallace, 2005; Kumar et al., 2006, 2010; Malik et al., 2017
1555 [H, P] Kashmir	33.5°N 75.5°E	~7.6	~100 km	Ambraseys and Jackson, 2003 Malik et al., 2010
1697 [H,P] Sadiya	Upper Assam region	~7.9	~100 km	Iyengar et al., 1999 Rajendran et al., 2004; Reddy et al., 2009 Pandey et al., 2021
1714 [H, P] Bhutan	26.7–27.5°N 88.8–91.2°E	~8.0	200–300 km	Ambraseys and Jackson, 2003 Berthet et al., 2014; Hetényi et al., 2016b Le Roux-Mallouf et al., 2016, 2020
1803 [H] Kumaon-Garhwal	31°N 79°E	~7.5	*	Ambraseys and Jackson, 2003; Ambraseys and Douglas, 2004; Kumar et al., 2006; Malik et al., 2017
1833 [H]	25.1°N 85.3°E	~7.6	*	Bilham, 1995; Mugnier et al., 2011 Grandin et al., 2015
1905 [H, I,P] Kangra	32.22°N 76.32°E	~7.8	*	Ambraseys and Bilham, 2000; Kumar et al., 2001, 2006; Bilham and Wallace, 2005; Malik et al., 2015; Bilham, 2019
1934 [H, I,P] Bihar-Nepal	27.55°N 87.09°E	~8.4	Debated	Chen and Molnar, 1977 Ambraseys and Douglas, 2004 Sapkota et al., 2013; Bollinger et al., 2014 Wesnousky et al., 2018; Rizza et al., 2019
1950 [H, I,P] Assam	28.38°N 96.76°E	~8.6	> 200 km	Ben-Menahem et al., 1974 Chen and Molnar, 1977 Kumar et al., 2010; Priyanka et al., 2017 Coudurier-Curveur et al., 2020 Singh et al. 2021
2005 [I, P] Muzaffarabad	34.493°N 73.629°E	7.6	*	Avouac et al., 2006 Kondo et al., 2008; Kaneda et al., 2008
2015 [I] Gorkha	28.230°N 84.731°E	7.8	*	Grandin et al., 2015; Elliott et al., 2016

Note: * represents that the surface rupture did not occur or was not investigated along the MFT.

[H] -Historically recorded; [I] -Instrumentally recorded; [P] -Paleoseismology study.

1255 and 1934 great earthquakes and several older and comparable seismic events identified at the same paleoseismological investigation site (Sir Bardibas) in eastern Nepal. It has been confirmed by geomorphologic and paleoseismic studies at the Piping site in western Bhutan (Le Roux-Mallouf et al., 2020).

1.1.1 Himalayan Seismic Gaps

The segments of the MHT between the rupture areas of these large earthquakes in the Himalayan orogen are known as seismic gaps, where no seismic events have been recorded or no earthquakes have occurred for a long time. Since 1505, the largest seismic gap is in western Nepal (80–84.5°E) whereas the second largest is between Kangra and Garhwal (30.5–32°N, 77–78.5°E) (Figure 1.4). Several small seismic gaps are evident in Kishtwar (between Kashmir and Kangra, 32.5–33.5°N, 75.7–76.2°E), Sikkim, eastern Bhutan (Gahalaut et al., 2011; Bilham, 2019), and western Arunachal Pradesh (Figure 1.4). Where along-strike three of these seismic gaps are distributed to coincide with the segment boundaries defined by lower plate inherited structures, i.e., three subsurface Indian basement ridges at 77.5–78°E, 82.8–83.3°E, and 87.2–87.7°E respectively, which extend northward across the Himalayan foothills (Godin and Harris, 2014; Hetényi et al., 2016a; Dal Zilio et al., 2020). In other words, no evidence shows that large earthquakes in the last millennium propagated across the segment boundaries. Further geophysical and paleoseismological investigations are therefore required to constrain the rupture extent of paleoseismic events in such fields and to better characterize the features of these segment boundaries. It is crucial to raise concerns about seismic gaps in the Himalayas that may have the potential to produce future great earthquakes since the strain keeps building up with the ongoing Himalayan continental collision and is mostly accumulated along the MHT (Sharma et al., 2020; Bilham, 2004; Bilham, 2019; Berthet et al., 2014; Burgess et al., 2012).

1.1.2 Limitations of Paleoseismology

For most major or great earthquakes, the records of surface rupture are insufficient or missing in the Himalaya region (Table 1). This limits the application of

paleoseismic studies as they depend on identification and age dating of surface rupture. There are two likely obstacles for finding field evidence for large earthquakes. One is that some of these earthquakes may be associated with blind thrusts, i.e., there was no surface slip during the large earthquake as was the case for the April 2015 Gorkha earthquake (M_w 7.8) (Grandin et al., 2015). Such blind faults would cause large stress accumulation in the frontal part of a thrust. This would pose the threat of an imminent earthquake to that area. Second, even if the surface rupture had occurred, the poorly preserved exposures, thick vegetation in the sub-tropical Himalayan front, and even postseismic sediment aggradation (Rizza et al., 2019) could hinder its identification. The long interval between large earthquakes coupled with natural and anthropogenic landscape modification also limit their preservations. The information about recurrence intervals of major or great earthquakes in the Himalaya is, therefore, incomplete. The estimate of recurrence interval of major earthquakes requires at least two successive paleoseismic events in each area. However, there has been only one major earthquake recorded along most of the Himalayan front (Figure 1.4). Another problem is that earthquakes may not repeat regularly since elastic strain accumulated in the setting of continental subduction may be released completely to generate a very large earthquake or partly to produce a series of smaller earthquakes (Goldfinger et al., 2013). Poor seismic information and insufficient paleoseismic evidence may yield misleading long recurrence intervals.

Thus, it is important to systematically investigate the known surface rupture and search for new ones to establish paleoseismic archives for post-paleoseismic investigations and the prediction of the potential for a future earthquake. However, establishing a complete record of major paleoseismic events depends on whether a study area has a complete geological record and preserved earthquake-related deformation structures. Paleoseismic investigations based on active surface faulting and existing geological archives have been successfully performed in many areas of the world and have complemented historic records with prehistoric seismic events into paleoseismic archives (Camelbeeck and Meghraoui, 1998; Galli et al., 2008). These historic records may cover one or two mega-earthquakes, which occur on a millennial time-scale. The concept of integrated paleoseismology, comparing evidence from different geological

archives that involved a variety of deformation features related to earthquakes including surface faulting, deformation in lake deposits, sand injections in flood deposits, unstable slope and cave collapse, has been applied successfully in Switzerland where for the earthquake catalogue could be extended back beyond historic records, into the late Pleistocene, spanning 15,000 years (Becker et al., 2005). Therefore, to improve the catalog of the Himalayan earthquakes, it will be also important to apply additional paleoseismological techniques such as speleotectonics (identifying and dating perturbations in the growth of speleothems; e.g., Rajendran et al., 2016), and study large rockfalls, which are generally the most widely reported earthquake-triggered slope failures on land (Prestininzi and Romeo, 2000).
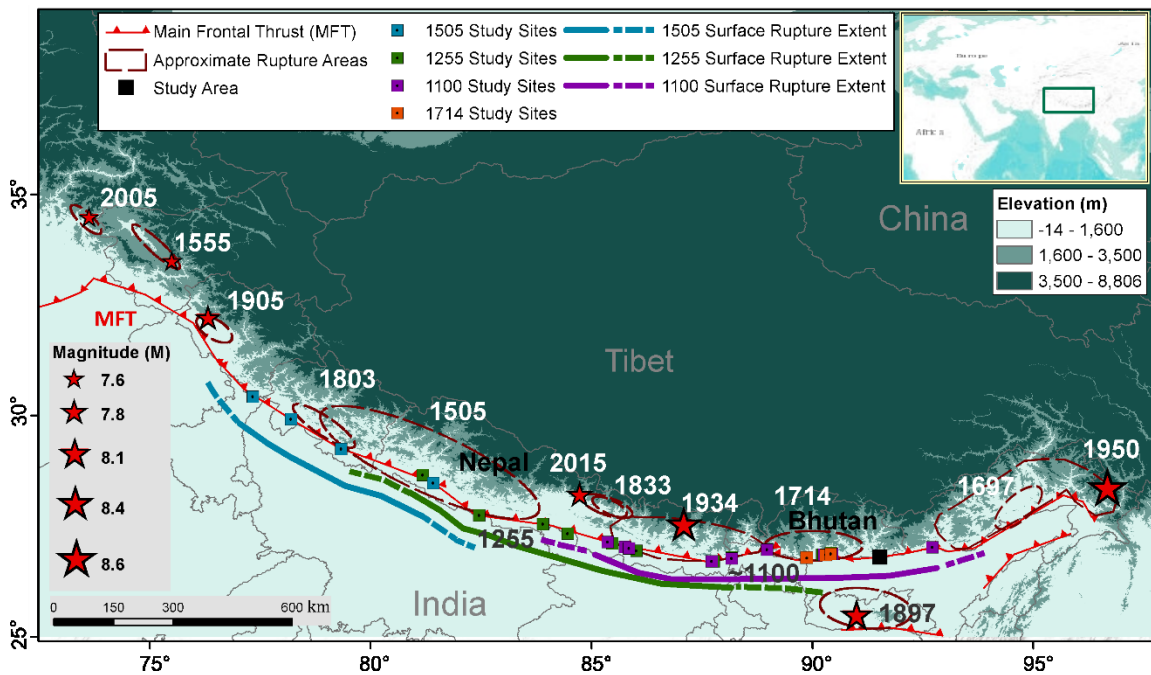
Figure 1.4 Map of major or great earthquakes ($M_w > \sim 7.5$) along the frontal Himalaya during the last millennium. The dark green box in the inset world map marks the Himalayan region. Red stars indicate known epicenters. Dark red ellipses indicate the areas of the MHT ruptured by known earthquakes schematically. The colored squares show paleoseismological investigation sites for the A.D. 1505 (blue), A.D. 1255 (green), A.D. ~1100 (purple) and A.D. 1714 (orange) events (Bilham and Wallace, 2005; Kumar et al., 2006; Kumar et al., 2010; Bollinger et al., 2014; Malik et al., 2017; Wesnousky et al., 2017a; Wesnousky et al., 2017b; Wesnousky et al., 2019; Upreti et al., 2000; Lavé et al., 2005; Mugnier et al., 2011; Berthet et al., 2014; Hetényi et al., 2016b; Le Roux-Mallouf et al., 2016; Le Roux-Mallouf et al., 2020). The thick colored solid and dash lines indicate the possible surface rupture extents of the A.D. 1505, A.D. 1255, and A.D. ~1100 events, using the same color codes as for the paleoseismic sites. The black square indicates the study area of this research. MFT—Main Frontal thrust.

1.2 Fault Motion and Seismicity in the Himalaya

9
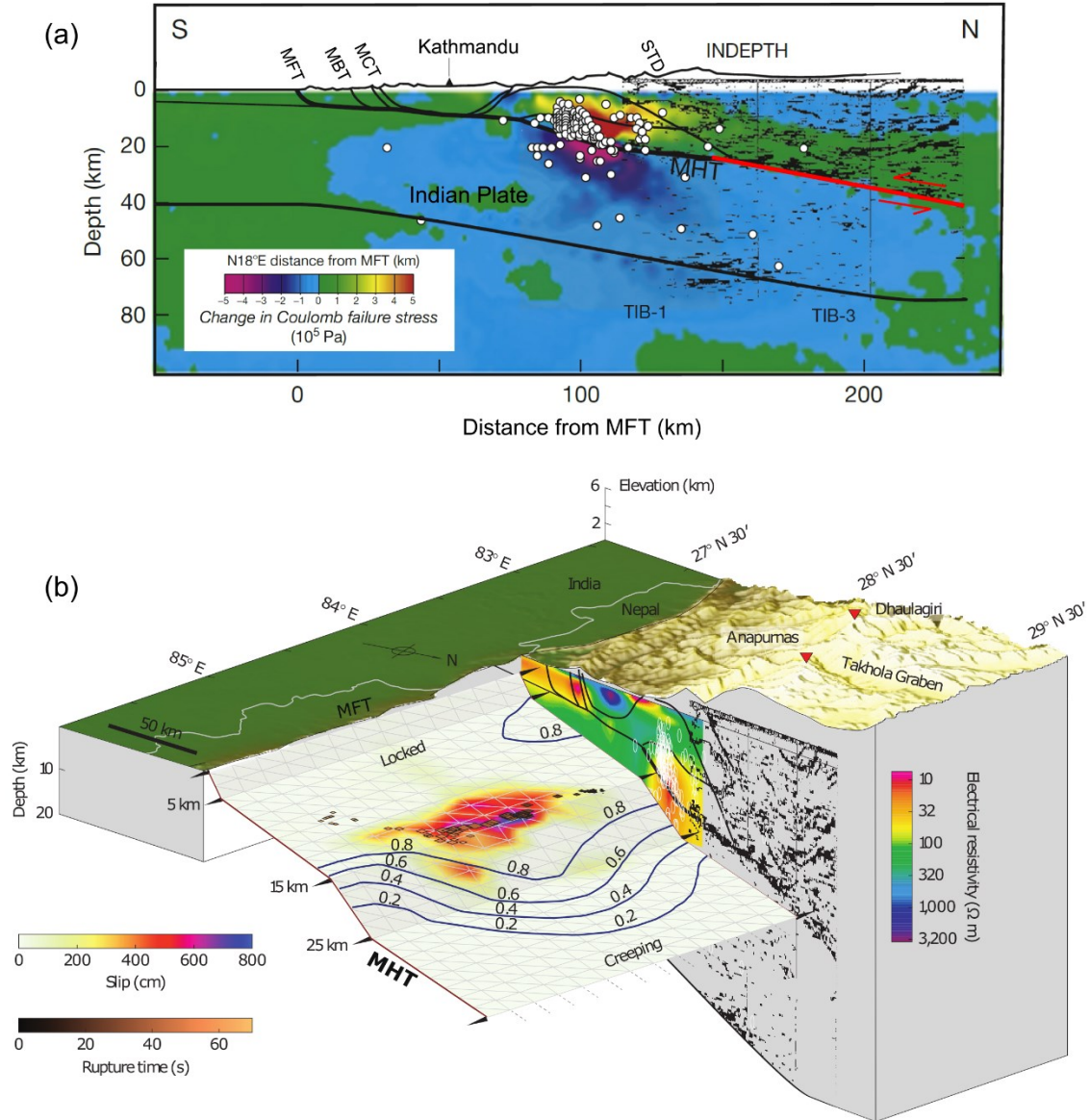
Figure 1.5 2D and 3D block diagrams of the geometry proposed for the MHT. (a) Coulomb stress changes on the structural cross section across central Nepal. Adapted from Avouac (2015). White dots indicate observed seismicity that was recorded on this section during the period of the temporary seismic network (Cattin and Avouac, 2000) and that is mainly clustered in the area of enhanced Coulomb stress, i.e., in the area of interseismic stress buildup where is the downdip transition from locked to creeping zone on the MHT. The seismic sections (TIB-1 and TIB-3) of the INDEPTH reflection profile are also reported (Brown et al., 1996; Nelson et al., 1996; Zhao et al., 1993). STD—South Tibetan detachment, MHT—Main Himalayan thrust, MCT—Main Central thrust, MBT—Main Boundary Thrust, and MFT—Main Frontal Thrust. (b) 3D block diagrams of the geometry proposed for the MHT. Adapted from Elliott et al. (2016). Colors on the fault plane of the MHT indicate earthquake slip relative to interseismic coupling denoted as blue lines, which are inferred from GPS-, leveling-, and InSAR-derived deformation rates before the 2015 Gorkha earthquake (Stevens and Avouac, 2015). Brown diamonds on the fault plane of the MHT show high-frequency seismic sources (Avouac et al., 2015) during the earthquake rupture, which run along the ramp-and-flat hinge line at 14–15 km depth. The INDEPTH reflection profile (Hauck et al., 1998) is shown in the cross-section, where the main faults are denoted as black lines, and an electromagneto-telluric image (Lemonnier et al., 1999) highlights the high conductivity (i.e., low resistivity) measured along the MHT. Note the gap between the fault plane of the MHT and the cross-section for clarity.

Due to the friction between the convergent plates, MHT is a fully locked zone over a width of 100 ± 20 km all along the whole Himalayan arc during the interseismic period (Stevens and Avouac, 2015) (Figures 1.5 and 1.6). Interseismic coupling refers to the ratio of the slip rate deficit to the long-term slip rate. Value of 1 means that the fault is purely locked while the value of 0 indicates that the fault is creeping at the long-term slip rate. When the frictional strength of the fault is surpassed, the fault moves, the slip along the fault starts, and an earthquake is triggered by the stress accumulated during the locking time of the fault. After the seismic event, the fault locks again, and stress restarts to build up. The seismic cycle is subsequently formed. The belt of seismicity is located in the area of interseismic stress buildup, where downdip the MHT transitions from locked to a creeping zone (Figure 1.5). The seismicity belt terminates abruptly to the north, where the surface elevation is higher than 3500 m (Avouac, 2015; Stevens and Avouac, 2015).

An earthquake cannot completely rupture the MHT. The rupture processes depend on the topography of fault surfaces (Power and Tullis, 1991), i.e., the locking of the fault. The MHT across the central Himalaya shows a ramp-flat-ramp-flat geometry (Avouac et al., 2015; Elliott et al., 2016; Wang et al., 2017; Jouanne et al., 2017) (Figure 1.5). The upper ramp of the MHT is very shallow and 30° north-dipping, and it reaches the surface as the MFT. The upper flat to the north is 7° north-dipping, nearly totally locked, 75 km wide, and at a depth of 5 km. The 20° north-dipping, 30-km-wide, mid-crustal ramp is partially locked and is termed interseismic decoupling zone, located between fully locked and fully unlocked. It is assumed that the temperature in this segment of the MHT is 350–450 °C (Bilham et al., 2017). The lower flat is 5°–7° north-dipping, the northern part of which is followed by ductile shear zone. The ramps on the MHT are the key to the arrest of seismic rupture and determine the width of the interseismic decoupling zone that is linked to the amount of the critical strain to nucleate rupture (Bilham et al., 2017). The wider the interseismic decoupling zone, the larger the capacity to store strain energy and hence potential slip during seismic rupture. For the temperature-dependent interseismic decoupling zone, if the local dip of the MHT is steep, moderate earthquakes may occur frequently with incomplete rupture and minor slip, but if the dip is gentle, great

11

earthquakes that have the potential to rupture the MHT and even the MFT may occur infrequently with a large slip (Bilham et al., 2017; Dal Zilio et al., 2021). In conclusion, a mega-earthquake may be looming in areas where strain energy was accumulated due to the former incomplete ruptures.
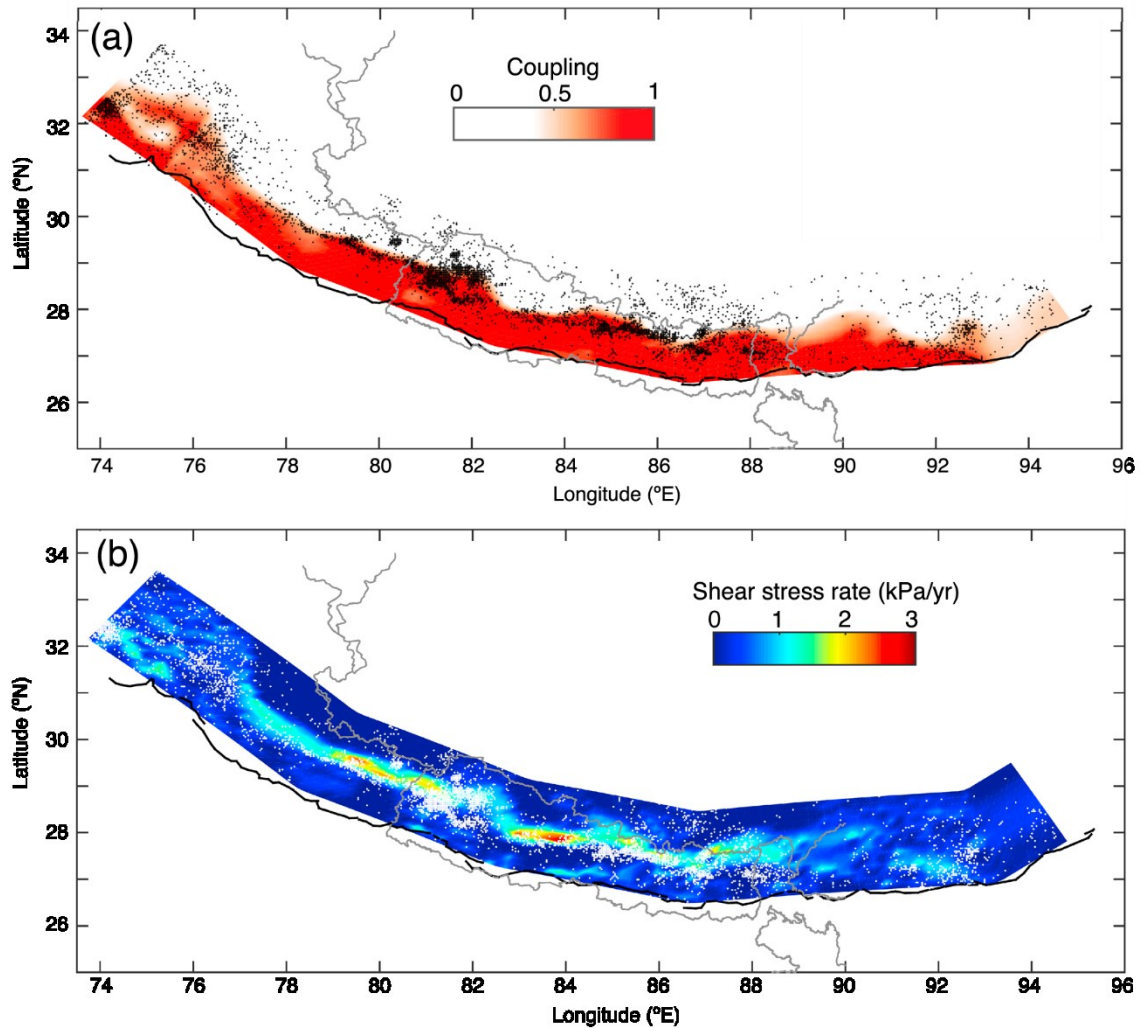
Figure 1.6 (a) Coupling model, adapted from Stevens and Avouac (2015). The distribution of instrumental earthquakes (M$_w$ > 4) is shown as black dots. The seismicity data involve an NSC catalog regarding Nepal (Ader et al., 2012; Rajaure et al., 2013), the record between ~77–81°E (Mahesh et al., 2013), and the others from NEIC. The MFT is indicated as the black line. (b) Shear stress buildup rate on the plane of the MHT, adapted from Avouac (2015). White dots point out the same location of microseismicity as Figure 1.6a.

1.3 Potential Mega-earthquakes in the Himalaya

The typical surface rupture length of subduction-type mega-earthquakes ($M_w >$ 9.0) is at least 1000 km (Wells and Coppersmith, 1994). Combining historical, instrumental, and paleoseismic earthquake catalogs with the use of stress accumulation rate (balancing the slip budget), it was inferred that $M_w \geqslant$ 9.0 mega-earthquakes are likely in the Himalaya with the average return time greater than ~800 years (Stevens and Avouac, 2016). Three of the known historic Himalayan paleo-earthquakes could have been mega-earthquakes: 1) the A.D. 1505 M_w ~8.2 earthquake (Bilham and Wallace, 2005; Kumar et al., 2006; Kumar et al., 2010; Malik et al., 2017), 2) the A.D. 1255 $M_w >$ 8.0 earthquake (Upreti et al., 2000; Mugnier et al., 2011; Sapkota et al., 2013; Bollinger et al., 2014; Wesnousky et al., 2017a; Wesnousky et al., 2017b), and 3) the A.D. ~1100 $M_w >$ ~8.7 earthquake (Lavé et al., 2005; Kumar et al., 2010; Mugnier et al., 2011; Le Roux-Mallouf et al., 2016; Wesnousky et al., 2017a; Wesnousky et al., 2017b; Wesnousky et al., 2019) (Figure 1.4).

1) the A.D. 1505 M_w ~8.2 earthquake. A single great earthquake in about 1505 probably took place even though historical reports of such large earthquake are lacking (Kumar et al., 2006). In Nepal Himalaya, mega-earthquakes with $M_w >$ 8.6 could also occur but be constrained to the Kathmandu area due to its location astride the transition between central and eastern seismotectonic segments of Himalaya (Mugnier et al., 2011; Rajendran et al., 2017).

2) the A.D. 1255 $M_w >$ 8.0 earthquake. Kathmandu was affected by two destructive earthquakes: the 1255 event ($M_w >$ 8) occurred in its west, and the ~1100 event ($M_w =$ ~8.8) in its east (Mugnier et al., 2011). But, according to the observations at three sites in central and eastern Nepal, a large rupture of about 800 km extending across entire Nepal might have occurred in around 1255 (Wesnousky et al., 2017b).

3) the A.D. ~1100 $M_w >$ ~8.7 earthquake. In the eastern Himalaya, the possibility of the rupture extending up to 700–800 km along the MFT and related to ~1100 event, was proposed (Kumar et al., 2010).

1.4 Motivation for the Study

The Himalayan foreland is an earthquake-stricken area. However, little is known about the Himalayan earthquakes in the 18th century and before. The return periods of large earthquakes and the largest possible magnitudes are poorly constrained in the Himalayas. To solve these problems, we need to improve the Himalayan earthquake record by identifying and dating new paleoseismic events and to more precisely constrain the surface rupture length of the known events.

In 2016, a surface rupture along the MFT was identified in eastern Bhutan, one putative seismic gap in the Himalayas. Paleoseismological investigations were conducted to identify and characterize paleoseismic events in eastern Bhutan. Based on surface ruptures investigated in western and central Bhutan and the ages of the known Himalayan large historical earthquakes (Hetényi et al., 2016b; Berthet et al., 2014; Le Roux-Mallouf et al., 2016; Le Roux-Mallouf et al., 2020) (Figure 1.4), I hypothesize that the surface rupture in eastern Bhutan was caused either by the 1714 Bhutan earthquake or by a medieval earthquake of A.D. ~1255 or A.D. ~1100. If the surface rupture in eastern Bhutan were caused by either A.D. ~1255 or A.D. ~1100 event, the location of the study area would extend its surface rupture length to ~1000 km, making it a likely M_w 9 earthquake (Wells and Coppersmith, 1994). Such mega-earthquakes have not yet been found in the Himalaya (Stevens and Avouac, 2016), or any other continental setting.

1.5 Aim and Scope of the Study

This research aims to reconstruct the seismic history of the exposed surface rupture in eastern Bhutan to help develop accurate hazard evaluations and determine the seismic risk in the region. The two main objectives are 1) to identify and characterize surface-rupturing paleoseismic events in eastern Bhutan: a) determine the fault geometry and the amount of coseismic slip along the surface rupture, b) determine the ages of paleo-earthquakes by dating the displaced river terraces applying radiocarbon (^{14}C) dating, conventional optically stimulated luminescence (OSL) thermochronology, and rock surface dating, and by trying to directly date fault gouge using Multi-OSL of feldspar, and c) calculate the most likely magnitudes of paleo-earthquakes, and 2) to estimate the recurrence interval of major earthquakes in the eastern Himalaya.

This research constitutes a major component of the main long-term objective of the Tectonics research group at Dalhousie, which is to understand the dynamic links between mega-earthquakes in the upper crust and deformation in the ductile crust in the continental collision zones.

1.6 Significance of the Study

The Himalayas are known for large, destructive earthquakes and are densely populated. For such areas, it is imperative to build a statistically relevant database of large earthquakes, precisely establish seismic history, and estimate the recurrence interval of large earthquakes for each identified fault. The seismic history of the surface rupture is critical to developing accurate hazard evaluations and determining the seismic risk in the region. The timing and magnitudes of paleo-earthquakes and their return periods are crucial to such evaluations. Therefore, the paleoseismic investigation of the newly identified surface rupture is important to improve the catalog of the Himalayan earthquakes. The results of this project will also contribute to the debate about a potential for subduction-type mega-earthquakes in the Himalaya in general and the understanding of mega-thrust fault mechanics in the continental collision zones.

In short, the projected applications of my research will involve four aspects: 1) increased knowledge on the seismic deformation along the continental mega-thrust, 2) attempt of a method for direct dating of fault slip, 3) improved accuracy of estimates on recurrence intervals of major earthquakes in the region, and 4) improved estimates of the seismic hazard in the region and in the Himalaya in general.

1.7 Structure of the Thesis

This thesis includes eight chapters and is structured as a research paper with an abstract, acknowledgements, introduction, seismotectonic setting of Bhutan Himalaya, dating methodology, paleoseismological results and analysis, respective discussions about the timing of the paleo-earthquakes, magnitudes, and recurrence interval estimation of large earthquakes, conclusion, references, and appendices that consist of specific analytical procedures and supplementary data.

While the first chapter introduces the context, motivation, objectives, significance, and thesis structure, the chapter of *Seismotectonic setting* includes geological setting and the background of the paleo-earthquakes in the Bhutan Himalaya.

Dating Methodology consists of five sections including radiocarbon dating, overview of luminescence dating, and three individual luminescence techniques used in this project. The overview section (3.2) of luminescence dating involves introduction to luminescence, overview of luminescence dating process, shortly introducing luminescence methods and dating aims, and two principal components for luminescence age estimation. Following overview of luminescence dating process, each of the other sections elaborates on what the approach is, what kind of samples were selected for the method, and how it was applied.

The chapter of *Paleoseismological analysis in eastern Bhutan* describes the field area, paleoseismic exposure, samples, sampling sites and locations, the dating results and their analysis. Also, chronostratigraphic frameworks are defined for related methods.

There are three chapters providing in-depth discussions: the timing of the paleo-earthquakes, the most likely magnitudes, and recurrence interval of large earthquakes in the eastern Himalaya. The chapters of *Magnitude calculations* and *Recurrence interval* include the explanations of how these values were calculated in addition to interpretation and discussion of corresponding results.

The conclusion summarizes all the findings and the essence of the research.

1.8 Note of Caution

This thesis uses a naming method for geological events that is contrary to the usual standard. E.g., U1 is the youngest stratigraphic unit, and U4 is the oldest unit in this study. Similarly, the youngest ones about the river terraces, faulting, and seismic events are T1, F1, and E1. The reason for naming this way is to maintain consistency with the previously published research papers regarding the Himalayan region, most of which used #1 as the youngest. It is because this thesis cited many previous works regarding the

Himalayan region and did a series of comparisons with the corresponding parts in these works. It is also to avoid unnecessary confusion during reading and searching the published work. We cannot revise others' works, which have been already published, but ours.

CHAPTER 2: SEISMOTECTONIC SETTING OF BHUTAN HIMALAYA

2.1 Geological Setting
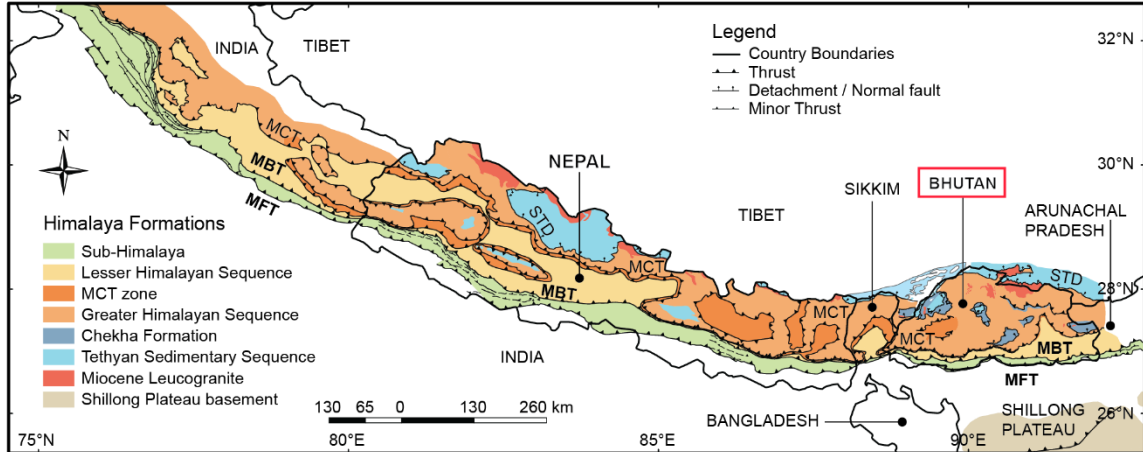
Figure 2.1 Geological map of the Himalayan orogen. Adapted from Hirschmiller et al. (2014). The major features presented within the orogen are: STD—South Tibetan detachment, KT—Kakhtang thrust, MCT—Main Central thrust, MBT—Main Boundary thrust, and MFT—Main Frontal thrust. The red rectangle highlights the area of Bhutan.

Similar to all other Himalayan segments (Hodges, 2000; Avouac, 2015), Bhutan Himalaya presents four distinct lithotectonic units bounded by faults and shear zones (Figure 2.1). From north to south, the four units are the Tethyan Sedimentary Sequence (TSS), Greater Himalayan Sequence (GHS), Lesser Himalayan Sequence (LHS), and Sub-Himalaya. Their boundary structures are the South Tibetan Detachment (STD), MCT, MBT, and MFT (Figures 2.2 and 2.3). All the thrust faults merge into the MHT (Nelson et al., 1996). The STD is a shallowly northward dipping normal ductile shear zone that separates the TSS from the GHS (Kellett and Grujic, 2012). The GHS consists of amphibolite-to-granulite metamorphic-grade rocks make the orogen's metamorphic core (Long and McQuarrie, 2010). Two major features different from the rest of the Himalayas are presented within the GHS in Bhutan (Grujic et al., 2002; Zeiger et al., 2015) (Figures 2.1 and 2.2): (1) extensive klippe of the STD, overlying the GHS, and (2) out-of-sequence Kakhtang thrust (KT) that structurally divides the GHS into the upper and lower parts and makes its thickness double.

2.1.1 Lesser Himalayan Sequence
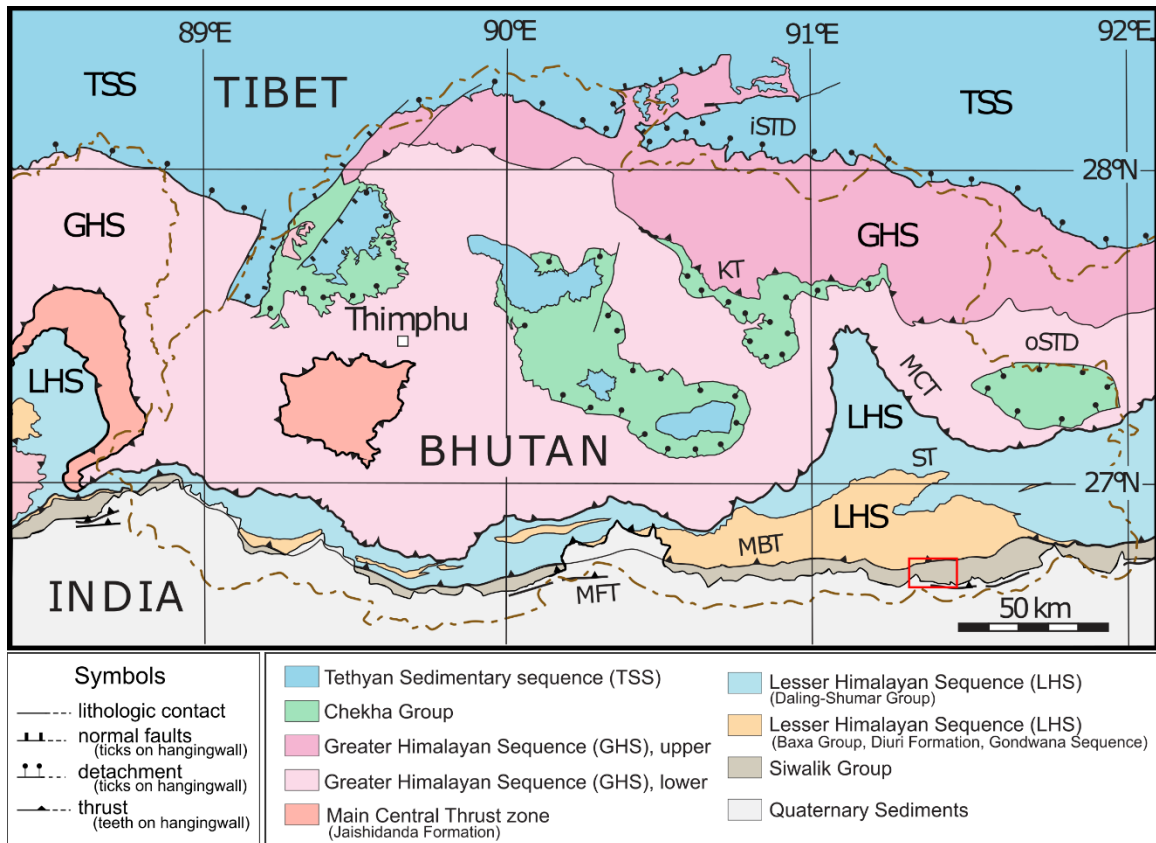
Figure 2.2 Geological map of Bhutan. Adapted from Grujic et al. (2020). Red square indicates the area of Figure 2.4. oSTD, iSTD—outer and inner South Tibetan detachment system, respectively; KT—Kakhtang thrust; MCT—Main Central thrust; ST—Shumar thrust; MBT—Main Boundary thrust; MFT—Main Frontal thrust.
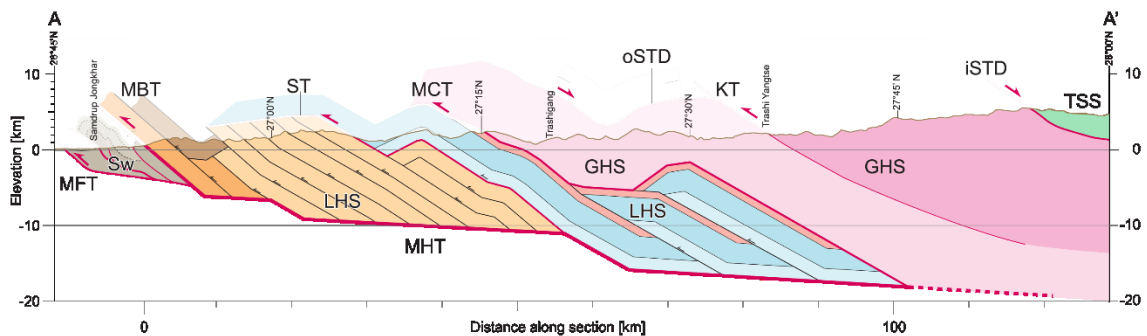
Figure 2.3 Structural cross section of eastern Bhutan along ~91.5°E. Adapted from Grujic et al. (2020). TSS—Tethyan sedimentary sequence, GHS—Greater Himalayan Sequence, LHS—Lesser Himalayan Sequence, Sw—Siwalik, oSTD & iSTD—outer & inner South Tibetan detachment, KT—Kakhtang thrust, MHT—Main Himalayan thrust, MCT—Main Central thrust, ST—Shumar Thrust, MBT—Main Boundary Thrust, MFT—Main Frontal Thrust.

The LHS is separated from the GHS by the MCT shear zone and from the Sub-Himalaya by the MBT. It contains four units: from north to south and oldest to youngest,

the Daling-Shumar Group, Baxa Group, Diuri Formation, and Gondwana Sequence (McQuarrie et al., 2008; McQuarrie et al., 2013; McQuarrie et al., 2014; Long et al., 2011c) (Figures 2.2 and 2.3). The Shumar Thrust (ST) (Ray et al., 1989; Long et al., 2011c; Grujic et al., 2020) separates the upper Daling-Shumar Group and the lower three units. The Daling-Shumar Group is a ~4 km thick phyllite-dominant Daling Formation, the Shumar Formation quartzite, and Proterozoic granitoid. The Baxa Group involves a combination, from quartzite to siltstone, from slate to dolomite and limestone. In western Bhutan, the Baxa Group represents similar lithological features to correlative strata in Sikkim and central Nepal but is different from the one in eastern Bhutan and Arunachal Pradesh regarding provenance and depositional environment (McQuarrie et al., 2008). While the Diuri Formation mainly consists of ~2–2.5 km thick diamictite and interbedded pebbly slates, the Gondwana Sequence is dominated by continental sediments containing sandstone, quartzite, shale, slate, and coal deposits.

2.1.2 Siwalik Group
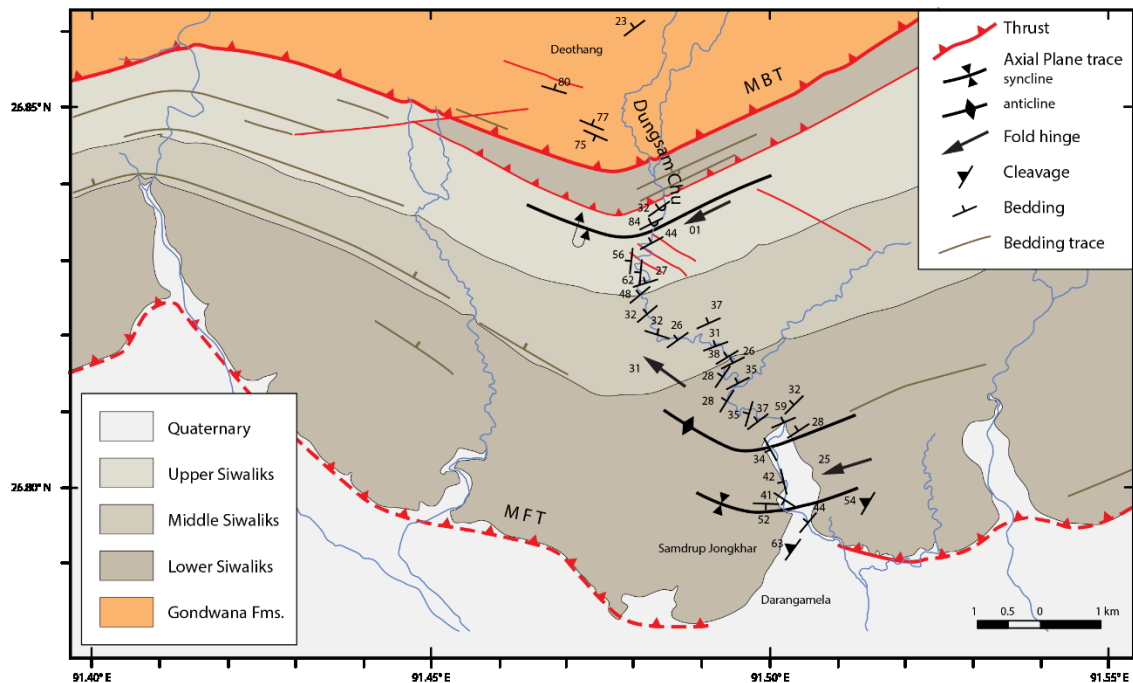
Figure 2.4 Geological map of the Siwalik Group. Adapted from Grujic et al. (2018). MBT—Main Boundary Thrust, MFT—Main Frontal Thrust.

The Sub-Himalaya in Bhutan consists of Siwalik Group sediments, but they are not exposed in the central and westernmost region (McQuarrie et al., 2014) (Figure 2.2). In western and eastern Bhutan, Late Miocene, Siwalik sediments were thrust over Quaternary fluvial sediments, whereas in central Bhutan, the thrusting over Quaternary alluvial sediments were metasediments of the LHS sequence. Synorogenic, Neogene-Quaternary foreland sediments of the Siwalik Group (Coutand et al., 2016) belong to the modern Himalayan foreland fold-and-thrust belt as defined by Hirschmiller et al. (2014), which is bounded to the north by the MBT and to the south by the MFT. The Siwalik Group is divided into three groups (Coutand et al., 2016): from oldest to youngest, lower, middle and upper (Figure 2.4). It mainly contains siltstone, sandstone and conglomerate, corresponding to the sequence from lower to upper, i.e., it coarsens upward (Long et al., 2011c; Coutand et al., 2016). The depositional ages of the Siwalik sediments along the Dungsam Chu were determined by magnetostratigraphy in combination with vitrinite reflectance data and detrital apatite fission track dating (Coutand et al., 2016). The base of the lower Siwalik was dated to ~7 Ma, middle Siwalik at ~6 Ma, and upper Siwalik at ~3.8 Ma, whereas the top of the upper Siwalik is ~1 Ma. The onset of folding and shortening of the Siwalik sediments in eastern Bhutan was constrained at approximately 1–2 Ma. Along the Dungsam Chu section, all three subgroups structurally show northward dipping with the range of 25° to 84°, and most of the dip angles are between 25°–45° (Figure 2.4).

2.1.3 Main Central Thrust

The MCT is a few kilometers thick ductile shear zone with top to the south shear sense. The related mylonitic belt contains the protolith boundary between the overlying GHS and the underlying LHS (Long et al., 2011a; Starnes et al., 2020) (Figure 2.3). In eastern Bhutan, the initiation of MCT displacement was ~23–20 Ma (Daniel et al., 2003; Chambers et al., 2011), and remained active until ca. 11 Ma (Grujic et al., 2020). In western Bhutan, MCT displacement occurred between ~20 and 15 Ma (Tobgay et al., 2012). The rate of displacement on the MCT in eastern Bhutan was 2.6–4 cm/yr whereas in western Bhutan was 3–7 cm/yr (Tobgay et al., 2012).
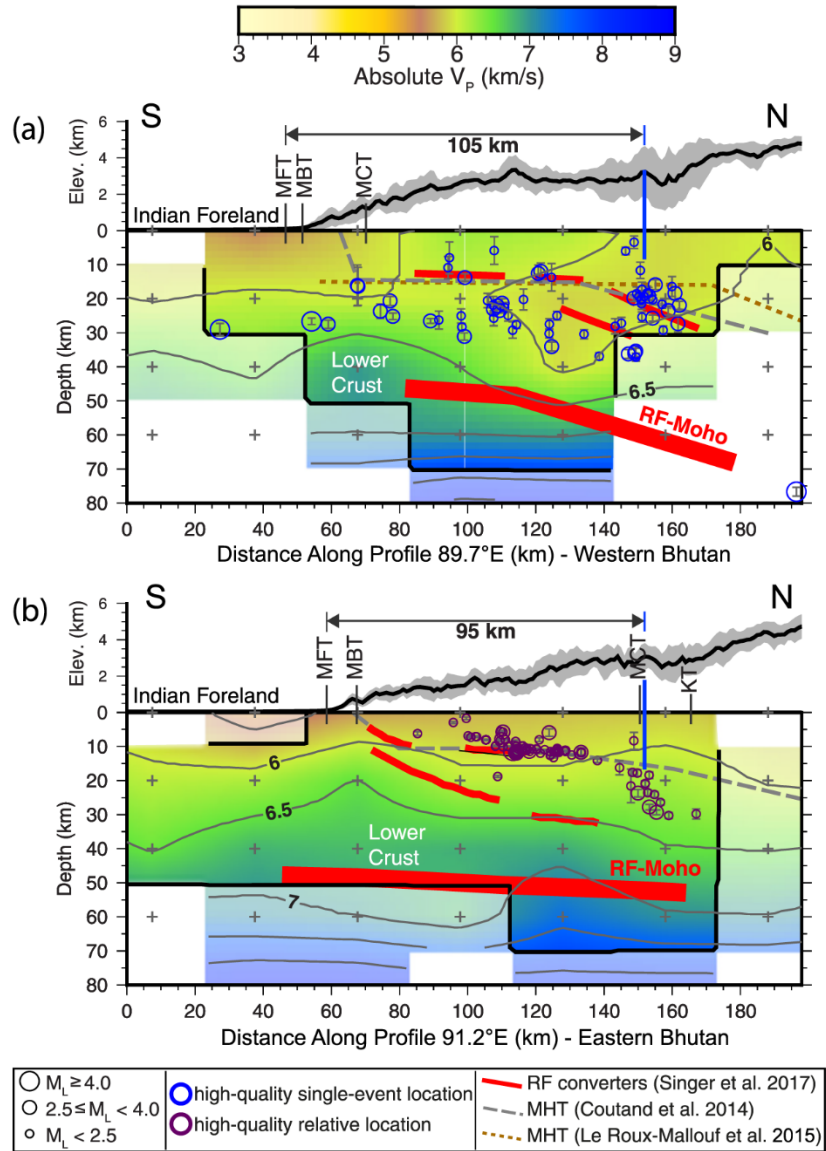
Figure 2.5 Cross-sections of the MHT geometry in the Bhutan Himalaya. Adapted from Diehl et al. (2017). (a) Profile along 89.7°E, western Bhutan. (b) Profile along 91.2°E, eastern Bhutan. Red solid lines show receiver-function (RF) converters (Singer et al., 2017). Thick gray dashed lines indicate the geometry of the MHT from Coutand et al. (2014). Brown short dash line marks the MHT geometry in western Bhutan (Le Roux-Mallouf et al., 2015). Blue circles point out the seismicity of single-event whereas purple circles show relocated seismicity using relative double-difference techniques. The colored base map represents crustal P-wave velocity (V_p) structure along the western and eastern profile of Bhutan, with the solid gray contour lines of absolute V_p in km/s. Bold black lines represent the topography along profiles generated by mean value and standard deviation. Blue vertical lines show seismicity position regarding potential mid-crustal ramps. KT—Kakhtang thrust, MHT—Main Himalayan thrust, MCT—Main Central thrust, MBT—Main Boundary Thrust, MFT—Main Frontal Thrust.

The LHS consists of two types of hinterland-dipping thrust duplex system (Long et al., 2011a) (Figure 2.3). The one within the hanging wall of the ST consists of a few

large horses, called the internal duplex, whose top is the MCT. The other is the external duplex formed by smaller horses, which has the ST as the roof thrust and the MBT as the floor thrust. The external duplex was developed between 14.9 and 10.5 Ma in eastern Bhutan (Long et al., 2011a) while between 12 and 9 Ma in western Bhutan (McQuarrie et al., 2014).

2.1.4 Main Boundary Thrust

The MBT is a north-dipping thrust that placed the LHS over the Subhimalaya (Long et al., 2011a) (Figure 2.3). The MBT were also folded and shortened in the eastern Himalaya since 10 Ma (McQuarrie et al., 2008; McQuarrie et al., 2014). While the development of the MBT in the northwestern Himalaya has been constrained between ~14–13 Ma (Singh and Patel, 2022), the onset age of the MBT is less well-constrained in Bhutan since there are no good, continuous outcrops found in the eastern Himalaya (McQuarrie et al., 2014). The GPS data (2013–2016) indicated that partial aseismic creep has been occurring on the MBT in eastern Bhutan, i.e., the MBT is presently part of the active thrusting front in eastern Bhutan (Marechal et al., 2016). This implies that a seismic event like the April 2015 Gorkha earthquake (M_w 7.8) might potentially occur in eastern Bhutan with incomplete rupture on the MHT and the absence of surface slip.

2.1.5 Main Frontal Thrust

The MFT places the Siwalik Group against the Quaternary sediments (Figures 2.3 and 2.4). The motion of the MFT contributed to the tilting of Late Miocene to Pleistocene foreland basin deposits (Hirschmiller et al., 2014; Coutand et al., 2016). The thrusting on the MFT started at ~2 Ma in Central Nepal (Mugnier et al., 2004; van der Beek et al., 2006) and at ~1 Ma in Arunachal Pradesh (Chirouze et al., 2013), but the onset timing of the MFT in Bhutan is still unknown.

The MFT is the surface expression of the MHT along the Himalayan front. In central Bhutan, there are at least three splays of the MFT (Nakata, 1972; Berthet et al., 2014) (Figure 2.2), the northernmost branch of which is known as the TFT (Topographic Frontal Thrust) and has been investigated in all paleoseismic studies in Bhutan. In

Bhutan, the MHT mainly consists of three segments, and its ramp-flat-ramp geometry varies along strike between the western and eastern (Coutand et al., 2014; Diehl et al., 2017) (Figure 2.5). The southernmost frontal ramp is north-dipping at 65–70° and rooted at ~15 km in the west while 40° north-dipping and rooted at ~10 km in the east. The middle flat section is wider in western Bhutan where it extends from 26.8 to 27.3°N relative to 27–27.3°N in the east. The northernmost segment of the MHT at the north of 27.5°N is a mid-crustal ramp dipping northward at 30°, the same in the west and east. The difference in the MHT geometry between western and eastern Bhutan contribute to the west-east variations in coupling along the detachment (Figure 2.6). In western and central Bhutan, the width of the fully locked zone on the MHT is reported as ~100 km (Li et al., 2020) to 135–155 km (Marechal et al., 2016) and limited by an abrupt downdip transition at its northernmost boundary. It is indicated as the area of interseismic stress buildup according to the location of the local seismicity belt (Diehl et al., 2017). Le Roux-Mallouf et al. (2015) suggested that the wider and gentle coupling zone on the MHT could have greater seismogenic potential in western Bhutan. In eastern Bhutan, the fully coupled zone is ~70 km (Li et al., 2020) to 100–120 km (Marechal et al., 2016) wide and confined updip and downdip by partial coupling zones. GPS data indicate that the updip frontal ramp shows an aseismic slip rate of 5.5–14.5 mm/yr within 50 km north of the MFT (Marechal et al., 2016). Diehl et al. (2017) inferred the potential to generate large earthquakes in eastern Bhutan attributed to the flat, seismogenic section of the MHT imaged using receiver functions and recorded seismicity. In the areas with a gentle dip of the MHT, a full rupture could occur on the MHT and even the MFT during great earthquakes. The segment in eastern Bhutan is thought to host a potential slip of more than 10–12 m (Bilham, 2019; Robinson, 2020), which implies a high seismic hazard (Stevens et al., 2020).

The MFT is the structure that almost completely accommodates the geodetic shortening rate of 15–21 mm/yr in the central and eastern Himalayas during the Holocene (Lavé and Avouac, 2000; Lavé and Avouac, 2001; Ader et al., 2012; Burgess et al., 2012; Berthet et al., 2014). According to Li et al. (2020), the estimated convergence rates in western and eastern Bhutan are 18.5 ± 1.0 and 16.2 ± 1.5 mm/a, respectively. Both are

24

consistent with the 17 ± 2 mm/a estimated by Marechal et al. (2016). The cumulative deformation values derived from paleoseismic data yield an average slip rate of 24.9 ± 10.4 mm/a along the MFT over the last 2,600 years (Le Roux-Mallouf et al., 2020). The age and geometry of uplifted river terraces across the eastern Himalayas indicate a convergence rate of 23 ± 6.2 mm/a (Burgess et al., 2012). The potential discrepancy between the millennial-scale slip rate from geological studies and geodetic estimates suggests that some of the interseismic deformations in Bhutan could be anelastic.
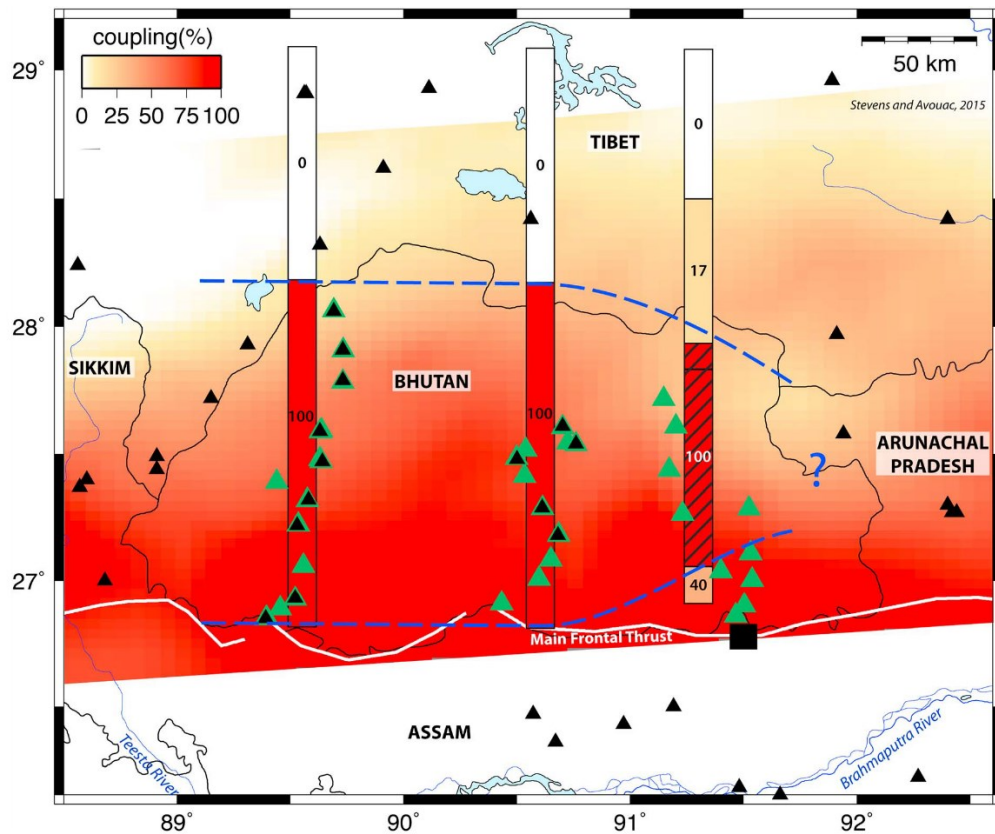
Figure 2.6 Interseismic coupling on the MHT in the Bhutan Himalaya. Adapted from Marechal et al. (2016). The estimates of interseismic coupling of the MHT segments are shown by rectangles. Blue dash lines mark the approximate limits of the fully coupling zone on the MHT. Triangles indicate the locations of GPS stations. The black square points out the Dungsam Chu site (the study area).

2.2 Active Tectonics of Bhutan

The Bhutan Himalaya and its foreland are bound by two oblique strike-slip zones, the Dhubri-Chungthang Fault (DCF) zone in the west evidently extending beneath the
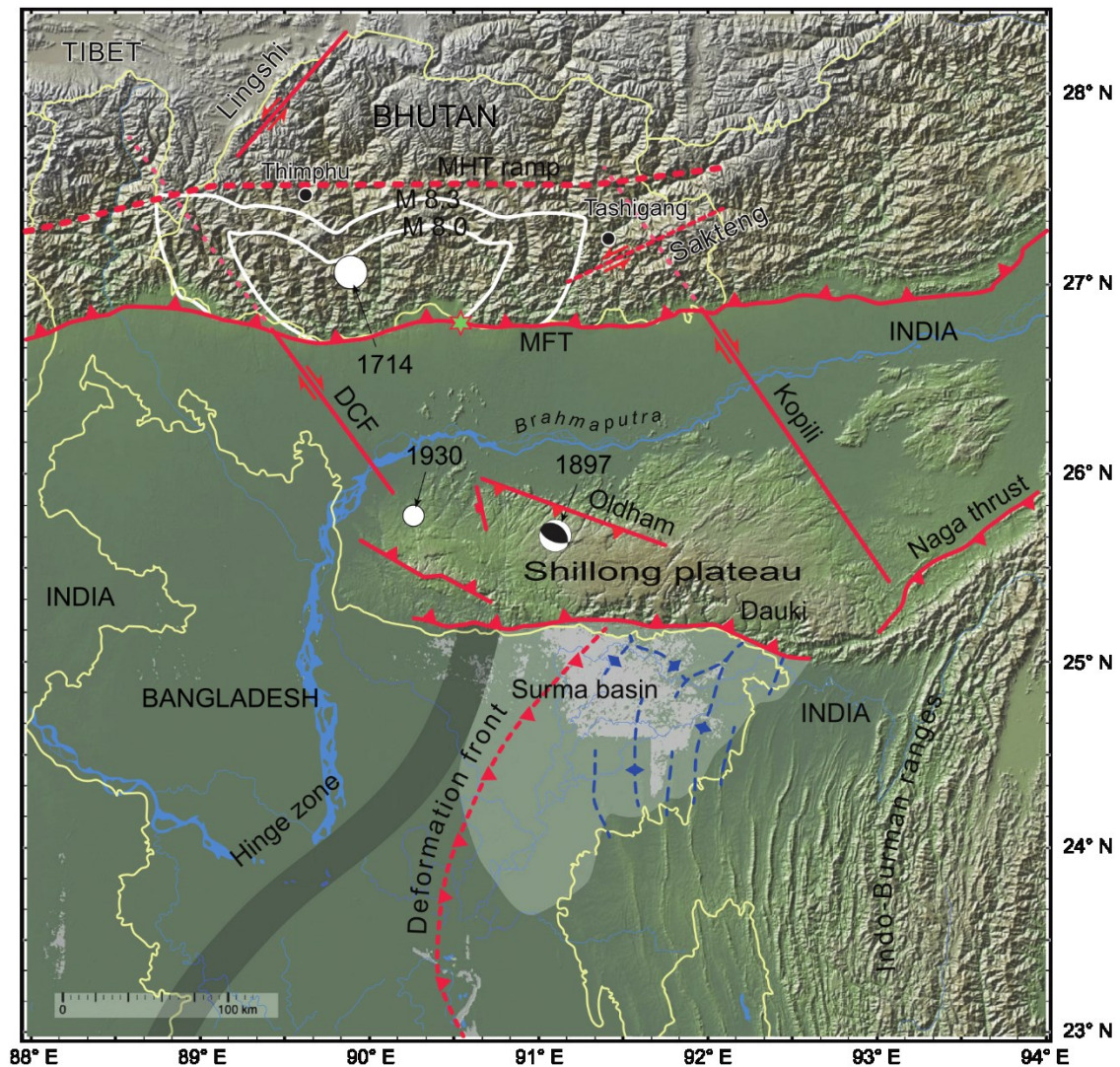
Figure 2.7 Active tectonic map showing the network of faults in the Bhutan Himalaya. Adapted from Grujic et al. (2018). Fault traces are represented in red, and those shown as dashed lines demonstrate that there is no surface trace in the seismogenic fault. Dashed fault traces in pink show that the fault is beneath the Himalayan orogenic wedge. The likely epicenters of the 1714 (M_w 8 ± 0.5), 1897 (8.15 < M_w < 8.35), and 1930 (M_w 7.1) earthquakes (Hetényi et al., 2016b; England and Bilham, 2015; Gee, 1934; Szeliga et al., 2010) are depicted as white circles. Regarding the 1714 earthquake, the presumed hypocenter location along the MHT is shown as white contours, and the surface rupture identified along the MFT is indicated as a green star (Hetényi et al., 2016b; Berthet et al., 2014; Le Roux-Mallouf et al., 2016). The deformation front is a blind thrust of the Indo-Burman Ranges (Steckler et al., 2016). The darker blue lines in the Surma basin illustrate hinges of buried anticlines within the same accretionary wedge (Najman et al., 2016). MHT—Main Himalayan thrust, MFT—Main Frontal Thrust, and DCF—Dhubri-Chungthang Fault.

Himalayan orogenic wedge (Diehl et al., 2017; Grujic et al., 2018) and the Kopili Fault zone in the east with a more diffuse and less clear continuation north of the Himalayan front (Sutar et al., 2017) (Figure 2.7). Both fault zones extend southeastward across the

Brahmaputra basin and border the Shillong Plateau to the west and east, respectively. The two seismic zones appear to affect only the Indian basement, i.e., the Himalayan crust beneath the MHT, and they are capable of generating earthquakes with $M_w > 7$ but have no associated surface or geological deformation (Diehl et al., 2017; Sutar et al., 2017; Grujic et al., 2018). Two other conjugate, sinistral, strike-slip faults, Lingshi and Sakteng (Gansser, 1983; Grujic et al., 2018), appear to affect only the orogenic wedge with the evidence of clear geological offsets (Long et al., 2011b) (Figure 2.7).

The Shillong Plateau is bound by two reverse faults, i.e., the northward-dipping Dauki Fault to the south (Biswas et al., 2007; Clark and Bilham, 2008) and the south-dipping Oldham Fault to the north (England and Bilham, 2015) (Figure 2.7). The Dauki fault shows a cumulative displacement of > 10 km (Biswas et al., 2007), but no related major earthquakes have been observed or recorded. In contrast, the Oldham fault produced an earthquake of $8.15 < M_w < 8.35$ in 1897 (England and Bilham, 2015) but has no mappable displacement, and its surface trace remains elusive (Rajendran et al., 2004).

2.3 Large Historical Seismic Events in the Bhutan Himalaya

The 2009 M_w 6.1 earthquake (USGS, 2020) is the only earthquake instrumentally observed in Bhutan with a focal solution compatible with slip along the MHT. No large earthquakes ($M_w > 6.4$) occurred in Bhutan in the past 300 years (Drukpa et al., 2006), which raises the possibility of a major or great earthquake striking this area. The most recent paleoseismological study at the Piping site in western Bhutan indicated at least five paleoseismic events (E1–E5) occurred between 610 B.C. and A.D. >895 (Le Roux-Mallouf et al., 2020).

2.3.1 The 1714 Bhutan Earthquake

The A.D. 1714 earthquake is the only historically recorded earthquake in Bhutan and has been identified in paleoseismic studies at Sarpang, Gelephu, and Piping in central and western Bhutan (Berthet et al., 2014; Le Roux-Mallouf et al., 2016; Le Roux-Mallouf et al., 2020). Combining recently historical and paleoseismic constraints, Hetényi et al. (2016b) determined that this earthquake occurred on May 4, 1714, and reached M_w 7.5–

8.5 with a modeled hypocenter located in central or western Bhutan (Figure 2.8). This surface-rupturing event caused 1.5 ± 0.5 m of coseismic dip-slip at the Piping site (western) and up to 0.5 m of vertical offset at the Sarpang Chu site (central).
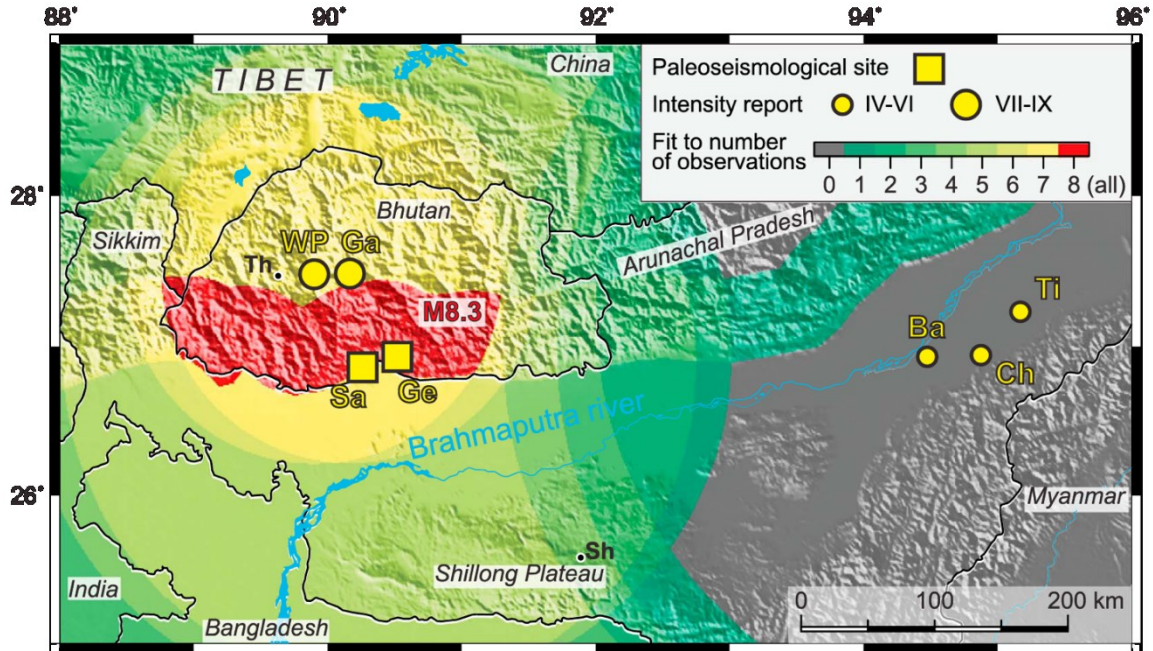
Figure 2.8 Hypocenter location of the A.D. 1714 earthquake. It was constrained by applying paleoseismological evidence of surface ruptures and historical intensity reports, for a M8.3 earthquake scenario, and labelled using red color. Adapted after Hetényi et al. (2016b). Two paleoseismological investigation sites of surface ruptures are at Sarpang (Sa) and Gelephu (Ge). Five intensity report locations include Wangdue Phodrang (WP), Gangteng (Ga), Bahgara (Ba), Charaideo Hill (Ch), and Tinkhong (Ti). Cities: Th—Thimphu, Sh—Shillong.

2.3.2 The Medieval Earthquake

At least one great medieval earthquake was observed in Bhutan. It was dated to A.D. 1344 ± 130 in western Bhutan and associated with 12.2 ± 2.8 m of coseismic dip-slip, which indicates the likely occurrence of a great ($M_w > 8.5$) earthquake (Le Roux-Mallouf et al., 2020), while in central region, it was constrained between A.D. 1025 and A.D. 1520 and produced a coseismic surface slip of 16–23 m, which corresponds to M_w ~8.7 (Le Roux-Mallouf et al., 2016).

Two known great paleo-earthquakes occurred during the age constraints yielded by Le Roux-Mallouf et al. (2016 & 2020) are the A.D. ~1100 and A.D. 1255 earthquakes, both reported in east-central Nepal (Lavé et al., 2005; Pant, 2002; Mugnier

et al., 2011; Sapkota et al., 2013; Bollinger et al., 2014; Wesnousky et al., 2017a; Wesnousky et al., 2017b; Wesnousky et al., 2019). The A.D. ~1100 earthquake is so far the greatest event identified in the Himalayas, mapped in trenches in West Bengal (Kumar et al., 2010), central Bhutan (Le Roux-Mallouf et al., 2016; Le Roux-Mallouf et al., 2020), and eastern Arunachal Pradesh (Kumar et al., 2010), all exhibiting consistent coseismic slip and chronology (Figure 2.9). Radiocarbon-modelled constraints on the timing of this event by Le Roux-Mallouf et al. (2016) yielded a scenario of a single mega-event between A.D. 1090 and A.D. 1145 with a 95.4% probability. This age constraint on the single giant seismic event results in the likely surface rupture length of ~800 km, making it reach M_w 8.9±0.2 (Le Roux-Mallouf et al., 2016) (Figure 1.2). Alternative modeling of radiocarbon data (Le Roux-Mallouf et al., 2016) also indicates that the A.D. ~1100 event may be part of a series of events between A.D. 1025 and A.D. 1520 instead of one mega-event.

The second great medieval earthquake was the historically recorded 1255 earthquake (Pant, 2002), which has also been identified in paleoseismic studies at Tribeni and Bagmati sites (Wesnousky et al., 2017a) in central Nepal, at Damak (Wesnousky et al., 2017b) in east-central Nepal, and at Horkse site (Upreti et al., 2000) and Chalsa site (Kumar et al., 2010) in West Bengal (Figure 2.9). Combined with the later paleoseismic evidence reported by Le Roux-Mallouf et al. (2016 & 2020), the 1255 event might have produced a large rupture of >800 km not only extending across entire Nepal but beyond Nepal to central Bhutan, which is associated with the magnitude of 8.6 to >9 (Wesnousky et al., 2017b).

2.3.3 The Earthquakes Before the Medieval Period

Three seismic events (E3–E5) reported by Le Roux-Mallouf et al. (2020) occurred at A.D. 300 ± 70, 100 ± 160 B.C., and 485 ± 125 B.C., respectively, and they noticeably constitute the oldest paleo-earthquakes characterized in the eastern Himalayas (Figure 2.9). The three events were associated with 14.7 ± 7.4 m, 13.5 ± 0.6 m, and at least 11.5 m of coseismic dip-slip, respectively (Le Roux-Mallouf et al., 2020).
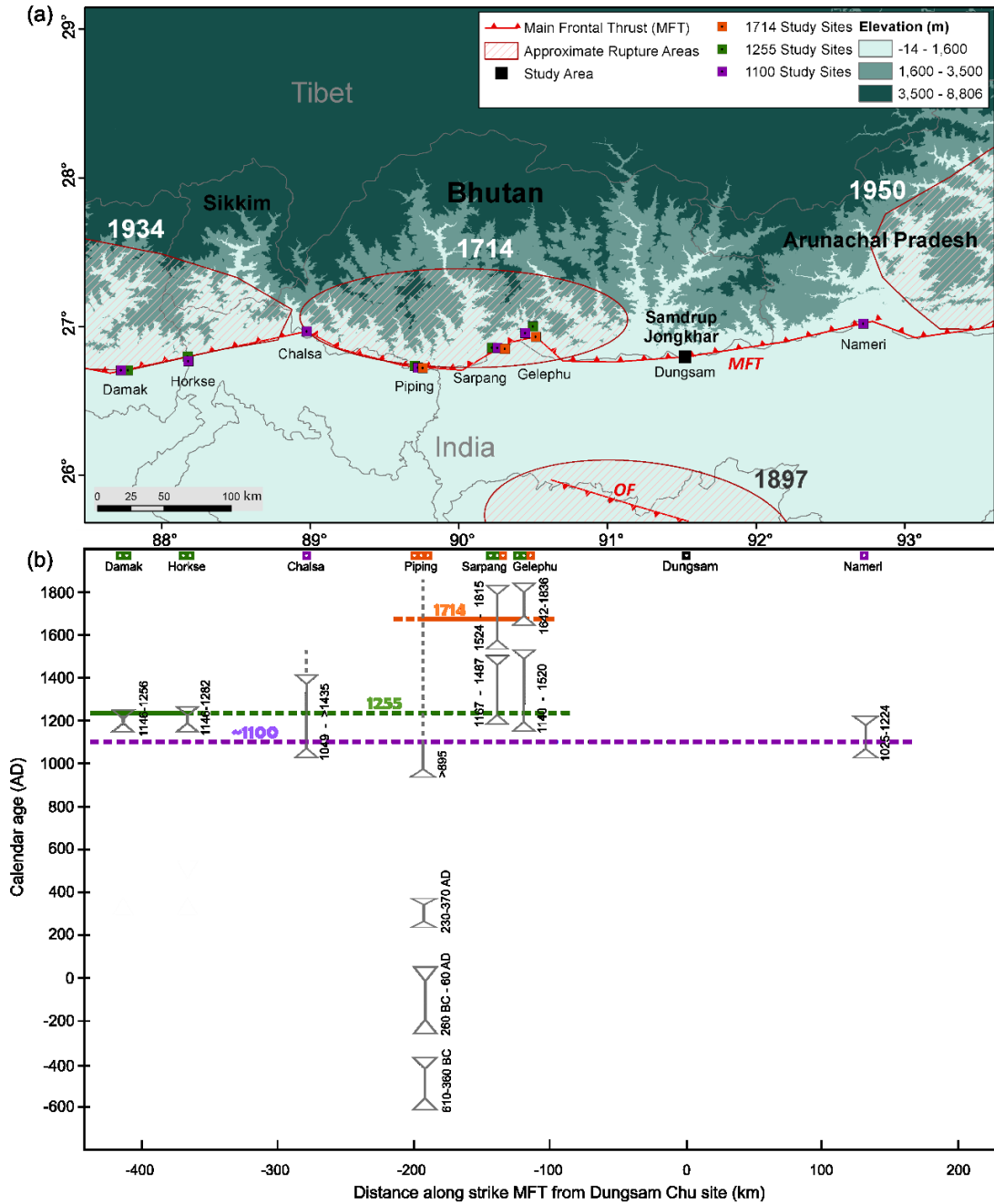
Figure 2.9 (a) Map of major earthquakes in the Bhutan Himalaya and vicinity. Dark-red stripe-pattern ellipses schematically indicate the rupture areas along the MHT, caused by known earthquakes. The small colored squares show paleoseismological investigation sites for the A.D. ~1100 (purple), A.D. 1255 (green), and A.D. 1714 (orange) events: Damak (A.D. 1146–1256; Wesnousky et al., 2017b), Horkse (A.D. 1146–1282; Upreti et al., 2000), Chalsa (A.D. 1049– >1435; Kumar et al., 2010), Piping (five events identified: after A.D. 895 for the most recent two, A.D. 300 ± 70, 100 ± 160 B.C., and 485 ± 125 B.C.; Le Roux-Mallouf et al., 2020), Sarpang (two events identified: A.D. 1167–1487 and A.D. 1524–1815; Le Roux-Mallouf et al., 2016), Gelephu (two events identified: A.D. 1140–1520 and A.D. 1642–1836; Le Roux-Mallouf et al., 2016), and Nameri (A.D. 1025–1224; Kumar et al., 2010). The black square points out the Dungsam Chu site (the study area). MFT—Main Frontal thrust. (b) Space-time diagram of surface-rupturing paleoseismic events identified along the MFT in the Bhutan Himalaya and vicinity.

30
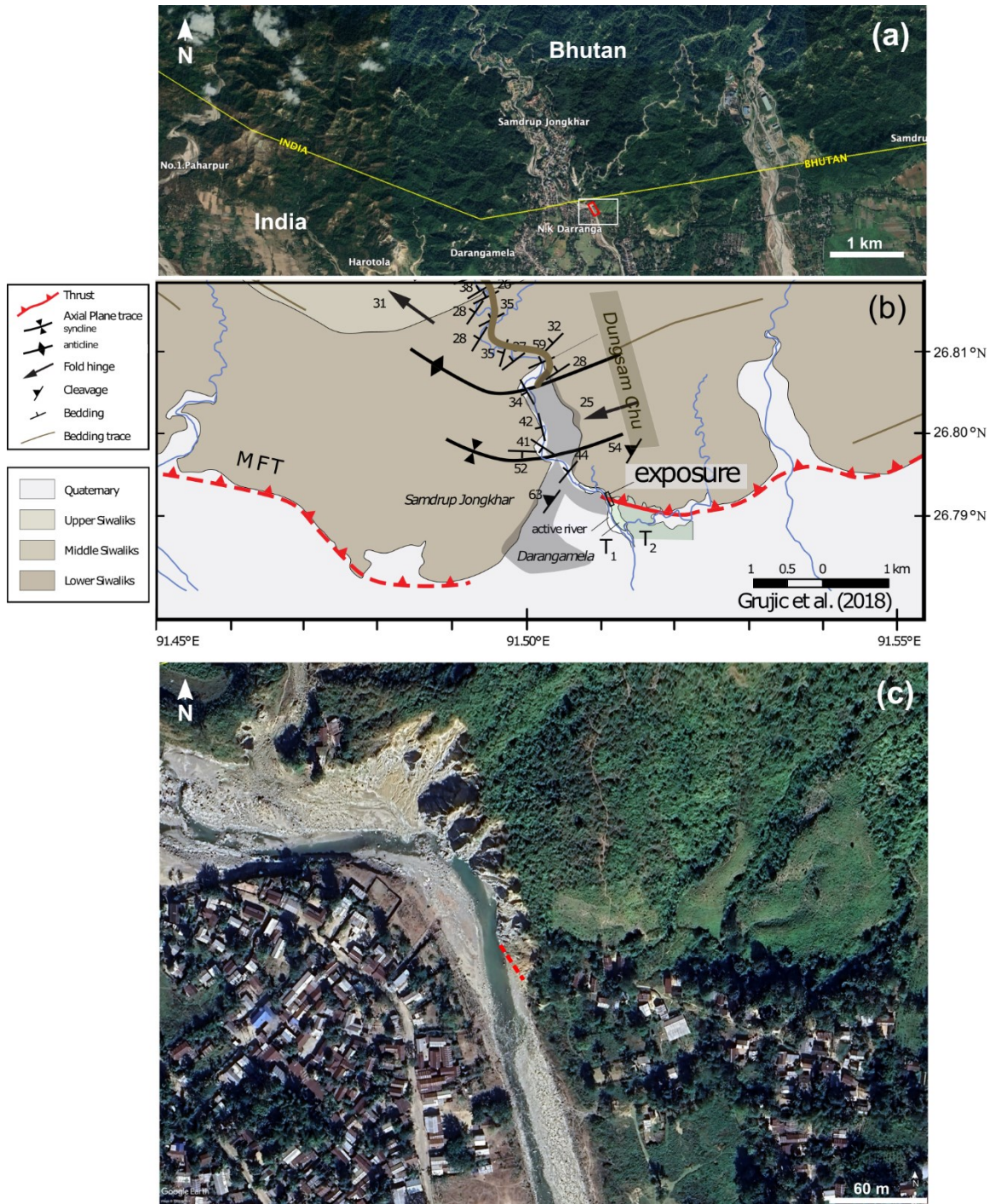
Figure 2.10 Location of the surface rupture exposure at the Dungsam Chu site (the study site), demonstrated as the red rectangular in (a) the Google map, as the corresponding black rectangular in (b) the geological map, and as the mark of the red dash line in (c) the zoom-in Google map. White rectangular in (a) indicates the area of (c). T1— a cut-in-fill terrace, T2— a fill terrace, and MFT—Main Frontal Thrust.

According to Le Roux-Mallouf et al. (2020), all five events (E1–E5) provide an average recurrence interval of 550 ± 211 years (Figure 2.9). For the earlier four events

(E2–E5), an average recurrence interval of 610 ± 238 years is indicated. A cumulative slip of 40.4 ± 10.8 m presents for E2, E3, and E4, with a slip rate of 24.9 ± 10.4 mm yr^{-1}.

2.4 Field Area

The primary study site (26.792014°N, 91.511164°E) of this research is located near the boundary between Samdrup Jongkhar in eastern Bhutan and Darangamela in Assam, India, and it is along the left riverbank of Dungsam Chu, which is a tributary of the Pagaldiya River that flows southwards to the Brahmaputra (Figure 2.10). There, the MFT crosses the Dungsam Chu. The river-cut exposure facing west-southwest (WSW) reveals two distinct Holocene terrace levels, a fill terrace (T2) and a cut-in-fill terrace (T1), and that the Late Miocene Lower Siwalik mudstone and siltstone were thrust over the river terraces by the shallow north dipping MFT (Figure 2.10b). The detailed results of field investigations are described in Chapter 4.

CHAPTER 3: DATING METHODOLOGY

Four dating techniques have been applied in this research to avoid the limitation caused by any single one and to constrain the timing of the paleo-earthquakes accurately and precisely. They include (1) indirect dating of faulting by dating rock layers affected by faulting and (2) direct dating of faulting by dating the rocks formed during faulting.

Three indirect fault-dating methods were used together to determine the burial age of the youngest displaced river terrace layer yielding the maximum ages of a paleo-earthquake. These methods are: (a) radiocarbon (^{14}C) dating (Section 3.1), (b) conventional optically stimulated luminescence (OSL) (Section 3.3), and (c) rock surface dating (Section 3.4). They were selected based on the sedimentary features and structure of the outcrop, including the presence of organic materials, fluvial deposits, and cobbles in the layer. However, the lack of the undisturbed layer significantly reduces the accuracy of these indirect fault-dating techniques despite their high analytical precision. To obtain the direct ages of the seismic events, two OSL methods were attempted. (c) Multi-OSL of feldspar (Section 3.5) have been tested to date fault gouge produced during the paleoseismic movement. (d) High precision rock surface dating (Section 3.4) of the cobbles trailed along the thrust surface was performed.

3.1 Radiocarbon Dating

3.1.1 Introduction

Radiocarbon dating is among the first developed radiometric techniques and has been most widely promoted and applied even though its effective time range is relatively short and just within the late Holocene (Walker, 2005). In 1946, physical chemist Willard F. Libby first proposed a ground-breaking idea that organic materials might be dated by the measurement of their ^{14}C content, which was newly discovered radioactive isotope of carbon (Taylor, 1987). In 1949, radiocarbon dating was successfully tested by Libby and Arnold, and the results were subsequently published (Libby, 1961).

Radiocarbon ^{14}C is the heaviest but the least abundant of three naturally occurring isotopes of carbon: it only accounts for 10^{-10}% of the element while ^{12}C forms around 98.9% and ^{13}C around 1.1% (Walker, 2005; Hajdas, 2008). ^{14}C is the only unstable isotope of carbon, and it goes through beta (β) decay process constantly, by which β particles are released as atoms of ^{14}C decay to stable atoms of nitrogen ^{14}N (Walker, 2005; Hajdas, 2008).

$$^{14}_{6}C \rightarrow {}^{14}_{7}N + {}^{0}_{-1}\beta^- \tag{3.1}$$

^{14}C is formed continuously in the upper atmosphere as cosmic ray neutrons, which are produced when cosmic rays reach the Earth's atmosphere from deep space, react with nitrogen ^{14}N.

$$^{14}_{7}N + n \rightarrow {}^{14}_{6}C + p \tag{3.2}$$
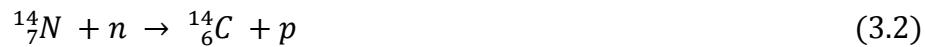
where n represents a neutron and p refers to a proton (Libby, 1961; Hajdas, 2008; Ramsey, 2008) (Figure 3.1). ^{14}C is rapidly converted into carbon dioxide ($^{14}CO_2$) through oxidation in air and enters the global carbon cycle (Libby, 1961; Hajdas, 2008; Ramsey, 2008) (Figure 3.1). Plants take up ^{14}C from carbon dioxide by photosynthesis, and animals obtain ^{14}C by digesting plants, ^{14}C is consequently distributed throughout the biosphere (Libby, 1961; Ramsey, 2008). ^{14}C also enters the ocean through gas exchange, and more than 95% of ^{14}C is assimilated into the ocean and stored in the form of dissolved carbonate (Walker, 2005). Thus, the ^{14}C levels in plants, animals, and the oceans remain stable over time, the same as in the contemporaneous atmosphere (Libby, 1961; Walker, 2005). In other words, the ratio of ^{12}C to ^{14}C is approximately the same in all living organisms except in the case of organisms that feed off depleted sources of ^{14}C, for example, chemotrophs, detritus feeders (Walker, 2005; Hajdas, 2008). Once plants or animals die, they stop exchanging carbon with the surroundings, so their ^{14}C content will decay with time while their amount of ^{12}C remains constant (Libby, 1961; Ramsey, 2008). Radiocarbon dating determines the age of death of an organic sample by measuring how much ^{14}C remains in the sample and comparing the ratio of ^{14}C to ^{12}C in the sample to that in living organisms (Libby, 1961; Walker, 2005; Hajdas, 2008). Thus, ^{14}C age calculation is based on the following equation (Walker, 2005; Scott et al., 2007; Hajdas, 2008):

$$t \; = \; \frac{1}{\lambda} \ln \left(\frac{A_0}{A_t} \right) \tag{3.3}$$

where t is the age of the death of an organic sample, λ is decay constant ($\lambda = \ln2/t_{1/2}$ where $t_{1/2} = 5{,}568 \pm 30$ years, also called Libby half-life that was agreed to be used for the conventional radiocarbon ages), A_0 is the initial ^{14}C activity of the sample at the time of death by measuring modern equilibrium living activity of the sample using the primary standards of the National Institute of Standards and Technology (NIST) OxI and/or OxII (standard reference materials) in the laboratory, and A_t is the activity of the sample material t years after death. Since the radioactive decay of ^{14}C is exponential with a half-life of 5,730 years, the upper age limit for the method's applicability is around 50,000 years (Walker, 2005; Hajdas, 2008).
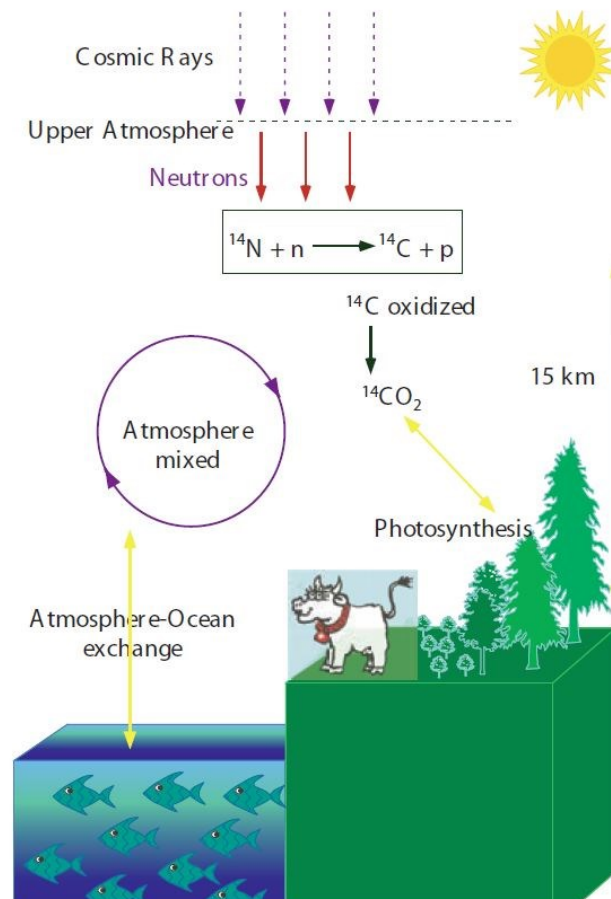
Figure 3.1 Basic principles of ^{14}C dating, showing the production process and distribution of ^{14}C. From Hajdas (2008).

3.1.2 Analytical Procedures

A total of 22 organic samples were collected from the MFT outcrop throughout two field studies in 2018 and 2019. Twelve samples were selected for radiocarbon analysis (Table B.1): ten overbank fluvial deposits and two colluvial wedge samples. Three of the ten fluvial deposit samples originated from the cut-in-fill terrace T1, whereas the others were taken from the fill terrace T2. The details about the samples, sampling sites, and locations are described in Chapter 4.

3.1.2.1 Sample Preparation

Datable materials discovered in the samples include charcoal, bulk sediments (<125 μm), isolated plant and animal microfossils such as leaves, seeds and insect shells. Charcoal was identified as the most suitable for ^{14}C analysis in this research due to its abundance (Figure 3.2). Before the samples were analyzed for their ^{14}C content, physical and chemical pretreatments have been done to isolate the samples from the surrounding matrix and remove post-depositional contaminants so that the samples can provide the most accurate ^{14}C ages (Ramsey, 2008; Hajdas, 2008). Physical pretreatments were carried out at Dalhousie University (Canada) while chemical treatments were performed at the ETH accelerator facility in Zurich (Switzerland). The procedure for physical cleaning and inspection involved (1) manual picking with tweezers after visual examination of large pieces of organic matter, (2) flotation using deionized water, accompanied by ultrasonic bath, to separate the large pieces from its surrounding matrix if it is hard to pick them up by hands, (3) drying below 60 °C in the oven for 12–24 hours after flotation, and (4) sieving for bulk sediments <125 μm, following microscope observation of carbon content. To remove contamination, two chemical pretreatments were performed. Soxhlet treatment was first carried out for one hour to remove the contamination resulting from conservative materials by placing the samples in the Soxhlet apparatus (Figure 3.3), immersing them sequentially in the vapors of heated solvents (hexane, acetone and methanol), and cooling after the vapor cleaning. The ABA (acid-base-acid) treatment was next applied at 60 °C to remove the contamination caused by carbonates and humic acids: (1) the initial acid treatment washed carbonates away from the sample surfaces using 0.5M HCl solution, followed by sample rinsing with

deionized water, (2) the base wash using 0.1M NaOH solution removed humic acids, also followed by sample rinsing with deionized water, and (3) using a weak acid solution (0.1M HCl), carbonates dissolved during the previous pretreatments were removed, and the ABA treatment ended with a final rinsing with deionized water.
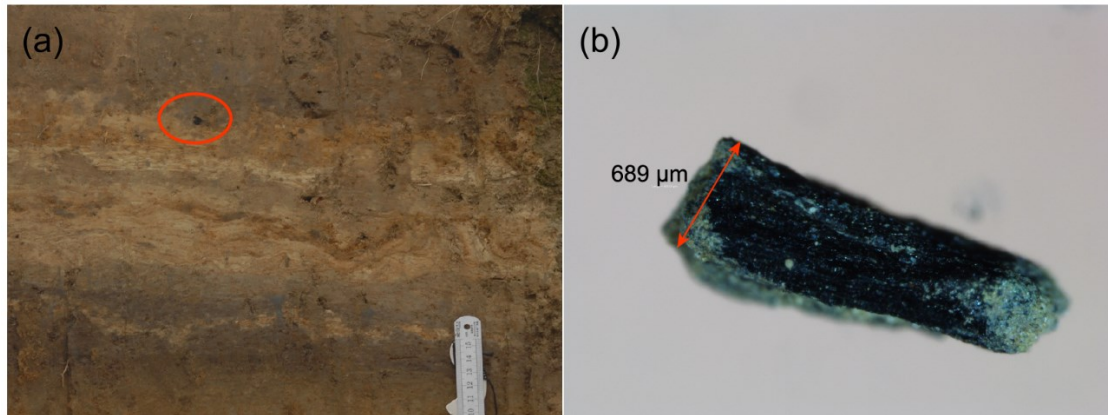
Figure 3.2 (a) Charcoal identified at the bottom of organic staining sublayer in the soil layer of cut-in-fill terrace T1; (b) Micrograph of charcoal sample.
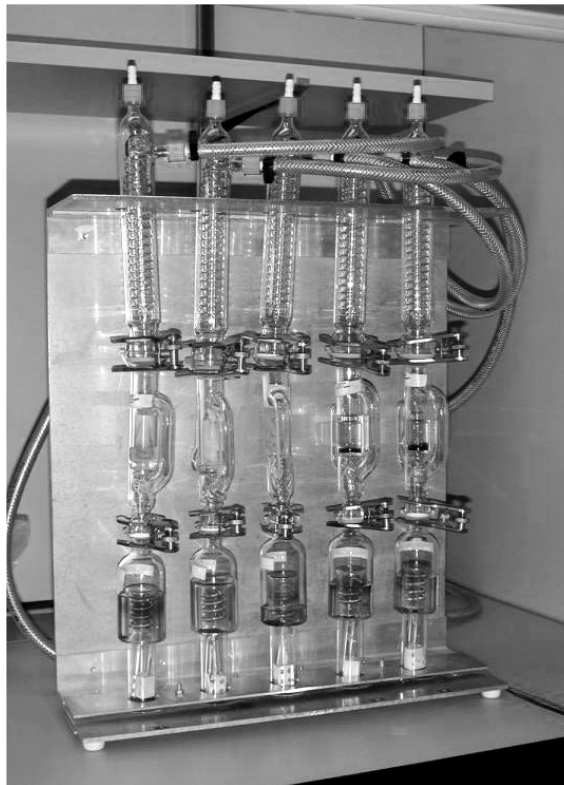
Figure 3.3 Soxhlet treatment system at the ETH lab (Switzerland), including Soxhlet apparatus (middle), heated bottle of solvents (bottom), and cooled bottle of solvent vapors (top). From Hajdas (2008).

3.1.2.2 Radiocarbon Measurements and Calibration

Two methods can be used to measure the activity of ^{14}C in a sample relative to modern standard: (1) beta counting, which indirectly estimates the residual ^{14}C activity in the sample by detecting and counting β particles released from ^{14}C atoms, and (2) accelerator mass spectrometry (AMS) that directly counts the relative number of ^{14}C atoms to the other carbon isotopes in a sample because the abundance of ^{14}C atoms is so small (Walker, 2005; Hajdas, 2008; Ramsey, 2008). The AMS was applied in this research for two reasons: (1) samples as small as 0.5 mg can be used (Ramsey, 2008), and (2) a high degree of precision 1%, i.e., on the order of 10 years for an ~1000-year-old sample (Scott et al., 2007; Ramsey, 2008). Two processes of graphite preparation for the AMS measurements, the combustion of dried organic sample producing CO_2 and the reduction of CO_2 to graphite (Hajdas, 2008; Ramsey, 2008), have been performed at the ETH accelerator facility in Zurich (Switzerland).
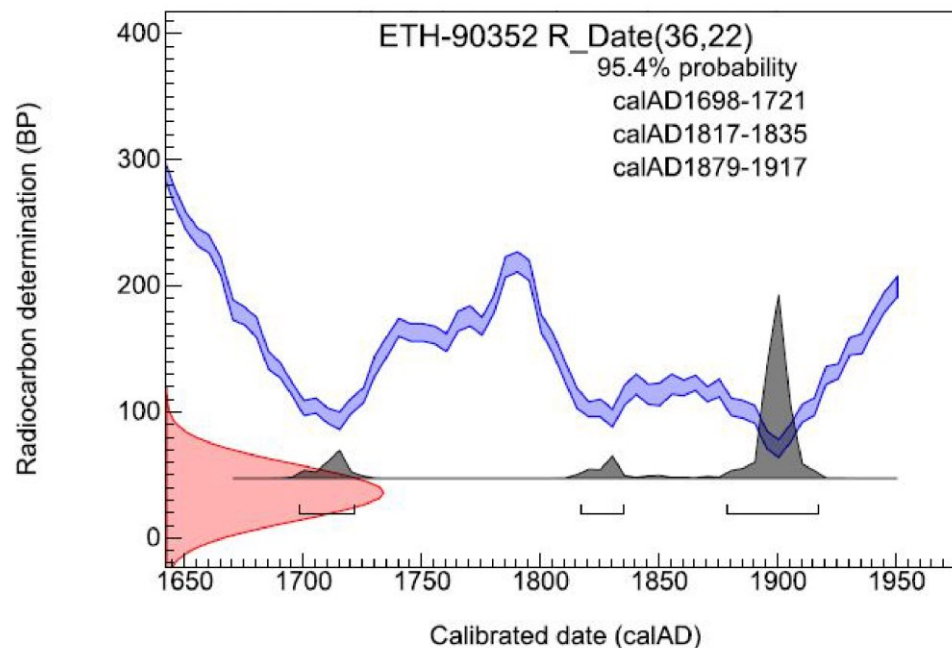
Figure 3.4 Diagram showing how the measured radiocarbon years are calibrated. The pair of blue curves show the radiocarbon measurements performed at the ETH accelerator facility in Zurich with a 1σ counting error. The radiocarbon concentration in the sample (ETH-90352, the fluvial deposits from cut-in-fill terrace T1) is indicated by the red curve. The grey histogram shows the possible ages for the sample, and the higher the peak, the more likely that age is. The results of the analysis are with 95.4% confidence interval for 2σ error. OxCal V4.3 (Ramsey, 2017) and the atmospheric calibration curve IntCal13 (Reimer et al., 2013) were used to calibrate calendric dates for the sample.

Due to long- and short-term variations in ^{14}C production in the atmosphere, radiocarbon ages calculated using equation (3.3) generally show underestimates relative to the ages obtained by applying other dating techniques (Walker, 2005). The main factors contributing to the change in atmospheric ^{14}C activities are changes in the Earth's magnetic field and changes in solar activity, either of which influences the cosmic ray flux (Walker, 2005). There is, however, a way to convert measured radiocarbon years to calendar ages, called radiocarbon calibration (Walker, 2005; Hajdas, 2008; Ramsey, 2008). The radiocarbon results are reported as 'BP' ('before present'), referring to the reference date of 1950, i.e., the ^{14}C concentration is assumed as constant and equal to that of the atmosphere in 1950, while the calibrated or calendar ages are expressed as 'cal AD/BC' (Hajdas, 2008; Ramsey, 2008) (Figure 3.4). In this research, calendric dates were calibrated using OxCal V4.4 (Ramsey, 2020) and the atmospheric calibration curve IntCal20 (Reimer et al., 2020), with a 95.4% confidence interval for 2σ error.

3.2 Luminescence Dating

3.2.1 Introduction to Luminescence

The best way to understand the concept of luminescence is the energy band model of insulated crystalline solids, involving the valence band (VB), the conduction band (CB), and the forbidden band (FB) (Duller, 2008; Pradhan et al., 2008) (Figure 3.5). In insulators, the VB refers to the most distributed band of electrons at room temperature while the CB, which is at a higher energy level compared with the VB, is the unfilled band because electrons in this band have enough energy to move freely. An electron in the VB can be excited to the CB by absorbing enough energy from ionizing radiation to leave an empty spot with a positive charge in the VB called a hole (Preusser et al., 2008; Duller, 2008; Rhodes, 2011; Pradhan et al., 2008). FB is the energy gap between the VB and the CB, within which energy states exist due to imperfections in crystal lattice. Lattice defects in a crystal can trap both excited electrons and holes, named 'electron traps' and 'recombination centers' respectively (Preusser et al., 2008; Duller, 2008; Rhodes, 2011). Since different types of defects are contained within different minerals, various kinds of electron traps and recombination centers exist. Also, the deeper the trap

below the CB, the higher the energy required for electron excitation, i.e., the longer the electron remains trapped at the location.
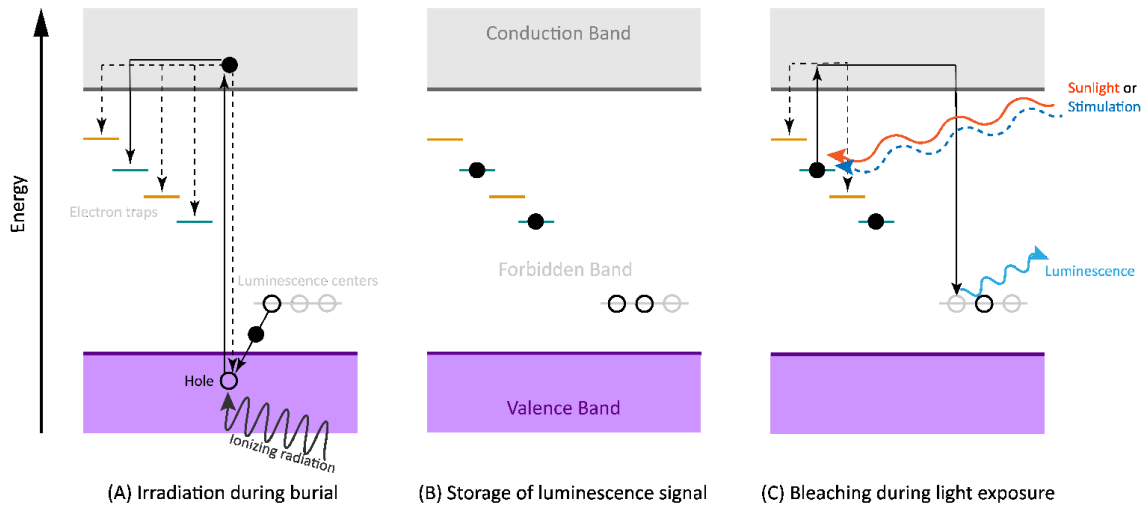
Figure 3.5 Energy band model of luminescence. Two types of electron traps are shown: light-sensitive in green and light-insensitive in orange. Light gray lines denote luminescence centers. Black dots represent electrons while black circles stand for holes. (A) During burial, ionizing radiation releases energy so that an electron is excited to the conduction band (CB) and a hole is left in the valence band (VB). The excited electron may be trapped into localized energy levels or recombine immediately with a hole in the VB. The hole newly generated may be transferred from the VB to the nearest localized energy level above the VB by attracting an electron from the nearest localized energy level. (B) The trap population increases with the time during burial. The trapped electrons remain for the burial period. (C) During light exposure (to sunlight or stimulating light), trapped electrons may be re-excited to other localized energy levels or to recombine with the holes at luminescence centers. If the recombination of the electron with a hole occurs, light photons called luminescence signal are emited.

The luminescence signal is the photon emission produced during the transition of excited electrons into localized luminescence traps and recombination centers (Preusser et al., 2008; Duller, 2008). It is sensitive to light or heat so that the luminescence trap population within minerals is increased with time during burial due to ionizing radiation and can reach a saturation state (i.e., all available traps become populated) but decreases with the exposure of the grains to light or heat. The luminescence traps can be emptied if the exposure time is long enough, that is called as the resetting or complete bleaching of luminescence signal (Preusser et al., 2008; Duller, 2008; Rhodes, 2011).

Using intensity of luminescence signal corresponds to the burial time since the last resetting event (Preusser et al., 2008; Duller, 2008). The intensity of the natural luminescence signal is measured to determine the total radiation energy, termed the

equivalent dose (D_e), that was deposited within the mineral during the period that the grains are shielded from daylight or heat (Duller, 2008). Thus, the luminescence age is calculated by dividing the D_e (in Grays (Gy), where 1 Gy = 1 Joule/kg) by the amount of radiation received from the environment surrounding the measured material per year, known as the environmental dose rate ($\dot{D}$, in Gy/year) (Preusser et al., 2008; Duller, 2008):

$$Luminescence\ age\ \text{(years)} = \frac{D_e\ \text{(Gy)}}{\dot{D}\ \text{(Gy/year)}} \qquad (3.4).$$

The uncertainty of 5–10 % in luminescence age is the combination of uncertainties in the measurement of the D_e and $\dot{D}$ (Rhodes, 2011; Duller, 2008). The overview of luminescence dating process is shown in Figure 3.6.
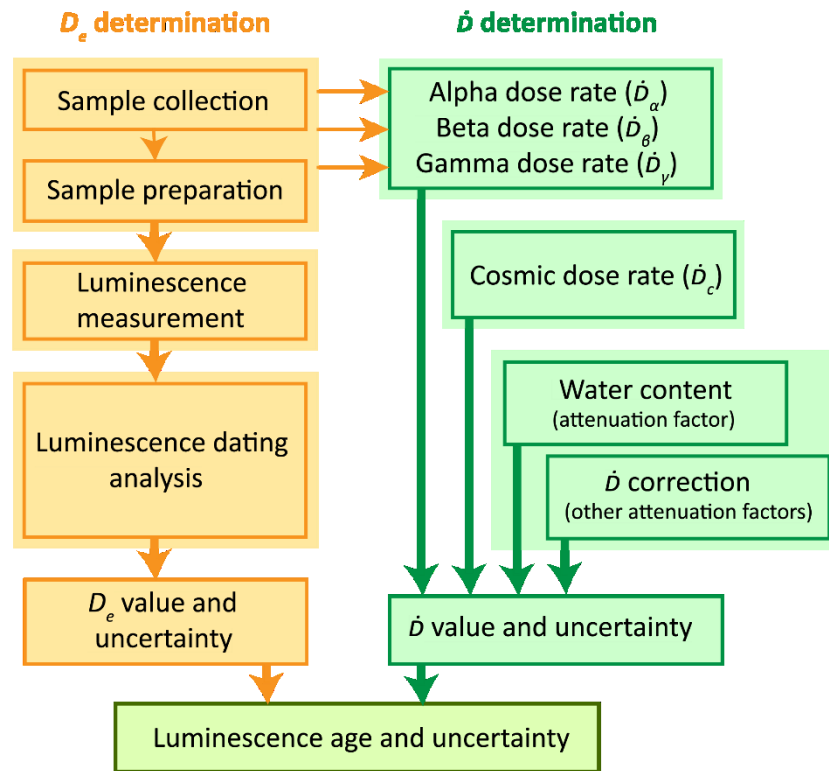
Figure 3.6 Overview of luminescence dating process. The methods used to analyze luminescence data vary in different dating techniques.

3.2.2 Luminescence Methods

Quartz and feldspar are the major minerals providing space for the storage of luminescence signal. Stimulated luminescence signals are applied to calculate the D_e (Preusser et al., 2008). There are a range of techniques that can be used to stimulate the accumulated radiation: thermoluminescence (TL), optically stimulated luminescence (OSL), and infrared stimulated luminescence (IRSL) (Rhodes, 2011; Duller, 2008). While the TL signal is produced by heating mineral grains during measurement, either the OSL or IRSL signal is emitted by exposing samples to certain light source (Rhodes, 2011; Duller, 2008). The OSL or IRSL signal is reset much faster than the TL signal and thus has been used most widely. The OSL signal can be observed from both quartz and feldspar using visible light whereas the IRSL signal is only produced from feldspar under infrared light (Duller, 2008; Preusser et al., 2008).

Three luminescence dating techniques have been applied to determine the ages of the paleo-earthquakes. Conventional quartz OSL dating yielded the burial ages of the displaced river terrace layers, the same as the ^{14}C method. Multi-OSL dating of feldspar on fault gouge utilizing multi-elevated-temperature (MET) measurement protocol has been tested to see if it can directly determine the age of the seismic event. High precision rock surface dating was applied to the cobbles along the layer boundaries and dragged along the fault to constrain the burial age of the layer that the cobble belongs to. A description for each luminescence method is provided in the following sections 3.3–3.5.

3.2.3 Determination of the Equivalent Dose

Single aliquot regenerative-dose (SAR) protocol is the most frequently used approach to determine the D_e. It consists of measuring the intensity of the natural signal and comparing it with laboratory signals regenerated from known radiation doses (Preusser et al., 2008; Duller, 2008). The SAR protocol comprises a series of measurement cycles: while in the first cycle, the natural dose is measured, in the following cycles, known laboratory doses are given to the aliquot, and regenerated luminescence signals are measured (Duller, 2008). The resulting curve that shows the growth of the luminescence signal with dose is used to read the D_e by matching the natural signal with it (Duller, 2008) (Figure 3.7). To allow comparison between

measurement of the natural luminescence signal and laboratory regenerated doses, preheating is performed prior to each measurement to remove unstable signal induced by the laboratory radiation (Rhodes, 2011; Duller, 2008). Sensitivity correction is additionally used in the SAR protocol to ensure the accuracy of the measurements (Rhodes, 2011; Duller, 2008). There are several factors influencing the luminescence sensitivity such as preheat temperature and duration during the laboratory procedures and environmental temperature during the burial of the sample. The dose value will not be accurate if any possible changes in luminescence are ignored (Rhodes, 2011; Duller, 2008). A small fixed test dose is therefore used to assess the luminescence signal sensitivity in the second half of each cycle, so that the sensitivity can be corrected by plotting a graph using the ratio of the signal measurement (L_x) to signal sensitivity assessment (T_x) each cycle (Rhodes, 2011; Duller, 2008). Thus, each SAR cycle consists of at least irradiation, preheat, luminescence signal measurement, a small uniform test dose for sensitivity correction, second heating, and luminescence signal sensitivity measurement (Rhodes, 2011; Duller, 2008).
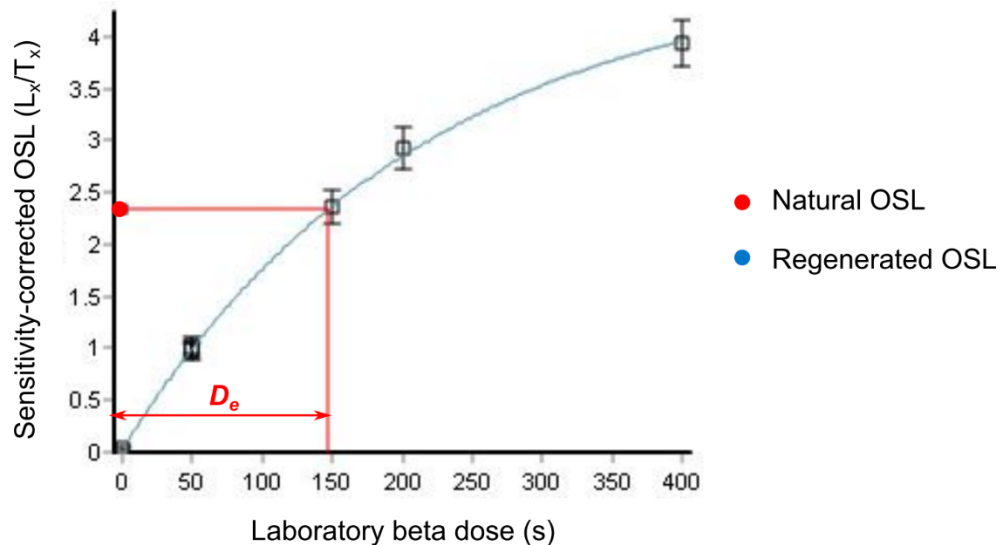
Figure 3.7 Example of a dose response curve generated after a quartz OSL measurement using Risø TL-DA-20 reader with a dose rate of 0.089 ± 0.003 Gy·s^{-1}.

The reproducibility of the D_e within each sample is crucial to assess the bleaching level of the sample before burial (Duller, 2008). If all the D_e replicate measurements for one same sample are grouped together and close to a certain value (Figure 3.8a), it

implies that the sample was completely bleached before burial, so an age will be estimated accurately (Preusser et al., 2008; Duller, 2008). In contrast, a broad distribution of the D_e (Figure 3.8b) indicates incomplete bleaching occurred prior to deposition, which results in overestimated age (Preusser et al., 2008; Duller, 2008).
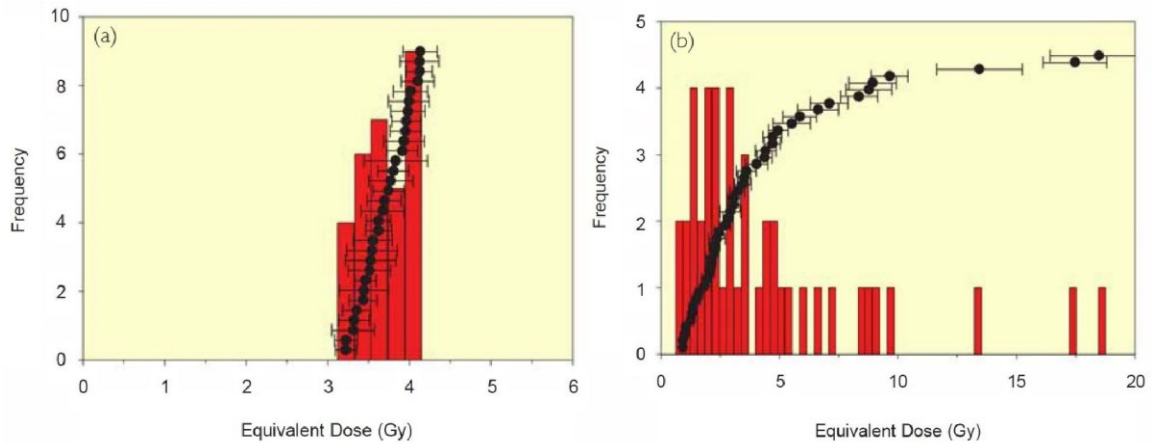
Figure 3.8 Examples of the D_e distribution from replicate measurements of D_e using small aliquot (60–100 grains) quartz OSL SAR protocol. Histograms indicate the frequency of D_e values, which are shown as dots with uncertainty bars. From Duller (2008). (a) A tight cluster of the D_e values obtained from sand dune samples. (b) A broad distribution of the D_e values determined from fluvial deposits.

The outcomes of single aliquot measurements additionally depend on aliquot size ranging from a single grain to a thousand grains in each aliquot under situations where different mineral grains have different D_e values (Duller, 2008). According to Duller (2008), the smaller the aliquot size of the sample, the larger the variation in the D_e because the measurements on large aliquots produced an average of the results of many grains concealing their D_e variations. To explore D_e variability further, the SAR uses small aliquot size or single grain measurement that applies a focused laser to stimulate individual grains in turn (Duller, 2008). However, when using single grain measurements, 95% or greater of the grains do not emit sufficient OSL to determine the D_e in most cases, so time-saving small aliquot analyses are frequently applied (Rhodes, 2011; Duller, 2008).

This research used the SAR protocol for each luminescence dating technique. All luminescence measurements were performed using Risø TL-DA-20 reader at the

University of Lausanne, Switzerland. The details are elaborated in each chapter of luminescence methods.

3.2.4 Determination of the Dose Rate

There are four sources of radiation to the $\dot{D}$ including alpha particles (α), beta particles (β), gamma rays (γ), and cosmic rays (Duller, 2008; Durcan et al., 2015). The first three mainly originate from naturally occurring radioactive isotopes, such as uranium (U), thorium (Th), and potassium (K), in the sample and its surroundings (Duller, 2008). While the penetration range of α is very short (no more than 0.02 mm), the β range is about 2–3 mm through most sediments, and γ can penetrate up to 30 cm (Duller, 2008). For cosmic rays, three main factors determine their dose rate ($\dot{D}_c$): latitude, altitude, and depth (Duller, 2008; Durcan et al., 2015). The $\dot{D}$ can be directly measured by counting the emission of radiation or calculated by using the concentrations of the radioactive elements surrounding the sample (Duller, 2008; Durcan et al., 2015).

A series of attenuation factors of radiation must be additionally considered to correct the $\dot{D}$: alpha efficiency (a-value), grain size, chemical etching, and water content (Durcan et al., 2015). Relatively highly ionized α particles result in the saturation of traps along the track of α decay within crystal lattices of minerals. Grain size may affect the α and β dose rates owing to its comparable diameter with the penetration range of these particles. Chemical etching used to clean quartz extracts cannot be uniform for all the grains, some deep etch pits causing the change in $\dot{D}_\beta$ may be thus produced during this process. Water absorbs the radiation by removing water-soluble radioactive daughter products from the surroundings. Water content typically dominates uncertainty in the measurement of the $\dot{D}$.

To determine the $\dot{D}$ for this project, bulk samples of the surrounding matrix were collected and the concentrations of U, Th, and K were measured using inductively coupled plasma mass spectrometry (ICP-MS) in ActLabs, Canada. The details are elaborated in each section of luminescence methods.

3.3 Conventional Optically Stimulated Luminescence (OSL)

3.3.1 Introduction
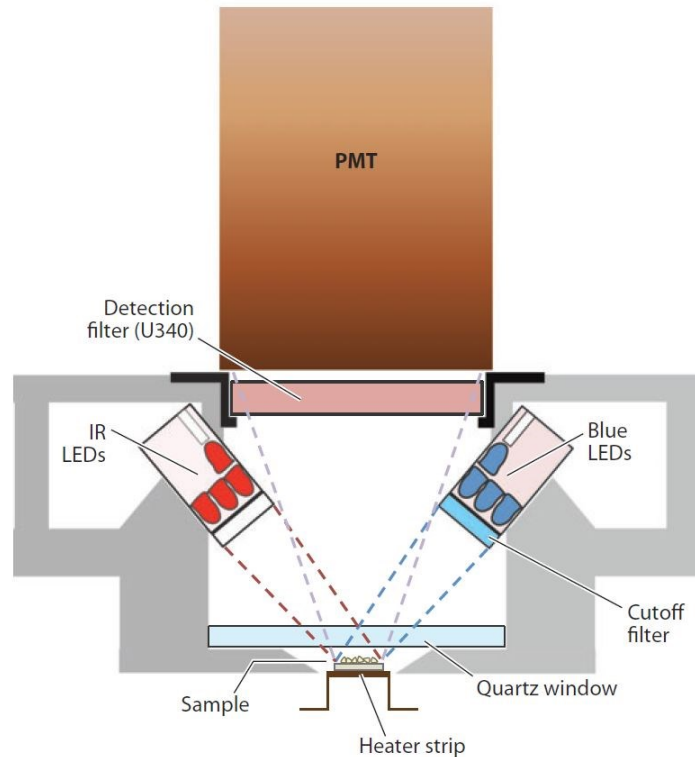
Figure 3.9 Schematic diagram of light detection system in Risø TL-DA-20 reader for OSL/IRSL. From Rhodes (2011). The detection system mainly includes the photomultiplier tube (PMT), light emitting diodes (LEDs), and quartz window. Detection filter such as U340 is commonly used for quartz OSL measurement.

Conventional OSL dating uses visible light to stimulate the minerals to release luminescence signals (Preusser et al., 2008). Since the intensity of the stimulation light is much larger than luminescence, it is limited to a certain wavelength by using suitable detection filters so that the sensitive light detector PMT (photomultiplier tube) can measure the emitted signal (Duller, 2008) (Figure 3.9). For OSL, blue (470 nm) or green (532 or 514 nm) light-emitting diodes (LEDs) are used (Rhodes, 2011). When measurement starts, the OSL signal observed from quartz decays more rapidly than the signal from feldspars (Rhodes, 2011; Duller, 2008) (Figure 3.10). Laboratory experiments have shown that electrons from deep traps are quite stable in quartz but much less stable in feldspar (Duller, 2008). This instability in feldspar is known as anomalous fading, which leads to age underestimation (Rhodes, 2011; Duller, 2008). Where fading is observed in samples, anomalous fading correction should be performed by calculating the rate of fading (Rhodes, 2011; Preusser et al., 2008; Duller, 2008).
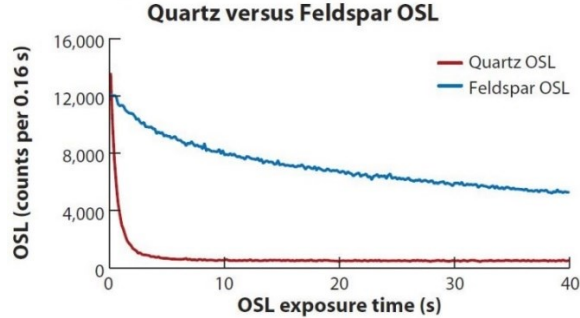
Figure 3.10 Comparison of quartz and feldspar OSL decay curves. From Rhodes (2011).

3.3.2 Analytical Procedures

Nine samples were selected for conventional OSL analysis in this research: eight overbank fluvial deposits and one colluvial wedge sample collected from the MFT outcrop. The MFT fluvial deposit samples consist of two T1 samples and six T2 samples. Due to the common occurrence of quartz in these samples and the advantages, i.e., no anomalous fading offered by quartz dating and relatively rapid signal resetting (Rhodes, 2011; Duller, 2008; Preusser et al., 2008), the quartz OSL SAR protocol was applied to define a chronostratigraphic framework for these fluvial deposits. The details about the samples, sampling sites, and locations are described in Chapter 4.

3.3.2.1 Sample Preparation

All the preparations of the samples were carried out under subdued red-light conditions at Dalhousie University (Canada). The chemical etching with 40% HF for clean quartz extracts was performed at the University of Lausanne (Switzerland). Laboratory procedures following Preusser et al. (2008), King et al. (2016a), and Şahiner et al. (2017) included physical and chemical pretreatments and were performed to extract quartz, Na-feldspar, and K-feldspar. (1) The samples were taken out from steel tubes. (2) The core part (light safe section) of each tube sample was separated and dried in an oven at 30 °C. The temperature was selected to avoid potential thermal detrapping. (3) The dried section was crushed using a pestle and mortar. To avoid potential luminescence signal resetting, it is essential not to grind the samples. (4) The sand-sized fraction of

47

100–250 µm was isolated by sieving. (5) Hand magnet was used to remove magnetic materials. (6) The extracted fraction was treated with 10% HCl and 30% H_2O_2 to remove carbonates and organic materials respectively. (7) Lithium Metatungstate (LMT) heavy liquid was used to separate quartz and two feldspar fractions with densities of 2.62–2.70 $g \cdot cm^{-3}$, 2.58–2.62 $g \cdot cm^{-3}$, and <2.58 $g \cdot cm^{-3}$. (8) The quartz fraction was treated with 40% HF acid for 60 minutes, followed by the final treatment with 10% HCl to remove potential fluorides formed during etching. The feldspar fractions were not etched.

3.3.2.2 OSL Measurements and Analysis

Quartz OSL measurements were done by illuminating the samples with blue LEDs and using small aliquots of 2 mm ø (in diameter) including 100–150 grains. Three Risø TL-DA-20 readers were used with dose rates of 0.089 ± 0.003 Gy·s^{-1}, 0.240 ± 0.007 Gy·s^{-1}, and 0.192 ± 0.006 Gy·s^{-1}. To attain optimal D_e determination to estimate the age with high precision, a series of tests involving preheat plateau, recycling ratio, IR depletion, and dose recovery were carried out before the actual measurements.
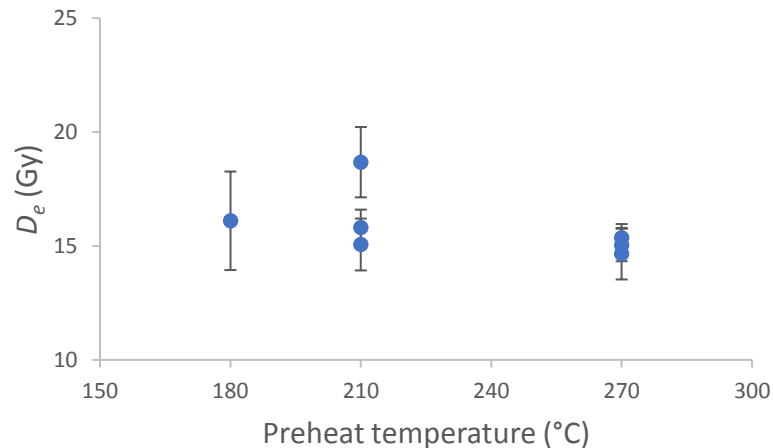
Figure 3.11 Preheat plateau for sample T1-2 showing D_e measurements at preheat temperatures 180 °C, 210 °C, 240 °C, and 270 °C. At each temperature, 3 aliquots were measured. The result from 7 successful measurements indicates that the preheat temperature of 270 °C is most suitable with all three D_e measurements yielding ~15 Gy.

The preheat temperature of 270 °C was determined by measuring the D_e for 12 aliquots: every three aliquots were preheated at 180 °C, 210 °C, 240 °C, and 270 °C for 10 s (Figure 3.11). Additionally, the recycling test was applied to assess whether the

sensitive correction used in the SAR protocol works well by repeating the OSL measurement in the final cycle using the second regenerative dose. If the recycling ratio between the two sensitivity-corrected OSL signals in the final and the second cycles is between 0.9 and 1.1, the measurements from the same aliquot will be appropriate and accepted (Rhodes, 2011; Duller, 2008). To investigate the presence of feldspar, the IRSL signal at 40 °C was applied for 40 s before blue OSL signal was measured in the last cycle (Table 3.1). If a quartz sample has feldspar contamination, the measurement of the last SAR cycle will produce a smaller value than others using the same regenerative dose because only feldspar can emit the IRSL signal while both quartz and feldspar produce the OSL signal (Duller, 2008; Preusser et al., 2008). Furthermore, dose recovery test was done by performing aliquot bleaching with a known dose (e.g., 15 Gy), treating the dose as an unknown, and applying the quartz OSL SAR protocol to measure it. As a result, the calculated dose (e.g. ~15.46 Gy) closely matches the known dose, that means the D_e value of the sample can be correctly calculated.

In addition, a zero-dose SAR cycle was applied to ensure that the luminescence signal curve passes through the origin and to test for thermal transfer caused by heating and recuperation resulting from light exposure, both of which refer to charge movement (Rhodes, 2011). To avoid dose overestimation caused by any residual signal from each SAR cycle, blue OSL signal at 280 °C was also used at the end of each cycle to release the remaining energy (Table 3.1). In brief, the quartz extracts were analyzed using OSL SAR protocol which comprised a preheat at 270 °C for 10 s, followed by blue stimulation at 125 °C for 40 s.

Combined with Risø Analyst, RStudio (Durcan et al., 2015) was used to analyze the OSL results and determine the D_e. At least 25 D_e values were obtained for age modelling and D_e determination. Data were accepted using exponential fit for the dose-response curve and the sample acceptance criteria of recycling ratio within 10% of unity, maximum test dose error <10%, and recuperation <10% of the natural signal. Two age models can be applied for D_e determination (Galbraith et al., 1999): (1) the central age model (CAM), based on the assumption that all the grains have been completely bleached prior to burial, includes two unknown parameters, the mean of the true paleodoses in the

49

relevant population of grains (δ), and standard deviation of these log paleodoses (σ); (2) the minimum age model (MAM), considering incomplete bleaching and using δ and σ as adjustable parameters to capture the unknown spread in the log paleodoses caused by partially bleached grains, statistically selects the younger population of D_e, i.e., the portion of grains that were most likely to have been well bleached before deposition, to allow more accurate D_e and age estimation. The selection of statistical age models depends on the overdispersion (σ_b) value representing the degree of scatter in D_e values (Galbraith et al., 1999). The σ_b value, ranging from 0 to 1, can be calculated using the CAM in RStudio. If $\sigma_b < 0.2$, indicating that the sample has been well bleached on the deposition, the CAM can be applied for D_e calculation. Otherwise, it is implied that partial bleaching occurred prior to deposition, thus the MAM must be used (Galbraith et al., 1999; Rhodes, 2011). For D_e uncertainty analysis, the number of aliquots involved in the age estimate was counted using the lower and upper limit of D_e value calculated by the age model. The burial OSL age is reported with 1σ uncertainty.

Table 3.1 Single aliquot regenerative dose (SAR) procedure applied to measure quartz grains.

Step	Treatment	Observed	Purpose
1	Dose, D_x No dose in the first cycle while different regenerative doses in later cycles (β = 50s, 150s, 200s, …, 0s, 50s, 50s).		β = 0s, for ensuring the origin plotting and testing thermal transfer. β = 50s in the second last cycle, for recycling test.
2	Pre-heat to 270°C, β=5°C/s, 10s		To remove unstable signal
3	IR stimulation at 40°C, β=2°C/s, 40s (Only used in last cycle)	L_x	IR depletion test
4	Blue stimulation at 125°C, β=5°C/s, 40s	L_x	OSL measurement
5	Test dose, D_t		Sensitivity correction
6	Pre-heat at 260°C, β=5°C/s, 10s		To remove unstable signal
7	Blue stimulation at 125°C, β=5°C/s, 40s	T_x	OSL sensitivity measurement
8	Blue stimulation at 280°C, β=5°C/s, 40s		To remove the residual signal before next cycle

3.3.2.3 Dose Rate Determination

A standardized online Dose Rate and Age Calculator (DRAC) that applies published datasets was used to calculate the total $\dot{D}$. In DRAC, the internal, external, and the cosmic dose rates are calculated respectively, followed by $\dot{D}$ correction (Durcan et al., 2015). According to Durcan et al. (2015), the internal dose rate can be negligible for the fine-grained quartz samples in the fluvial environment, which commonly contain a small

amount of U and Th and have too low alpha efficiency to be considered. The conversion factors by Guérin et al. (2011) were used to calculate dose rates from radionuclide concentrations. The grain size of 150–250 µm was used for all the samples. The grain size attenuation factors of Brennan et al. (1991) for the alpha dose rate ($\dot{D}_\alpha$) and the factors of Guérin et al. (2012) were used together with the etch depth attenuation factors of Bell (1979) for the beta dose rate ($\dot{D}_\beta$). Different water contents were estimated for six distinct river terrace layers or colluvial wedge based on saturated water content measurements in the laboratory. All the key input variables are shown in Table 3.2.

Table 3.2 Input variables for individual samples used for Dose Rate and Age Calculator.

Sample	U (ppm)	Th (ppm)	K (%)	Water (%)	Lat. (°)	Long. (°)	Alt. (m)	Depth (m)
T1-1	1.8 ± 0.1	7.4 ± 0.3	0.81 ± 0.02	2 ± 2	26.792	91.511	156	0.36 ± 0.02
T1-2	2.5 ± 0.1	11.9 ± 0.5	1.18 ± 0.03	4 ± 2	26.792	91.511	156	0.50 ± 0.02
T2H-1	2.9 ± 0.1	13.0 ± 0.5	1.12 ± 0.03	5 ± 3	26.792	91.511	159	0.43 ± 0.02
T2F-1	3.1 ± 0.1	14.3 ± 0.5	1.55 ± 0.04	12 ± 5	26.792	91.511	159	5.4 ± 0.3
T2F-2	3.1 ± 0.1	15.0 ± 0.6	1.39 ± 0.04	7 ± 7	26.792	91.511	159	1.2 ± 0.1
T2F-3	3.0 ± 0.1	14.2 ± 0.5	1.26 ± 0.03	7 ± 7	26.792	91.511	159	2.4 ± 0.1
T2F-4	3.6 ± 0.2	17.4 ± 0.7	1.38 ± 0.04	6 ± 4	26.792	91.511	159	3.4 ± 0.2
T2F-5	2.0 ± 0.1	8.6 ± 0.3	0.85 ± 0.02	4 ± 2	26.792	91.511	159	3.9 ± 0.2
T2-1	3.5 ± 0.1	20.5 ± 0.8	1.88 ± 0.05	3 ± 3	26.792	91.511	159	2.0 ± 0.1

Note: F – footwall and H – hanging wall.

3.4 Rock Surface Dating

3.4.1 Introduction

Rock surface dating is a luminescence technique based on the investigations of the resetting of luminescence signals with depth into rock surfaces (Freiesleben et al., 2015; Jenkins et al., 2018; Sohbati, 2015; Sohbati et al., 2011). The OSL traps within buried cobble-sized clasts are emptied by the penetration of light into rocks at different rates with depth during the exposure time to light and get refilled from ionizing radiation during burial (Freiesleben et al., 2015). Trap emptying during light exposure and trap filling during burial cannot be considered as two mutually exclusive processes on the scale of a thousand years because trap filling also takes place during light exposure but can be ignored for short timescales (Freiesleben et al., 2015). Thus, the bleaching extent with depth into cobble can be assessed and used to precisely and accurately constrain luminescence ages for completely bleached clasts (Freiesleben et al., 2015; Jenkins et al.,

51

2018; Rades et al., 2018). This significant advantage of dating cobbles can also be utilized to reveal multiple events of bleaching and burial in sequence.

3.4.2 Model for Multiple Events

The multiple sequential exposure and burial events can be identified from a luminescence-depth profile and modelled based on their interrelated mathematical expressions (Freiesleben et al., 2015) (Figure 3.12). The model is constructed on the assumption that the final condition of each event is produced by the previous event and becomes the initial condition of the latter event.

3.4.2.1 Burial Events

Only trap filling is processing during rock burial. Based on the assumption that trap filling is proportional to the dose rate, the charge trapping rate can be written as:

$$F(x) = \dot{D}(x)/D_0 \qquad (3.5)$$

where $\dot{D}(x)$ is the dose rate and D_0 is the constant regarding the filling rate. The change in the concentration of the trapped charge during rock burial can be expressed as:

$$\frac{\partial n(x,t)}{\partial t} = F(x)[N(x) - n(x,t)] \qquad (3.6)$$

where $n(x,t)$ is the instantaneous trapped charge concentration, $N(x)$ is the concentration of trapping sites available at depth x, and $F(x)$ is calculated using the total dose rate including the internal dose rate from the rock and the external dose rate from the surroundings. The expression for burial events is derived from the solution to equation (3.6).

$$n(x) = (n_i(x) - N(x))e^{-F(x)t_b} + N(x) \qquad (3.7)$$

where $n_i(x)$ is the initial charge concentration at depth x before burial and t_b is the burial time. Since the $N(x)$ is greatest near the surface after an exposure event, the final charge concentration $n(x)$ at the surface reaches its highest during burial, i.e., most of the luminescence signal accumulated during burial focus at the surface. When the traps

available at the surface are saturated with sufficient burial time, the luminescence signal at the surface ceases to increase.

3.4.2.2 Exposure Events

During the time that a rock is exposed to daylight, detrapping and trap filling are processed simultaneously. The change in the concentration of the trapped charge during light exposure can be written as:

$$\frac{\partial n(x,t)}{\partial t} = -E(x)n(x,t) + F(x)[N(x) - n(x,t)] \qquad (3.8)$$

where $E(x)$ is the trap emptying rate, and $F(x)$ is different to the one in equation (3.6) and calculated using the internal dose rate from the rock and the external dose rate from cosmic rays and from the buried side of the cobble. The $E(x)$ depends on a detrapping probability $(\overline{\sigma\varphi_0})$, which is the product of the photon flux, $\sigma(\lambda,x)$ (cm^{-1}S^{-1}), and the photoionization cross-section $\sigma(\lambda)$, and is expressed as:

$$E(x) = e^{-\mu x} \int_{\lambda_i}^{\lambda_f} \varphi(\lambda,x)\sigma(\lambda)d_\lambda = \overline{\sigma\varphi_0} \, e^{-\mu x} \qquad (3.9)$$

where μ is the light attenuation factor assumed independent of λ. The expression for exposure events is derived from the solution to equation (3.8).

$$n(x) = \frac{-\left[F(x)\big(N(x) - n_i(x)\big) - E(x)n_i(x)\right]e^{t_e(E(x)+F(x))} + F(x)}{E(x) + F(x)} \qquad (3.10)$$

where t_e is the daylight exposure time. However, trap filling during light exposure can usually be negligible, so equation (3.10) can be simplified as:

$$n(x) = n_i(x)e^{-E(x)t_e} = n_i(x)e^{-\overline{\sigma\varphi_0}t_e e^{-\mu x}} . \qquad (3.11)$$

The simple equation indicates that the higher the detrapping rate at the surface or the longer the daylight exposure time, the deeper into the rock the detrapping, i.e., the further into the rock the inflection point on the luminescence profile for the exposure event (Figure 3.12).

3.4.2.3 Multiple Events

Combining equations (3.7) and (3.10) or (3.11), a full history involving multiple sequential exposure and burial events can be expressed. If luminescence signal $L(x)$ is assumed proportional to $n(x)$ and no trap filling during light exposure has been considered, a series of burial and exposure events in order from the oldest to the youngest can be modelled in luminescence profile, as shown in Figure 3.12. The luminescence signal near the surface decreases during light exposure but increases during burial. A saturation profile independent on subsequent events can be predicted by the resulting model. However, for the case of double exposure events (exposure – burial – exposure) when the later exposure time is long enough to empty the traps at the surface saturated during the previous burial, the burial event can be hidden, and the slope of the luminescence profile appears lower than normal. Therefore, the cobble-sized rocks most likely recording multiple events are better collected for luminescence dating.
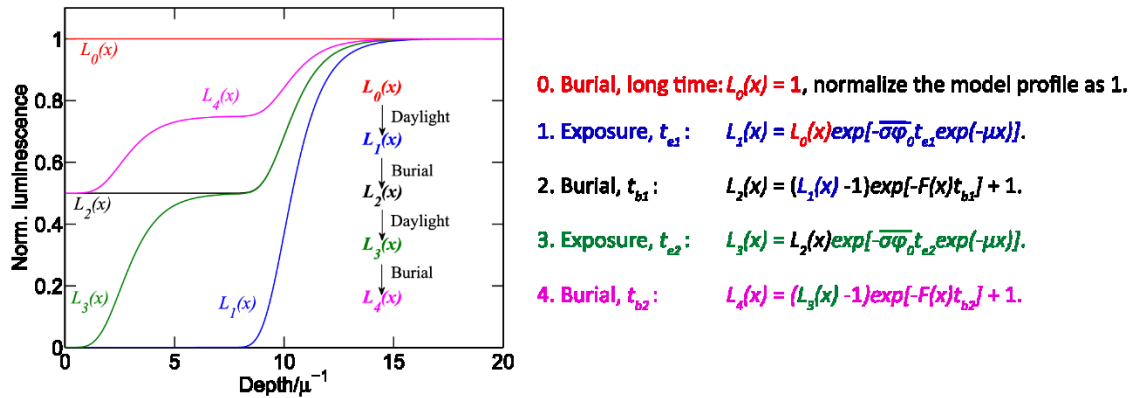
Figure 3.12 Model for multiple sequential exposure and burial events in a normalized luminescence-depth profile, based on the assumptions that trap filling during light exposure can be ignored and that the dose rate is constant with depth. All traps are assumed full in the initial condition labelled as red line. The x-axis is normalized to μ^{-1}. Adapted from Freiesleben et al. (2015). Sequential burial and exposure events involve a) burial $L_0(x)$ for the time long enough to be saturated, b) exposure $L_1(x)$ for time t_{e1}, c) burial $L_2(x)$ for time t_{b1}, d) exposure $L_3(x)$ for time t_{e2}, and e) burial $L_4(x)$ for time t_{b2}.

3.4.3 Analytical Procedures

3.4.3.1 Sample Selection, Preparation and Measurement

The 13 cobbles of quartzite or graywacke were collected along the layer boundaries or the thrust surface from the MFT outcrop for rock surface dating analysis: (1) thrust surface samples (a) 14A, 14B and 14C and (2) layer boundary samples (b) 15A, 15B and 15C at the base of the top colluvial wedge, (c) 16A, 16B and 16C within T2, and (d) 17A, 17B, 17C and 17D within T1. It was identified that cobbles 14A, 14C, 15A, and 16A are quartzite while the others are graywacke. The details about sampling sites and locations are described in Chapter 4.
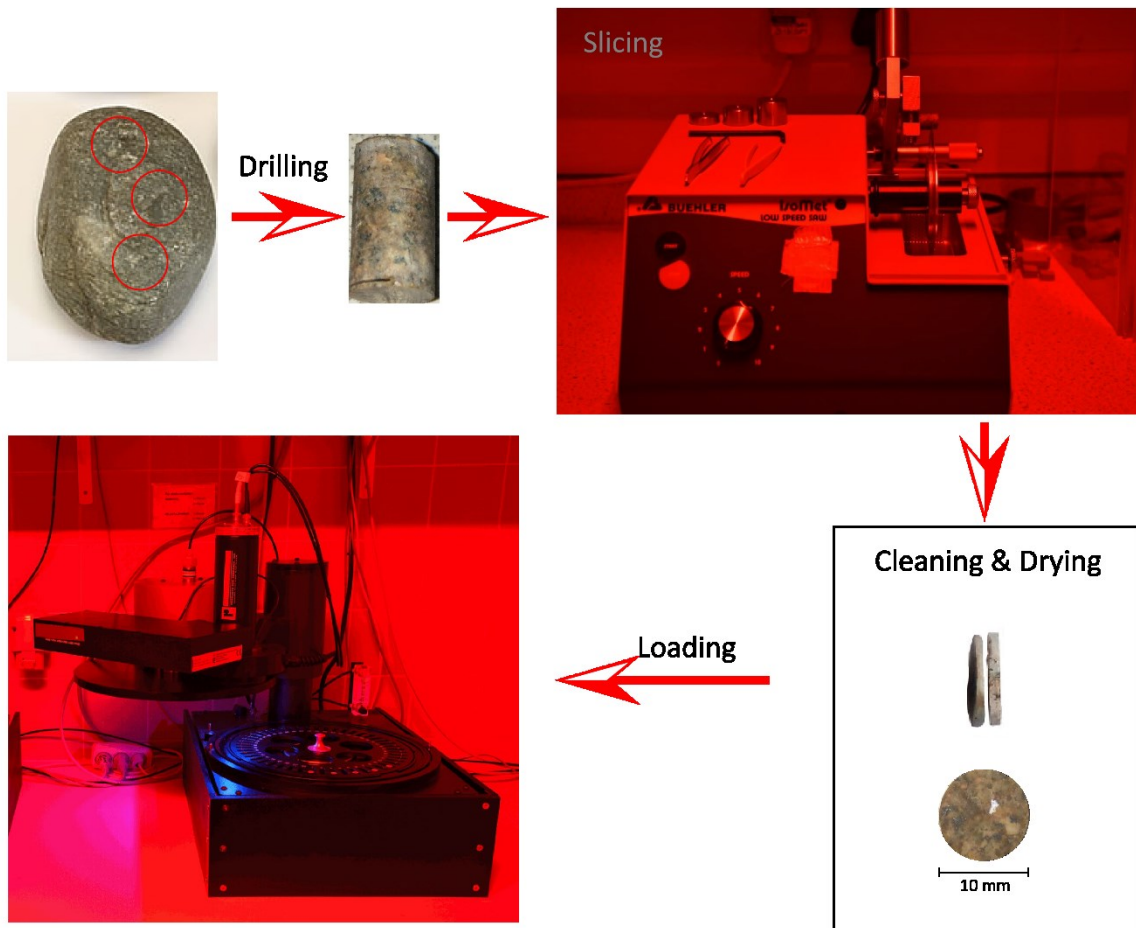
Figure 3.13 Procedure for cobble sample preparation, including sample drilling, core slicing, slice cleaning and drying, and sample loading for luminescence measurements.

Three smaller cobbles (17B, 17C, and 17D) are too thin to be used. Two largest cobbles 15A and 16C from each lithology were left for surface exposure dating tests to calibrate the bleaching properties of the cobble materials. For the remaining eight cobbles, each sample was examined by assessing whether the cobble surface was well-

bleached on deposition to ensure efficiency and determine suitability for further measurements (Jenkins et al., 2018). A luminescence-depth profile was reconstructed to verify the bleaching level of the cobble surface by using the measurements for each sliced first core extracted from individual cobble.

All sample preparation was done under subdued red-light conditions at the University of Lausanne, Switzerland. On average, two cores of 10 mm diameter and at least 35 mm length were drilled from each cobble using a Husqvarna water-cooled diamond-tipped drill. A Buehler IsoMet low-speed saw with a diamond-edged wafering blade of 0.3 mm thickness subsequently sliced the top 20–30 mm lengths of the rock cores from the buried side into discs of ~0.64 mm thickness on average (0.64 ± 0.08 mm for 170 slices). The slicing was done using a lubricant, and the rock slices produced were cleaned using acetone and dried prior to luminescence analysis. The procedure for preparing samples is shown in Figure 3.13.

Table 3.3 Single aliquot regenerative dose (SAR) procedure applied to measure ~0.65 mm thick quartzite rock slices.

Step	Description	Observed
1	Dose, D_x. No dose in the first cycle while different regenerative doses in later cycles ($\beta = 0$ s, 250 s, 500 s, 1000 s, 2000 s, 4000 s, 0 s, 250 s).	
2	Pre-heat to 250 °C at 1 °C/s for 60 s	
3	Heat to 50 °C at 1 °C/s for 100 s, and measure IRSL for 200 s	Lx_{50}
4	Heat to 225 °C at 1 °C/s for 100 s, and measure IRSL for 200 s	Lx_{225}
5	Heat to 125 °C at 1 °C/s for 100 s, and measure OSL for 200 s	Lx_{125}
6	Test dose (60 Gy), D_t	
7	Pre-heat to 250 °C at 1 °C/s for 60 s	
8	Heat to 50 °C at 1 °C/s for 100 s, and measure IRSL for 200 s	Tx_{50}
9	Heat to 225 °C at 1 °C/s for 100 s, and measure IRSL for 200 s	Tx_{225}
10	Heat to 125 °C at 1 °C/s for 100 s, and measure OSL for 200 s	Tx_{125}

All luminescence measurements were carried out using a Risø TL-DA-20 reader with a 0.240 ± 0.007 Gy·s^{-1} beta source at the University of Lausanne, Switzerland. The cobble slices were placed on a sample carousel using stainless steel cups for the measurements. A calibrated $^{90}Sr/^{90}Y$ beta source was used for sample irradiation, and the combination filters of Schott BG39/BG3 (2 mm and 3 mm thick, respectively) for feldspars and a 7.5 mm Hoya U-340 glass filter for quartz were mounted for photon

detection. According to Elkadi et al. (2021) and Jenkins et al. (2018), a standard post-IR IRSL225 SAR protocol for feldspar measurements involving an IR signal and a post-IR signal was applied, followed by the quartz OSL SAR protocol. After a preheat temperature of 250 °C held for 60 s, each sample was held at the feldspar measurement temperatures of 50 °C and 225 °C for 100 s, respectively, before starting IR stimulation. For quartz measurement, a temperature of 125 °C for 100 s was used prior to blue stimulation. A slow heating rate of 1 °C/s and 100s extended pause duration was used to lessen the effect of thermal lag within cobble slices (Jenkins et al., 2018). A test dose of ~60 Gy was used in the second half of each cycle. The protocols used in this study are summarized in Table 3.3.

3.4.3.2 Dose Rate Determination

According to Freiesleben et al. (2015), the dose rates derived from the rock and surrounding sediments can differ in rock surface dating due to different concentrations of radioactive isotopes and water contents. All the measurements of the radionuclide concentrations (U, Th, and K) within the cobbles and in the surrounding sediments were performed using ICP-MS in ActLabs, Canada. Based on saturated water content measurements in the laboratory, water content was estimated for each surrounding sediment matrix (Table 3.4). The water content in the cobble is very small in this study, so it can be negligible. The grain size of quartz was assumed to be from 250 to 1000 µm based on visual inspections of the rock slices. The depth that the variation of dose rate depends on must also be considered. If it is assumed that the rock was part of a flat layer, which has a thickness of h and infinite lateral extent, for a rock buried in sediments, the β dose rate can be described as the following expression of the variation in β radiation with the depth (x) into the rock (Freiesleben et al., 2015).

$$\dot{D}(x)_{\beta}^{Cobble} = \dot{D}_{Rock,\beta}^{inf}\left[1 - 0.5\left(e^{-bx} + e^{-b(h-x)}\right)\right] + \dot{D}_{Sed,\beta}^{inf}0.5\left(e^{-bx} + e^{-b(h-x)}\right) \quad (3.12)$$

where the β attenuation factor b is 1.9 mm^{-1} (Sohbati et al., 2012), and $\dot{D}^{inf}_{Rock,\ \beta}$ and $\dot{D}^{inf}_{Sed,\ \beta}$ are the infinite matrix β dose rates from the rock and surrounding sediments

respectively, corrected for water contents and grain attenuation where relevant. A similar expression is applied to the γ contribution $\dot{D}(x)_\gamma{}^{Cobble}$ but using an attenuation factor of 0.01 mm^{-1}. The equation is also valid for the α contribution $\dot{D}(x)_\alpha{}^{Cobble}$. Since the range of α is very short, the sediment α contribution $\dot{D}^{inf}_{Sed,\,\alpha}$ is ignored, and the rock α contribution $\dot{D}^{inf}_{Rock,\,\alpha}$ is calculated using an a-value for coarse-grained quartz of 0.10 ± 0.02 mm^{-1} (Olley et al., 1998). The total dose rate at the specific depth (x) is the sum of the $\dot{D}(x)_\alpha{}^{Cobble}$, $\dot{D}(x)_\beta{}^{Cobble}$, $\dot{D}(x)_\gamma{}^{Cobble}$, the internal α and β dose rates, and additional cosmic dose rate ($\dot{D}_c$). In addition, equation (3.12) can be used to calculate the dose rate at a certain slice by integrating it over the depth of the slice.

Table 3.4 Summary of radionuclide concentrations, estimated water content values, and depth of the rock.

Sample name	Sample type	Depth (m)	Water cont. (%)	U (ppm)	Th (ppm)	K (%)
14	Sediment		4 ± 2	3.1 ± 0.2	16.9 ± 1.0	0.76 ± 0.02
14A	Cobble	10	0	0.9 ± 0.1	7.3 ± 0.3	0.77 ± 0.02
14C	Cobble	10	0	0.4 ± 0.0	1.9 ± 0.1	0.21 ± 0.01
16	Sediment		12 ± 6	3.2 ± 0.2	15.7 ± 0.9	1.53 ± 0.04
16A	Cobble	5.5	0	0.3 ± 0.0	1.2 ± 0.0	0.08 ± 0.00

3.4.3.3 Luminescence Age Determination From Cobbles

Quartz was selected as the preferred dosimeter by comparing the sensitivity of quartz and feldspar after initial investigations of luminescence-depth profiles. Thus, anomalous fading was not considered for cobble dating in this research. Duplicate cores extracted from each cobble were also examined for surface slices in buried side. For each slice, luminescence age was calculated by dividing the D_e per slice by the $\dot{D}$ for the specific slice-depth. If the OSL$_{125}$ ages obtained from slices in the outermost portion of one core are not significantly different from the ages given by the second core drilled from the same cobble, it is verified that the OSL signal was well bleached at the cobble surface before burial (Freiesleben et al., 2015; Jenkins et al., 2018). The luminescence age for each cobble was determined by averaging the OSL$_{125}$ ages at each slice-depth point from all the outermost portions of the cobble.

3.5 Multi-OSL Dating of Feldspar

3.5.1 Introduction

Multi-OSL thermochronometry of feldspar (Li and Li, 2011a; King et al., 2016a; Ogata et al., 2022) is a tool not only capable of determining the cooling history of rocks at a crustal depth of less than 2 km but showing the potential for constraining the timing of past geological events by utilizing MET measurement protocol (Li and Li, 2011a). This technique exploits the thermal dependence of IRSL signal accumulation within feldspar and involves analyzing multiple IRSL signals from different charge-trapping centers within feldspar grains extracted from a single sample (Li and Li, 2011; King et al., 2016a). IRSL on feldspar is known as a more suitable candidate for the application, having higher luminescence sensitivity and saturating later than quartz OSL signals (Guralnik et al., 2015a). The trapped charge within feldspar has accumulated during rock cooling since passing through the closure temperature (T_c), at which thermal detrapping becomes negligible (King et al., 2016a). These different IRSL signals utilized in this method are sensitive to different temperature ranges and thus have different T_c values and distinct thermal properties (King et al., 2016a). By performing sequential IRSL measurements at increasing temperatures of the MET protocol (Li and Li, 2011a; King et al., 2016a), a multi-OSL low-temperature thermochronometer has been developed to provide multiple constraints on cooling histories over recent (0.1–0.2 Ma) timescales, meaning a more detailed and accurate thermal history of the rock can be obtained with reliable ages.

However, multi-OSL thermochronometry has two main limitations: (1) Signal saturation limits its application to high-temperature settings (e.g. boreholes or tunnels; Guralnik et al., 2015b; Schmidt et al., 2015) or to very rapidly exhuming settings (e.g. Herman et al., 2010; King et al., 2016b) because over time all available traps are filled, i.e., signals reach saturation, after which the thermal history is no longer recorded (Guralnik et al., 2015b; King et al., 2016a). (2) Feldspar athermal charge detrapping, called anomalous fading, may result in unreliable ages for relatively older samples due to dose-dependent changes in anomalous fading rate (Kars et al., 2008; Li and Li, 2008; Li and Li, 2011a), even though anomalous fading correction is performed.

3.5.2 Kinetic Model of Luminescence Response

A general order kinetic model for OSL signal growth and thermal decay (Guralnik et al., 2015b), combined with the athermal detrapping model of Huntley (2006) and the band-tail states model of Li and Li (2013) accounting for thermal loss, applied to describe the rate of trapped charge accumulation, i.e., the rate of radiation-induced charge trapping minus the sum of the rates of thermal and athermal detrapping (King et al., 2016a; Ogata et al., 2022).

$$\frac{d\left[\frac{n}{N}(r', E_b, t)\right]}{d_t} = \frac{\dot{D}}{D_0}\left[1 - \frac{n}{N}(r', E_b, t)\right] - s\, e^{-\frac{E_t - E_b}{k_B T}}\left[\frac{n}{N}(r', E_b, t)\right] - \tilde{s}\, e^{-\rho'^{-\frac{1}{3}}r'}\left[\frac{n}{N}(r', E_b, t)\right] \quad (3.13)$$

where (n/N) is the fraction of occupied electron traps possessing the nearest neighboring hole at r' and a band-tail at E_b, called the saturation ratio as a function of time (t, ka). The first term on the right-hand side of the equation is charge trapping (i.e., luminescence signal accumulation) depending on two key items, $\dot{D}$ (Gy ka^{-1}), the environmental radiation dose rate, and D_0 (Gy), the fading corrected characteristic dose of saturation. The second term on the right-hand side of the equation is thermal detrapping which depends on the frequency factor (s, ka^{-1}), activation energy or trap depth (E_t, eV), the band-tail state energy level (E_b, eV), the Boltzmann constant (k_B, eV K^{-1}), and temperature (T, K). Athermal detrapping, the third term on the right-hand side, is dependent on the athermal frequency factor ($\tilde{s} = 3 \times 10^{15}$ s^{-1}), the distance between trapped electrons and their nearest neighboring recombination centers (r', dimensionless), and the density of the recombination centers (ρ', dimensionless). The total accumulation of charge with time ($\frac{n}{N}(t)$) is then obtained by integrating $\frac{n}{N}(r', E_b, t)$ over the range of the band-tail states (E_b) and an infinite range of dimensionless distances:

$$\frac{n}{N}(t) = \int_{r'=0}^{\infty} \int_{E_b=0}^{E_t} p(r')P(E_b)\frac{n}{N}(r', E_b, t)\, dE_b\, dr' \quad (3.14)$$

where $p(r')$ and $P(E_b)$ refer to the probability density distributions of the nearest recombination centers and of the band-tail states, respectively.

Considering how much signal has accumulated after accounting for thermal and athermal losses is therefore crucial to quantifying the saturation ratio (n/N) of a sample (King et al., 2016a). The constraint of signal accumulation and thermal and athermal signal loss is achieved using a combination of laboratory measurements and kinetic models, discussed in sections 3.5.3.3–3.5.3.5.

3.5.3 Analytical Procedures

3.5.3.1 Sample Preparation

Three fault gouge samples were taken along the MFT throughout two fieldworks in 2018 and 2019: Bt1BBY1, Bt1BTY2, and BT19FG, all within a depth of ~12 m from the Earth's surface. The samples Bt1BBY1 and Bt1BTY2 were prepared at Dalhousie University (Canada) and BT19FG at the University of Lausanne (Switzerland), both under subdued red light conditions. The samples were taken out from steel tubes. The core part (light-safe section) of each tube sample was separated and dried in an oven at 30 °C. The temperature was selected to avoid potential thermal detrapping. The light safe section was crushed using a pestle and mortar. To avoid potential luminescence signal resetting, it is essential not to grind the samples. For crushed samples, the sand-sized fraction of 150–250 μm was isolated by sieving and then treated with 10% HCl and 30% H_2O_2 to remove carbonates and organic materials, respectively. The K-feldspar grains with density of <2.58 g·cm^{-3} were separated using LMT heavy liquid or sodium polytungstate. The feldspar fractions were not etched.

3.5.3.2 Dose Rate Determination

The $\dot{D}$ value was calculated from the concentration of U, Th, K, and Rb, measured in ActLabs (Canada), and from within the minerals under investigation (Durcan et al., 2015). The alpha attenuation factors of Bell (1980) and the beta attenuation factors of Guérin et al. (2012) were used together with the radionuclide conversion factors of Guérin et al. (2011). A grain size of 150–250 μm was used for all the samples. An a-value of 0.15 ± 0.05 was used based on Balescu and Lamothe (1994). A water content of 13 ± 5% has been estimated for all three samples. No cosmic dose rate component has

61

been incorporated because these samples have been shielded from cosmic rays for their signal accumulation period. The key input variables used to calculate $\dot{D}$ are shown in Table 3.5.

Table 3.5 Dosimetry data.

	U (ppm)	Th (ppm)	K (%)	Internal K (%)	Water (%)	$\dot{D}$ (Gy ka^{-1})
Bt1BBY1	3.5 ± 0.2	17.2 ± 0.7	1.44 ± 0.04	12.5 ± 0.5	13 ± 5	4.14 ± 0.25
Bt1BTY2	3.4 ± 0.2	16.4 ± 0.6	1.23 ± 0.04	12.5 ± 0.5	13 ± 5	3.94 ± 0.25
BT19FG	3.1 ± 0.2	16.9 ± 1.0	0.76 ± 0.02	12.5 ± 0.5	13 ± 5	3.42 ± 0.15

3.5.3.3 OSL Measurements

Table 3.6 The single-aliquot-regenerative-dose (SAR) protocol for multi-elevated-temperatures post-IR IRSL.

Step	Treatment	Observed
1	Give regenerative dose, D_i[a]	
2	Pre-heat at 250 °C for 60 s	
3	IRSL measurement at 50 °C for 100 s	Lx_{50}
4	IRSL measurement at 100 °C for 100 s	Lx_{100}
5	IRSL measurement at 150 °C for 100 s	Lx_{150}
6	IRSL measurement at 225 °C for 100 s	Lx_{225}
7	Give test dose, D_t	
8	Pre-heat at 250 °C for 60 s	
9	IRSL measurement at 50 °C for 100 s	Tx_{50}
10	IRSL measurement at 100 °C for 100 s	Tx_{100}
11	IRSL measurement at 150 °C for 100 s	Tx_{150}
12	IRSL measurement at 225 °C for 100 s	Tx_{225}
13	IR bleaching at 290 °C for 100 s	
14	Return to step 1	

[a] For the 'natural' sample, i = 0 and $D_0 = 0$. The whole sequence is repeated for several regenerative doses including a zero dose and a repeat dose.

Luminescence measurements were done at the University of Lausanne (Switzerland) using Risø TL-DA-20 readers equipped with infrared light-emitting diodes for stimulation and a ^{90}Sr/^{90}Y beta source, with dose rates of 0.119 ± 0.004 Gy·s^{-1} and 0.240 ± 0.007 Gy·s^{-1}. Based on Li and Li (2011a) and King et al. (2016a), the feldspar extracts were analyzed using a MET protocol summarized in Table 3.6. A preheat temperature of 250 °C for 60 s was applied after both regenerative and test doses to

remove unstable trapped electrons, followed by infra-red luminescence at 50, 100, 150, and 225 °C for 100 s. At the end of each measurement cycle, a high-temperature infrared bleach at 290 °C for 100 s was conducted to ensure no residual IRSL signal for the next cycle. Three small (2 mm ø in diameter) aliquots for each sample were measured, and luminescence was detected through the combination filters of Schott BG39/BG3. Signals were integrated over the first 4 s stimulation while background signals were integrated over the final 20 s stimulation. The beta doses ranged from 60 to 3840 Gy, and the test dose was 96 Gy for all measurements. Samples were corrected for sensitivity changes relative to each IRSL signal. All aliquots fulfilled the sample acceptance criteria of recycling ratio within 10% of unity, maximum test dose error <10%, and recuperation <10% of the natural signal.

Based on the assumption of homogeneous trap filling (i.e. the probability that a trap is filled is independent of the nearest hole at r' or the band-tail states E_b associated with that particular trap), the measurement data were fitted using a first-order exponential function (Guralnik et al., 2015b; King et al., 2016a):

$$\frac{n}{N}(t) = \varphi(t^*) \cdot A \left(1 - e^{-\frac{\dot{D}_{lab}t}{D_0}} \right) \tag{3.15}$$

where $n(t)$ is the amount of trapped electrons at time (t), N is the finite number of trapping sites, A is a pre-exponential multiplier, $\dot{D}_{lab}$ is the laboratory dose rate, D_0 is the characteristic dose of saturation, and a time-dependent factor for athermal detrapping,

$$\varphi(t^*) = e^{-\rho' \ln(1.8\tilde{s}t^*)^3} \tag{3.16}$$

where t^* is the fading time, the athermal frequency factor $\tilde{s} = 3 \times 10^{15}$ s^{-1}, and the density of recombination centers $\rho' \equiv \frac{4\pi\rho}{3\alpha^3}$, where α is a constant and ρ is the randomly distributed density of recombination centers within a feldspar mineral (Huntley, 2006; Kars et al., 2008).

3.5.3.4 Fading Measurements

Athermal signal loss is difficult to measure precisely because it imitates a slower power-law decay relative to the (semi-) exponential thermal losses. However, athermal signal loss can be measured using a fading test, which characterizes it over long timescales as possible within the laboratory (King et al., 2016a).

Fading measurements were performed for each aliquot using the same SAR MET protocol, which consists of a given laboratory radiation dose and then a range of different holding durations ($t = 0$ to >10,000 s) at room temperature before measurement. To ensure good counting statistics, regenerative doses of 46 Gy, the same as the test dose, were used in the fading experiments detected using the Schott BG39/BG3 filters. The measurement data were fitted using equation (3.15), with t^*, calculated as half the irradiation time of 500 s plus the measurement delay time. According to the approach of Huntley (2006), faded trapped charge $n(t^*)$ is related to its initial quantity $n(0)$:

$$n(t^*) = n(0)\varphi(t^*) \tag{3.17}$$

where $\varphi(t^*)$ is a time-dependent factor for athermal detrapping as seen in equation (3.16). The premise of the model is that the rate of fading is controlled by the tunneling distance (r) from the charge to its nearest recombination center. Also, a dose-invariant density of recombination centers ρ' is assumed using the model, and potential changes in charge trapping with changing doses are ignored.

3.5.3.5 Isothermal Holding Measurements

Thermal signal loss can be measured using an isothermal holding experiment with the same SAR MET protocol (King et al., 2016a), whereby each aliquot of a sample was irradiated with a regenerative dose of 46 Gy and held at elevated temperatures ($T = 170$, 190, 210, 230, 250, 300, and 350 °C) for a range of different durations ($t = 0$–10,240 s). Experiments took ~5 days for each sample, and they were used to calculate thermal kinetic parameters (E_t, E_u, and s values) for one representative aliquot of each sample. Based on the band-tail state model (Poolton et al., 2009; Li and Li, 2013; King et al.,

2016a), experimental data can be fitted using the following equation, which is derived

from equations (3.13) and (3.14) by assuming $\dot{D} = 0$:

$$\frac{n(t)}{n(0)} = \varphi(t^*) \int_0^{E_t} P(E_b) e^{\left(-ste^{-\frac{E_t - E_b}{k_B T}}\right)} dE_b \tag{3.18}$$

where $n(t)$ is the amount of trapped electrons at time (t) and $n(0)$ is the initial number of

trapped electrons. The probability of thermally evicting electrons into the band-tail states

of energy in the range of $E_b + dE_b$, i.e., $P(E_b)dE_b$, is given by:

$$P(E_b) \, dE_b = Be^{\left(-\frac{E_b}{E_u}\right)} dE_b \tag{3.19}$$

where B is a pre-exponential multiplier and E_u refers to the width of the Urbach tail (eV).

Unfortunately, in the case of my samples, the isothermal holding data for all the IRSL

signals somehow exhibit a misfit with the modeled values, so the calculation of E_t, E_u,

and s values cannot be achieved. The raw data, including all the measurements (i.e., four

IRSL signals, fading, and isothermal holding data), are shown in Tables C.1–C.12.

3.5.3.6 Screening for Thermal Signals in Feldspar

The Kars et al. (2008) approach was used to determine whether the measured

(n/N) value reflects thermal signal loss or if it is only due to athermal signal losses,

through comparison of (n/N) values with field saturation ($(n/N)_{SS}$) values (King et al.,

2016a). Whether the samples contain a thermal signal is important because it relates to

chronometric information, i.e., the time elapsed since cooling below T_c. Athermal signal

losses can also be significant. An athermally stable (non-fading) IRSL signal should

exhibit an (n/N) ratio of unity when the feldspar is saturated well below the T_c. However,

for samples that have been at $T < T_c$, low (n/N) values can be exhibited due to athermal

losses. As a result, a sample in field saturation, where the total trapping rate is equal to

the total detrapping rate while not all traps are filled, may have (n/N)<1.

To screen the samples for the presence of a thermal signal, the model of athermal detrapping (Huntley, 2006) was used to calculate sample-specific field saturation values, $(n/N)_{SS}$, where $\dot{D}$ is known (Kars et al., 2008):

$$\left(\frac{n}{N}\right)_{SS} = \int_{r'=0}^{\infty} \frac{3r'^2 e^{-r'^3}}{1+\frac{D_0}{\dot{D}}\tilde{s}e^{-\rho'^{-\frac{1}{3}}r'}} dr' \tag{3.20}$$

where dimensionless distance $r' \equiv \left\{\frac{4\pi\rho}{3}\right\}^{\frac{1}{3}} r$, and $p(r')\, dr' = 3r'^2 e^{-r'^3}\, dr'$ is the probability of the nearest recombination centers at a distance between r' and $r'+dr'$ (Huntley, 2006). From the equation, field saturation $(n/N)_{SS}$ value is mainly dependent on ρ'.

A bi-plot between measured (n/N) values and estimated $(n/N)_{SS}$ values for measurement temperatures of 50, 100, 150, and 225 °C was utilized to screen for thermal signals in the samples. Should the data points fall within a 15% range around the 1:1 line, as depicted by the symbols of the IRSL$_{225}$ signals in Figure 3.14 (b) and (c), it indicates a state of athermal field saturation. In this condition, the data lacks chromometric information beyond a minimum cooling age.

3.5.3.7 Test Analysis and Interpretation

According to the plot of $(n/N)_{SS}$ against n/N in Figure 3.14, only the IRSL$_{225}$ signals for the samples Bt1BTY2 and BT19FG are in athermal field saturation and do not exhibit a thermal signal. This result may be because the IRSL$_{225}$ signals have higher thermal stability than the other IRSL signals (Li and Li, 2011a; Li and Li, 2011b), i.e., they are less sensitive to a temperature rise and have higher T_c than the others. The result also suggests that the IRSL signals for Bt1BTY2 and BT19FG may not be consistent in recording the same thermal history. This may be the main reason for the model misfitting of the isothermal holding experiments.
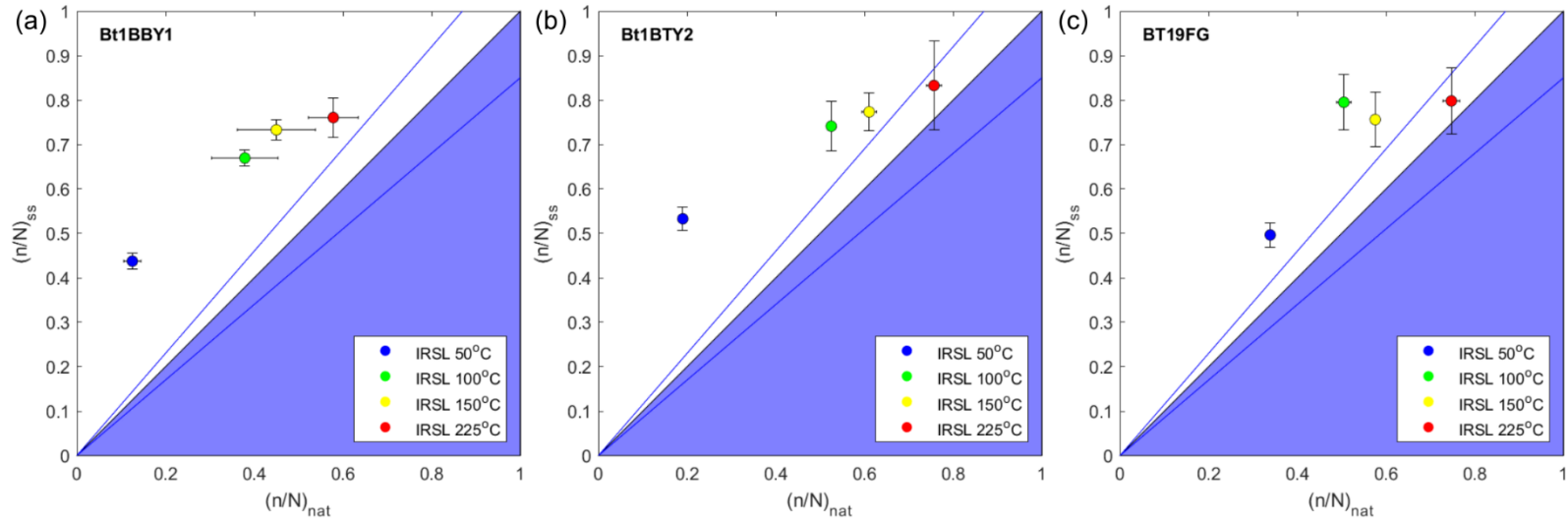
Figure 3.14 Bi-plot analysis of measured *(n/N)* values and estimated *(n/N)SS* values. The area between the blue lines is within 15% of the 1:1 line. The error bars represent 1σ. The blue field denotes the area without data falling in since the *(n/N)* value can never be greater than the *(n/N)SS* value.

Detectable anomalous fading was present in all the IRSL signals for each sample, so fading correction has been performed for all the measured ages (Table 3.7). The equivalent dose or age measured for each sample increases with the IRSL stimulation temperature, except for the $IRSL_{50}$ age estimate of BT19FG, which abnormally exhibits greater than the $IRSL_{100}$ age of the same (Figure 3.15; Table 3.7). Also, all the measured ages of BT19FG strangely appear to be greater than the corresponding fading-corrected ages (Figure 3.15; Table 3.7). Besides, the difference between the measured ages and the corresponding fading-corrected ages for each sample increases with stimulation temperature (Figure 3.15; Table 3.7). This result indicates the fading rate increasing from the lower to higher temperature IRSL signal, and it violates the conclusion that the athermal stability of the IRSL signals increases with stimulation temperature, as reported by Li and Li (2011a & 2011b) and confirmed by King et al. (2016a) and Ogata et al. (2022). The reason may be due to dose-dependent changes in anomalous fading rate (Kars et al., 2008; Li and Li, 2008; Li and Li,

2011a), i.e., an increased fading rate produced by a high laboratory dose, which results in great age overestimations and over-corrections.
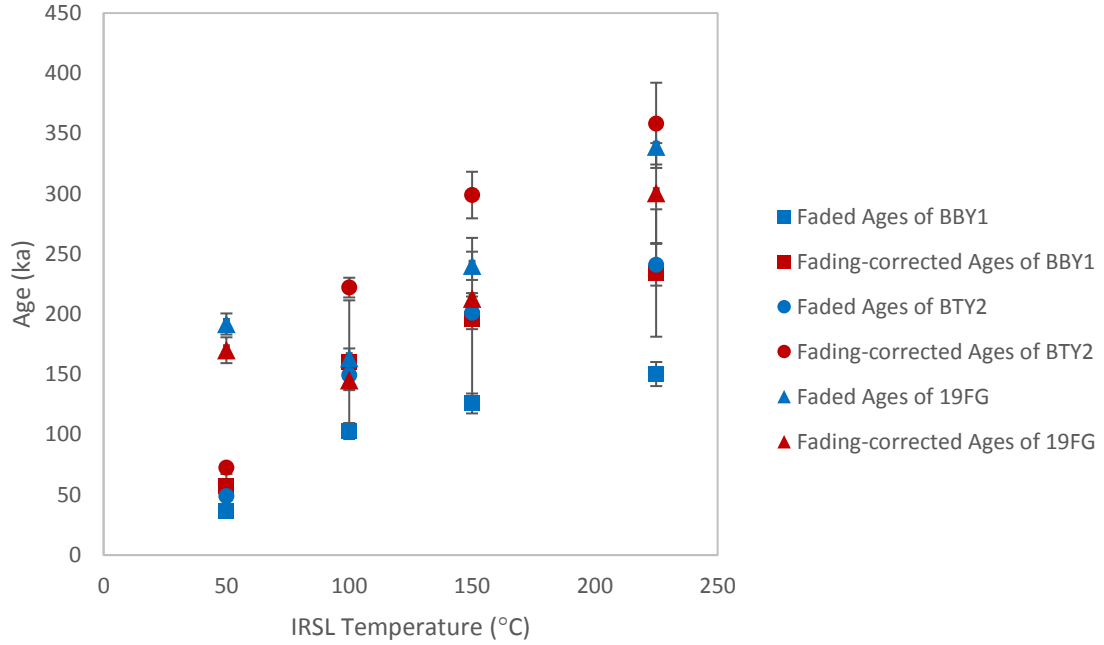
Figure 3.15 Comparison between the measured ages having anomalous fading depicted as blue and the fading-corrected ages shown as red for each sample.

Table 3.7 Summary of measured and estimated values for three fault gouge samples. (*n/N*) is the ratio of trapped charges to the total number of electron traps. (*n/N*)$_{SS}$ is the estimated specific field saturation value. Faded D_0 refers to the measured characteristic saturation dose, and faded D_e means the equivalent dose measured. FCorrAge means fading corrected ages.

	IRSL	(n/N)	(n/N)$_{SS}$	Faded D_0 (Gy)	Faded D_e (Gy)	FadedAge (ka)	FCorrAge (ka)
Bt1BBY1	50	0.13 ± 0.02	0.43 ± 0.02	693 ± 24	151 ± 3	36.4 ± 2.3	56.8 ± 10.5
	100	0.38 ± 0.08	0.67 ± 0.02	793 ± 58	426 ± 9	103.0 ± 6.6	160.5 ± 51.0
	150	0.45 ± 0.09	0.73 ± 0.03	850 ± 74	521 ± 13	125.9 ± 8.3	196.1 ± 67.2
	225	0.58 ± 0.05	0.76 ± 0.05	676 ± 58	622 ± 17	150.3 ± 10.0	234.2 ± 52.9
Bt1BTY2	50	0.19 ± 0.00	0.53 ± 0.03	647 ± 20	193 ± 4	48.8 ± 3.2	72.6 ± 2.5
	100	0.52 ± 0.00	0.74 ± 0.06	710 ± 23	589 ± 14	149.4 ± 9.9	222.1 ± 8.2
	150	0.61 ± 0.01	0.77 ± 0.05	756 ± 30	793 ± 21	201.1 ± 13.5	298.9 ± 19.3
	225	0.76 ± 0.01	0.83 ± 0.11	590 ± 38	951 ± 34	241.0 ± 17.3	358.2 ± 34.0
BT19FG	50	0.34 ± 0.00	0.50 ± 0.03	515 ± 15	655 ± 8	191.8 ± 8.8	170.1 ± 10.7
	100	0.51 ± 0.01	0.80 ± 0.06	494 ± 13	559 ± 12	163.5 ± 8.0	145.0 ± 8.0
	150	0.58 ± 0.00	0.76 ± 0.06	512 ± 12	820 ± 17	240.2 ± 11.7	213.0 ± 4.6
	225	0.75 ± 0.02	0.80 ± 0.08	379 ± 36	1158 ± 32	339.0 ± 17.6	300.5 ± 41.5

In conclusion, the inconsistent records about the thermal history revealed by the IRSL signals prevent us from determining whether these fault gouge samples experienced a heating event (e.g., a seismic movement) and whether the accumulated trapped electrons in the feldspar grains of each had been released or partially reset during the heating event. The age overestimations and over-corrections also make it impossible to achieve the direct dating fault gouge in my case using the Multi-OSL method.

CHAPTER 4: PALEOSEISMOLOGICAL ANALYSIS IN EASTERN BHUTAN

4.1 Geomorphology of the Study Area

At the Dungsam Chu site (26.79201°N, 91.51116°E) (the study area), geomorphic analyses were performed using transects acquired by differential GPS (dGPS) and landscape analysis of a digital terrain model (DTM) with a horizontal resolution of 0.5 m. Based on the detailed maps created on the DTM, the trace of the MFT (i.e., the TFT), consists of segments arranged en échelon and offset by N-S striking to NNE-SSW striking faults (Figure 4.1). Despite large vertical displacement along the MFT, the thalweg is flat along a stretch of ~240 m (Figures 4.2a and 4.2b). Fifty meters upstream of the MFT trace is a 1-m-high knickpoint (Figures 4.2a and 4.2b). A 1.5-m-high knickpoint is located ~180 m downstream, from which the river flows south at ~0.5° (Figures 4.2a and 4.2b). This indicates that the coseismic knickpoints migrated upstream and were rapidly eroded, as observed elsewhere in recent earthquakes (Liu and Yang, 2015). Such a rapid channel response is compatible with a high sediment supply and discharge.

Alluvial terraces deposited by the Dungsam Chu (Figure 4.2) were observed and characterized by the composition of well-stratified cobbles to boulders within a sandy matrix, the dominant lithologies of which are quartzite and slate from the LHS. The lower (younger) terraces (T1, T2) are located along the present stream at low elevations, ~3.5 m and ~9 m above the present stream, respectively. T2 is a fill terrace on which T1 forms as a cut-in-fill terrace. The intermediate terrace (T3) was strongly dissected by natural and anthropogenic processes. Alternatively, it could be interpreted as remnants of an alluvial fan. T4 was only mapped locally upstream of Dungsam Chu and was not

observed in the field, the same as T3. In the study site, a river-cut exposure reveals that the lower terraces T1 and T2 were deposited by the Dungsam Chu over the Siwalik Group and cut through by the MFT (Figure 4.2a). To the south of the MFT, the flat recent to active deposits of an alluvial plain are presented with mostly undeformed structures.
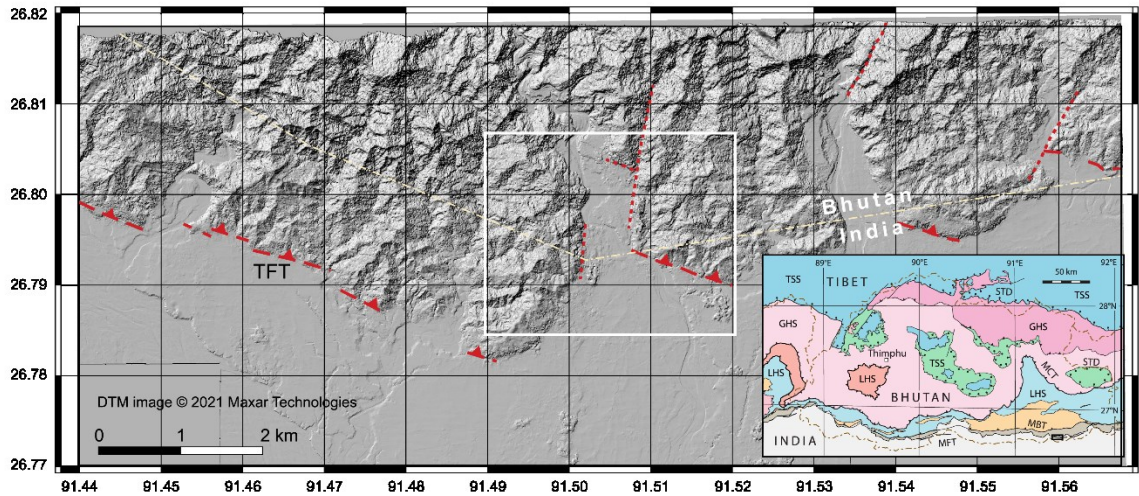
Figure 4.1 Topography of the Himalayan foothills and foreland basin in eastern Bhutan. The topographic frontal thrust (TFT) consists of segments arranged en échelon and offset by N-S striking to NNE-SSW striking faults. White square indicates the area of Figure 4.2a. The digital terrain model with a horizontal resolution of 0.5 m and vertical resolution of 8 m was derived from Maxar stereo pair imagery by Maxar Technologies and further processed using QGIS (v. 3.16.3).

4.2 Paleoseismic Exposure

The Dungsam Chu site shows a ~14 m high river-cut cliff facing WSW, the main section of which was cleaned and partly gridded for logging (Figure 4.3). The orthorectified photomosaic of the outcrop was constructed using Agisoft Metashape software. Because the MFT has a strike of 110° and the outcrop strikes 150°, the outcrop log (Figure 4.3b) is a projection of the photomosaic perpendicular to the fault strike and parallel to the slickenlines observed in the fault gouge.

The Siwalik bedding identified in the center of Samdrup Jongkhar is strongly overprinted by pervasive fracture cleavage, suggesting top down to the west movement (Figure 4.4a). The fracture cleavage has the same orientation as the N-S striking faults dissecting the MFT trace (Figure 4.2a). In the cross-section, the MFT is straight and

simple, dipping about 24° to the north, and places Late Miocene Lower Siwalik mudstone and siltstone on top of the lower river terraces (Figure 4.3).

The main section of the exposure exhibits two channels, each characterized by a fining upward sequence formed by rounded cobbles first settling at the base of channel fill and gradually gravels and finally sands (Figure 4.3a). Sandy-graded beds are shown below the channel deposits, with the lenses of granule or pebble gravel that are laterally extensive for more than 8 m (Figures 4.3 and A.2). All the characteristics above indicate a fluvial deposition environment in our study area.

The main lithological units were defined in the field and documented by simplified structural and stratigraphic log of mosaic (Figures 4.3 and A.2). The footwall block consists of the ~8.5-m-thick T2, which contains four interbedded fine-to-coarse sand and cobble gravel units with sharp boundaries. The four layers are labeled U4, U3, U2, and U1 from oldest to youngest. Unit U4, the oldest unit observed at the base of the section, is a clast-supported fluvial deposit composed of poorly-sorted and poorly-rounded granules, pebbles, and cobbles in a sandy matrix. The sandy matrix is overprinted by oxidation and local concentrations of manganese oxide. The base of U4 is currently below the water table; therefore, it could not be logged. Unit U3 overlying U4 is a ~2.0–3.3 m thick medium sand-sized fluvial deposit, including ~20–80 cm-thick granule or pebble gravel lenses. Unit U2, underlain by U3, is a ~1.2–3.0 m thick, poorly sorted, and well-rounded pebble-cobble-boulder gravel with a sandy matrix. Unit U2 is distinguished from unit U4 by a generally larger clast size and a lesser degree of orange coloration due to oxidation. The topmost unit, U1, is the youngest in the footwall, and it is up to 3.2 m thick sandy to silty fluvial deposit. It is finer for grain size and lighter in color than unit U3.

In the hanging wall, the late Miocene Lower Siwalik mudstone and siltstone is overlain by the ~4.5 m thick T2, which includes three layers, interbedded fine-to-coarse sand and cobble gravel. The bottommost sand layer in the T2 lies over a clear erosion and weathering surface that cuts through the Siwalik north-dipping stratigraphy while the top

72
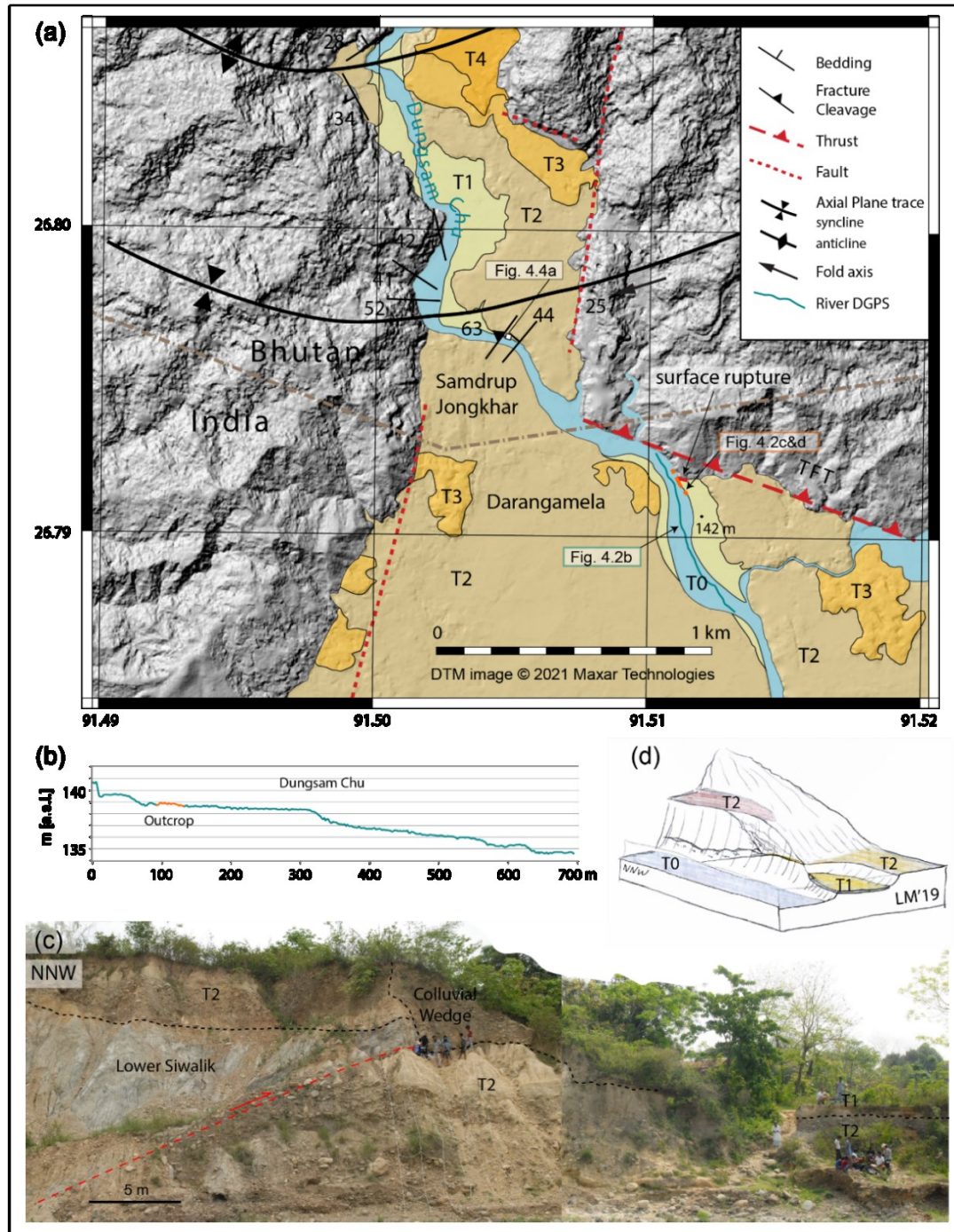
Figure 4.2 Dungsam Chu study site. (a) Geomorphic and structural map of the study area. The digital terrain model with a horizontal resolution of 0.5 m and vertical resolution of 8 m was derived from Maxar stereo pair imagery by Maxar Technologies and further processed using QGIS (v. 3.16.3). Alluvial terraces were mapped on the original DTM and are labeled from T0 (active channel) to T4 (oldest). The geological observations are from Grujic et al. (2018) and this research. The black dot indicates the elevation of 142 m above sea level and the location of the base station for the dGPS survey. (b) Elevations of the segment of the active river in the location of the outcrop. (c) Panorama photography (view looking East-Northeast) of the outcrop. (d) Draft of the paleoseismic exposure drawn by Luca Malatesta (U of Lausanne, 2019). T2 in the hanging wall is labeled as pink while light brown for T2 in the footwall and yellow for T1.

73
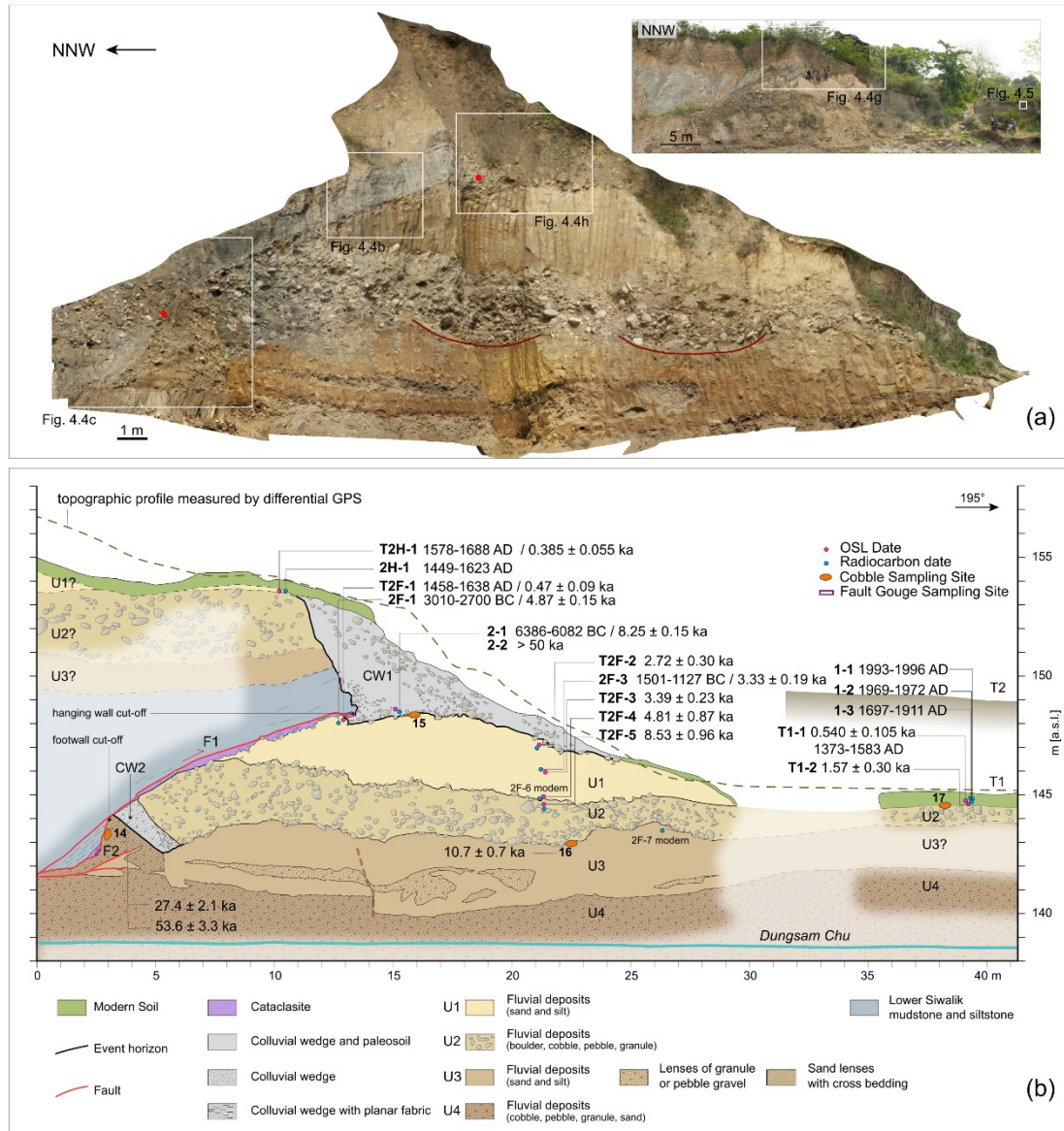
Figure 4.3 Dungsam Chu paleoseismic exposure. (a) Orthorectified photomosaic of the refreshed section of river-cut face (See Figure A.1 for the whole one). Red points indicate the tips of the surface ruptures identified by two different colluvial wedges. Dark red curves outline two channels, characterized by a fining upward sequence. The inset shows the non-refreshed river-cut face. (b) Simplified structural and stratigraphic log of mosaic in Figure 4.2c. The orthorectified photomosaic of the outcrop was constructed with Agisoft Metashape software using 136 field photographs, and it is a projection of the photomosaic perpendicular to the fault strike and parallel to the slickenlines observed along the clay smears within the F1 surface. The topographic profile, including the surface of T1 and T2 to the south of the MFT trace, was measured along the slope (where it was slightly higher and away from the cliff edge) by a dGPS and projected onto the exposure map. The Dungsam Chu bed is also measured by the dGPS, demonstrated as a cyan line in this figure, and labeled as an orange segment in Figure 4.2b. Red lines are main faults. Blue dots indicate the locations and 2σ-calibrated calendar ages of the ^{14}C samples which have reasonable results while reddish-purple dots show OSL sampling sites and OSL ages with 1σ uncertainty. Orange ellipses are cobbles collected along layer surfaces or the fault surface. At least 3 cobbles were collected in each cobble sampling site. Purple rectangular marks the sampling sites of fault gouge along the fault surface. Faded colors indicate a lack of exposure. T2— a fill terrace, and T1— a cut-in-fill terrace.

74

sandy bed is covered by modern soil, mainly including horizon A. Over the fault trace, there were no continuous deposits observed except for modern soil.

The cut-in-fill terrace T1 exposed to the south of the paleoseismic exposure is ~65 cm thick, comprising organic material-rich soil that caps the pebble-to-boulder gravel layer U2 (Figure 4.4). The top of T1 shows likely four soil profiles, each of which mainly consists of soil horizons A and B. The uppermost and lowermost soil profiles 0 and 3 both exhibit a clear sequence of local soil with horizons A, Bt (showing clay accumulation in the form of coatings on ped surfaces or in pores), and B. The middle soil profiles 1 and 2 display white-leached clay or clayey silt clasts identified as 1Aeb in the top section, overlying a weakly developed 1Bwb horizon and a possible fluvial sand deposit 1C horizon that buried a soil simply including horizons 2Ab and 2Btb. The presence of 1Aeb, 1Bwb, and 1C indicates that no erosion but abundant water leaches the sediments in the middle layer. A large lump of clay appears at the bottom of soil profile 3, and it seems probably an ephemeral sag pond deposit because it contains too much clay to be considered all pedogenic in a short time.

Two additional units display wedge-shaped geometries, and both exhibit little stratigraphy and debris and wash facies and contain sub-angular clasts and unsorted sediments of all particle sizes (from boulder to clay), which were deposited along the base of fault scarps (Figures 4.5c, 4.5d, 4.5g, and 4.5h). The two units are interpreted as scarp-derived colluvial wedges, labeled CW1 and CW2. Unit CW1, marking the tip of the latest surface rupture, is stratigraphically the youngest unit observed at our study site. It originates from the T2 in the hanging wall and consists of loosely unconsolidated sediments (Figure 4.5g). Unit CW2 is presumably derived from U3 and U4 and contemporary soil and composed of dragged pebbles in a dark sandy matrix with rare cobbles, and it caps the tips of the uppermost and middle splays of the older fault F2 (Figures 4.5c and 4.5d). CW1 and CW2 marking fault tips were deposited during or shortly after seismic displacement along the fault, which indicates at least two seismic events along the same fault.
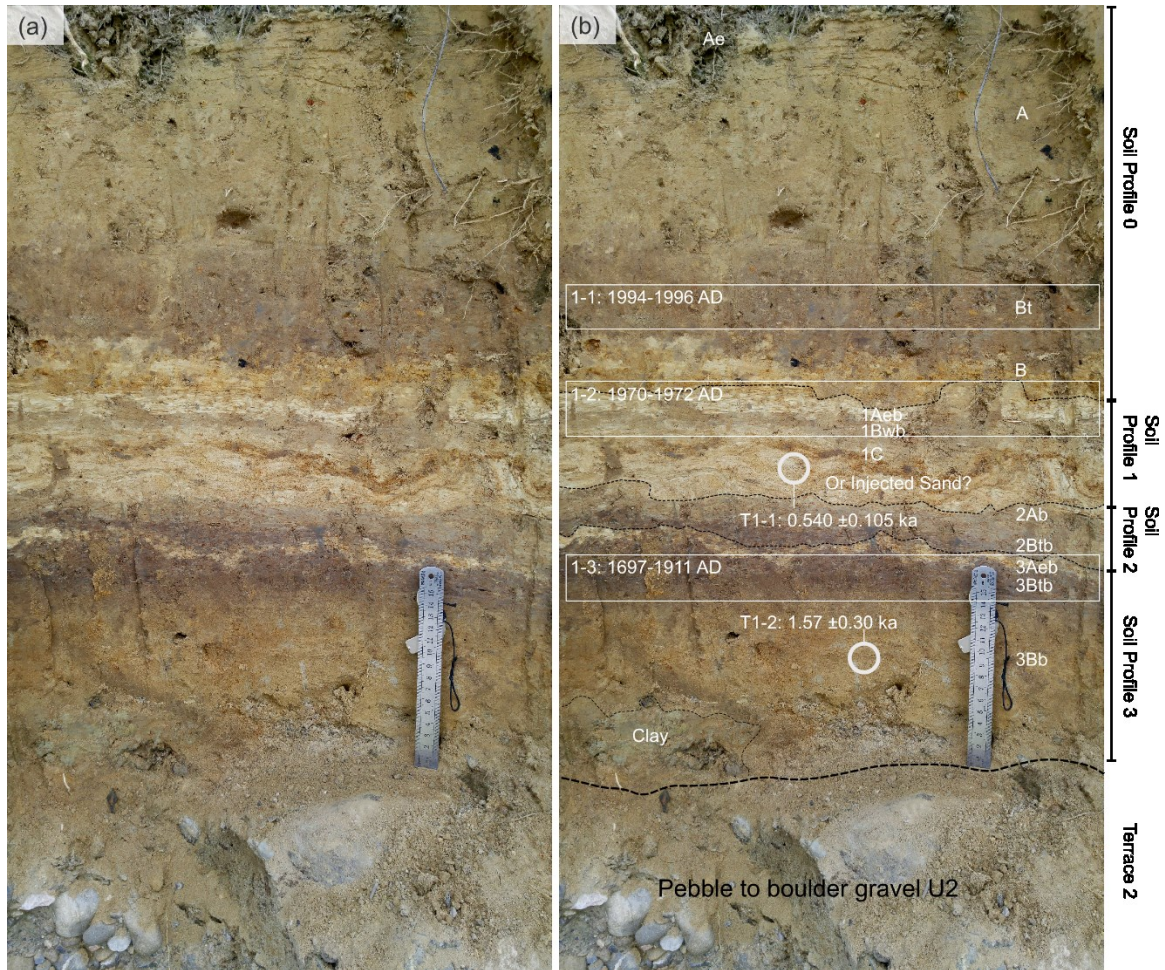
Figure 4.4 Fill terrace T1 at the southern end of the Dungsam Chu exposure. (a) Original photograph. (b) Interpreted photograph. T1 lies on top of layer U2 of the cut terrace T2 and consists of likely four soil profiles, each of which mainly consists of soil horizons A and B. The deposits of T1 are interpreted as overbank deposits being converted to modern soil. Material for radiocarbon dating was collected along horizons indicated with white rectangles. White circles point out OSL sampling sites. An alternative interpretation would be a possible earthquake-induced injected sand in the middle section instead of C1, based on the age distribution and photograph analysis.

A lens of clay-rich fault gouge presents near the tip of each surface rupture. They were likely either produced or dragged by each paleoseismic movement (Figures 4.3, 4.5e, 4.5f, 4.5h, and 4.5i). Both are in structural contact with sandy deposits: the top fault gouge lies over U1 in the footwall (Thin sections in Figure A.3), and the bottom one is between U4 in the footwall and the cataclasite identified between the two F2 splays and at the tip of the younger fault F1. Three fault gouge samples were collected to attempt to obtain the direct ages of the seismic events using the Multi-OSL of feldspar dating

technique. However, all failed due to age overestimations and over-corrections (Details seen in section 3.5).

4.3 Dating Analysis

4.3.1   AMS ^{14}C and OSL Dating Results

To constrain the deposition ages of the stratigraphic units, we collected pairs of organic materials and OSL samples from seven locations on the top units of the northern side of the paleoseismic exposure, i.e., footwall block (Figure 4.3b; Tables 4.1, 4.2, and B.1). One single ^{14}C sample (2F-7) was collected from the topmost section of the lower sand gravel layer U3 of the footwall, above which, i.e., along the boundary between U2 and U3, a series of cobbles (16A, 16B, and 16C) were collected (Figure 4.3b). For two different organic materials identified from the same sample, we renamed them with consecutive codes (See all in Table B.1).

In the hanging wall, charcoal sample 2H-1 and OSL sample T2H-1 were both collected from the lowermost section of the top unit U1. While 2H-1 yielded a calibrated age of A.D. 1449–1623, T2H-1 produced the OSL burial age of 0.385 ±0.055 ka, i.e., A.D. 1578–1688.

In the footwall, three pairs of ^{14}C and OSL samples were collected from the much thicker unit U1 than the one in the hanging wall, and two pairs from the top section of U2 (Figure 4.3b): from top to bottom within the two units U1 and U2, (a) 2F-1 (macrofossil) and T2F-1 (OSL) collected at 15 cm from the fault zone, (b) 2F-2 (sediment) and T2F-2 (OSL), (c) 2F-3 (charcoal) and T2F-3 (OSL), (d) 2F-4 (sediment) and T2F-4 (OSL) near the layer boundary between U1 and U2, and (e) 2F-5 (sediment), 2F-6 (undefined organic material) and T2F-5 (OSL). For radiocarbon dating here, three samples, 2F-1, 2F-3, and 2F-6, yielded radiocarbon ages that are dendrochronologically corrected (Reimer et al., 2020). The remaining three (2F-2, 2F-4, and 2F-5) failed because the C content was too low. However, the calibrated age of 3010–2700 B.C. obtained by measuring one piece of macrofossil identified in sample 2F-1 is much older than the OSL burial age A.D. 1458–

1638 (0.47 ± 0.09 ka) of sample T2F-1 at the same site. Considering the too few macrofossils in layer U1, the ^{14}C age of sample 2F-1 was not used to constrain U1 deposition. Also, the mismatched ^{14}C and OSL ages demonstrate material mixing in the fault zone. Besides, sample 2F-6, which is the same as 2F-5 but different material and collected from the top section of U2, yielded a modern age. This age may have been caused by the in situ biological activity. Thus, for the samples from the same site in the footwall, only the ^{14}C age of 1501–1127 B.C. (3.33 ± 0.19 ka) yielded by charcoal sample 2F-3 is consistent with 3.39 ± 0.23 ka, the OSL burial age of sample T2F-3.

All five OSL samples from top to bottom in the footwall yielded an increasing age trend consistent with the stratigraphic column of T2 (Figure 4.3b). For U1 in the footwall, three OSL samples (T2F-1, T2F-2, and T2F-3) yielded ages of 0.47 ± 0.09 ka (A.D. 1458–1638), 2.72 ± 0.30 ka, and 3.39 ± 0.23 ka, that suggest the ~3-m thick U1 was deposited during around three thousand years. Two OSL samples in the topmost and top sections of U2 in the footwall yielded ages of 4.81 ± 0.87 ka and 8.53 ± 0.96 ka, respectively. Considering all the deposition dates and stratigraphic features in U1 and U2, a low deposition process with a higher energy fluvial regime is implied. In addition, another ^{14}C sample 2F-7 from U3 was likewise identified as an undefined organic material and yielded a modern age like 2F-6 (Table B.1), which obviously may not represent the U3 deposition either.

Two charcoal samples (2-1 and 2-2) and one OSL sample (T2-1) were collected from coarsely sandy section of the top colluvial wedge CW1. Sample 2-1 yielded the age of 6386–6082 B.C. (8.25 ± 0.15 ka), which confirms the origin of unit CW1 but cannot be used to constrain the deposition of CW1 caused by the later coseismic slip. The other sample 2-2 is detrital charcoal and yielded the age >50 ka (Table B.1), which implies this sample is most likely a Permian coal fragment from the Gondwana unit outcropping at the headwaters of Dungsam Chu. On the other hand, however, OSL sample T2-1 failed due to feldspar contamination.

Three charcoal samples and two OSL samples were collected from the cut-in-fill terrace T1 at the southern side of the paleoseismic exposure (Figures 4.3d and 4.5). Three

charcoal samples found respectively in each B horizon (Bt or Bw) of soil profiles 0, 1, and 3 yielded the calibrated ages of A.D. 1993–1996, A.D. 1969–1972, and A.D. 1697–1911. The relatively broader age range of A.D. 1697–1911 correlates to three corrected ages: A.D. 1697–1724 with 29.7%, A.D. 1812–1836 with 28.5%, and A.D. 1881–1911 with 37.3%. Two OSL samples taken from C horizon of soil profile 1 (C1) and from the middle of B horizon in soil profile 3 (B3) yielded the ages of 0.540 ± 0.105 ka (A.D. 1373–1583) and 1.57 ± 0.30 ka, respectively. Considering all the age constraints in T1 (Figure 4.5), soil profile 1 with horizons 1Aeb, 1Bwb, and 1C might be influenced seismically, and the lowermost soil may be formed pre-seismically. Based on the overlying 1C having an older burial age than the underlying buried soil, an alternative interpretation would be a possible earthquake-induced injected sand in the middle section instead of 1C, even though the burial OSL ages calculated using the MAM might still be overestimated due to incompletely bleached grains in the samples. However, no other injection features were exposed to confirm this possibility.

In summary, only five of the twelve ^{14}C samples (1-1, 1-2, 1-3, 2H-1, and 2F-3) yielded reasonably calibrated ages (Table 4.1) that can be further used to constrain the timing of the paleoseismic events. For conventional quartz OSL dating, almost all produced OSL ages (Table 4.2), except for T2-1. However, most OSL samples had some population of incompletely bleached grains as evidenced by the overdispersion value greater than 20% ($\sigma_b > 0.2$), so the MAM for D_e determination with the parameter

Figure 4.5 Field photographs of characteristic structures at the Dungsam Chu exposure. (a) Moderately west-dipping Siwaliks siltstone layering strongly overprinted by steeper fracture cleavage indicating top down to the west faulting. Location in the centre of Samdrup Jongkhar indicated in Figure 4.2a. (b) The later fault placing Siwalik on top of the U1 unit of T2 and dragging up pebbles from lower stratigraphic levels during E1. (c) Photomosaic showing colluvial wedge CW2 and main faults. (d) Interpretation of unit CW2. Solid black lines are contacts between lithological units. Dashed black lines show dragged pebble layers in unit CW2, which were formed during E1. (e) The bottom of the north end of the paleoseismic exposure indicates the branching of older faults F2 cut off by the most recent fault. Between the two F2 splays and at the tip of the later fault is a lens of cataclasite. (f) Close up of Figure 4.4e showing the cataclasite, which is derived both from Siwalik and T2 lithologies. (g) Interpretation of unit CW1. Dashed white lines are approximate contacts between lithological units. (h) Unit CW1 showing the tip of the younger fault (circle), the leading edge of the Siwalik in the hanging wall (white dashed line), and the Event Horizon 1 (EH1, bold white dashed line). Location of the photograph in Figure 4.4i is in the lower-left corner. (i) Tip of the younger fault, looking NNW. In the hanging wall, there is a lens of clay-rich fault gouge, probably derived from Siwalik sediments.
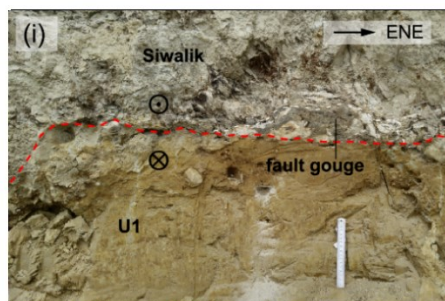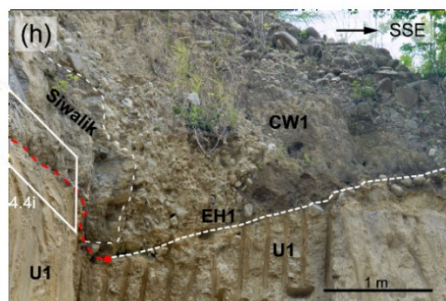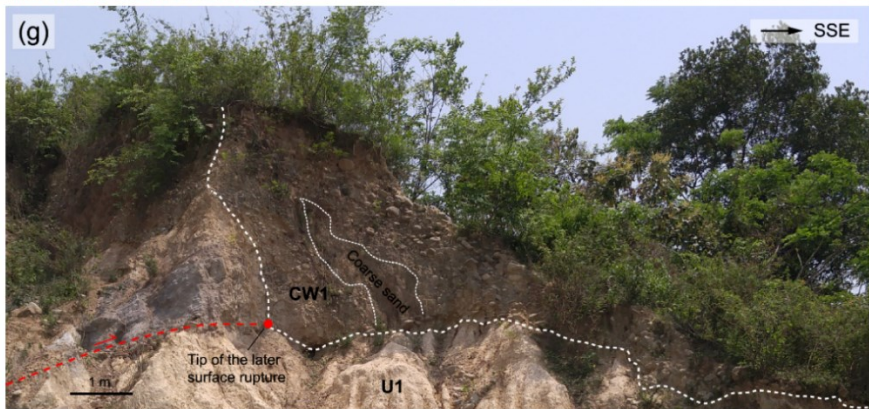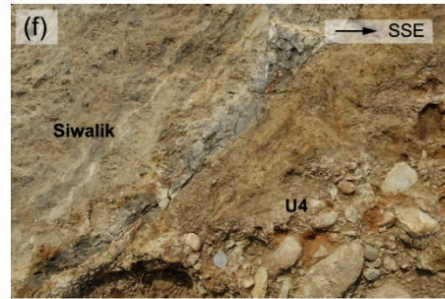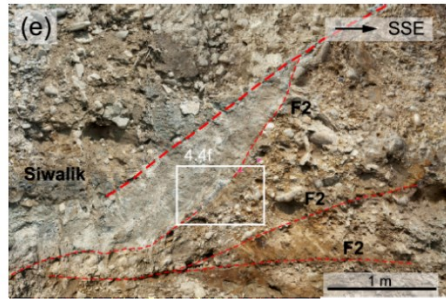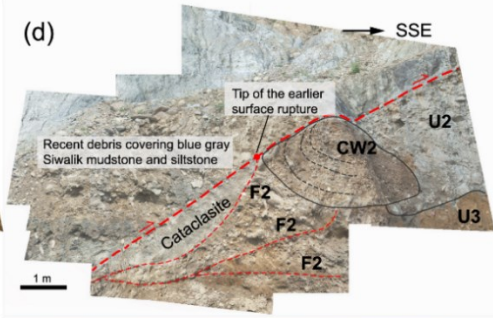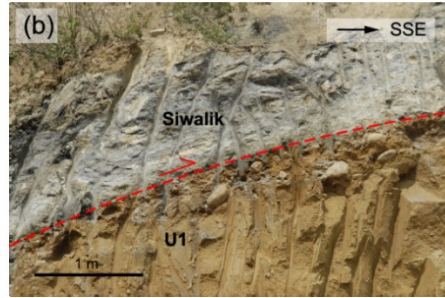
Table 4.1 Major results of AMS ^{14}C analyses on organic materials collected from the Dungsam Chu exposure (see all results from Table B.1 for details).

Unit[a]	Material	Sample Name	ETH Lab No.[b]	Measured Radiocarbon Age (B.P.)[c]	Calibrated Ages (Calendric, 2σ)[d]
T1-soil 0	charcoal	1-1	90350	112.2 ± 0.3 pMC	Cal A.D. 1993-1996
T1-soil 1	charcoal	1-2	90351	151.29 ± 0.62 pMC	Cal A.D. 1969-1972
T1-soil 3	charcoal	1-3	90352	36 ± 22	Cal A.D. 1697-1911
CW1-sand	charcoal	2-1	101046	7376 ± 61	Cal B.C. 6386-6082
T2-U1	charcoal	2H-1	101038	383 ± 22	Cal A.D. 1449-1623
T2-U1	macrofossil	2F-1	90353	4266 ± 40	Cal B.C. 3010-2700
T2-U1	charcoal	2F-3	90357	3082 ± 74	Cal B.C. 1501-1127

[a]See trench log for stratigraphic unit designations.
[b]Laboratory sample codes. All samples have been dated by the ETH accelerator facility in Zurich (Switzerland).
[c]Radiocarbon years B.P. relative to A.D. 1950 with 1σ counting error.
[d]Calendric dates were calibrated using OxCal and the atmospheric calibration curve IntCal20.

Table 4.2 Results of OSL analysis on samples collected from the Dungsam Chu exposure (see all results from Table B.1 for details). The input variables for individual samples used for dose rate and age calculations are listed in Table 3.2.

Sample [a]	No. of aliquots [b]	OD [c] (%)	Equivalent Dose [d] (Gy)	Dose Rate (Gy/ka)				Age [d] (ka)
				Beta	Gamma	Cosmic	Total	
T1-1	4 (41)	67.49 ± 7.82	1.02 ±0.20	0.943 ±0.034	0.740 ±0.025	0.215 ±0.021	1.897 ±0.047	0.540 ±0.105
T1-2	4 (25)	72.92 ± 10.79	4.16 ±0.78	1.349 ±0.051	1.093 ±0.036	0.203 ±0.020	2.644 ±0.066	1.57 ±0.30
T2H-1	14 (38)	59.96 ± 7.28	1.05 ±0.15	1.358 ±0.059	1.159 ±0.046	0.209 ±0.021	2.725 ±0.078	0.385 ±0.055
T2F-1	4 (29)	72.81 ± 9.76	1.39 ±0.26	1.576 ±0.096	1.247 ±0.068	0.129 ±0.013	2.951 ±0.119	0.47 ±0.09
T2F-2	17 (34)	23.19 ± 3.40	8.31 ±0.79	1.571 ±0.133	1.306 ±0.101	0.179 ±0.018	3.056 ±0.168	2.72 ±0.30
T2F-3	18 (31)	19.58 ± 2.92	9.65 ±0.37	1.455 ±0.124	1.231 ±0.095	0.158 ±0.016	2.844 ±0.157	3.39 ±0.23
T2F-4	3 (26)	48.17 ± 7.17	15.89 ±2.83	1.683 ±0.092	1.478 ±0.074	0.145 ±0.015	3.306 ±0.119	4.81 ±0.87
T2F-5	17 (29)	37.56 ± 5.43	16.60 ±1.82	0.995 ±0.038	0.810 ±0.026	0.140 ±0.014	1.945 ±0.048	8.53 ±0.96

[a] F – footwall, H – hanging wall.
[b] Number of aliquots used in age calculation and total number of aliquots analysed in parentheses.
[c] Overdispersion (OD, i.e., σ_b) calculated as part of central age model (CAM) (Galbraith et al., 1999).
[d] De and ages calculated using either the CAM or minimum age model, MAM-3 for small-aliquot of Galbraith et al. (1999).

Table 4.3 Summary of radionuclide concentrations, calculated dose rates, estimated water content values, and depth of the rock.

Sample name	Sample type	Depth (m)	Water cont. (%)	Radionuclide concentration			Infinite matrix dose rate			Cosmic (Gy/ka)	Internal beta (Gy/ka)
				U (ppm)	Th (ppm)	K (%)	Beta (Gy/ka)	Gamma (Gy/ka)	Alpha (Gy/ka)		
14	Sediment	-	4 ± 2	3.1 ± 0.2	16.9 ± 1.0	0.76 ± 0.02	1.052 ± 0.114	1.286 ± 0.058	-	-	-
14A	Cobble	10	0	0.9 ± 0.1	7.3 ± 0.3	0.77 ± 0.02	0.702 ± 0.002	0.642 ± 0.017	0.034 ± 0.016	0.068 ± 0.007	0.263 ± 0.090
14C	Cobble	10	0	0.4 ± 0.0	1.9 ± 0.1	0.21 ± 0.01	0.206 ± 0.000	0.188 ± 0.005	0.011 ± 0.005	0.068 ± 0.007	0.078 ± 0.025
16	Sediment	-	12 ± 6	3.2 ± 0.2	15.7 ± 0.9	1.53 ± 0.04	1.362 ± 0.186	1.311 ± 0.090	-	-	-
16A	Cobble	5.5	0	0.3 ± 0.0	1.2 ± 0.0	0.08 ± 0.00	0.103 ± 0.000	0.111 ± 0.003	0.007 ± 0.003	0.106 ± 0.011	0.04 ± 0.01

σ_b = 0.2 was used for these samples (Figure 4.6). The CAM was applied only on sample T2F-3, which was well bleached (Figure 4.6). The low number of aliquots involved in the age estimate for samples T1-1, T1-2, T2F-1, and T2F-4 suggests the low bleaching level of the samples (Table 4.2; Figure 4.6). The uncertainties of over 15% in the OSL ages are therefore shown for the four samples, and these burial OSL ages might still be overestimated despite using the MAM for D_e calculation.

4.3.2 Rock Surface Dating Results

4.3.2.1 Verifying Cobble Surface Bleaching Level With Luminescence-Depth Profiles

To assess whether the cobble surface was well bleached before burial, eight cobbles (14A, 14B, 14C, 15B, 15C, 16A, 16B, and 17A) were first selected for initial investigations of luminescence-depth profiles by using one core extracted from each cobble and measuring slices of each core. Cobbles 14A, 14B and 14C were entrained along the thrust surface from U4 in the footwall while 15B and 15C were collected at the base of the colluvial wedge CW1. While 16A and 16B were from the boundary between U2 and U3 in the footwall, sample 17A was collected from the top of U2 within T1.

Based on initial investigations, cobbles from graywacke, including 14B, 15B, 15C, 16B, and 17A, were unsuitable for further investigations (Figures D.1–D.4). Samples 15C and 16B crumbled so readily that all slices from the cobble surface to the interior were impossibly obtained in succession. Samples 15B and 15C showed quite weak OSL/IRSL signals, yielding the Lx/Tx ratios with large errors. Most importantly, all the luminescence-depth profiles produced for each graywacke cobble using either the OSL or IRSL signals (Figure D.5) showed no bleaching or incomplete bleaching occurred on the surfaces of these samples. A great scatter was observed in the luminescence profile of 16B (Figure 4.7a, only showing the better OSL signal with depth), which may imply unbleached surface on the cobble. The luminescence profiles of 14B, 15B, 15C, and 17A have no obvious trend for any signal (e.g., 15B shown in Figure 4.7b), which suggests no bleaching occurred on the cobble surface.

For each quartzite cobble (14A, 14C, or 16A), the Lx/Tx ratios with depth for either $IRSL_{50}$ or post-IR $IRSL_{225}$ signals have large errors (Figures D.6–D.8). The reason for the error of the IRSL signal ratio may be the low sensitivity of feldspar caused by its low content in the samples. However, all their first-core luminescence profiles produced using the OSL_{125} signal showed an obvious plateau near the surface on the buried side in addition to a saturation plateau with depth into the cobble (Figure 4.8), which implies each sample experienced burial only once after daylight exposure and that they were well bleached prior to deposition. This means that samples 14A and 14C were not or little affected by frictional heating produced during the paleo-seismic event. Thus, the attempt to obtain the direct age of the paleo-seismic event by dating the cobbles trailed along the thrust surface failed. For 16A, due to missing the slices of the topmost ~ 2.6 mm segment

Figure 4.6 Small-aliquot D_e distributions for conventional OSL samples from the Dungsam Chu site. For each row sample, the probability distribution function is shown in the left column while the radial plot in the right where the axis about the value of D_e is logarithmic. The gray shadow represents the application of the age model for age determination and show the D_e value with uncertainties. Most samples that had some population of incompletely bleached grains evidenced by the overdispersion value (OD, i.e., σ_b) greater than 20% used the MAM (Minimum Age Model). Sample T2F-3 which was well bleached applied the CAM (Central Age Model). Three vertical lines in the left diagrams represent the D_e value and its lower and upper limits calculated by the age model and show the number of aliquots involved in the age estimate, which is expressed as a percentage in 2σ in the right graphs.
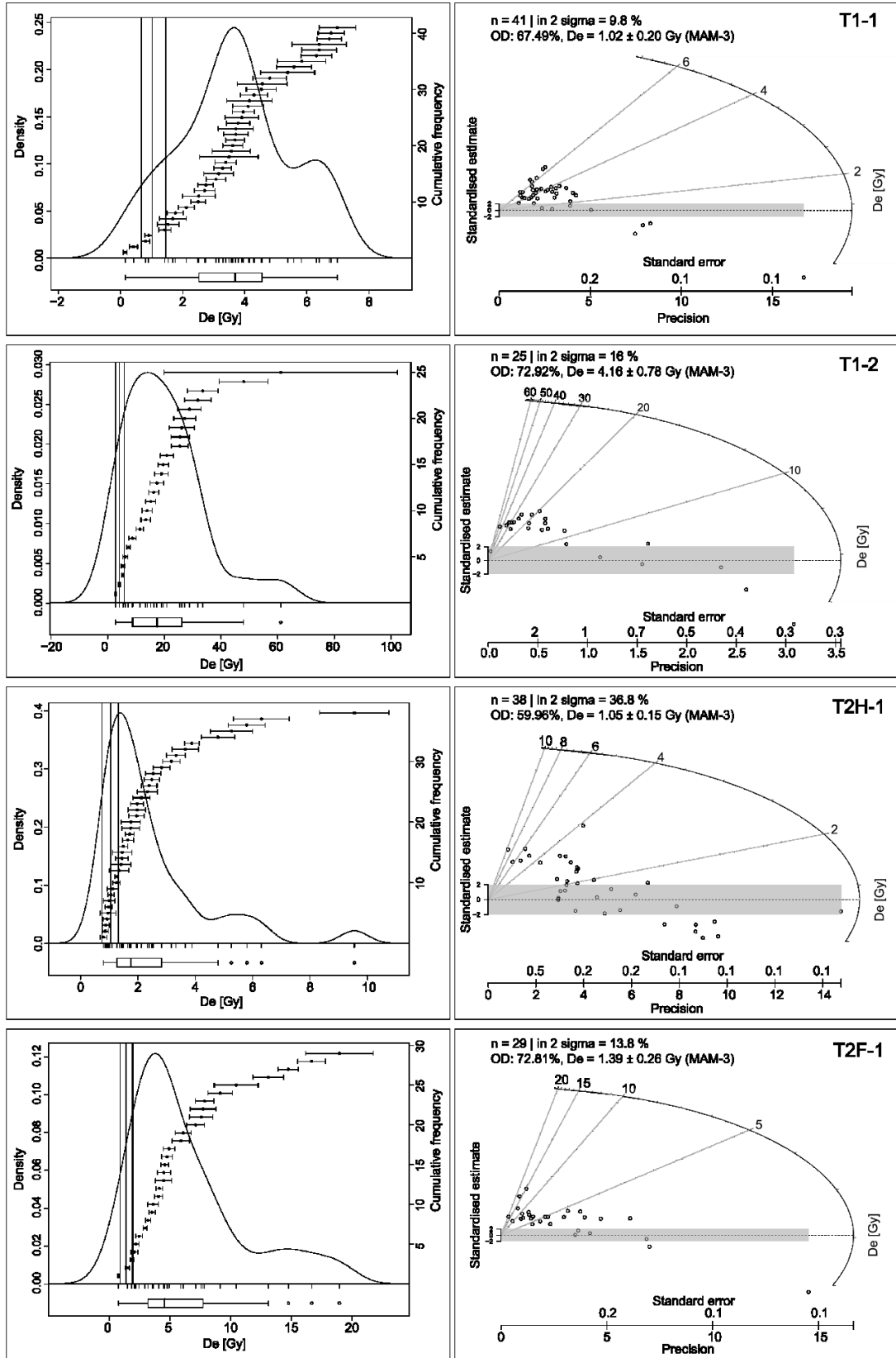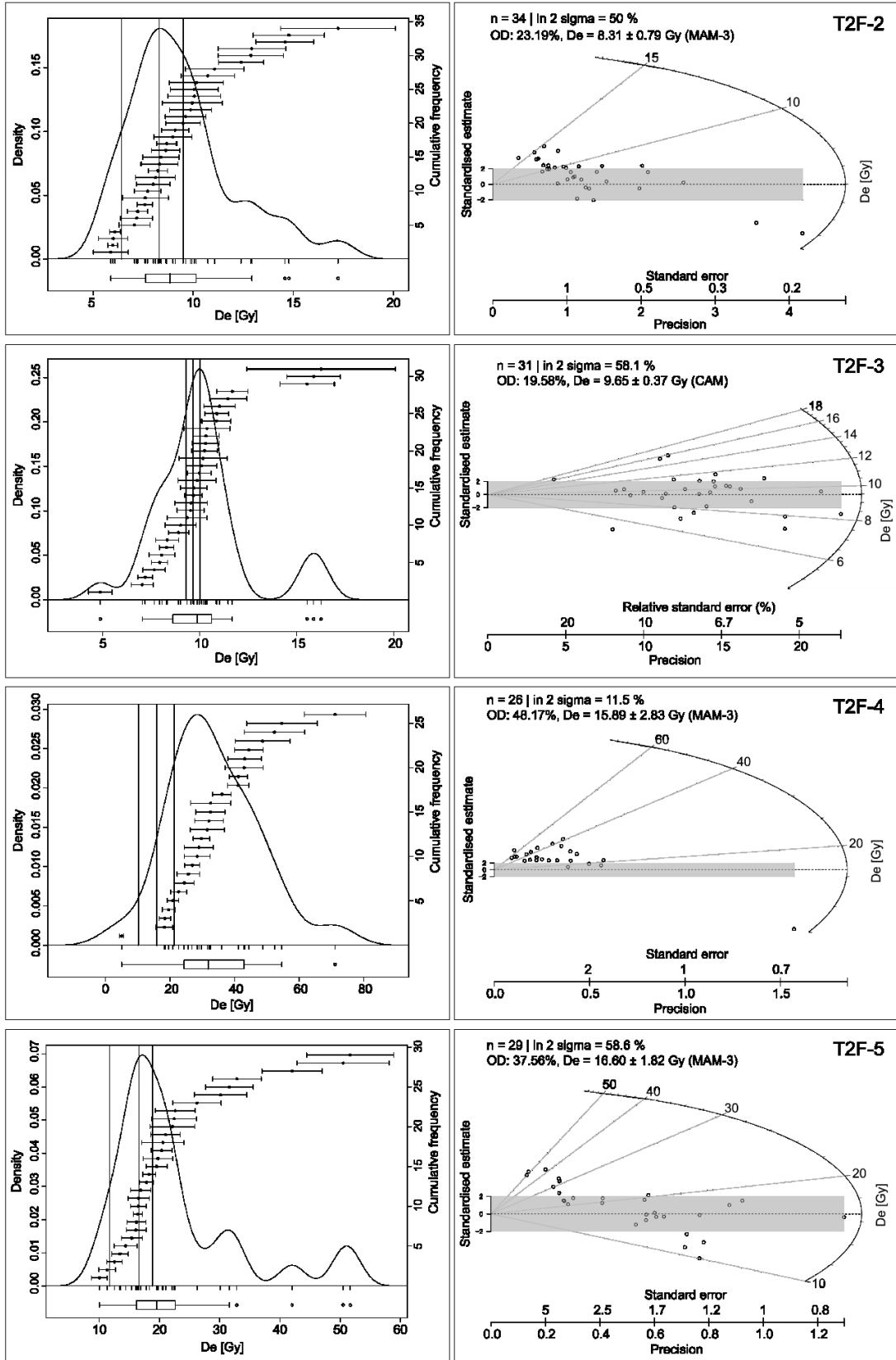
for the first core, the luminescence signal with depth for the second core was assessed to ensure if this cobble can be used for luminescence age determination. There was no big difference in the OSL_{125} L_x/T_x ratios observed between the topmost four slices of the first core and the first seven slices of the second core. Quartzite cobbles 14A, 14C, and 16A with two extracted cores were selected for further investigations as they were deemed completely bleached.
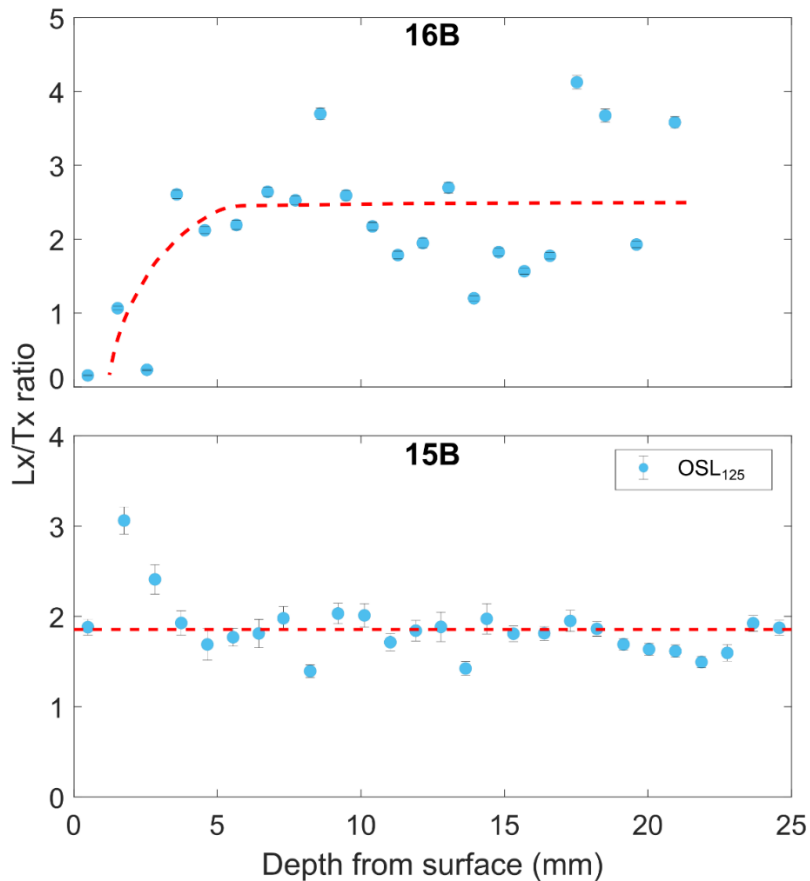
Figure 4.7 Examples of bleaching extent with depth into cobble indicated by reconstructing luminescence-depth profile (L_x/T_x ratio with depth for the OSL_{125} signal), labeled as the red dashed line, for each graywacke cobble after rapid assessment. For graywacke 16B, the obvious slope near the surface in the luminescence profile implies that partial bleaching occurred on the cobble surface. And, the flat profile shown for graywacke 15B illustrates unbleached cobble surface.
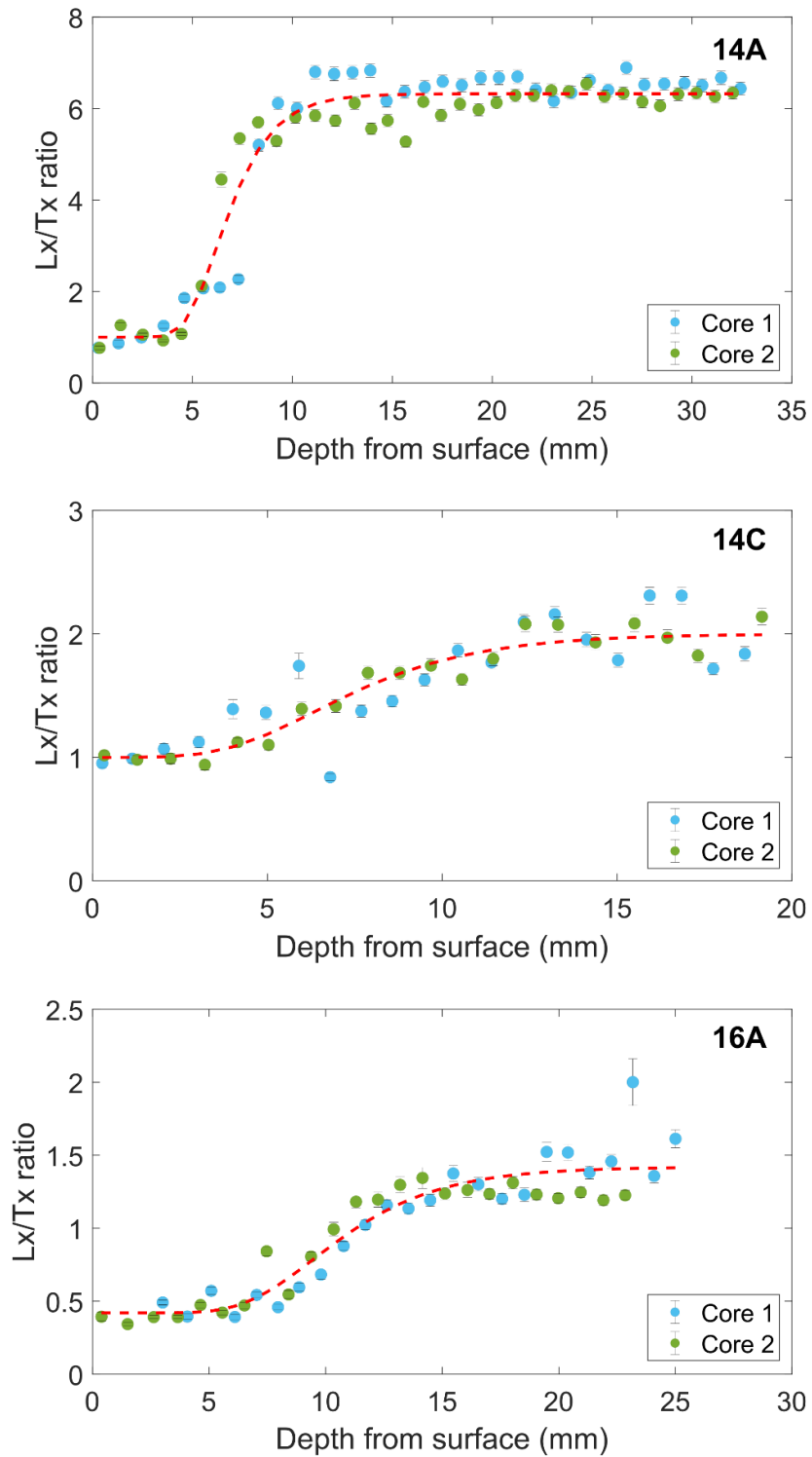
Figure 4.8 Luminescence-depth profiles generated for the OSL_{125} signal from each quartzite cobble (14A, 14C, and 16A). Each profile shown as the red dashed line is constructed using two separate cores and illustrates the fit to the model for multiple sequential exposure and burial events expressed by Freiesleben et al. (2015).
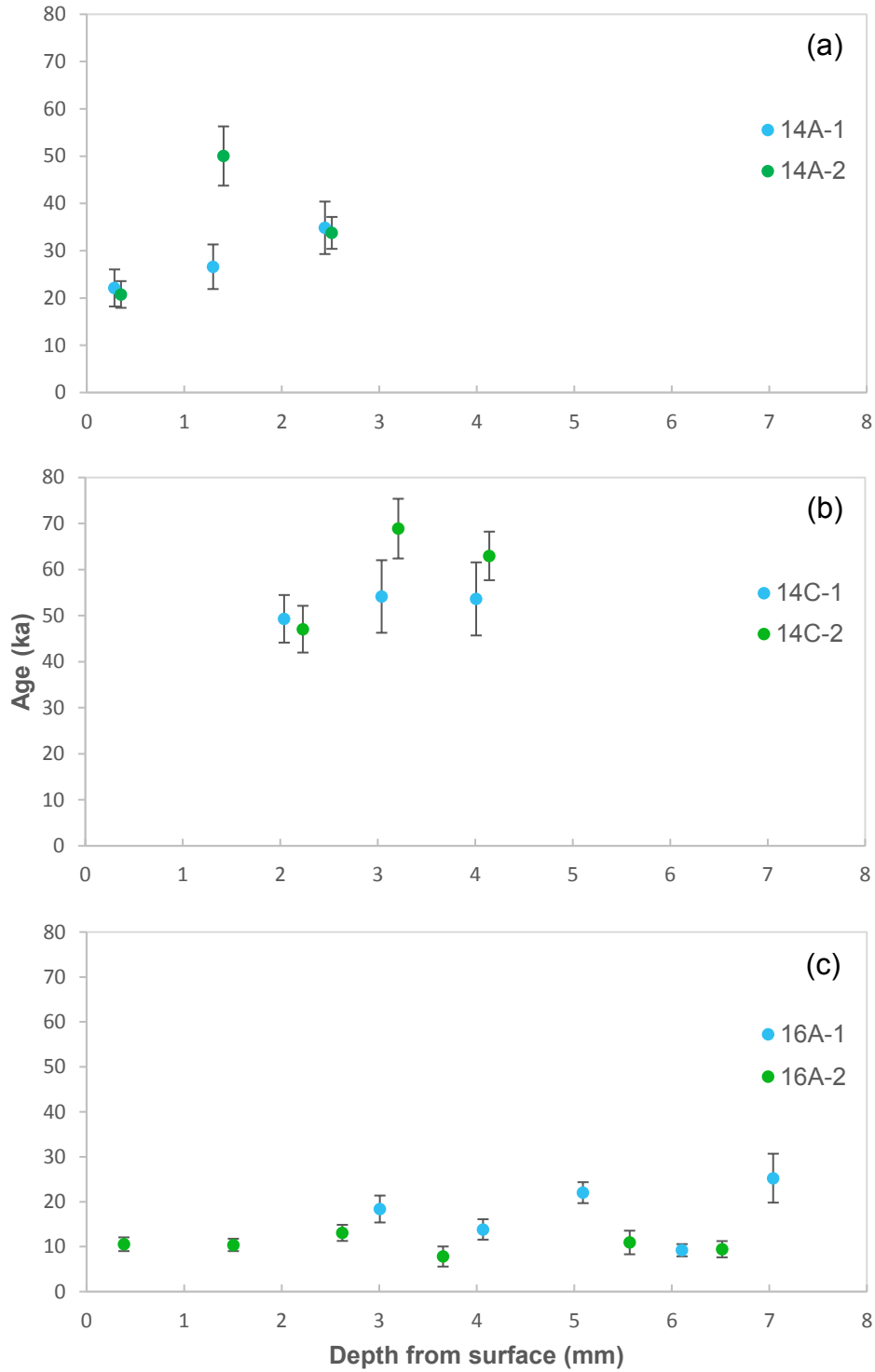
Figure 4.9 OSL$_{125}$ ages for the outermost at least three rock slices in each cobble core. (a) 14A, (b) 14C, and (c) 16A.
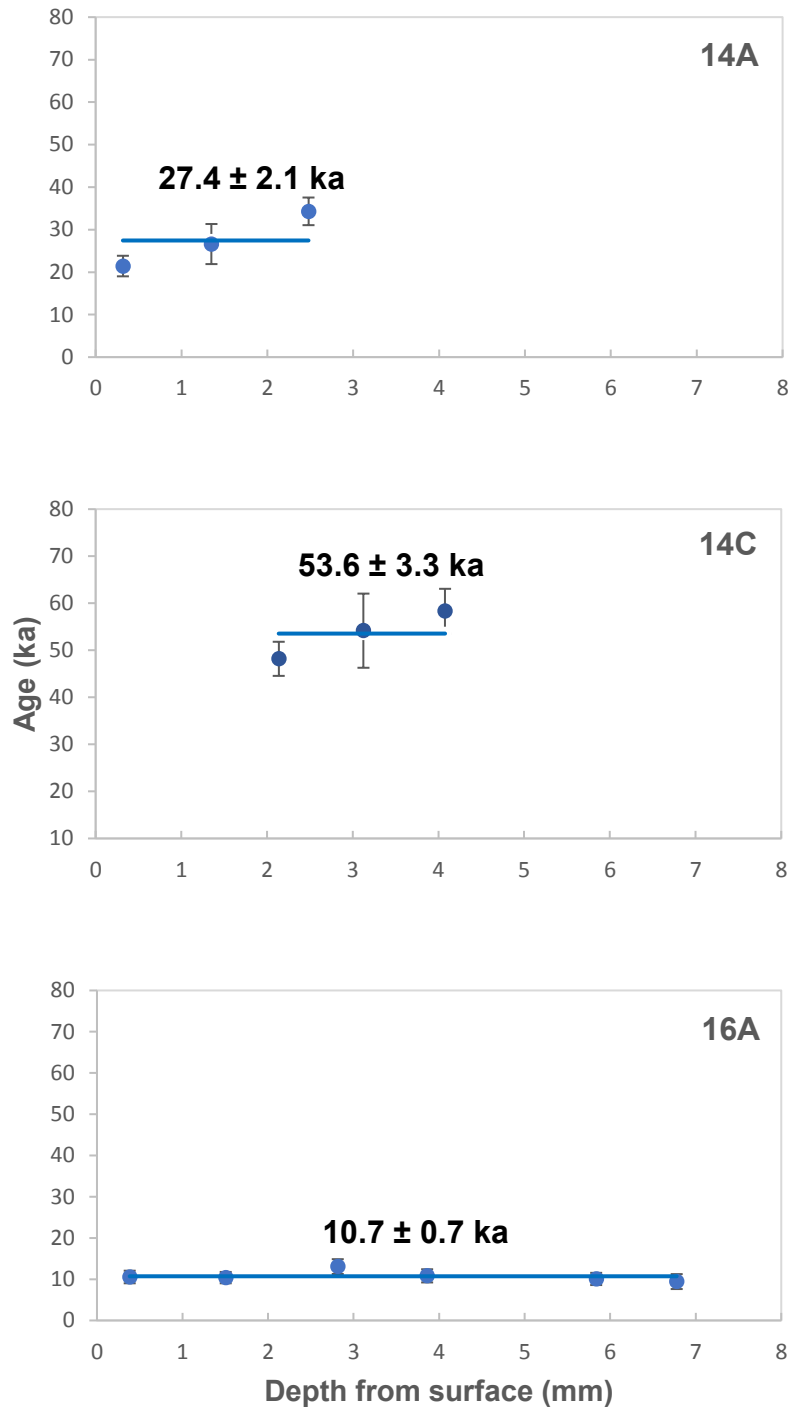
Figure 4.10 OSL$_{125}$ ages with depth into cobble. Each data point is the average age per slice from the same depth, based on reasonably calculated age data. Blue line shows the burial age for each cobble.

4.3.2.2 Dose Rate to the Cobble

The infinite matrix dose rates for the cobble and sediment calculated from radionuclide concentrations are summarized in Table 4.3. The dose rate to quartz grains in rock slices from every cobble core shows a maximum value at the surface of the cobble and decreases with depth into the cobble (Table D.1). The trend of the dose rate with depth is mainly due to the significant variation of the β dose rate from the matrix and the rock (Table 4.3). The γ dose varies little with depth and is the major contributor to the total dose rate together with the β dose. This reveals that over 92% of the total dose rate arises from the cobble itself. The rock α contribution was also included in the dose rates even though it is very small with less than 0.3% of the total dose rate. The contribution from cosmic radiation is ~3–7% of the total dose rate.

4.3.2.3 Cobble Burial Age Results

The OSL_{125} ages for at least the outermost three rock slices in each cobble core are shown in Figure 4.9, while the age calculation for each slice of each cobble core is shown in Table D.1. The uppermost 2.5 mm slices from the first core (14A-1) of cobble 14A produce consistent ages, but the ages derived from the same part of the second core (14A-2) show discrepancies. However, two pairs of the first and third slices in two cores of 14A give similar ages for each pair. For cobble 14C, the first five slices nearest the surface of each core were measured for D_e determination, but the slices from the uppermost 2 mm failed to yield D_e due to large errors caused by pieces being too small. The ages obtained from slices within the depth of 2.1–4.1 mm in the first core (14C-1) are consistent, and similar to 14A, the slices within the same range of depth in the second core (14C-2) are inconsistent. The difference to 14A is that similar ages from each pair slices at the same depth are shown in 14C. Likewise, ages for slices from the outermost portion of ~6.5 mm in the second core of 16A (16A-2) agree with one another, while in the first core (16A-1) do not. It should be mentioned that the uppermost segment of 2.6 mm of 16A-1 failed to be sliced and that for both two cores of 16A, one pair of slices at ~4.8 mm in depth failed for yield D_e estimate.

For all three cobbles, the OSL_{125} ages determined from surface slices of one core agree with one another, but the ages from the topmost slices of the other core are

inconsistent. This might mean that when one core reveals the cobble surface was well bleached before burial, the other core shows partial bleaching. The reason could be caused by different faces of the same cobble (Jenkins et al., 2018), i.e., the core near the well-bleached surface gives similar ages while the other close to the unbleached or partially-bleached surface does not. However, similar ages from at least two pairs of slices at the same depth are indicated for each cobble, therefore, to constrain cobble burial ages more accurately, mean burial ages were determined using all consistent pairs of surface slices instead of only from slices of one core. For cobble 14A, an average OSL_{125} age of 27.4 ± 2.1 ka was obtained from the uppermost three slices (n = 5 slices). The mean OSL_{125} ages for cobble 14C and 16A are 53.6 ± 3.3 ka (n = 5 slices) and 10.7 ± 0.7 ka (n = 8 slices) respectively. All the mean OSL_{125} burial ages of rock slices from three cobbles are shown in Figure 4.10.

The burial age of cobble 16A (10.7 ± 0.7 ka) taken at the bottom of unit U2 follows the increasing age trend with depth in T2. Combining this cobble burial age with the other two OSL burial ages (4.81 ± 0.87 ka and 8.53 ± 0.96 ka) in the same unit, I suggest that the deposition of U2 was between ~10.7 and ~4.81 ka. For cobbles 14A and 14C entrained along the fault surface from unit U4, inconsistent ages are shown. The reason is most likely that 14C originated from the deeper part in U4 than 14A, i.e., 14C had been buried longer than 14A before it was trailed along the fault surface.

CHAPTER 5: THE TIMING OF THE PALEO-EARTHQUAKES

5.1 Faulting Events and Associated Coseismic Displacements

To further identify and demonstrate faulting events along the MFT at the Dungsam Chu site, an attempt was made by retro-deforming all the deformed deposits to their undeformed position. Combining all field observations on the exposure, i.e., the stratigraphic contacts and disconformities between different litho units and the tips of the surface ruptures, I propose a schematic sequential retro-deformation in a total of four faulting stages along the MFT at the Dungsam Chu site (Figure 5.1).
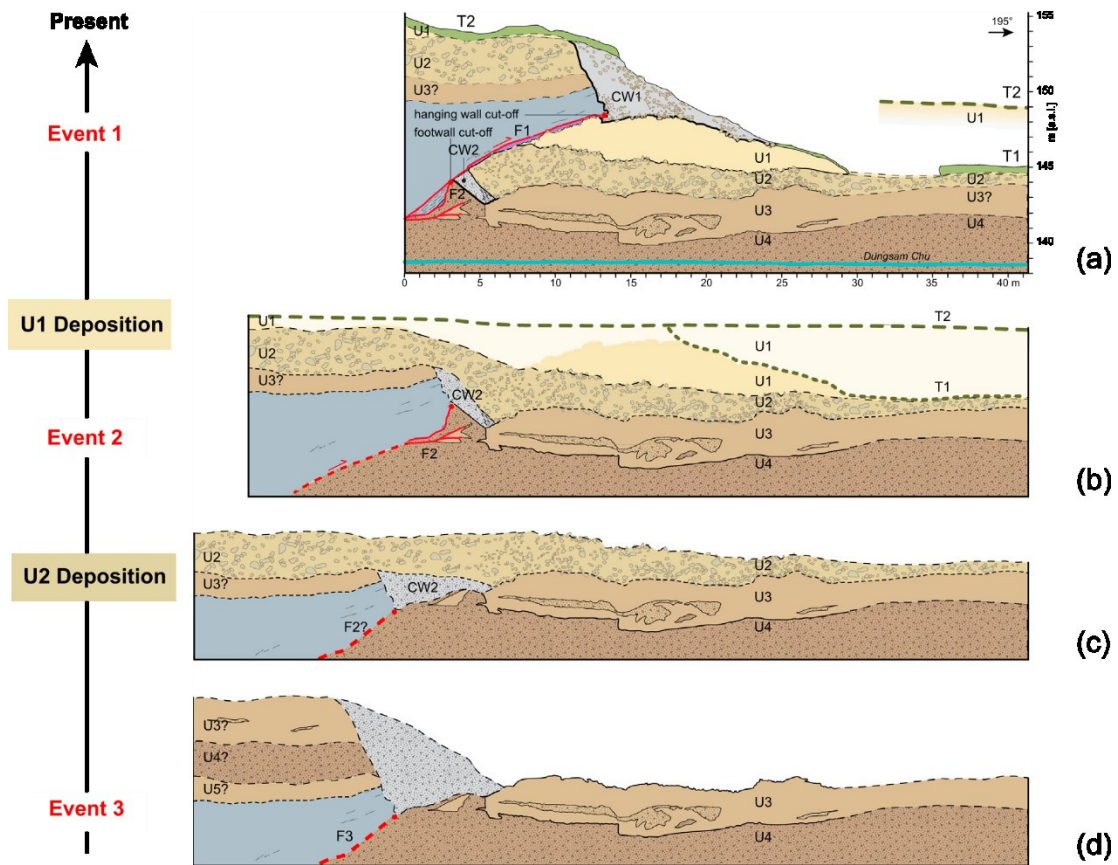
Figure 5.1 Sequentially retro-deformed cross-section along the MFT at the Dungsam Chu site, illustrating four faulting stages. (a) Current stage. (b) Pre-E1 stage. This is a conservative restoration in which the inferred cut-off lines were placed together. No other ajustments were made. (c) Pre-E2 stage. The position of unit U2 was restored to form a near-horizontal unit, i.e., before E2 occurred along the uppermost splay of blind thrust fault F2. (d) The formation of colluvial wedge CW2 during E3. Units U3 and older were displaced.

The most recent faulting event occurred along F1, dipping ~24° NNE and striking ESE (Figure 4.2). It displaced units U1 and U2, triggered the latest paleo-earthquake E1, and produced a surface rupture followed by the development of a ~5 m thick colluvial wedge CW1 (Figure 5.1a). Cataclasite was developed between F1 and the uppermost F2 splay during the event. Based on all the age constraints in T1, soil profile 1 might be also influenced by E1, while soil profile 3 may have formed pre-seismically. Thus, E1 occurred after the deposition of the youngest faulted unit U1 and before the deposit of modern soil covering the topmost of U1 in the hanging wall. The vertical offset along F1 of ~4.3 ± 0.2 m was estimated based on the two tips of the surface ruptures formed during the respective seismic events, i.e., 10.5 ± 0.5 m of coseismic slip was produced during E1.

Removing the undeformed modern soil, then retro-deforming along F1 from the tip of the latest surface rupture to the tip of the previous one, reveals that significant folding and faulting remain on units U2 and older (Figure 5.1b). Retrodeforming the E1 slip along the MFT places the terrace on the hanging wall of the MFT at the same level as the event horizon 1 and the top of terrace T2. Lateral variations of layer thicknesses are interpreted as a common feature of alluvial deposits, as well as the result of the incision of T1 into T2. Tapering of U1 deposits may be due to their overlapping with an older fill-cut terrace or a minor displacement of U2 by F2, the latter being more likely.

The penultimate paleo-earthquake E2 occurred along the uppermost splay of blind thrust fault F2 after the deposition of unit U2 and before the deposition of unit U1 (Figure 5.1b). Unit U2 was not cut by E2 but apparently folded by F2. The different height between the bottom boundaries of unit U2 in the hanging wall and in the footwall, therefore, yields the vertical offset of ~2.7 m along the uppermost F2 splay with an average dip of ~55° ± 2°. The coseismic slip for E2 along F2 can be estimated to 3.3 ± 0.2 m. The uppermost and middle F2 splays were terminated below the colluvial wedge CW2 formed during an earlier event (E3). Restoring the position of unit U2 to form a near-horizontal unit suggests that U2 was deposited against a pre-existing scarp formed in units U3 and U4 (Figure 5.1c).

The earlier paleo-earthquake E3 occurred along F3 after the deposition of unit U3 and before erosion, which was followed by the deposition of unit U2 (Figure 5.1d). The faulting event along F3 displaced units U3 and older and produced a surface rupture followed by the development of a ~7.6 m thick colluvial wedge CW2. Based on the restored cross-section, the difference in height between the top boundaries of unit U3 in the hanging wall and footwall produces a vertical offset of ~5.5 m along F3, dipping ~42° NNE. Thus, the coseismic slip for E3 along F3 might have been ~8.2 m.

5.2 Paleoseismic Event Chronology

We built an OxCal chronostratigraphic model with Bayesian analysis for surface-rupturing events (Figure 5.2) using all the samples from the deformed and undisturbed layers associated with such events. We evaluated several scenarios to constrain the latest event E1. The age of the uppermost section of U1 in the footwall given by the topmost OSL sample T2F-1 is consistent with the pair of radiocarbon and OSL dates in the hanging wall, confirming the identity of U1 from the footwall to the hanging wall and constrains E1 from rupturing the surface after A.D. 1690. In addition to the simple calibration, an OxCal model was used to calibrate all samples and constrain E1. If we do not consider the possibility that T1 might be influenced seismically, the latest event horizon can be constrained between the youngest faulted layer U1 and unbroken modern soil. While detrital charcoal samples 2H-1 and 2F-3 and OSL samples T2H-1, T2F-1, T2F-2, and T2F-3 are in unit U1, charcoal samples 1-1 and 1-2 are in top modern soil of T1 and used as the upper age limit of E1. The occurrence of E1 is therefore between A.D. 1586 and A.D. 1926 (Figure E.1). In the second scenario, considering the seismic impact on T1, the timing of the underlying layer of the injected sand (i.e., ^{14}C date of A.D. 1697–1911 produced by charcoal sample 1-3) would constrain the causative earthquake of the liquefaction feature to have occurred after A.D. 1697. In the third scenario, we included both deformed U1 and T1 to constrain the lower age limit of E1, thus charcoal sample 1-3 and OSL samples T1-1 and T1-2 within T1 were included in the model (Figures 5.2 and E.1). As a result, E1 occurred during the time between A.D. 1710 and A.D. 1945.
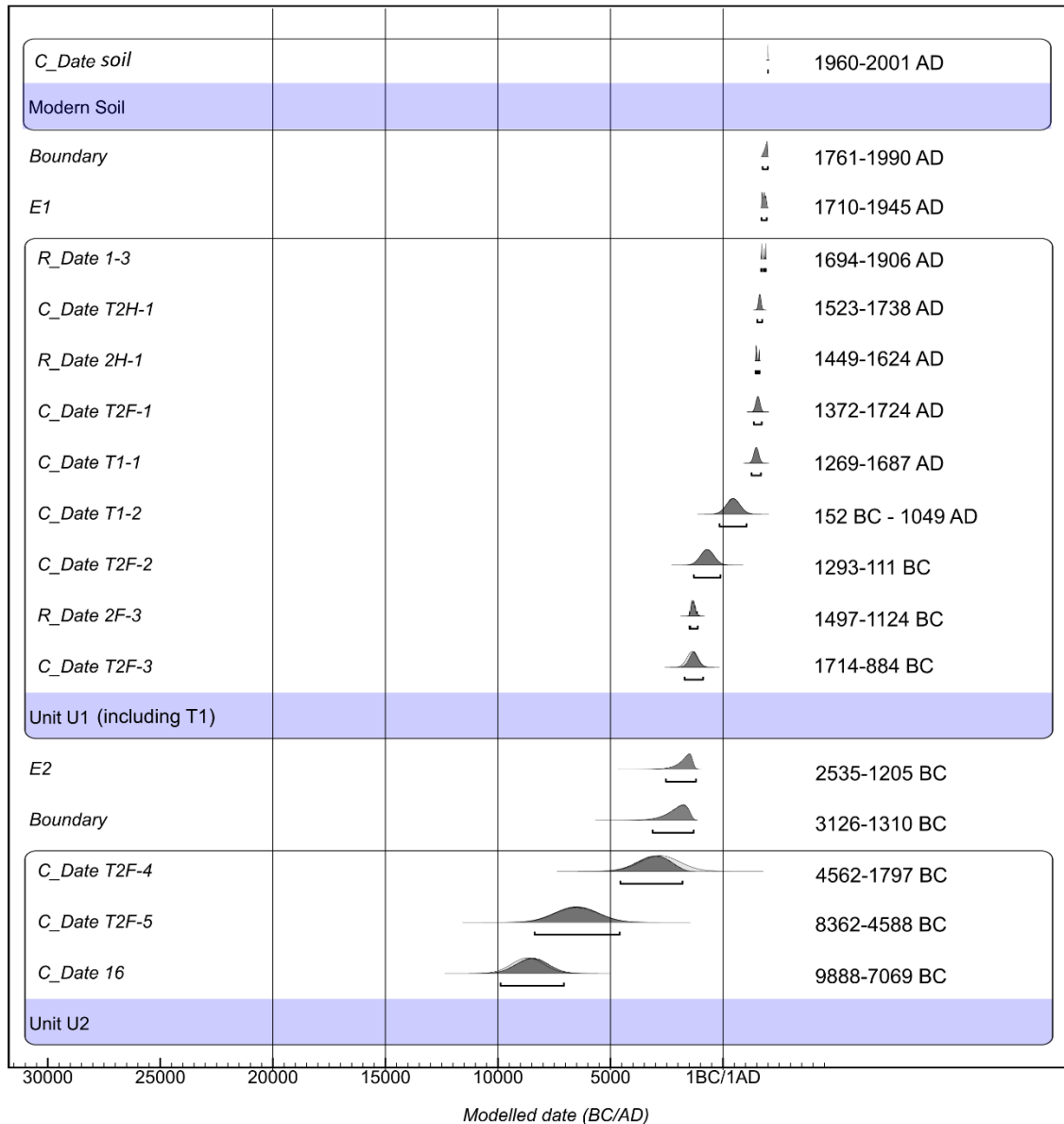
Figure 5.2 OxCal chronostratigraphic model for surface-rupturing events E1 and E2 at the Dungsam Chu exposure. The model is constrained by three detrital charcoal samples, eight OSL samples, one cobble sample, and one inferred age corresponding to the modern soil unit. The OSL and cobble data were input by converting the laboratory OSL ages with the laboratory uncertainties to calendar dates (Lienkaemper and Ramsey, 2009).

Similarly, to constrain E2, two OSL samples (T2F-4 and T2F-5) and cobble sample 16A from the deformed layer U2 were added to the OxCal model. E2 is constrained between the youngest faulted layer U2 and the oldest unfaulted layer U1, i.e., between 2535 B.C. and 1205 B.C. (Figure 5.2). However, for the earliest seismic event E3, unfortunately, we did not have any useful result from the faulted layer U3, so only

95

the upper age limit can be roughly constrained by the oldest undisturbed layer U2. E3 might have occurred before ~10.7 ka.

5.3 Discussion of the Paleo-earthquakes

Only three paleoseismic events have been identified at the Dungsam Chu site since all the faulting movements were exhibited along the same simple trace: from the latest to the earliest, E1 occurred between A.D. 1710–1945 with a coseismic slip of 10.5 ± 0.5 m, E2 between 2535 B.C. and 1205 B.C. (1870 ± 665 B.C.) with a slip of 3.3 ± 0.2 m, and E3 before ~10.7 ka with ~8.2 m slip. This result indicates that the three paleo-earthquakes at our study site occurred within the past over 10,000 years. The apparently large age span is most likely caused by the lack of preservation of surface rupture events due to climate and environmental reasons, i.e., a low deposition process resulting from a higher energy fluvial regime in the Dungsam Chu River, which has a shallow riverbed and experiences frequent flooding during monsoon season. Alternatively, the surface ruptures not discovered along the TFT (the northernmost branch of the MFT) might have occurred along branches of the MFT further in the foreland basin. Besides, the relatively large ranges of constraint ages of E2 and E3 are also due to insufficient data.

E3 would be the oldest paleoseismic event investigated in the Himalayan region, without related historical records or any paleoseismological reports. E2 only overlaps in time with two or three paleoseismic events identified at Sir-Bardibas in eastern Nepal by Bollinger et al. (2014) (Figure 5.3). These two paleoseismic events in this study are documented for the first time and constitute the oldest paleo-earthquakes characterized in the Himalayas (Figure 5.3), together with the four relatively earlier events in the study of Bollinger et al. (2014) and the three events observed at the Piping site in western Bhutan (i.e., E3–E5 that occurred at A.D. 300 ± 70, 100 ± 160 B.C., and 485 ± 125 B.C., respectively) (Le Roux-Mallouf et al., 2020).

5.3.1 Great Medieval Earthquakes
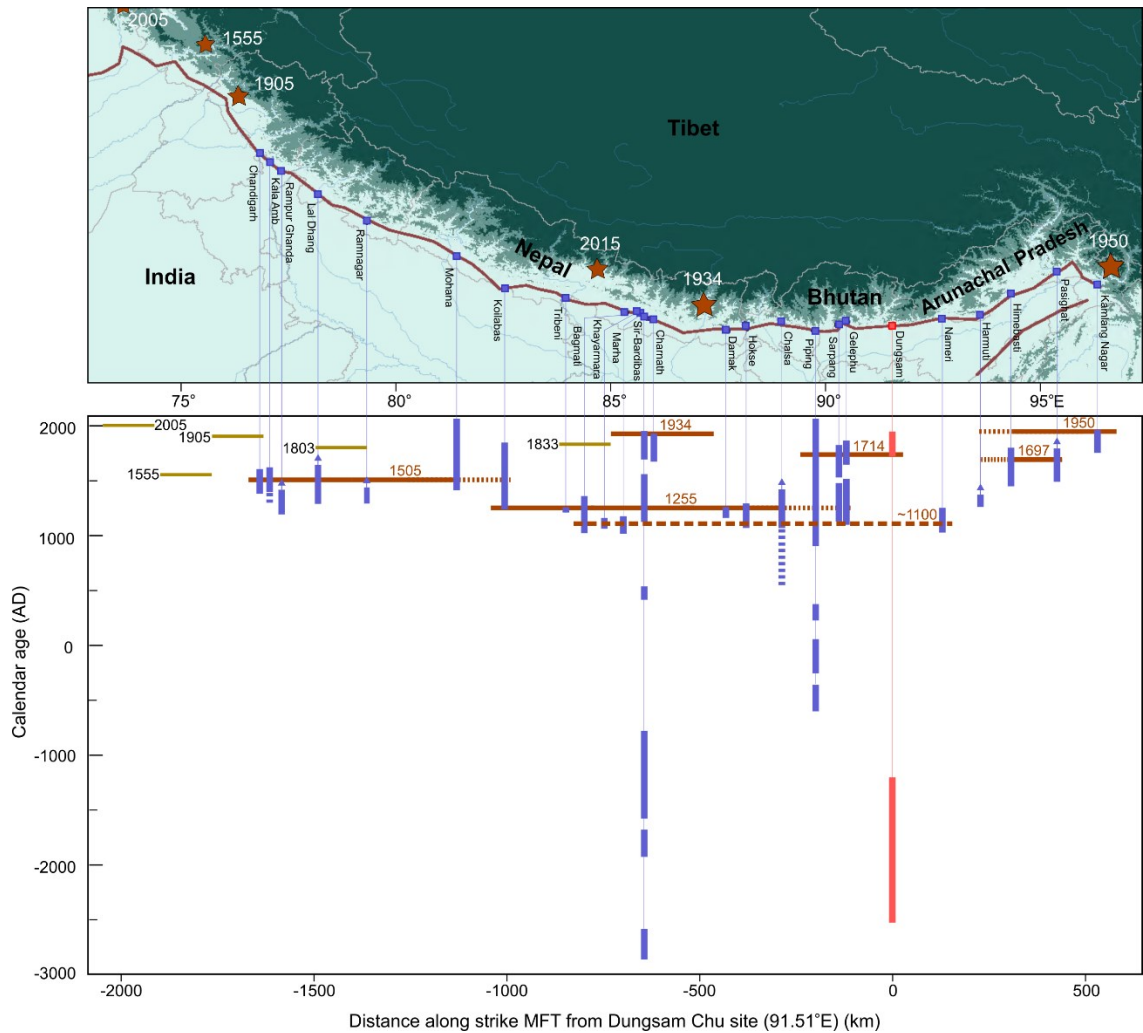
Figure 5.3 Synoptic calendar and positions of major/great (M_w > ~7.5) earthquake sources along the Himalayan Frontal Thrust (including both known instrumental/historical and inferred paleoseismic events). Squares indicate paleoseismological investigation sites from west to east: Chandigarh (1401– ~1600 AD) (Kumar et al., 2006; Kumar et al., 2010), Kala Amb (between 1294 and 1423–1622 AD) (Kumar et al., 2006; Kumar et al., 2010), Rampur Ghanda (1222– >1422 AD) (Kumar et al., 2006; Kumar et al., 2010), Lal Dhang (1282– >1632 AD) (Kumar et al., 2006; Kumar et al., 2010), Ramnagar (1278– >1433 AD) (Kumar et al., 2006; Kumar et al., 2010), Mohana (after 1410–1470 AD) (Yule et al., 2006), Koilabas (1241–1824 AD) (Mugnier et al., 2005; Mugnier et al., 2011), Tribeni (1221–1262 AD) (Wesnousky et al., 2017a), Bagmati (1031–1321) (Wesnousky et al., 2017a), Khayarmara (1059–1150 AD) (Wesnousky et al., 2019), Marha (1020–1160 AD) (Lavé et al., 2005), Sir Bardibas (1672–1942 AD, 1090–1554 AD, 411–543 AD, 787–1587 BC, 1923–1695 BC, and 2866–2578 BC) (Sapkota et al., 2013; Bollinger et al., 2014), Charnath (1645–1923 AD) (Rizza et al., 2019), Damak (1146–1256 AD) (Wesnousky et al., 2017b), Hokse (1050–1300 AD) (Nakata et al., 1998; Upreti et al., 2000), Chalsa (after 544– >648 AD and 1049– >1435 AD) (Kumar et al., 2010), Piping (>895 AD, 230–370 AD, 260 BC–60 AD, and 610–360 BC) (Le Roux-Mallouf et al., 2020), Sarpang (1167–1487 AD and 1524–1815 AD) (Le Roux-Mallouf et al., 2016), Gelephu (1140–1520 AD and 1642–1836 AD) (Le Roux-Mallouf et al., 2016), Dungsam (this study) (1710–1945 AD and 2535–1205 BC) (Zhao et al., 2021), Nameri (1025–1224 AD) (Kumar et al., 2010), Harmuti (1273– >1393 AD) (Kumar et al., 2010), Himebasti (1445–1795 AD) (Pandey et al., 2021), Pasighat (1492– >1798 AD) (Priyanka et al., 2017), and Kamlang Nagar (1761–1968 AD) (Singh et al. 2021). Lateral red bars show the possible surface rupture extents of investigated events. Dark yellow bars denote the events without observed surface rupture along the MFT (labeled as the dark red curve along the Himalayan arc). Red stars are known epicenters.

Two great medieval earthquakes of $M_w > 8$ have been recorded in historical documents or corroborated by paleo-seismologic studies: 1) a large historical rupture around A.D. 1100 reported in east-central Nepal (Lavé et al., 2005), West Bengal (Kumar et al., 2010), central Bhutan (Le Roux-Mallouf et al., 2016; Le Roux-Mallouf et al., 2020), and eastern Arunachal Pradesh (Kumar et al., 2010); 2) the A.D. 1255 earthquake historically recorded (Pant, 2002) and also reported in east-central Nepal (Mugnier et al., 2011; Sapkota et al., 2013; Bollinger et al., 2014; Wesnousky et al., 2017b), West Bengal (Upreti et al., 2000; Kumar et al., 2010), and central Bhutan (Le Roux-Mallouf et al., 2016; Le Roux-Mallouf et al., 2020). The nearest trenches to the Dungsam Chu site lie 124 km to the west (Le Roux-Mallouf et al., 2016) and 130 km to the east (Kumar et al., 2010), where the A.D. ~1100 great medieval event was recorded. Likewise, the A.D. 1255 earthquake probably occurred in western and central Bhutan, based on the studies of Le Roux-Mallouf et al. (2016, 2020). Therefore, evidence of at least one medieval earthquake would also be expected at our study site. However, according to our structural interpretation and dating, the penultimate paleoseismic event E2 (this study) is older than ~3.2 ka. If the great medieval events had affected this segment of the MHT, the evidence for surface rupture might have been overprinted by the event E1 or eroded by surface processes. Alternatively, the slip caused by medieval events may not have reached the surface or has propagated further south into the foreland basin. The lack of traces of medieval events reduces the likeliness of one mega-event rupturing the whole front, and the hypothesis that the lateral discontinuities of the MHT prevent lateral slip propagation puts more weight on the scenario of multiple events.

5.3.2 The 1714 Bhutan Earthquake

The most recent surface-rupturing event (E1) at our study site in eastern Bhutan was dated between A.D. 1710 and A.D. 1945, which most likely corresponds to the historical earthquake of 1714 (Ambraseys and Jackson, 2003; Hetényi et al., 2016b), which has been identified in paleoseismological trenches in western (Le Roux-Mallouf et al., 2020) and central Bhutan (Berthet et al., 2014; Le Roux-Mallouf et al., 2016) and calculated the magnitude of 7.5–8.5 by Hetényi et al. (2016b).

The 1714 event was not recognized at paleoseismological sites west and east of Bhutan (Kumar et al., 2010). All the paleoseismological investigations in Bhutan have been conducted along the northernmost branch of the MFT (i.e., the TFT). In contrast, the paleoseismic trenches in West Bengal and Arunachal Pradesh lie across the southernmost branch of the MFT, south of the topographic front, where Quaternary sediments are thrust over other Quaternary sediments. Neither the traces in the Bhutan Himalaya foreland nor surface ruptures along with the TFT in West Bengal and Arunachal Pradesh were dated.

The 1714 earthquake does not appear to have affected areas beyond Bhutan, only the Bhutan region. The reason might be that the lateral extent of surface rupture along the MHT would have been constrained by the two oblique strike-slip zones in the underthrusting basement. Based on the update above about the 1714 event, such as the extension of the surface rupture and the amount of slip, which has been newly identified in this study, the most likely magnitude of the event can be further precisely calculated utilizing the model of the 1714 earthquake (Hetényi et al., 2016b). The details about the magnitude calculation are described in Chapter 6.

CHAPTER 6: MAGNITUDE CALCULATION AND INTERPRETATION

6.1 Constraint on Magnitude for the 1714 Bhutan Earthquake

6.1.1 Methods

The most likely magnitude of the A.D. 1714 Bhutan earthquake is constrained using the historical data and methodology presented in Hetényi et al. (2016b) with the newly published paleoseismic evidence for the event in both western and eastern Bhutan. The data include (1) five historical damage reports indicating intensity estimates (Ambraseys and Jackson, 2003; Hetényi et al., 2016b), i.e., the intensity of VII–IX at Wangdue Phodrang and Gangteng and the intensity of IV–VI at Bahgara, Charaideo, and Tinkhang, (2) paleoseismological observations of four surface ruptures at Piping, Sarpang, Gelephu, and Dungsam (Berthet et al., 2014; Le Roux-Mallouf et al., 2016; Le Roux-Mallouf et al., 2020), and (3) four nearby paleoseismological sites where no surface rupture associated with the 1714 event was observed, i.e., Panijhora, Chalsa, Nameri, and Harmutty (Kumar et al., 2010; Mishra et al., 2016; Hetényi et al., 2016b).

The intensity prediction equations (IPE) we have tested are of Allen et al. (2012) defined for shallow active crustal earthquakes and of Szeliga et al. (2010) calibrated in the Himalayas. The IPEs we primarily used are a function of the distance along the fault plane to the hypocentre R_{hyp} and magnitude M. The IPE of Allen et al. (2012) is expressed as:

$$I(M, R_{hyp}) = c_0 + c_1 M + c_2 \ln \sqrt{R_{hyp}^2 + R_M^2} + S, for\ R \leq 50\ km, \text{ and} \qquad (6.1)$$

$$I(M, R_{hyp}) = c_0 + c_1 M + c_2 \ln \sqrt{R_{hyp}^2 + R_M^2} + c_4 \ln(R_{hyp}/50) + S, for\ R > 50\ km$$

where $R_M = m_1 + m_2 e^{(M-5)}$, coefficients $c_0 = 2.085$, $c_1 = 1.428$, $c_2 = -1.402$, $c_4 = 0.078$, $m_1 = -0.209$, and $m_2 = 2.042$, all of which are ascertained using regression on many earthquake intensity observations worldwide, and S is the site amplification factor assumed as 0 in this study. The other IPE is of Szeliga et al. (2010):

$$I(M, R_{hyp}) = a + bM + cR_{hyp} + d\log_{10} R_{hyp},\tag{6.2}$$

where $a = 6.05$, $b = 1.11$, $c = -0.0006$, and $d = -3.91$. The intensity calculations using either IPE should match intensity estimates recorded in the historical damage reports for each data point.

To best constrain the hypocenter location and the magnitude of the 1714 noninstrumental earthquake, we applied not only the conventional method based on the empirical scaling relationships between surface rupture length, width, and the moment magnitude established using global data of large earthquakes (Wells and Coppersmith, 1994) but also the self-consistent equations derived by Leonard (2010) that describe the same scaling and use parameters representative for the Himalaya. There are two points used to constrain the possible location of the hypocenter: (1) subsurface rupture length (RLD) is the upper limit of the distance between the earthquake and each surface rupture observed at four paleoseismological sites, and (2) downdip rupture width (RW) is also the upper limit of the distance between the earthquake and the surface trace of the MHT where the surface rupture was investigated. Two sets of equations relating *RLD* and *RW* to the magnitude *M* are used. The first set is of Wells and Coppersmith (1994):

$$\log_{10} RLD = a_1 + b_1 M \tag{6.3}$$

$$log_{10} RW = a_2 + b_2 M \tag{6.4}$$

where coefficients $a_1 = -2.42$, $b_1 = 0.58$, $a_2 = -1.61$, and $b_2 = 0.41$, all of which are ascertained based on earthquake data on reverse faults, and *RLD* and *RW* in km. The other set is of Leonard (2010):

$$M = 2/3 \log M_0 - 6.07 \tag{6.5}$$

$$M_0 = \mu C_1{}^{3/2} C_2 (RLD)^{5/2} \tag{6.6}$$

$$RW = C_1 (RLD)^{2/3} \tag{6.7}$$

where M_0 refers to scalar moment (N·m), shear modulus $\mu = 3.3 \times 10^{10}$ N·m^{-2}, parameters $C_1 = 17.5$ and $C_2 = 3.8 \times 10^{-5}$, all of which are determined based on the dip-slip interplate earthquake data, and *RLD* and *RW* in meters.
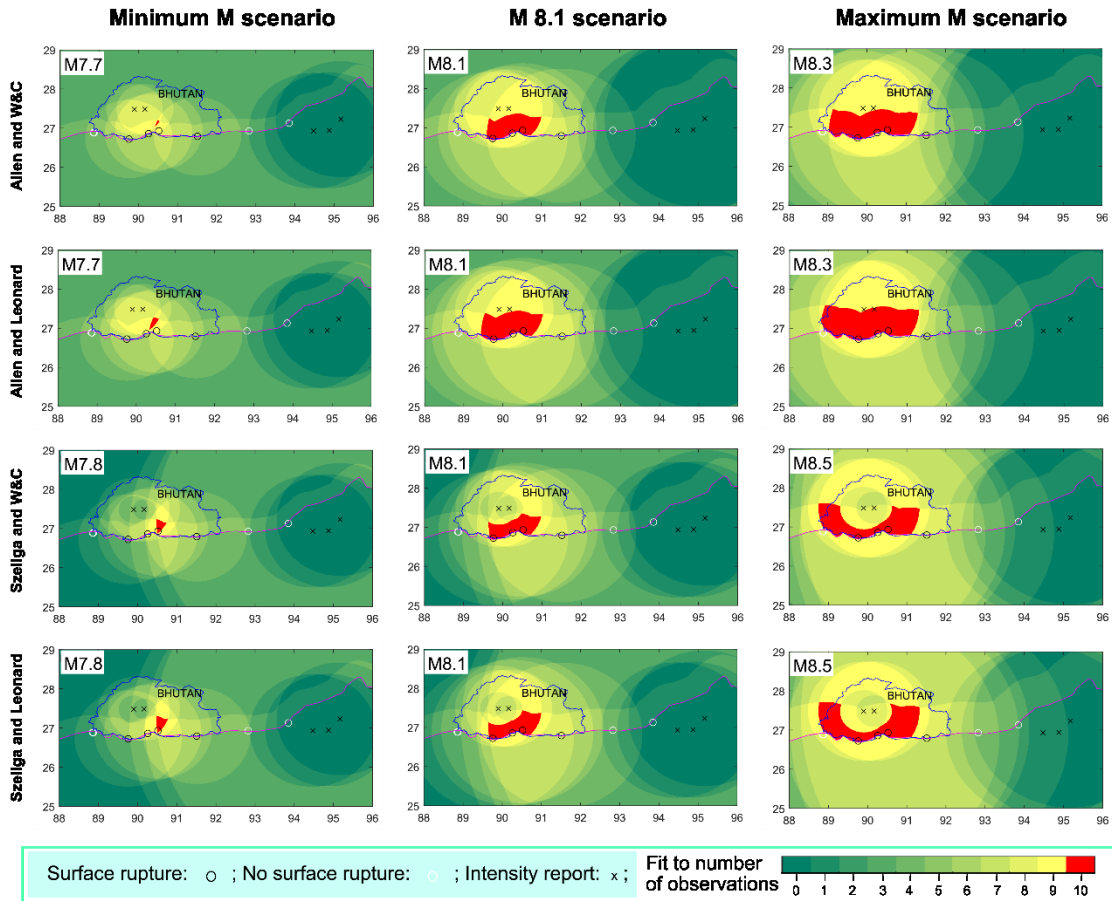
Figure 6.1 Various earthquake magnitude scenarios, fitting historical damage and paleoseismology observations. Each row shows each set of results using the combination of each intensity prediction equation (equations (6.1) or (6.2)) and each scaling equation (of Leonard or Wells and Coppersmith). Different columns list the minimum magnitude, M8.1, and the maximum magnitude scenarios. The red area exhibits the possible hypocenter locations fitting all the observed data points.

All the constraints on the earthquake intensity and the possible location of the hypocenter were implemented in MatLab based on the script by Hetényi et al. (2016b). Earthquake location and magnitude scenarios fitting all the above constraints were obtained by a map grid search. For each magnitude scenario, the possible hypocenter area fitting all the observations is shown in Figure 6.1. Tested scenarios and parameters used in the magnitude calculations are listed in Table 6.1.

6.1.2 Results and Interpretation

Four sets of results on the range of magnitudes of the 1714 earthquake were obtained under the condition of hypocentral area fitting all the observations: (i) using

Allen's IPE and Leonard's scaling relations, a possible range of magnitude is from 7.7 to 8.3; (ii) using Allen's IPE and scaling equations of Wells and Coppersmith, M_w 7.7–8.3; (iii) using Szeliga's IPE and Leonard's, M_w 7.8–8.5; (iv) using Szeliga's IPE and of Wells and Coppersmith, M_w 7.8–8.5 (Figures 6.1 and 6.2). Based on the observation of each set of results, the minimum magnitude solutions are less likely than larger magnitude solutions due to the too-small area of possible hypocenter locations. However, for the maximum magnitude solutions, the possible hypocenter area is very close to the Chalsa site in West Bengal, where no related surface rupture was observed. Combined with two scaling equations, respectively, Allen's IPE constrains the possible magnitude between 7.7 and 8.3. At a magnitude larger than 8.3, the results show the possible area of hypocenters much more towards the West and across the Chalsa site (West Bengal), which is less realistic (Figure F.1). Using Szeliga's IPE and two scaling equations, the magnitude range between 7.8 and 8.5 is obtained. At a magnitude beyond 8.5, the results produce the possible hypocenter area expanding east-west but also across the Chalsa site (West Bengal) (Figure F.1). Any result using Leonard's scaling relations produces a larger possible hypocentral area than the one using the scaling equations of Wells and Coppersmith. Combining all the results, the minimum magnitude of M_w 7.7 and the maximum magnitude of M_w 8.5 are obtained for the 1714 Bhutan earthquake.

The magnitude range of 7.7 to 8.5 is also compatible with the estimates produced by other scaling relations between surface rupture length (*SRL*) and magnitude (Wells and Coppersmith, 1994; Leonard, 2010). The distance between the trenches in which the 1714 event was observed (from Piping to Dungsam) was 175 km; the nearest trenches where no related surface rupture was observed (Kumar et al., 2010) were 96 and 130 km to the west and east, respectively. Therefore, the minimum length of the surface rupture was 175 km, and the maximum was ~400 km, which is likely unrealistic. For the SRL of 175–400 km, M_w 7.73–8.17 and M_w 8.03–8.57 are yielded based on Wells and Coppersmith (1994) and Leonard (2010), respectively. If we consider the possibility that the two oblique strike-slip zones in the underthrusting basement constrain the extent of surface rupture along the MHT (Figure 6.2), the maximum SRL could have been ~290 km. The ~290 km SRL corresponds to M_w 8 (Wells and Coppersmith, 1994) and M_w 8.37

(Leonard, 2010). The other estimate for the magnitude is based on the fault slip of ~11 m at the Dungsam Chu exposure produced by the 1714 earthquake. Using the empirical scaling between *SRL*, the average slip, and M_0 (Leonard, 2010; Wells and Coppersmith, 1994), the average slip of ~5.5 m constrains the magnitude of the 1714 event to M_w 8.35.

Table 6.1 Tested scenarios and parameters used in the magnitude calculations.

Tested scenarios	Allen and W&C: M_w 7.7–8.3	Szeliga and Leonard: M_w 7.8–8.5
Allen and Leonard: M_w 7.7–8.3	**IPE of Allen et al. (2012):** $I\ (M, R_{hyp})$, where $c_0 = 2.085$, $c_1 = 1.428$, $c_2 = -1.402$, $c_4 = 0.078$, $S = 0$, $m_1 = -0.209$, and $m_2 = 2.042$	**Scaling relations of Leonard (2010):** $RW \sim RLD$, $M_0 \sim RLD$, $M \sim M_0$, where $\mu = 3.3 \times 10^{10}$ Nm^{-2}, $C_1 = 17.5$ and $C_2 = 3.8 \times 10^{-5}$, and *RLD* and *RW* in meters.
Szeliga and W&C: M_w 7.8–8.5	**Scaling relations of Wells and Coppersmith (1994):** $M \sim RLD$, $M \sim RW$, where $a_1 = -2.42$, $b_1 = 0.58$, $a_2 = -1.61$, and $b_2 = 0.41$, and *RLD* and *RW* in km.	**IPE of Szeliga et al. (2010):** $I\ (M, R_{hyp})$, where $a = 6.05$, $b = 1.11$, $c = -0.0006$, and $d = -3.91$

Note: *I* – expected intensity, *M* – magnitude, R_{hyp} – hypocentral distance to the earthquake focus, *RW* – downdip rupture width, *RLD* – subsurface rupture length, and M_0 – scalar moment (N·m).

All the fits shown in the scenario maps indicate that the zone of possible hypocenter locations of the 1714 earthquake is constrained between about longitude 88.8°E and 91.3°E, that is ~250 km long (Figure 6.2). Such a zone is typical for a M_w 8.3 thrust earthquake based on Wells and Coppersmith (1994) and corresponds to M_w 8.2 according to Leonard (2010). It is also inferred that the possible focus was located on the fully locked zone of the MHT in western and central Bhutan. The $RLD \sim M$ and $RW \sim M$ relations provided by Leonard (2010) for thrust faults yield rupture length and width of ~118 and ~42 km for M_w 7.7 and of 358 and 88 km for M_w 8.5, which implies that only frontal third to half of the fully locked MHT (Li et al., 2020) would have slipped during the 1714 Bhutan earthquake. Based on the model of bimodal seismicity (Dal Zilio et al., 2019), the width parameter is poorly constrained to the earthquake so that the great seismic events ($M_w > 8.0$) transfer the deformation to the frontmost of the Sub-Himalayan range. Therefore, we can certainly conclude that based on observed surface rupture and slip at four paleoseismological sites, the 1714 M_w 7.7–8.5 Bhutan earthquake

ruptured the flat portion of the MHT and the frontal ramp between the two basement oblique strike-slip zones (Figure 6.2).
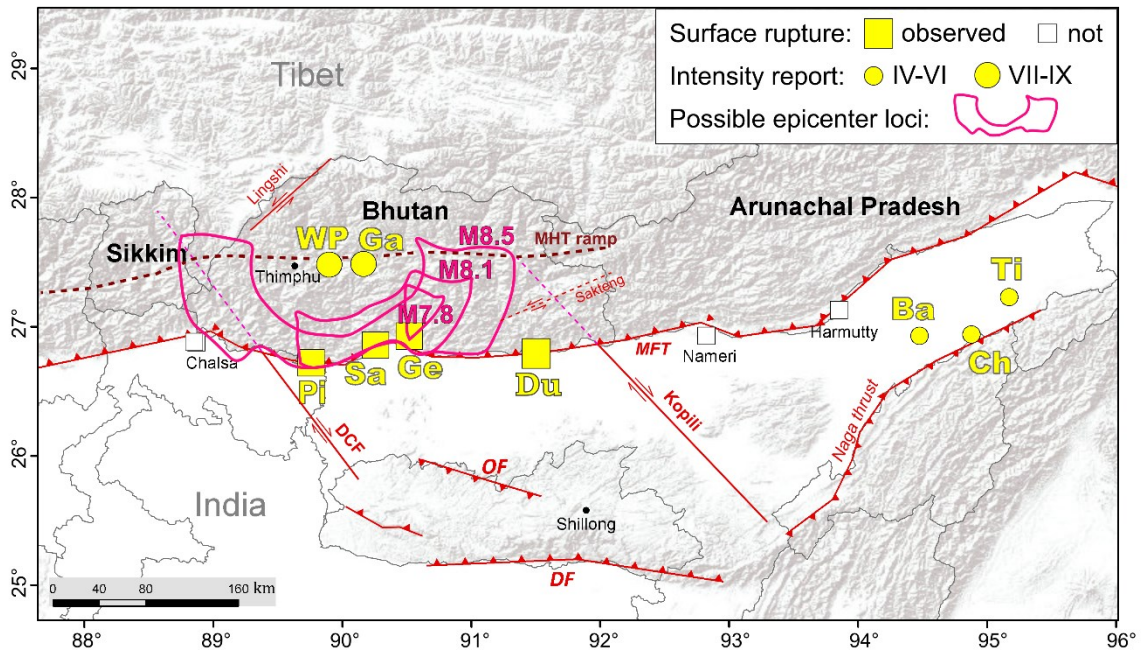
Figure 6.2 Model epicenter loci of the A.D. 1714 earthquake for three magnitude scenarios. The magenta contours outline the area of possible hypocenter locations, not that of the rupture extent. Four paleoseismological investigation sites of surface ruptures are at Piping (Pi), Sarpang (Sa), Gelephu (Ge), and Dungsam (Du). Five intensity report locations include Wangdue Phodrang (WP), Gangteng (Ga), Bahgara (Ba), Charaideo Hill (Ch), and Tinkhong (Ti). Fault traces are represented in red, and those shown as dashed lines demonstrate that there is no surface trace in the seismogenic fault. Dashed fault traces in light purple show that the fault is beneath the Himalayan orogenic wedge. MHT—Main Himalayan thrust, MFT—Main Frontal Thrust, DCF—Dhubri-Chungthang Fault, DF—Dauki Fault, and OF—Oldham Fault.

In summary, the combination of two scaling equations and two IPEs provides a robust estimate with uncertainties. They indicate a magnitude range of 7.7–8.5 for plausible solutions, i.e., the 1714 Bhutan earthquake most likely had a magnitude of M_w 8.1 ± 0.4. Adding the two locations of surface rupture observed at the Piping and Dungsam Chu sites to the 1714 earthquake model improved the constraint on the minimum magnitude of the earthquake (i.e., from M_w 7.5 to M_w 7.7) and its epicenter loci.

CHAPTER 7: RECURRENCE INTERVAL OF LARGE EARTHQUAKES IN THE EASTERN HIMALAYA

In our study, at least three paleoseismic events occurred at the Dungsam Chu site over 10,000 years , including inferred great medieval earthquakes missing evidence. The age constraints of the two older events (E2–E3) are inaccurate due to insufficient data. Therefore, estimating the return times of major earthquakes near our study site mainly depends on the latest paleo-earthquake E1, i.e., the 1714 M8.1 earthquake, the only one confidently determined.

Since the recurrence interval is the time required to accumulate the stress released during the investigated paleoseismic event, we can calculate it by dividing the stress by the stress accumulation rate. The stress released will be obtained by calculating the seismic moment (M_0) related to the subsurface rupture area and the amount of displacement. The rate of stress accumulation will be calculated based on the fault orientation, geodetic (GPS) strain rates (Marechal et al., 2016; Li et al., 2020), and crustal mechanical properties (Verdecchia and Carena, 2016). All calculations can be performed using the software Coulomb 3.4, assuming no significant Coulomb stress transfer (CST) from the neighboring faults (Lin and Stein, 2004). However, this method produces a large error due to the uncertainty in the rupture area of probably up to $\pm\ 2\times10^3$ km^2 caused by the empirical scaling relationships by Wells and Coppersmith (1994) implemented in the Coulomb 3.4.

CST causes a change of stress around the rupture fault, with some areas experiencing an increase in Coulomb stress while others experiencing a decrease (Lin and Stein, 2004). Stress changes due to one earthquake can influence not only the immediate vicinity of the rupture but also nearby faults, potentially triggering subsequent earthquakes. CST can be used to estimate the likelihood of future earthquakes in a region. Additionally, we use CST to try and determine the potential interaction and triggering between deep ramp earthquakes and the shallow ramp and flat portion of the MHT.

7.1 Recurrence Interval Estimation

According to Grujic et al. (2018), there is no significant stress transfer between the Bhutan Himalaya and the Shillong Plateau. The Coulomb stress change on a given fault is not influenced by regional stress but depends on the fault geometry, sense of slip, and friction coefficient (King et al., 1994). Therefore, we calculated Coulomb stress change only on the rupture fault identified at our study site without considering any CST from the neighboring faults.

Changes in stress along the strike are investigated for a planar fault with fault parameters of 290/24/90 of strike/dip/rake, a 14.5 km depth, a 10.5 m slip, and a magnitude of 8.1 over the subsurface rupture area of 230 km × 70 km (estimated by using the scaling relationships in Wells and Coppersmith (1994)). The CST calculation on the rupture fault were performed with the friction coefficient of 0.4 and a Young's modulus of 80 GPa (Grujic et al., 2018) (Figure G.1). The result indicates the Coulomb stress drop of ~17 bar due to the 1714 M8.1 Butan earthquake. Since the stress loading rate on the MHT in Bhutan is on the order of ~0.03 bar/a (Grujic et al., 2018), the return time of major earthquakes near the Dungsam Chu site might be ~570 years. The uncertainty produced by using the method is ~270 years. In the other approach, the recurrence interval of 620 ± 80 years is obtained based on a coseismic slip of 10.5 ± 0.5 m (this study) and an estimated convergence rate of 17 ± 2 mm/a in Bhutan (Marechal et al., 2016). It assumed a complete coupling between the surface rupture and the seismic event. The results (either 570 ± 270 years or 620 ± 80 years) are comparable to both the corresponding values obtained by Le Roux-Mallouf et al. (2020) (550 ± 211 years at Piping in western Bhutan) and by Bollinger et al. (2014) (between 750 ± 140 and 870 ± 350 years in eastern Nepal), both of whom used the average calculation of several events over the entire age span investigated at their field areas (illustration in Figure 5.3). All these together indicate the mean value of 672 ± 230 years as the recurrence interval of large earthquakes along the MHT in the eastern Himalayas.

7.2 Stress Transfer

We performed calculations of coseismic stress changes using a realistic ramp-flat geometry of the MHT, which is based on Coutand et al. (2014) and Singer et al. (2017),

and the strike-variable surface trace of the MFT. The method used to generate strike-variable fault planes from surface fault traces was developed by Mildon et al. (2016) and dip-variable fault planes in Hughes et al. (2020). The MHT was modeled as a series of 20-km rectangular elements comprising the non-planar fault surface (e.g. Hughes et al., 2020). All CST calculations were also performed in Coulomb 3.4 (Toda et al., 2005), with the coefficient of friction as 0.4 and a Young's modulus of 80 GPa (Grujic et al., 2018). An earthquake of magnitude 8.1 with a concentric slip distribution (ref. Mildon et al., 2016) over an area of 230×70 km^2 was generated. This is a simple assumption, but it is worth noting that the hypocenter does not need to be in the middle of the fault or where the shaking is strongest (e.g. Cattin et al., 2009). Besides, under the condition that the area of the fault slips stays the same, the regions of positive and negative stress remain approximately the same even though the distribution in this area varies, but the magnitudes undoubtedly vary (Mildon et al., 2017).

Two earthquake scenarios were modeled, one with the slip on the deep ramp and the other with the slip on the flat section. Although it has been documented that the MHT ramp has been creeping (Dal Zilio et al., 2021), we use this scenario to simulate earthquakes on the internal part of the MHT. The magnitude of Coulomb stress changes caused by coseismic slip on a fault also depends on the assumed elastic structure, which in this work is oversimplified as a homogeneous half-space. For, no viscoelastic behavior of the mantle is taken into account.

When a great earthquake slip is along the deep ramp on the MHT, considerable amounts (up to and over 10 bar) of positive Coulomb stress would be transferred onto the flat portion of the fault; however, much less (<2 bar) is transferred onto the frontal ramp (Figure 7.1A,B). In cross-section (Figure 7.2), we show the distribution of stress changes projected on subhorizontal planes and the optimally oriented thrust faults. Seismic slip along the ramp of the MHT would cause positive changes in the Coulomb stress along the shallow, flat segment of the MHT located in the end-fault lobe of the ramp (Figure 7.2A). However, clamping effects (i.e., compressive changes of normal stress) in the frontal part of the MHT (Figure 7.2B) are crucial for impeding propagation of the slip to the surface (i.e., MFT). For the optimally oriented thrust faults, a similar stress pattern is

observed; although the Coulomb stress change along the MHT is neutral, the unclamping effect (i.e., tensile changes of normal stress) is modest (Figures 7.2C,D). Consequently, deep slip on the MHT may increase elastic strain in upper crustal levels, including shallow MFT, which is then accommodated by slip on the shallow MFT.
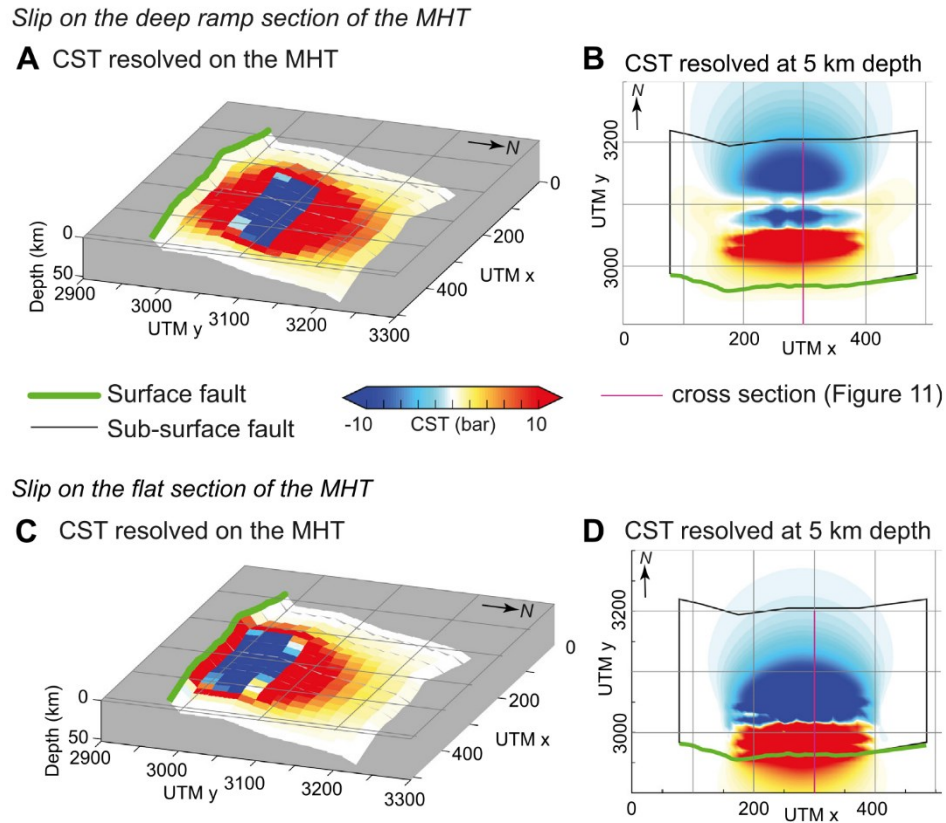
Figure 7.1 Models of Coulomb Stress Transfer (CST) for representative earthquakes. (A) Slip on the deep ramp section (>15 km in depth) of the MHT with stress resolved onto the rest of the MHT. (B) Slip on the deep ramp with stress resolved at 5 km depth onto receiver faults with the geometry 270/45/90 (strike/dip/rake). (C) Slip on the flat section of the MHT with stress resolved onto the rest of the MHT. (D) Slip on the flat section with stress resolved at 5 km depth onto receiver faults with the geometry 270/45/90.

The CST calculations indicate that a great earthquake slip on the flat portion of the MHT (between 14 and 15 km depth) would transfer more than 10 bar of high positive Coulomb stresses onto the frontal thrust (Figure 7.1C,D). This means that the earthquakes that predominantly slip on the flat section will promote rupture on the frontal thrust and are likely to generate surface ruptures. In this earthquake scenario, the cross-section shows that the down-dip end-fault stress lobes for horizontal and optimally oriented faults are positive (Figures 7.2A′–D′), which is not the same as the deep slip (Figures 7.2A–D).

It is important to note that the up-dip end-fault Coulomb stresses lobe is associated with a lobe of positive normal stress change (unclamping effect) (Figures 7.2A′,B′). Although the positive Coulomb stress change is larger for the thrust faults (cf. Figures 7.2A′,C′), there is a significant clamping effect (Figure 7.2D′), promoting MHT propagation into the foreland basin in the form of a blind basal décollement. Such a structure has been observed within or below the lower Siwalik Group in the subsurface of the foreland basin of the eastern Nepalese Himalaya (Duvall et al., 2020). Blind basal décollement may exist in the Bhutan Himalayan foreland basin as suggested by juvenile triangle zones in West Bengal and western Assam (Dasgupta et al., 2013; Chakrabarti Goswami et al., 2019). Therefore, paleoseismic studies around the surface trace of the MFT may overestimate the slip potential where unrecognized faults or distributed deformation provide additional sources of strain release. In the case of the blind basal décollement in the foreland basin, the region of pre-seismic strain accumulation is only 20–40 km wide, and the maximum slip that can be stored and released, no matter how long the interval since the previous earthquake, is only a couple of meters (Bilham, 2019).
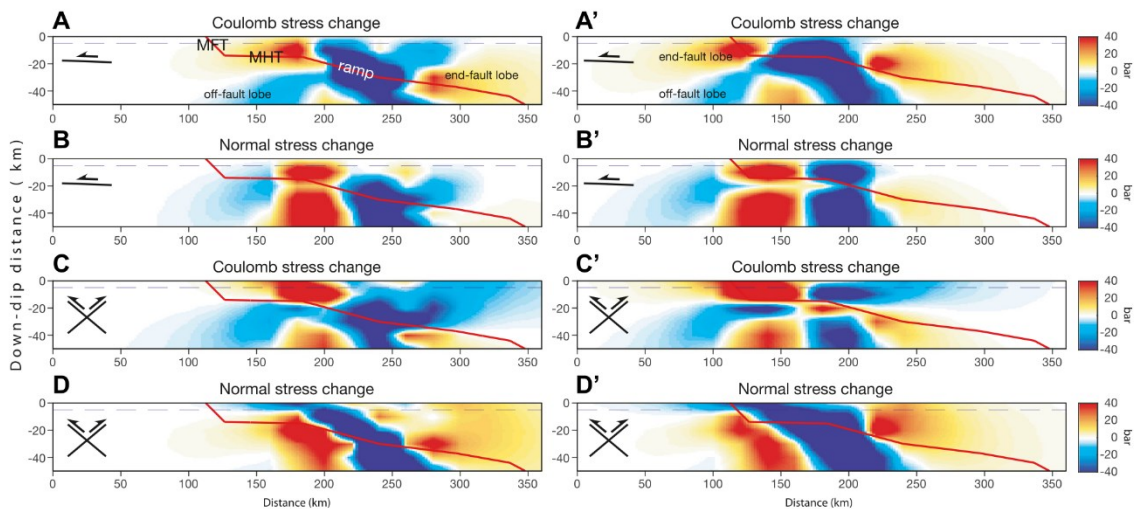
Figure 7.2 Cross-section view of the distribution of static stress changes caused by the 1714 Bhutan earthquake along a profile perpendicular to the strike of the MFT. Static stress changes are calculated for the subhorizontal planes with the geometry 270/02/90 (A, A′, B, B′) and optimally oriented thrust faults with the geometry 270/40/90 (C, C′, D, D′). The left-hand panels show the Coulomb stress (A, C) and normal stress (B, D) changes caused by a shock with hypocentre on the deep ramp of the MHT. The righthand panels show the Coulomb stress (A′, C′) and normal stress (B′, D′) changes caused by a shock with hypocentre on the flat segment of the MHT.

CHAPTER 8: Conclusion

8.1 Summary

In this study, a ~14 m high river-cut paleoseismic exposure striking 150°
identified at the Dungsam Chu site in eastern Bhutan reveals that the lower (younger)
terraces (T1 and T2) were deposited over the Siwalik Group and cut through by the MFT
of striking 290° and dipping 24°. To constrain the timing of paleoseismic events more
precisely, we used four dating methods on deformed fluvial terraces: radiocarbon dating,
conventional OSL dating, rock surface dating, and Multi-OSL dating. Regrettably, the
results were much less than expected. Twelve out of twenty-two organic samples were
selected for radiocarbon analysis, and only five charcoals were used for the
chronostratigraphic model for age constraints due to the low C content or unfittable
modern ages caused by in situ biological activity. Eight out of nine OSL samples
successfully yielded the burial ages and showed an age trend consistent with the
stratigraphic column. For thirteen cobbles of quartzite or graywacke, only three quartzite
samples were suitable for further investigations due to their complete bleaching level, and
they finally yielded the deposition ages of clast-supported fluvial deposits. However, the
attempt to obtain the direct age of the paleo-seismic event by dating the cobble dragged
along the thrust surface failed because the luminescence-depth profiles of these cobbles
exhibited that they were not or little affected by frictional heating produced during the
paleo-seismic event. Unfortunately, the other approach using Multi-OSL of feldspar to
attempt to directly date fault gouge produced during the paleoseismic movement also
failed due to age overestimations and over-corrections.

The detailed study of deformed sedimentary sequence dated from five
radiocarbon samples, eight OSL samples, and three cobble samples, a retro-deformation
analysis, magnitude calculation, and return time calculations (based on Coulomb stress
transfer) reveal the occurrence of at least three paleo-earthquakes along the MFT in
eastern Bhutan during the past over 10,000 years. The large age span covering these
paleoseismic events is most likely caused by the lack of preservation of surface rupture
events due to a low deposition process resulting from a higher energy fluvial regime in

the Dungsam Chu River, which frequently floods during monsoon season owing to a shallow riverbed.

The two earlier paleoseismic events (E2–E3) occurred before the medieval times and exhibit relatively large age ranges due to insufficient data. Event E3, estimated before ~10.7 ka with ~8.2 m slip, seems to be the oldest paleoseismic event recognized in the Himalayan region, without related historical records or any paleoseismological reports. E2 was yielded between 2535 B.C. and 1205 B.C. (1870 ± 665 B.C.) with a slip of 3.3 ± 0.2 m and only overlaps in time with two or three events identified at Sir-Bardibas in eastern Nepal by Bollinger et al. (2014). Together with those older events in the studies of Bollinger et al. (2014) and of Le Roux-Mallouf et al. (2020), E2 and E3 (this study) documented for the first time constitute the oldest paleo-earthquakes characterized in the Himalayas.

The most recent surface rupture along the MFT in eastern Bhutan was caused by the 1714 Bhutan earthquake based on the age dating of five radiocarbon samples and six OSL samples and supported by historical records. The surface rupture length was at least 175 km, likely up to ~290 km, considering that the two oblique strike-slip zones in the underthrusting basement might constrain the lateral extent of surface rupture along the MHT. The maximum observed coseismic surface displacement was ~10.5 m. The scaling relationship between the rupture length and magnitude (Wells and Coppersmith, 1994; Leonard, 2010) indicated a minimum magnitude of Mw of 7.7–8.0. Computations using empirical scaling relationships, historical intensity data, and paleoseismologically determined surface ruptures in the Bhutan Himalaya yielded plausible magnitudes of 7.7–8.5. The same calculations placed the epicenter of the 1714 Bhutan earthquake on the flat segment of the MHT.

Besides, the paleoseismological evidence recorded near our study site, at least one medieval great earthquake is inferred likely to have occurred in the Bhutan Himalayas: the A.D. ~1100 event of $M_w > {\sim}8.7$ or the A.D. 1255 earthquake of $M_w > 8$. However, evidence of a medieval earthquake was not discovered at our study site. The reason may be the coseismic faulting occurred along the same fault surface at our study site or

probably along the other splays of the MFT rather than the TFT. That means that the evidence for surface rupture might have been overprinted by the event E1 or eroded by surface processes and was not even discovered in the field if the great medieval events had affected the frontal segment of the MHT. Another possibility is that the slip caused by medieval events may not have reached the surface or has propagated further south into the foreland basin. The lack of evidence for medieval events reduces the likeliness of one mega-event rupturing the whole MFT front, i.e., the minimum 760 km rupture length corresponding to an M9 mega-earthquake (Leonard, 2010). This puts more weight on the scenario of multiple events with the hypothesis that the lateral discontinuities of the MHT prevent lateral slip propagation.

The recurrence interval of large earthquakes near the Dungsam Chu site was calculated according to the stress released during the 1714 M8.1 Bhutan earthquake, the only one safely determined in this study. The result of ~570 ± 270 years is comparable to the corresponding average calculations in previous works (between 750 ± 140 and 870 ± 350 years in eastern Nepal, Bollinger et al., 2014; 550 ± 211 years at Piping in western Bhutan, Le Roux-Mallouf et al., 2020), and all these together infer the mean value of 672 ± 230 years as the recurrence interval of large earthquakes along the MHT in the eastern Himalayas. Moreover, the result of return time in eastern Bhutan implies that the previous earthquake before 1714 was a medieval event between A.D. 894 and A.D. 1434 if we assume that the stress accumulated along the MHT had been released completely during the event. The lack of traces of medieval events at our study site may be because these great earthquakes would promote the propagation of the MHT into the foreland basin in the form of a blind thrust under the condition that they slip on the flat portion of the MHT, or in contrast, if the slip is along the deep ramp on the MHT, such distal earthquakes would not promote rupture on the frontal thrust, as CST calculations suggested.

The current state of Himalayan paleoseismological knowledge (Bilham, 2019) suggests that most great surface-rupturing earthquakes during the last millennium have been identified, even though the dating precision for some of them is low. However, great

earthquakes that did not lead to surface rupture caused stress transfer into the flat frontal portion, promoting subsequent surface-rupturing events along the MFT.

8.2 Thoughts for Future Work

This study has relatively successfully achieved the research objectives, even though during the study period, due to changes in regional policies and increased restrictions on visiting researchers at the research site, the field investigations and sample collections were conducted in 2018 and 2019, and even though during the COVID pandemic, it was forced to have numerous delays due to interrupted sample measurements and healthy issues. The seismic history in eastern Bhutan has been unraveled by investigating the MFT surface rupture at the Dungsam Chu paleoseismic exposure. This means one putative seismic gap has been removed from the Himalayan paleo-earthquake map. The research regarding Himalayan paleoseismology made further progress owing to the contributions from this study, but it still has a long way to go. There is still much paleoseismic evidence hidden and undiscovered in the Himalayas. Therefore, searching for new deformation features related to earthquakes, including surface faulting, sand injections in flood deposits, and perturbations in the growth of speleothems, is essential. For instance, the results in this study imply the possibility that the trace of medieval events undiscovered along the TFT might have occurred along branches of the MFT further in the foreland basin. Future research regarding the Himalayan foreland should consider and explore such information. Unfortunately, related fieldwork is hampered by the restrictive policies of local governments on international visiting researchers. All these logistic constraints delay the research progress in the Himalayas. Finally, I quote the words of an ancient Chinese wise man to encourage us (all the Himalayan researchers): The way ahead is long, and we shall search high and low.

REFERENCES

Ader, T., Avouac, J.P., Liu-Zeng, J., Lyon-Caen, H., Bollinger, L., Galetzka, J., Genrich, J., Thomas, M., Chanard, K., Sapkota, S.N. and Rajaure, S. 2012. Convergence rate across the Nepal Himalaya and interseismic coupling on the Main Himalayan Thrust: Implications for seismic hazard. Journal of Geophysical Research: Solid Earth, **117(B4)**.

Allen, T.I., Wald, D.J. and Worden, C.B. 2012. Intensity attenuation for active crustal regions. Journal of seismology, **16**: 409-433.

Ambraseys, N. and Bilham, R. 2000. A note on the Kangra M s= 7.8 earthquake of 4 April 1905. Current Science, **79(1)**: 45-50.

Ambraseys, N.N. and Douglas, J. 2004. Magnitude calibration of north Indian earthquakes. Geophysical Journal International, **159(1)**: 165-206.

Ambraseys, N. and Jackson, D. 2003. A note on early earthquakes in northern India and southern Tibet. Current Science, 570-582.

Avouac, J.P. 2015. Mountain building: from earthquakes to geologic deformation. Treatise Geophys, **6**: 381-432.

Avouac, J.P., Ayoub, F., Leprince, S., Konca, O. and Helmberger, D.V. 2006. The 2005, Mw 7.6 Kashmir earthquake: Sub-pixel correlation of ASTER images and seismic waveforms analysis. Earth and Planetary Science Letters, **249(3-4)**: 514-528.

Avouac, J.P., Meng, L., Wei, S., Wang, T. and Ampuero, J.P. 2015. Lower edge of locked Main Himalayan Thrust unzipped by the 2015 Gorkha earthquake. Nature Geoscience, **8(9)**: 708-711.

Balescu, S. and Lamothe, M. 1994. Comparison of TL and IRSL age estimates of feldspar coarse grains from waterlain sediments. Quaternary Science Reviews, **13(5-7)**: 437-444.

Becker, A., Ferry, M., Monecke, K., Schnellmann, M. and Giardini, D. 2005. Multiarchive paleoseismic record of late Pleistocene and Holocene strong earthquakes in Switzerland. Tectonophysics, **400(1-4)**: 153-177.

Bell, W.T. 1979. Attenuation factors for the absorbed radiation dose in quartz inclusions for thermoluminescence dating. Ancient TL, **8**: 12.

Bell, W.T. 1980. Alpha dose attenuation in quartz grains for thermoluminescence dating. Ancient Tl, **12(8)**: 4-8.

Ben-Menahem, A., Aboodi, E. and Schild, R. 1974. The source of the great Assam earthquake—an interplate wedge motion. Physics of the Earth and Planetary Interiors, **9**: 265-289.

Berthet, T., Ritz, J.F., Ferry, M., Pelgay, P., Cattin, R., Drukpa, D., Braucher, R. and Hetényi, G. 2014. Active tectonics of the eastern Himalaya: New constraints from the first tectonic geomorphology study in southern Bhutan. Geology, **42(5)**: 427-430.

Bilham, R. 1995. Location and magnitude of the 1833 Nepal earthquake and its relation to the rupture zones of contiguous great Himalayan earthquakes. Current Science, **69(2)**: 101-128.

Bilham, R. 2004. Earthquakes in India and the Himalaya: tectonics, geodesy and history. Annals of GEOPHYSICS.

Bilham, R. 2019. Himalayan earthquakes: a review of historical seismicity and early 21st century slip potential. Geological Society, London, Special Publications, **483(1)**: 423-482.

Bilham, R., Gaur, V.K. and Molnar, P. 2001. Himalayan seismic hazard. Science, **293**: 1442-1444.

Bilham, R. and Wallace, K. 2005. Future Mw> 8 earthquakes in the Himalaya: implications from the 26 Dec 2004 Mw= 9.0 earthquake on India's eastern plate margin. Geol. Surv. India Spec. Publ, **85**: 1-14.

Biswas, S., Coutand, I., Grujic, D., Hager, C., Stöckli, D. and Grasemann, B. 2007. Exhumation and uplift of the Shillong plateau and its influence on the eastern Himalayas: New constraints from apatite and zircon (U‑Th‑[Sm])/He and apatite fission track analyses. Tectonics, **26(6)**.

Bollinger, L., Sapkota, S.N., Tapponnier, P., Klinger, Y., Rizza, M., Van Der Woerd, J., Tiwari, D.R., Pandey, R., Bitri, A. and Bes de Berc, S. 2014. Estimating the return times of great Himalayan earthquakes in eastern Nepal: Evidence from the Patu and Bardibas strands of the Main Frontal Thrust. Journal of Geophysical Research: Solid Earth, **119(9)**: 7123-7163.

Brennan, B.J., Lyons, R.G. and Phillips, S.W. 1991. Attenuation of alpha particle track dose for spherical grains. International Journal of Radiation Applications and Instrumentation. Part D. Nuclear Tracks and Radiation Measurements, **18**: 249-253.

Brown, L.D., Zhao, W., Nelson, K.D., Hauck, M., Alsdorf, D., Ross, A., Cogan, M., Clark, M., Liu, X. and Che, J. 1996. Bright spots, structure, and magmatism in southern Tibet from INDEPTH seismic reflection profiling. Science, **274(5293)**: 1688-1690.

Burgess, W.P., Yin, A., Dubey, C.S., Shen, Z.K. and Kelty, T.K. 2012. Holocene shortening across the Main Frontal Thrust zone in the eastern Himalaya. Earth and Planetary Science Letters, **357**: 152-167.

Camelbeeck, T. and Meghraoui, M. 1998. Geological and geophysical evidence for large palaeo-earthquakes with surface faulting in the Roer Graben (northwest Europe). Geophysical Journal International, **132**: 347-362.

Cattin, R. and Avouac, J.P. 2000. Modeling mountain building and the seismic cycle in the Himalaya of Nepal. Journal of Geophysical Research: Solid Earth, **105(B6)**: 13389-13407.

Cattin, R., Chamot-Rooke, N., Pubellier, M., Rabaute, A., Delescluse, M., Vigny, C., Fleitout, L. and Dubernet, P. 2009. Stress change and effective friction coefficient along the Sumatra-Andaman-Sagaing fault system after the 26 December 2004 (Mw= 9.2) and the 28 March 2005 (Mw= 8.7) earthquakes. Geochemistry, Geophysics, Geosystems, **10(3)**.

Center for International Earth Science Information Network - CIESIN - Columbia University, 2020. Gridded Population of the World, Version 4 (GPWv4): Population Density. Palisades, NY: NASA Socioeconomic Data and Applications Center (SEDAC) [online]. Available from http://dx.doi.org/10.7927/H4NP22DQ. [cited 13 February 2022].

Chakrabarti Goswami, C., Jana, P. and Weber, J.C. 2019. Evolution of landscape in a piedmont section of Eastern Himalayan foothills along India-Bhutan border: A tectono-geomorphic perspective. Journal of Mountain Science, **16(12)**: 2828-2843.

Chambers, J., Parrish, R., Argles, T., Harris, N. and Horstwood, M. 2011. A short-duration pulse of ductile normal shear on the outer South Tibetan detachment in Bhutan: Alternating channel flow and critical taper mechanics of the eastern Himalaya. Tectonics, **30(2)**.

Chen, W.P. and Molnar, P. 1977. Seismic moments of major earthquakes and the average rate of slip in central Asia. Journal of Geophysical Research, **82(20)**: 2945-2969.

Chirouze, F., Huyghe, P., Van Der Beek, P., Chauvel, C., Chakraborty, T., Dupont-Nivet, G. and Bernet, M. 2013. Tectonics, exhumation, and drainage evolution of the eastern Himalaya since 13 Ma from detrital geochemistry and thermochronology, Kameng River Section, Arunachal Pradesh. Bulletin, **125**: 523-538.

Clark, M.K. and Bilham, R. 2008. Miocene rise of the Shillong Plateau and the beginning of the end for the Eastern Himalaya. Earth and Planetary Science Letters, **269(3-4)**: 337-351.

Coudurier-Curveur, A., Tapponnier, P., Okal, E., Van der Woerd, J., Kali, E., Choudhury, S., Baruah, S., Etchebes, M. and Karakaş, Ç. 2020. A composite rupture model for the great 1950 Assam earthquake across the cusp of the East Himalayan Syntaxis. Earth and Planetary Science Letters, **531**: 115928.

Coutand, I., Barrier, L., Govin, G., Grujic, D., Hoorn, C., Dupont-Nivet, G. and Najman, Y. 2016. Late Miocene-Pleistocene evolution of India-Eurasia convergence partitioning between the Bhutan Himalaya and the Shillong Plateau: New evidences from foreland basin deposits along the Dungsam Chu section, eastern Bhutan. Tectonics, **35(12)**: 2963-2994.

Coutand, I., Whipp, D.M., Grujic, D., Bernet, M., Fellin, M.G., Bookhagen, B., Landry, K.R., Ghalley, S.K. and Duncan, C. 2014. Geometry and kinematics of the Main Himalayan Thrust and Neogene crustal exhumation in the Bhutanese Himalaya derived from inversion of multithermochronologic data. Journal of Geophysical Research: Solid Earth, **119(2)**: 1446-1481.

Dal Zilio, L., Hetényi, G., Hubbard, J. and Bollinger, L. 2021. Building the Himalaya from tectonic to earthquake scales. Nature Reviews Earth & Environment, **2(4)**: 251-268.

Dal Zilio, L., Jolivet, R. and van Dinther, Y. 2020. Segmentation of the Main Himalayan Thrust illuminated by Bayesian inference of interseismic coupling. Geophysical Research Letters, **47(4)**.

Dal Zilio, L., van Dinther, Y., Gerya, T. and Avouac, J.P. 2019. Bimodal seismicity in the Himalaya controlled by fault friction and geometry. Nature communications, **10(1)**: 48.

Daniel, C.G., Hollister, L.S., Parrish, R.T. and Grujic, D. 2003. Exhumation of the Main Central Thrust from lower crustal depths, eastern Bhutan Himalaya. Journal of Metamorphic Geology, **21(4)**: 317-334.

Dasgupta, S., Mazumdar, K., Moirangcha, L.H., Gupta, T.D. and Mukhopadhyay, B. 2013. Seismic landscape from Sarpang re-entrant, Bhutan Himalaya foredeep, Assam, India: Constraints from geomorphology and geology. Tectonophysics, **592**: 130-140.

Diehl, T., Singer, J., Hetényi, G., Grujic, D., Clinton, J., Giardini, D., Kissling, E. and GANSSER Working Group, 2017. Seismotectonics of Bhutan: Evidence for segmentation of the Eastern Himalayas and link to foreland deformation. Earth and Planetary Science Letters, **471**: 54-64.

Drukpa, D., Velasco, A.A. and Doser, D.I. 2006. Seismicity in the Kingdom of Bhutan (1937–2003): Evidence for crustal transcurrent deformation. Journal of Geophysical Research: Solid Earth, **111(B6)**.

Duller, G. A. 2008. Luminescence Dating: guidelines on using luminescence dating in archaeology. English Heritage.

Durcan, J.A., King, G.E. and Duller, G.A. 2015. DRAC: Dose Rate and Age Calculator for trapped charge dating. Quaternary Geochronology, **28**: 54-61.

Duvall, M.J., Waldron, J.W., Godin, L. and Najman, Y. 2020. Active strike-slip faults and an outer frontal thrust in the Himalayan foreland basin. Proceedings of the National Academy of Sciences, **117(30)**: 17615-17621.

Elkadi, J., King, G.E., Lehmann, B. and Herman, F. 2021. Reducing variability in OSL rock surface dating profiles. Quaternary Geochronology, **64**: 101169.

Elliott, J.R., Jolivet, R., González, P.J., Avouac, J.P., Hollingsworth, J., Searle, M.P. and Stevens, V.L. 2016. Himalayan megathrust geometry and relation to topography revealed by the Gorkha earthquake. Nature Geoscience, **9(2)**: 174-180.

England, P. and Bilham, R. 2015. The Shillong Plateau and the great 1897 Assam earthquake. Tectonics, **34(9)**: 1792-1812.

Freiesleben, T., Sohbati, R., Murray, A., Jain, M., Al Khasawneh, S., Hvidt, S. and Jakobsen, B. 2015. Mathematical model quantifies multiple daylight exposure and burial events for rock surfaces using luminescence dating. Radiation Measurements, **81**: 16-22.

Gahalaut, V.K., Rajput, S. and Kundu, B. 2011. Low seismicity in the Bhutan Himalaya and the stress shadow of the 1897 Shillong Plateau earthquake. Physics of the Earth and Planetary Interiors, **186**: 97-102.

Galbraith, R.F., Roberts, R.G., Laslett, G.M., Yoshida, H. and Olley, J.M. 1999. Optical dating of single and multiple grains of quartz from Jinmium rock shelter, northern Australia: Part I, experimental design and statistical models. Archaeometry, **41(2)**: 339-364.

Galli, P., Galadini, F. and Pantosti, D. 2008. Twenty years of paleoseismology in Italy. Earth-Science Reviews, **88(1-2)**: 89-117.

Gansser, A. 1983. Geology of the Bhutan Himalaya. 181. Birkhäuser Verlag, Denkschriften der Schweizerischen Naturforschenden Geselschaft, Basel-Boston-Stuttgart, pp. 188.

Gee, E.R., 1934. The Dhubri earthquake of the 3rd July, 1930. Office of the Geological Survey, India **65**: 1-106.

Godin, L. and Harris, L.B. 2014. Tracking basement cross-strike discontinuities in the Indian crust beneath the Himalayan orogen using gravity data–relationship to upper crustal faults. Geophysical Journal International, **198(1)**: 198-215.

Goldfinger, C., Ikeda, Y., Yeats, R.S. and Ren, J. 2013. Superquakes and supercycles. Seismological Research Letters, **84(1)**: 24-32.

Grandin, R., Vallée, M., Satriano, C., Lacassin, R., Klinger, Y., Simoes, M. and Bollinger, L. 2015. Rupture process of the Mw= 7.9 2015 Gorkha earthquake (Nepal): insights into Himalayan megathrust segmentation. Geophysical Research Letters, **42(20)**: 8373-8382.

Grujic, D., Ashley, K.T., Coble, M.A., Coutand, I., Kellett, D.A., Larson, K.P., Whipp Jr, D.M., Gao, M. and Whynot, N. 2020. Deformational temperatures across the Lesser Himalayan Sequence in eastern Bhutan and their implications for the deformation history of the Main Central Thrust. Tectonics, **39(4)**.

Grujic, D. and Coutand, I. 2023. The Major Thrust Faults and Shear Zones. Himalaya, Dynamics of a Giant 1: Geodynamic Setting of the Himalayan Range, 57-100.

Grujic, D., Govin, G., Barrier, L., Bookhagen, B., Coutand, I., Cowan, B., Hren, M.T. and Najman, Y. 2018. Formation of a rain shadow: O and H stable isotope records in authigenic clays from the Siwalik Group in eastern Bhutan. Geochemistry, Geophysics, Geosystems, **19**: 3430-3447.

Grujic, D., Hetényi, G., Cattin, R., Baruah, S., Benoit, A., Drukpa, D. and Saric, A. 2018. Stress transfer and connectivity between the Bhutan Himalaya and the Shillong Plateau. Tectonophysics, **744**: 322-332.

Grujic, D., Hollister, L.S. and Parrish, R.R. 2002. Himalayan metamorphic sequence as an orogenic channel: insight from Bhutan. Earth and Planetary Science Letters, **198**: 177-191.

Guérin, G., Mercier, N. and Adamiec, G. 2011. Dose-rate conversion factors: update. Ancient TL, **29**: 5-8.

Guérin, G., Mercier, N., Nathan, R., Adamiec, G. and Lefrais, Y. 2012. On the use of the infinite matrix assumption and associated concepts: a critical review. Radiation Measurements, **47**: 778-785.

Guralnik, B., Ankjærgaard, C., Jain, M., Murray, A.S., Müller, A., Wälle, M., Lowick, S.E., Preusser, F., Rhodes, E.J., Wu, T.S. and Mathew, G. 2015a. OSL-thermochronometry using bedrock quartz: A note of caution. Quaternary Geochronology, **25**: 37-48.

Guralnik, B., Jain, M., Herman, F., Ankjærgaard, C., Murray, A.S., Valla, P.G., Preusser, F., King, G.E., Chen, R., Lowick, S.E. and Kook, M. 2015b. OSL-thermochronometry of feldspar from the KTB borehole, Germany. Earth and Planetary Science Letters, **423**: 232-243.

Hajdas, I. 2008. Radiocarbon dating and its applications in Quaternary studies. Quaternary Science Journal (Eiszeitalter and Gegenwart), **57**: 2-24.

Hammer, P., Berthet, T., Hetényi, G., Cattin, R., Drukpa, D., Chophel, J., Lechmann, S., Moigne, N.L., Champollion, C. and Doerflinger, E. 2013. Flexure of the India plate underneath the Bhutan Himalaya. Geophysical Research Letters, **40(16)**: 4225-4230.

Hauck, M.L., Nelson, K.D., Brown, L.D., Zhao, W. and Ross, A.R. 1998. Crustal structure of the Himalayan orogen at~ 90 east longitude from Project INDEPTH deep reflection profiles. Tectonics, **17(4)**: 481-500.

Herman, F., Rhodes, E.J., Braun, J. and Heiniger, L. 2010. Uniform erosion rates and relief amplitude during glacial cycles in the Southern Alps of New Zealand, as revealed from OSL-thermochronology. Earth and Planetary Science Letters, **297(1-2)**: 183-189.

Hetényi, G., Cattin, R., Berthet, T., Le Moigne, N., Chophel, J., Lechmann, S., Hammer, P., Drukpa, D., Sapkota, S.N., Gautier, S. and Thinley, K. 2016a. Segmentation of the Himalayas as revealed by arc-parallel gravity anomalies. Scientific reports, **6(1)**: 1-10.

Hetényi, G., Le Roux-Mallouf, R., Berthet, T., Cattin, R., Cauzzi, C., Phuntsho, K. and Grolimund, R. 2016b. Joint approach combining damage and paleoseismology observations constrains the 1714 AD Bhutan earthquake at magnitude 8±0.5. Geophysical Research Letters, **43(20)**: 10,695-10,702.

Hirschmiller, J., Grujic, D., Bookhagen, B., Coutand, I., Huyghe, P., Mugnier, J.L. and Ojha, T. 2014. What controls the growth of the Himalayan foreland fold-and-thrust belt?. Geology, **42(3)**: 247-250.

Hodges, K.V. 2000. Tectonics of the Himalaya and southern Tibet from two perspectives. Geological Society of America Bulletin, **112(3)**: 324-350.

Hughes, A., Bell, R.E., Mildon, Z.K., Rood, D.H., Whittaker, A.C., Rockwell, T.K., Levy, Y., DeVecchio, D.E., Marshall, S.T. and Nicholson, C. 2020. Three-dimensional structure, ground rupture hazards, and static stress models for complex nonplanar thrust faults in the Ventura basin, southern California. Journal of Geophysical Research: Solid Earth, **125(7)**: e2020JB019539.

Huntley, D.J. 2006. An explanation of the power-law decay of luminescence. Journal of Physics: Condensed Matter, **18(4)**: 1359.

Iyengar, R.N., Sharma, D. and Siddiqui, J.M. 1999. Earthquake history of India in medieval times. Indian Journal of history of science, **34**: 181-238.

Jenkins, G.T.H., Duller, G.A.T., Roberts, H.M., Chiverrell, R.C. and Glasser, N.F. 2018. A new approach for luminescence dating glaciofluvial deposits-High precision optical dating of cobbles. Quaternary Science Reviews, **192**: 263-273.

Kaneda, H., Nakata, T., Tsutsumi, H., Kondo, H., Sugito, N., Awata, Y., Akhtar, S.S., Majid, A., Khattak, W., Awan, A.A. and Yeats, R.S. 2008. Surface rupture of the 2005 Kashmir, Pakistan, earthquake and its active tectonic implications. Bulletin of the Seismological Society of America, **98**: 521-557.

Kars, R.H., Wallinga, J. and Cohen, K.M. 2008. A new approach towards anomalous fading correction for feldspar IRSL dating—tests on samples in field saturation. Radiation Measurements, **43(2-6)**: 786-790.

Kellett, D.A. and Grujic, D. 2012. New insight into the South Tibetan detachment system: Not a single progressive deformation. Tectonics, **31(2)**.

Khattri, K.N. 1987. Great earthquakes, seismicity gaps and potential for earthquake disaster along the Himalaya plate boundary. Tectonophysics, **138(1)**: 79-92.

King, G.E., Herman, F. and Guralnik, B. 2016b. Northward migration of the eastern Himalayan syntaxis revealed by OSL thermochronometry. Science, **353(6301)**: 800-804.

King, G.E., Herman, F., Lambert, R., Valla, P.G. and Guralnik, B. 2016a. Multi-OSL-thermochronometry of feldspar. Quaternary Geochronology, **33**: 76-87.

King, G.C., Stein, R.S. and Lin, J. 1994. Static stress changes and the triggering of earthquakes. Bulletin of the Seismological Society of America, **84(3)**: 935-953.

Kondo, H., Nakata, T., Akhtar, S.S., Wesnousky, S.G., Sugito, N., Kaneda, H., Tsutsumi, H., Khan, A.M., Khattak, W. and Kausar, A.B. 2008. Long recurrence interval of faulting beyond the 2005 Kashmir earthquake around the northwestern margin of the Indo-Asian collision zone. Geology, **36(9)**: 731-734.

Kumar, S., Wesnousky, S.G., Jayangondaperumal, R., Nakata, T., Kumahara, Y. and Singh, V. 2010. Paleoseismological evidence of surface faulting along the northeastern Himalayan front, India: Timing, size, and spatial extent of great earthquakes. Journal of Geophysical Research: Solid Earth, **115(B12)**: 1-20.

Kumar, S., Wesnousky, S.G., Rockwell, T.K., Briggs, R.W., Thakur, V.C. and Jayangondaperumal, R. 2006. Paleoseismic evidence of great surface rupture earthquakes along the Indian Himalaya. Journal of Geophysical Research: Solid Earth, **111(B3)**: 1-19.

Kumar, S., Wesnousky, S.G., Rockwell, T.K., Ragona, D., Thakur, V.C. and Seitz, G.G. 2001. Earthquake recurrence and rupture dynamics of Himalayan Frontal Thrust, India. Science, **294**: 2328-2331.

Lavé, J. and Avouac, J.P. 2000. Active folding of fluvial terraces across the Siwaliks Hills, Himalayas of central Nepal. Journal of Geophysical Research: Solid Earth, **105(B3)**: 5735-5770.

Lavé, J. and Avouac, J.P. 2001. Fluvial incision and tectonic uplift across the Himalayas of central Nepal. Journal of Geophysical Research: Solid Earth, **106(B11)**: 26561-26591.

Lavé, J., Yule, D., Sapkota, S., Basant, K., Madden, C., Attal, M. and Pandey, R. 2005. Evidence for a great Medieval earthquake (~ 1100 AD) in the central Himalayas, Nepal. Science, **307**: 1302-1305.

Le Roux-Mallouf, R., Ferry, M., Cattin, R., Ritz, J.F., Drukpa, D. and Pelgay, P. 2020. A 2600-year-long paleoseismic record for the Himalayan Main Frontal Thrust (western Bhutan). Solid Earth, **11(6)**: 2359-2375.

Le Roux-Mallouf, R., Ferry, M., Ritz, J.F., Berthet, T., Cattin, R. and Drukpa, D. 2016. First paleoseismic evidence for great surface-rupturing earthquakes in the Bhutan Himalayas. Journal of Geophysical Research: Solid Earth, **121(10)**:7271-7283.

Le Roux-Mallouf, R., Godard, V., Cattin, R., Ferry, M., Gyeltshen, J., Ritz, J.F., Drupka, D., Guillou, V., Arnold, M., Aumaître, G. and Bourlès, D.L. 2015. Evidence for a wide and gently dipping Main Himalayan Thrust in western Bhutan. Geophysical Research Letters, **42(9)**: 3257-3265.

Lemonnier, C., Marquis, G., Perrier, F., Avouac, J.P., Chitrakar, G., Kafle, B., Sapkota, S., Gautam, U., Tiwari, D. and Bano, M. 1999. Electrical structure of the Himalaya of central Nepal: High conductivity around the mid-crustal ramp along the MHT. Geophysical Research Letters, **26(21)**: 3261-3264.

Leonard, M. 2010. Earthquake fault scaling: Self-consistent relating of rupture length, width, average displacement, and moment release. Bulletin of the Seismological Society of America, **100(5A)**: 1971-1988.

Li, B. and Li, S.H. 2008. Investigations of the dose-dependent anomalous fading rate of feldspar from sediments. Journal of Physics D: Applied Physics, **41(22)**: 225502.

Li, B. and Li, S.H. 2011a. Luminescence dating of K-feldspar from sediments: a protocol without anomalous fading correction. Quaternary Geochronology, **6(5)**: 468-479.

Li, B. and Li, S.H. 2011b. Thermal stability of infrared stimulated luminescence of sedimentary K-feldspar. Radiation Measurements, **46(1)**: 29-36.

Li, B. and Li, S.H., 2013. The effect of band-tail states on the thermal stability of the infrared stimulated luminescence from K-feldspar. Journal of Luminescence, **136**: 5-10.

Li, S., Tao, T., Gao, F., Qu, X., Zhu, Y., Huang, J. and Wang, Q. 2020. Interseismic coupling beneath the Sikkim–Bhutan Himalaya constrained by GPS measurements and its implication for strain segmentation and seismic Activity. Remote Sensing, **12(14)**: 2202.

Libby, W.F. 1961. Radiocarbon Dating. American Association for the Advancement of Science, **133**: 621-629.

Lin, J., Stein, R.S., 2004. Stress triggering in thrust and subduction earthquakes and stress interaction between the southern San Andreas and nearby thrust and strike-slip faults. Journal of Geophysical Research: Solid Earth, **109**: 1-19.

Liu, F. and Yang, S. 2015. The effect of the Wenchuan earthquake on the fluvial morphology in the Longmen Shan, eastern Tibetan Plateau: Discussion and speculation. Quaternary International, **371**: 280-289.

Long, S. and McQuarrie, N. 2010. Placing limits on channel flow: Insights from the Bhutan Himalaya. Earth and Planetary Science Letters, **290**: 375-390.

Long, S., McQuarrie, N., Tobgay, T. and Grujic, D. 2011a. Geometry and crustal shortening of the Himalayan fold-thrust belt, eastern and central Bhutan. Bulletin, **123(7-8)**: 1427-1447.

Long, S., McQuarrie, N., Tobgay, T., Grujic, D. and Hollister, L. 2011b. Geologic map of Bhutan. Journal of Maps, **7(1)**: 184-192.

Long, S., McQuarrie, N., Tobgay, T., Rose, C., Gehrels, G. and Grujic, D. 2011c. Tectonostratigraphy of the Lesser Himalaya of Bhutan: Implications for the along-strike stratigraphic continuity of the northern Indian margin. Bulletin, **123(7-8)**: 1406-1426.

Mahesh, P., Rai, S.S., Sivaram, K., Paul, A., Gupta, S., Sarma, R. and Gaur, V.K. 2013. One-dimensional reference velocity model and precise locations of earthquake hypocenters in the Kumaon–Garhwal himalaya. Bulletin of the Seismological Society of America, **103(1)**: 328-339.

Malik, J.N., Naik, S.P., Sahoo, S., Okumura, K. and Mohanty, A. 2017. Paleoseismic evidence of the CE 1505 (?) and CE 1803 earthquakes from the foothill zone of the Kumaon Himalaya along the Himalayan Frontal Thrust (HFT), India. Tectonophysics, **714**: 133-145.

Malik, J.N., Sahoo, S., Satuluri, S. and Okumura, K. 2015. Active fault and paleoseismic studies in Kangra valley: evidence of surface rupture of a great Himalayan 1905 Kangra earthquake (M w 7.8), northwest Himalaya, India. Bulletin of the Seismological Society of America, **105**: 2325-2342.

Malik, J.N., Sahoo, A.K., Shah, A.A., Shinde, D.P., Juyal, N. and Singhvi, A.K., 2010. Paleoseismic evidence from trench investigation along Hajipur fault, Himalayan Frontal Thrust, NW Himalaya: implications of the faulting pattern on landscape evolution and seismic hazard. Journal of Structural Geology, **32(3)**: 350-361.

Marechal, A., Mazzotti, S., Cattin, R., Cazes, G., Vernant, P., Drukpa, D., Thinley, K., Tarayoun, A., Le Roux-Mallouf, R., Thapa, B.B. and Pelgay, P. 2016. Evidence of interseismic coupling variations along the Bhutan Himalayan arc from new GPS data. Geophysical Research Letters, **43(24)**: 12-399.

McQuarrie, N., Long, S.P., Tobgay, T., Nesbit, J.N., Gehrels, G. and Ducea, M.N. 2013. Documenting basin scale, geometry and provenance through detrital geochemical data: Lessons from the Neoproterozoic to Ordovician Lesser, Greater, and Tethyan Himalayan strata of Bhutan. Gondwana Research, **23(4)**: 1491-1510.

McQuarrie, N., Robinson, D., Long, S., Tobgay, T., Grujic, D., Gehrels, G. and Ducea, M. 2008. Preliminary stratigraphic and structural architecture of Bhutan: Implications for the along strike architecture of the Himalayan system. Earth and Planetary Science Letters, **272**: 105-117.

McQuarrie, N., Tobgay, T., Long, S.P., Reiners, P.W. and Cosca, M.A. 2014. Variable exhumation rates and variable displacement rates: Documenting recent slowing of Himalayan shortening in western Bhutan. Earth and Planetary Science Letters, **386**: 161-174.

Michel, S., Jolivet, R., Rollins, C., Jara, J. and Dal Zilio, L. 2021. Seismogenic potential of the Main Himalayan Thrust constrained by coupling segmentation and earthquake scaling. Geophysical Research Letters, **48(13)**.

Mildon, Z.K. 2017. The link between earthquakes and structural geology; the role of elapsed time, 3D geometry and stress transfer in the central Apennines, Italy (Doctoral dissertation, UCL (University College London)).

Mildon, Z.K., Toda, S., Faure Walker, J.P. and Roberts, G.P. 2016. Evaluating models of Coulomb stress transfer: Is variable fault geometry important?. Geophysical Research Letters, **43(24)**: 12-407.

Mishra, R.L., Singh, I., Pandey, A., Rao, P.S., Sahoo, H.K. and Jayangondaperumal, R. 2016. Paleoseismic evidence of a giant medieval earthquake in the eastern Himalaya. Geophysical Research Letters, **43(11)**: 5707-5715.

Molnar, P. and Stock, J.M. 2009. Slowing of India's convergence with Eurasia since 20 Ma and its implications for Tibetan mantle dynamics. Tectonics, **28**.

Mugnier, J.L., Huyghe, P., Gajurel, A.P., Upreti, B.N. and Jouanne, F. 2011. Seismites in the Kathmandu basin and seismic hazard in central Himalaya. Tectonophysics, **509(1-2)**: 33-49.

Mugnier, J.L., Huyghe, P., Leturmy, P. and Jouanne, F. 2004. Episodicity and rates of thrust-sheet motion in the Himalayas (western Nepal), AAPG Memoir **82**: 91 – 114.

Najman, Y., Appel, E., Boudagher-Fadel, M., Bown, P., Carter, A., Garzanti, E., Godin, L., Han, J., Liebke, U., Oliver, G. and Parrish, R. 2010. Timing of India-Asia collision: Geological, biostratigraphic, and palaeomagnetic constraints. Journal of Geophysical Research: Solid Earth, **115(B12)**.

Najman, Y., Bracciali, L., Parrish, R.R., Chisty, E. and Copley, A. 2016. Evolving strain partitioning in the Eastern Himalaya: The growth of the Shillong Plateau. Earth and Planetary Science Letters, **433**: 1-9.

Nakata, T. 1972. Geomorphic history and crustal movements of the foothills of the Himalayas. Science Reports of the Tohoku University, 7th Series (Geography), **22**: 39-177.

Nelson, K.D., Zhao, W., Brown, L.D. and Kuo, J. 1996. Partially molten middle crust beneath southern Tibet: synthesis of project INDEPTH results. Science, **274**: 1684.

Ogata, M., King, G.E., Herman, F. and Sueoka, S. 2022. Reconstructing the thermal structure of shallow crust in the Tono region using multi-OSL-thermometry of K-feldspar from deep borehole core. Earth and Planetary Science Letters, **591**: 117607.

Olley, J., Caitcheon, G. and Murray, A. 1998. The distribution of apparent dose as determined by optically stimulated luminescence in small aliquots of fluvial quartz: implications for dating young sediments. Quaternary Science Reviews, **17(11)**: 1033-1040.

Pandey, A., Jayangondaperumal, R., Hetényi, G., Priyanka, R.S., Singh, I., Srivastava, P. and Srivastava, H.B. 2021. Establishing primary surface rupture evidence and magnitude of the 1697 CE Sadiya earthquake at the Eastern Himalayan Frontal thrust, India. Scientific reports, **11(1)**: 1-14.

Pant, M.R. 2002. A step toward a historical seismicity of Nepal. Adarsa, **2**: 29-60.

Poolton, N.R.J., Kars, R.H., Wallinga, J. and Bos, A.J.J. 2009. Direct evidence for the participation of band-tails and excited-state tunnelling in the luminescence of irradiated feldspars. Journal of Physics: Condensed Matter, **21(48)**: 485505.

Pradhan, A.S., Lee, J.I. and Kim, J.L. 2008. Recent developments of optically stimulated luminescence materials and techniques for radiation dosimetry and clinical applications. Journal of medical physics/Association of Medical Physicists of India, **33**: 85.

Preusser, F., Degering, D., Fuchs, M., Hilgers, A., Kadereit, A., Klasen, N., Krbetschek, M., Richter, D. and Spencer, J.Q. 2008. Luminescence dating: basics, methods and applications. Eiszeitalter & Gegenwart= Quaternary Science Journal, **57**: 95-149.

Prestininzi, A., Romeo, R. 2000. Earthquake-induced ground failures in Italy. Engineering Geology, **58(3-4)**: 387–397.

Priyanka, R.S., Jayangondaperumal, R., Pandey, A., Mishra, R.L., Singh, I., Bhushan, R., Srivastava, P., Ramachandran, S., Shah, C., Kedia, S. and Sharma, A.K. 2017. Primary surface rupture of the 1950 Tibet-Assam great earthquake along the eastern Himalayan front, India. Scientific reports, **7(1)**: 5433.

Rades, E.F., Sohbati, R., Lüthgens, C., Jain, M. and Murray, A.S. 2018. First luminescence-depth profiles from boulders from moraine deposits: Insights into glaciation chronology and transport dynamics in Malta valley, Austria. Radiation Measurements, **120**: 281-289.

Rajaure, S., Sapkota, S.N., Adhikari, L.B., Koirala, B., Bhattarai, M., Tiwari, D.R., Gautam, U.G., Shrestha, P., Maske, S., Avouac, J.P. and Bollinger, L. 2013. Double difference relocation of local earthquakes in the Nepal Himalaya. Journal of Nepal Geological Society, **46**: 133-142.

Rajendran, C.P., Rajendran, K., Duarah, B.P., Baruah, S. and Earnest, A. 2004. Interpreting the style of faulting and paleoseismicity associated with the 1897 Shillong, northeast India, earthquake: Implications for regional tectonism. Tectonics, **23(4)**.

Ramsey, C.B. 2008. Radiocarbon dating: revolutions in understanding. Archaeometry, **50(2)**: 249-275.

Ramsey, C.B. 2017. Methods for summarizing radiocarbon datasets. Radiocarbon, **59**: 1809-1833.

Ramsey, C.B. 2020. OxCal Online. Available from https://c14.arch.ox.ac.uk/oxcal.html [Accessed 26 March 2021].

Ray, S.K., Bandyopadhyay, B.K. and Razdan, R.K. 1989. Tectonics of a part of the Shumar allochthon in eastern Bhutan. Tectonophysics, **169(1-3)**: 51-58.

Reddy, D.V., Nagabhushanam, P., Kumar, D., Sukhija, B.S., Thomas, P.J., Pandey, A.K., Sahoo, R.N., Prasad, G.R. and Datta, K. 2009. The great 1950 Assam Earthquake revisited: Field evidences of liquefaction and search for paleoseismic events. Tectonophysics, **474(3-4)**: 463-472.

Reimer, P.J., Austin, W.E., Bard, E., Bayliss, A., Blackwell, P.G., Ramsey, C.B., Butzin, M., Cheng, H., Edwards, R.L., Friedrich, M. and Grootes, P.M. 2020. The IntCal20 Northern Hemisphere radiocarbon age calibration curve (0–55 cal kBP). Radiocarbon, **62(4)**: 725-757.

Reimer, P.J., Bard, E., Bayliss, A., Beck, J.W., Blackwell, P.G., Ramsey, C.B., Buck, C.E., Cheng, H., Edwards, R.L., Friedrich, M. and Grootes, P.M. 2013. IntCal13 and Marine13 radiocarbon age calibration curves 0–50,000 years cal BP. Radiocarbon, **55**: 1869-1887.

Rhodes, E. J. 2011. Optically stimulated luminescence dating of sediments over the past 200,000 years. Annual Review of Earth and Planetary Sciences, **39(1)**: 461-488.

Rizza, M., Bollinger, L., Sapkota, S.N., Tapponnier, P., Klinger, Y., Karakaş, Ç., Kali, E., Etchebes, M., Tiwari, D.R., Siwakoti, I. and Bitri, A. 2019. Post earthquake aggradation processes to hide surface ruptures in thrust systems: The M8. 3, 1934, Bihar-Nepal earthquake ruptures at Charnath Khola (Eastern Nepal). Journal of Geophysical Research: Solid Earth, **124(8)**: 9182-9207.

Robinson, T.R. 2020. Scenario ensemble modelling of possible future earthquake impacts in Bhutan. Natural hazards, **103(3)**: 3457-3478.

Şahiner, E., Meriç, N. and Polymeris, G.S. 2017. Thermally assisted OSL application for equivalent dose estimation; comparison of multiple equivalent dose values as well as saturation levels determined by luminescence and ESR techniques for a sedimentary sample collected from a fault gouge. Nuclear Instruments and Methods in Physics Research Section B: Beam Interactions with Materials and Atoms, **392**: 21-30.

Sapkota, S.N., Bollinger, L., Klinger, Y., Tapponnier, P., Gaudemer, Y. and Tiwari, D. 2013. Primary surface ruptures of the great Himalayan earthquakes in 1934 and 1255. Nature Geoscience, **6(1)**: 71-76.

Schmidt, C., Friedrich, J. and Zöller, L. 2015. Thermochronometry using red TL of quartz?–Numerical simulation and observations from in-situ drill-hole samples. Radiation measurements, **81**: 98-103.

Scott, E.M., Cook, G.T. and Naysmith, P. 2007. Error and uncertainty in radiocarbon measurements. Radiocarbon, **49**: 427-440.

Sharma, Y., Pasari, S., Ching, K.E., Dikshit, O., Kato, T., Malik, J.N., Chang, C.P. and Yen, J.Y. 2020. Spatial distribution of earthquake potential along the Himalayan arc. Tectonophysics, **791**: 228556.

Singer, J., Kissling, E., Diehl, T. and Hetényi, G. 2017. The underthrusting Indian crust and its role in collision dynamics of the Eastern Himalaya in Bhutan: Insights from receiver function imaging. Journal of Geophysical Research: Solid Earth, **122(2)**: 1152-1178.

Singh, I., Pandey, A., Mishra, R.L., Priyanka, R.S., Brice, A., Jayangondaperumal, R. and Srivastava, V. 2021. Evidence of the 1950 great Assam earthquake surface break along the Mishmi Thrust at Namche Barwa Himalayan Syntaxis. Geophysical Research Letters, **48(11)**: e2020GL090893.

Singh, P. and Patel, R.C. 2022. Miocene development of the Main Boundary Thrust and Ramgarh Thrust, and exhumation of Lesser Himalayan rocks of the Kumaun-Garhwal region, NW-Himalaya (India): Insights from Fission Track Thermochronology. Journal of Asian Earth Sciences, **224**: 104987.

Sohbati, R., Murray, A.S., Chapot, M.S., Jain, M. and Pederson, J. 2012. Optically stimulated luminescence (OSL) as a chronometer for surface exposure dating. Journal of Geophysical Research: Solid Earth, **117(B9)**.

Sohbati, R., Murray, A.S., Jain, M., Buylaert, J.P. and Thomsen, K.J. 2011. Investigating the resetting of OSL signals in rock surfaces. Geochronometria, **38**: 249-258.

Sohbati, R., Murray, A.S., Porat, N., Jain, M. and Avner, U. 2015. Age of a prehistoric "Rodedian" cult site constrained by sediment and rock surface luminescence dating techniques. Quaternary Geochronology, **30**: 90-99.

Starnes, J.K., Long, S.P., Gordon, S.M., Zhang, J. and Soignard, E. 2020. Using quartz fabric intensity parameters to delineate strain patterns across the Himalayan Main Central thrust. Journal of Structural Geology, **131**: 103941.

Steckler, M.S., Mondal, D.R., Akhter, S.H., Seeber, L., Feng, L., Gale, J., Hill, E.M. and Howe, M. 2016. Locked and loading megathrust linked to active subduction beneath the Indo-Burman Ranges. Nature Geoscience, **9(8)**: 615-618.

Stevens, V.L. and Avouac, J.P. 2015. Interseismic coupling on the main Himalayan thrust. Geophysical Research Letters, **42(14)**: 5828-5837.

Stevens, V.L., De Risi, R., Le Roux-Mallouf, R., Drukpa, D. and Hetényi, G. 2020. Seismic hazard and risk in Bhutan. Natural Hazards, **104(3)**: 2339-2367.

Sutar, A.K., Verma, M., Pandey, A.P., Bansal, B.K., Prasad, P.R., Rao, P.R. and Sharma, B. 2017. Assessment of maximum earthquake potential of the Kopili fault zone in northeast India and strong ground motion simulation. Journal of Asian Earth Sciences, **147**: 439-451.

Szeliga, W., Hough, S., Martin, S. and Bilham, R. 2010. Intensity, magnitude, location, and attenuation in India for felt earthquakes since 1762. Bulletin of the Seismological Society of America, **100(2)**: 570-584.

Taylor, R.E. 1987. Radiocarbon dating: an archaeological perspective. *In* Archaeological Chemistry—II. Edited by G.F. Carter. Left Coast Press, Inc., Walnut Creek, California. pp. 33-69.

Tobgay, T., McQuarrie, N., Long, S., Kohn, M.J. and Corrie, S.L. 2012. The age and rate of displacement along the Main Central Thrust in the western Bhutan Himalaya. Earth and Planetary Science Letters, **319**: 146-158.

Toda, S., Stein, R.S., Richards-Dinger, K. and Bozkurt, S.B. 2005. Forecasting the evolution of seismicity in southern California: Animations built on earthquake stress transfer. Journal of Geophysical Research: Solid Earth, **110(B5)**.

Upreti, B. N., Nakata, T., Kumahara, Y., Yagi, H., Okumura, K., Rockwell, T. K., Virdi, N. S., and Maemoku, H. 2000. The latest active faulting in southeast Nepal, Proceedings of the Kohudan International Symposium and School in Active Faulting, 17–26 January, 2000, 533–536.

USGS, 2020. M6.1 - 11 km W of Trashigang, Bhutan [online]. Available from https://earthquake.usgs.gov/earthquakes/eventpage/usp000h1r4/executive. [cited 19 February 2021].

van der Beek, P., Robert, X., Mugnier, J.L., Bernet, M., Huyghe, P. and Labrin, E. 2006. Late Miocene–recent exhumation of the central Himalaya and recycling in the foreland basin assessed by apatite fission-track thermochronology of Siwalik sediments, Nepal. Basin Research, **18**: 413-434.

Verdecchia, A. and Carena, S. 2016. Coulomb stress evolution in a diffuse plate boundary: 1400 years of earthquakes in eastern California and western Nevada, USA. Tectonics, **35**: 1793-1811.

Walker, M. 2005. Quaternary dating methods. John Wiley & Sons, Ltd., The Atrium, Southern Gate, Chichester, West Sussex. pp. 17-55.

Wells, D.L. and Coppersmith, K.J. 1994. New empirical relationships among magnitude, rupture length, rupture width, rupture area, and surface displacement. Bulletin of the seismological Society of America, **84**: 974-1002.

Wesnousky, S.G., Kumahara, Y., Chamlagain, D. and Neupane, P.C. 2019. Large Himalayan Frontal Thrust paleoearthquake at Khayarmara in Eastern Nepal. Journal of Asian Earth Sciences, **174**: 346-351.

Wesnousky, S.G., Kumahara, Y., Chamlagain, D., Pierce, I.K., Karki, A. and Gautam, D. 2017a. Geological observations on large earthquakes along the Himalayan frontal fault near Kathmandu, Nepal. Earth and Planetary Science Letters, **457**: 366-375.

Wesnousky, S.G., Kumahara, Y., Chamlagain, D., Pierce, I.K., Reedy, T., Angster, S. and Giri, B., 2017b. Large paleoearthquake timing and displacement near Damak in eastern Nepal on the Himalayan Frontal Thrust. Geophysical Research Letters, **44(16)**: 8219-8226.

Wesnousky, S.G., Kumahara, Y., Nakata, T., Chamlagain, D. and Neupane, P. 2018. New observations disagree with previous interpretations of surface rupture along the Himalayan frontal thrust during the great 1934 Bihar-Nepal earthquake. Geophysical Research Letters, **45(6)**: 2652-2658.

Yin, A. and Harrison, T.M. 2000. Geologic evolution of the Himalayan-Tibetan orogen. Annual Review of Earth and Planetary Sciences, **28(1)**: 211-280.

Zhao, W., Nelson, K.D., Che, J., Quo, J., Lu, D., Wu, C. and Liu, X. 1993. Deep seismic reflection evidence for continental underthrusting beneath southern Tibet. Nature, **366(6455)**: 557-559.

Zeiger, K., Gordon, S.M., Long, S.P., Kylander-Clark, A.R.C., Agustsson, K. and Penfold, M. 2015. Timing and conditions of metamorphism and melt crystallization in Greater Himalayan rocks, eastern and central Bhutan: insight from U–Pb zircon and monazite geochronology and trace-element analyses. Contributions to Mineralogy and Petrology, **169**: 47.

APPENDIX A. Field Investigations
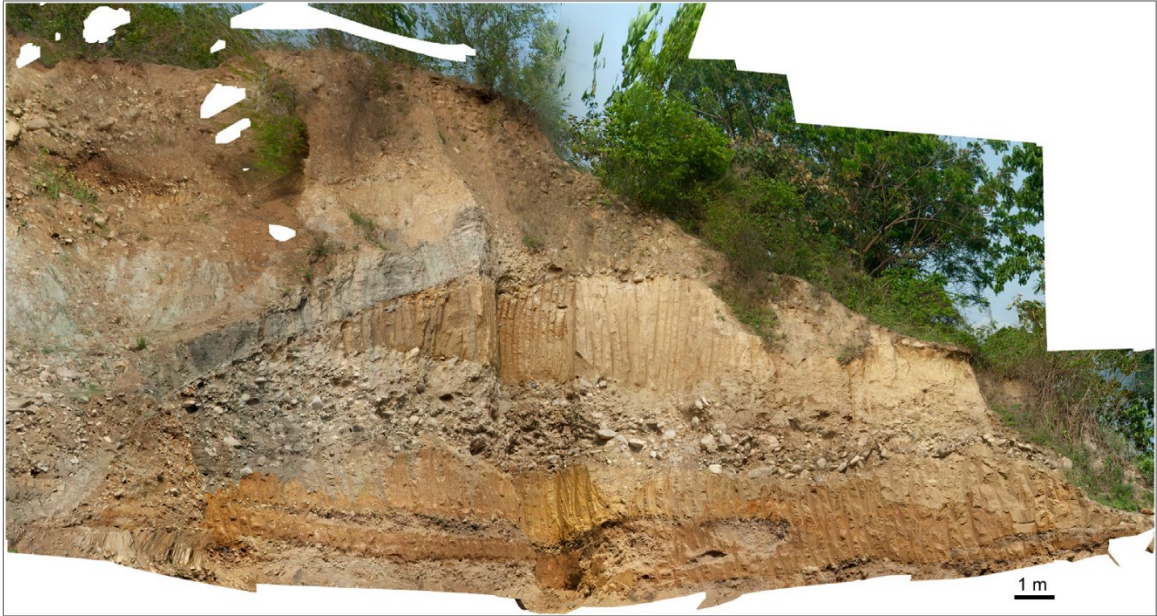
Figure A.1 The orthorectified photomosaic of the outcrop was constructed with Agisoft Metashape software using 136 field photographs. The composite part of the image above and to the upper left of the cleaned main section of the outcrop is distorted due to the angle of taking photos (because we could not reach that part at the field site).
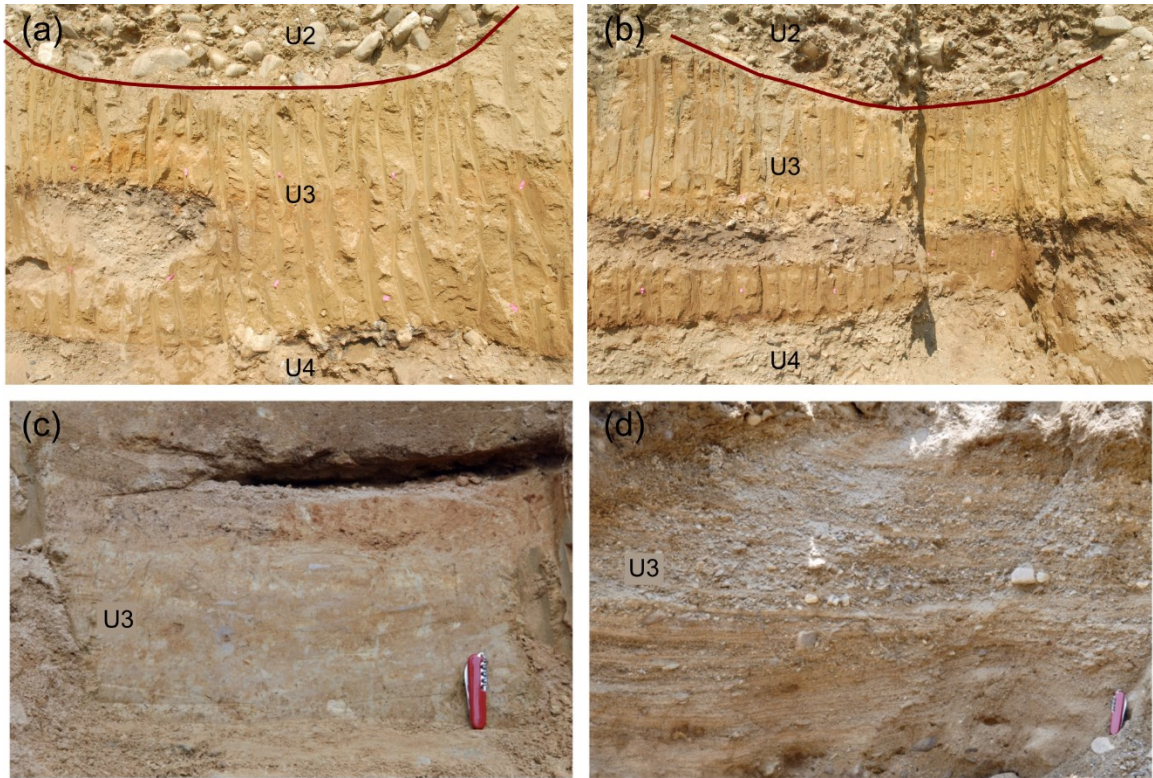
Figure A.2 Lithologies of the refreshed MFT exposure. (a) & (b) The middle of the outcrop shows the base of the right-side and left-side channel (denoted as the dark red curve), respectively, where rounded cobbles first settle (Figure 4.3). Unit U4, the oldest unit observed at the base of the section, is a clast-supported fluvial deposit composed of poorly-sorted and poorly-rounded granules, pebbles, and cobbles in a sandy matrix. Unit U3 is a ~2.0–3.3 m thick medium sand-sized fluvial deposit including ~20–80 cm-thick granule or pebble gravel lenses. Unit U2 is distinguished from unit U4 by a generally larger clast size and lesser degree of orange coloration due to oxidation. (c) The middle of unit U3. Silt layer with clay concentrations (paler yellow) overlain by poorly sorted coarse sand. (d) The base of unit U3. The lens of coarse sand to pebble with cross-bedding. In all the photographs, the south is to the right.
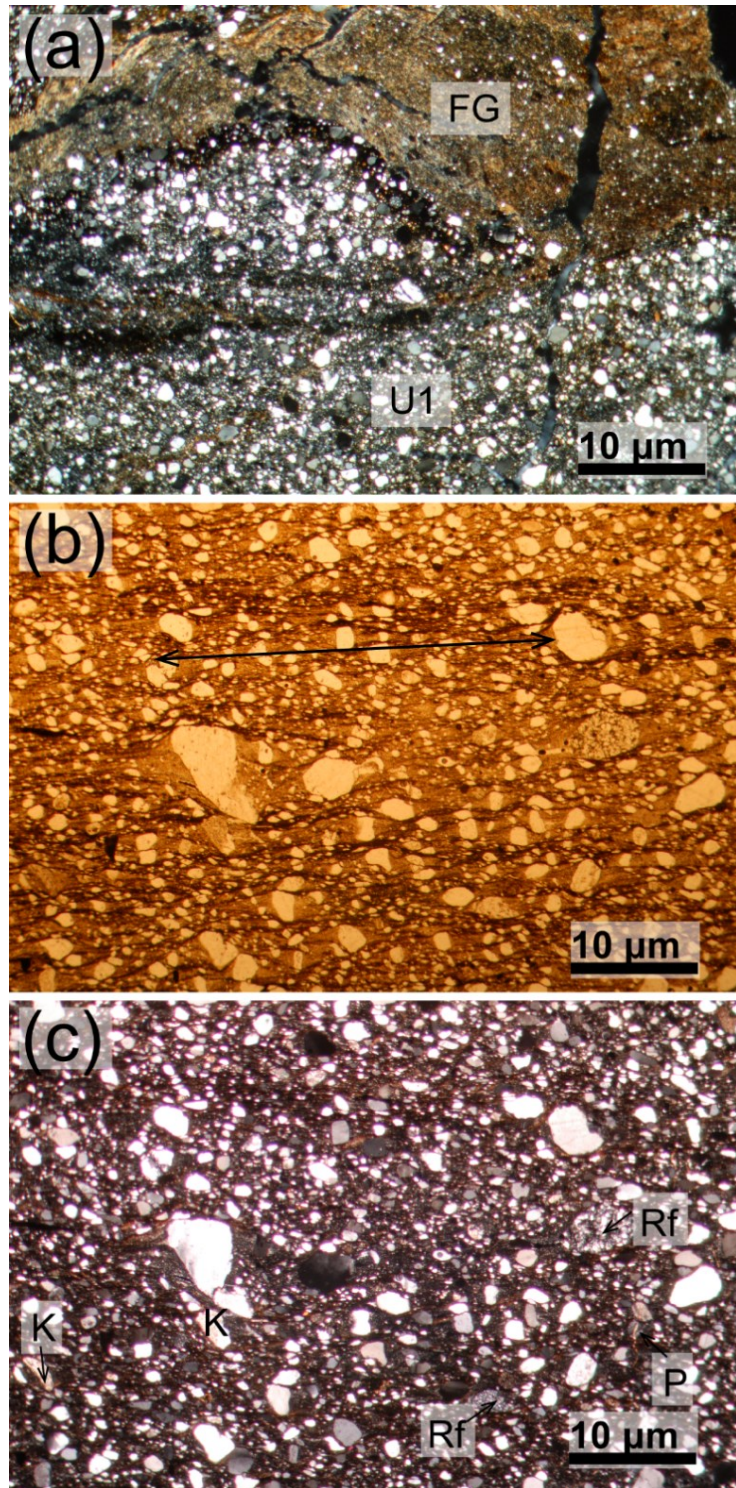
Figure A.3 Micrograph of fault gouge adjacent sand deposits near the tip of the younger fault. (a) Contact between clay-rich fault gouge (FG) and sand layer U1. (b) & (c) Thin sections of sandy deposits in U1 in PPL and XPL modes, showing aligned grains and the presence of plagioclase (P) and K-feldspar (K) grains with rock fragments (Rf). These features imply that pressure solution has occurred in the topmost section of U1. Black line with double arrows shows foliation formed by pressure solution.

APPENDIX B. Radiocarbon Analysis

Table B.1 Results of the accelerator mass spectrometry (AMS) radiocarbon (^{14}C) analyses from organic materials collected from the Dungsam Chu exposure. The sample with $F^{14}C > 1$ indicates presence of 'bomb peak ^{14}C' (post 1950 AD, modern).

Unit[a]	Material	Sample code	Sample No.[b]	C^{14} age BP[c]	± 1σ	F^{14}C[d]	±1σ	δ^{13}C[e] ‰	± 1σ	C[f] mg	C/N[g]	Calibrated ranges (95%conf. level)[h] AD, -BC	
T1-soil 0	charcoal	1-1	ETH-90350	-926	21	1.1222	0.0030	-28.7	1	1.00		1993	1996
T1-soil 1	charcoal	1-2	ETH-90351	-3326	33	1.5129	0.0062	-35.3	1	0.18	88.54	1969	1972
T1-soil 3	charcoal	1-3	ETH-90352	36	22	0.9956	0.0027	-25.0	1	0.99	111.38	1697	1911
CW1-sand	charcoal	2-1	ETH-101046	7376	61	0.3992	0.0030	-19.0	1	0.46	1.70	-6386	-6082
CW1-sand	charcoal	2-2	ETH-90354	>50,125		0.0019	0.0001	-21.1	1	0.99	48.78		
T2-U1	charcoal	2H-1	ETH-101038	383	22	0.9534	0.0026	-26.7	1	0.99	140.09	1449	1623
T2-U1	macrofossil	2F-1	ETH-90353	4266	40	0.588	0.0030	-30.9	1	0.20	110.17	-3010	-2700
T2-U1	charcoal	2F-3	ETH-90357	3082	74	0.6814	0.0063	-27.2	1	0.05		-1501	-1127
T2-U2	sediment	2F-4	ETH-90359										
T2-U2	sediment	2F-5	ETH-90360										
T2-U2	undefined	2F-6	ETH-101040	-123	21	1.0154	0.0027	-29.9	1	0.83	18.40	1955	1957
T2-U3	undefined	2F-7	ETH-101042	-177	21	1.0223	0.0027	-29.5	1	0.86	40.92	1955	1957

[a]See trench log for stratigraphic unit designations.
[b]Laboratory sample codes. All samples have been dated by the ETH accelerator facility in Zurich (Switzerland).
[c]Radiocarbon years B.P. relative to 1950 A.D. with 1σ counting error.
[d]F^{14}C refers to the concentration measured in the sample, corrected for fractionation, and normalized to the 1950 value and the corresponding ^{14}C age.
[e]δ^{13}C is a value measured on graphite and can include additional fractionation.
[f]The mass C is the final carbon content of the sample.
[g]C/N ratio is an atomic ration (C/N)×(14/12).
[h]Calendric dates were calibrated using OxCal and the atmospheric calibration curve IntCal20. '+' for AD while '-' for BC.

APPENDIX C. Raw Data of Multi-OSL Dating of Feldspar

Table C.1 Raw data of all IRSL$_{50}$ measurements for fault gouge sample Bt1BBY1, including fading and isothermal holding measurements.

Sample Bt1BBY1
Natural T (°C)

Natural Ḋ (Gy/ka)			4.14	0.25										
Lab calibration:														
T (°C)	15	*t (ks)*	Nat	0.000	0.250	0.500	1.000	2.000	4.000	8.000	16.000	0.000	0.250	
Ḋ (Gy/s)	0.240	*Lₓ/Tₓ*	0.944	0.004	0.635	1.151	2.014	3.107	4.283	5.083	5.261	0.006	0.64	
T (°C)	15	*t (ks)*	Nat	0.000	0.250	0.500	1.000	2.000	4.000	8.000	16.000	0.000	0.250	
Ḋ (Gy/s)	0.240	*Lₓ/Tₓ*	0.93	0.004	0.637	1.159	1.985	3.062	4.329	5.034	5.261	0.008	0.654	
T (°C)	15	*t (ks)*	Nat	0.000	0.250	0.500	1.000	2.000	4.000	8.000	16.000	0.000	0.250	
Ḋ (Gy/s)	0.240	*Lₓ/Tₓ*	0.736	0.004	0.63	1.159	2.007	3.152	4.404	5.252	5.482	0.006	0.638	
T (°C)	170	*t (ks)*	0.000	0.010	0.020	0.040	0.080	0.160	0.320	0.640	1.280	2.560	5.120	10.000
Ḋ (Gy/s)	0.119	*Lₓ/Tₓ*	0.961	0.954	0.957	0.95	0.951	0.946	0.938	0.934	0.918	0.892	0.864	0.825
T (°C)	190	*t (ks)*	0.000	0.010	0.020	0.040	0.080	0.160	0.320	0.640	1.280	2.560	5.120	10.000
Ḋ (Gy/s)	0.119	*Lₓ/Tₓ*	0.956	0.957	0.947	0.952	0.955	0.933	0.923	0.908	0.874	0.825	0.771	0.697
T (°C)	210	*t (ks)*	0.000	0.010	0.020	0.040	0.080	0.160	0.320	0.640	1.280	2.560	5.120	10.000
Ḋ (Gy/s)	0.119	*Lₓ/Tₓ*	0.956	0.953	0.952	0.943	0.934	0.91	0.89	0.843	0.776	0.69	0.591	0.487
T (°C)	230	*t (ks)*	0.000	0.010	0.020	0.040	0.080	0.160	0.320	0.64	1.280	2.560	5.120	10.000
Ḋ (Gy/s)	0.119	*Lₓ/Tₓ*	0.952	0.938	0.933	0.914	0.888	0.843	0.78	0.687	0.577	0.465	0.355	0.256
T (°C)	250	*t (ks)*	0.000	0.010	0.020	0.040	0.080	0.160	0.320	0.64	1.280	2.560	5.120	10.000
Ḋ (Gy/s)	0.119	*Lₓ/Tₓ*	0.939	0.916	0.887	0.849	0.785	0.699	0.595	0.479	0.358	0.251	0.166	0.101
T (°C)	300	*t (ks)*	0.000	0.010	0.020	0.040	0.080	0.160	0.320	0.64	1.280	2.560	5.120	10.000
Ḋ (Gy/s)	0.119	*Lₓ/Tₓ*	0.768	0.62	0.53	0.421	0.308	0.207	0.123	0.066	0.032	0.013	0.005	0.002
T (°C)	350	*t (ks)*	0.000	0.010	0.020	0.040	0.080	0.160	0.320	0.64				
Ḋ (Gy/s)	0.119	*Lₓ/Tₓ*	0.324	0.162	0.106	0.06	0.028	0.011	0.004	0.001				
T (°C)	15	*t (ks)*	0.414	14.324	20.322	32.321	56.315	0.414						
Ḋ (Gy/s)	0.119	*Lₓ/Tₓ*	0.98	0.931	0.908	0.903	0.898	0.972						
T (°C)	15	*t (ks)*	0.414	16.013	22.014	34.013	58.007	0.414						
Ḋ (Gy/s)	0.119	*Lₓ/Tₓ*	0.988	0.921	0.911	0.907	0.894	0.976						
T (°C)	15	*t (ks)*	0.414	17.705	23.706	35.705	59.699	0.414						
Ḋ (Gy/s)	0.119	*Lₓ/Tₓ*	0.992	0.910	0.919	0.911	0.895	0.974						

Table C.2 Raw data of all $IRSL_{100}$ measurements for fault gouge sample Bt1BBY1, including fading and isothermal holding measurements.

Sample Bt1BBY1
Natural T (°C)
Natural Ḋ (Gy/ka)   4.14   0.25
Lab calibration:

T (°C)	15	*t (ks)*	Nat	0.000	0.250	0.500	1.000	2.000	4.000	8.000	16.000	0.000	0.250	
Ḋ (Gy/s)	0.240	*Lx/Tx*	2.963	0.018	0.61	1.123	1.957	3.122	4.381	5.357	5.782	0.022	0.625	
T (°C)	15	*t (ks)*	Nat	0.000	0.250	0.500	1.000	2.000	4.000	8.000	16.000	0.000	0.250	
Ḋ (Gy/s)	0.240	*Lx/Tx*	1.983	0.020	0.616	1.133	1.94	3.094	4.352	5.283	5.735	0.03	0.624	
T (°C)	15	*t (ks)*	Nat	0.000	0.250	0.500	1.000	2.000	4.000	8.000	16.000	0.000	0.250	
Ḋ (Gy/s)	0.240	*Lx/Tx*	2.449	0.020	0.617	1.130	1.952	3.107	4.4	5.442	5.889	0.024	0.625	
T (°C)	170	*t (ks)*	0.000	0.010	0.020	0.040	0.080	0.160	0.320	0.640	1.280	2.560	5.120	10.000
Ḋ (Gy/s)	0.119	*Lx/Tx*	0.93	0.948	0.945	0.938	0.951	0.94	0.929	0.927	0.922	0.912	0.904	0.86
T (°C)	190	*t (ks)*	0.000	0.010	0.020	0.040	0.080	0.160	0.320	0.640	1.280	2.560	5.120	10.000
Ḋ (Gy/s)	0.119	*Lx/Tx*	0.936	0.951	0.942	0.933	0.924	0.944	0.917	0.919	0.898	0.87	0.82	0.763
T (°C)	210	*t (ks)*	0.000	0.010	0.020	0.040	0.080	0.160	0.320	0.640	1.280	2.560	5.120	10.000
Ḋ (Gy/s)	0.119	*Lx/Tx*	0.953	0.923	0.942	0.939	0.926	0.922	0.903	0.869	0.811	0.758	0.673	0.569
T (°C)	230	*t (ks)*	0.000	0.010	0.020	0.040	0.080	0.160	0.320	0.64	1.280	2.560	5.120	10.000
Ḋ (Gy/s)	0.119	*Lx/Tx*	0.932	0.942	0.936	0.921	0.905	0.865	0.826	0.756	0.654	0.556	0.431	0.32
T (°C)	250	*t (ks)*	0.000	0.010	0.020	0.040	0.080	0.160	0.320	0.64	1.280	2.560	5.120	10.000
Ḋ (Gy/s)	0.119	*Lx/Tx*	0.939	0.909	0.901	0.879	0.834	0.765	0.677	0.56	0.441	0.318	0.216	0.13
T (°C)	300	*t (ks)*	0.000	0.010	0.020	0.040	0.080	0.160	0.320	0.64	1.280	2.560	5.120	10.000
Ḋ (Gy/s)	0.119	*Lx/Tx*	0.81	0.716	0.624	0.524	0.397	0.287	0.173	0.099	0.054	0.024	0.013	0.004
T (°C)	350	*t (ks)*	0.000	0.010	0.020	0.040	0.080	0.160	0.320	0.64				
Ḋ (Gy/s)	0.119	*Lx/Tx*	0.43	0.241	0.177	0.103	0.056	0.026	0.01	0.004				
T (°C)	15	*t (ks)*	0.5832	14.486	20.488	32.486	56.477	0.5832						
Ḋ (Gy/s)	0.119	*Lx/Tx*	0.95	0.934	0.924	0.92	0.915	0.951						
T (°C)	15	*t (ks)*	0.5832	16.175	22.18	34.178	58.169	0.5832						
Ḋ (Gy/s)	0.119	*Lx/Tx*	0.956	0.923	0.918	0.918	0.916	0.952						
T (°C)	15	*t (ks)*	0.5832	17.867	23.872	35.87	59.864	0.5832						
Ḋ (Gy/s)	0.119	*Lx/Tx*	0.95	0.926	0.918	0.923	0.913	0.955						

Table C.3 Raw data of all IRSL$_{150}$ measurements for fault gouge sample Bt1BBY1, including fading and isothermal holding measurements.

Sample Bt1BBY1

Natural T (°C)														
Natural $\dot{D}$ (Gy/ka)			4.14	0.25										
Lab calibration:														
T (°C)	15	*t (ks)*	Nat	0.000	0.250	0.500	1.000	2.000	4.000	8.000	16.000	0.000	0.250	
$\dot{D}$ (Gy/s)	0.240	*L_x/T_x*	3.418	0.021	0.607	1.107	1.927	3.081	4.373	5.408	5.95	0.027	0.621	
T (°C)	15	*t (ks)*	Nat	0.000	0.250	0.500	1.000	2.000	4.000	8.000	16.000	0.000	0.250	
$\dot{D}$ (Gy/s)	0.240	*L_x/T_x*	2.327	0.028	0.608	1.116	1.932	3.108	4.367	5.441	6.036	0.039	0.625	
T (°C)	15	*t (ks)*	Nat	0.000	0.250	0.500	1.000	2.000	4.000	8.000	16.000	0.000	0.250	
$\dot{D}$ (Gy/s)	0.240	*L_x/T_x*	3.062	0.025	0.615	1.123	1.947	3.066	4.376	5.503	6.09	0.032	0.62	
T (°C)	170	*t (ks)*	0.000	0.010	0.020	0.040	0.080	0.160	0.320	0.640	1.280	2.560	5.120	10.000
$\dot{D}$ (Gy/s)	0.119	*L_x/T_x*	0.939	0.914	0.927	0.936	0.929	0.935	0.934	0.928	0.919	0.896	0.899	0.883
T (°C)	190	*t (ks)*	0.000	0.010	0.020	0.040	0.080	0.160	0.320	0.640	1.280	2.560	5.120	10.000
$\dot{D}$ (Gy/s)	0.119	*L_x/T_x*	0.934	0.93	0.911	0.928	0.916	0.93	0.925	0.91	0.906	0.89	0.848	0.826
T (°C)	210	*t (ks)*	0.000	0.010	0.020	0.040	0.080	0.160	0.320	0.640	1.280	2.560	5.120	10.000
$\dot{D}$ (Gy/s)	0.119	*L_x/T_x*	0.937	0.926	0.933	0.938	0.917	0.934	0.913	0.894	0.87	0.821	0.76	0.699
T (°C)	230	*t (ks)*	0.000	0.010	0.020	0.040	0.080	0.160	0.320	0.64	1.280	2.560	5.120	10.000
$\dot{D}$ (Gy/s)	0.119	*L_x/T_x*	0.923	0.917	0.92	0.933	0.929	0.89	0.871	0.824	0.767	0.688	0.59	0.486
T (°C)	250	*t (ks)*	0.000	0.010	0.020	0.040	0.080	0.160	0.320	0.64	1.280	2.560	5.120	10.000
$\dot{D}$ (Gy/s)	0.119	*L_x/T_x*	0.915	0.891	0.927	0.899	0.868	0.835	0.784	0.713	0.605	0.482	0.371	0.25
T (°C)	300	*t (ks)*	0.000	0.010	0.020	0.040	0.080	0.160	0.320	0.64	1.280	2.560	5.120	10.000
$\dot{D}$ (Gy/s)	0.119	*L_x/T_x*	0.863	0.796	0.756	0.687	0.579	0.463	0.325	0.212	0.124	0.063	0.029	0.015
T (°C)	350	*t (ks)*	0.000	0.010	0.020	0.040	0.080	0.160	0.320	0.64				
$\dot{D}$ (Gy/s)	0.119	*L_x/T_x*	0.572	0.405	0.309	0.212	0.131	0.068	0.03	0.011				
T (°C)	15	*t (ks)*	0.7704	14.67	20.671	32.67	56.664	0.7704						
$\dot{D}$ (Gy/s)	0.119	*L_x/T_x*	0.951	0.936	0.925	0.915	0.921	0.949						
T (°C)	15	*t (ks)*	0.7704	16.362	22.363	34.362	58.356	0.7704						
$\dot{D}$ (Gy/s)	0.119	*L_x/T_x*	0.941	0.93	0.921	0.922	0.916	0.949						
T (°C)	15	*t (ks)*	0.7668	18.054	24.055	36.054	60.052	0.7704						
$\dot{D}$ (Gy/s)	0.119	*L_x/T_x*	0.938	0.925	0.923	0.926	0.917	0.946						

Table C.4 Raw data of all IRSL$_{225}$ measurements for fault gouge sample Bt1BBY1, including fading and isothermal holding measurements.

Sample Bt1BBY1
Natural T (°C)
Natural Ḋ (Gy/ka) 4.14 0.25
Lab calibration:

T (°C)	15	*t (ks)*	Nat	0.000	0.250	0.500	1.000	2.000	4.000	8.000	16.000	0.000	0.250	
Ḋ (Gy/s)	0.240	*L$_x$/T$_x$*	3.054	0.033	0.605	1.061	1.772	2.67	3.591	4.291	4.662	0.039	0.619	
T (°C)	15	*t (ks)*	Nat	0.000	0.250	0.500	1.000	2.000	4.000	8.000	16.000	0.000	0.250	
Ḋ (Gy/s)	0.240	*L$_x$/T$_x$*	2.497	0.042	0.607	1.073	1.77	2.667	3.576	4.22	4.606	0.058	0.623	
T (°C)	15	*t (ks)*	Nat	0.000	0.250	0.500	1.000	2.000	4.000	8.000	16.000	0.000	0.250	
Ḋ (Gy/s)	0.240	*L$_x$/T$_x$*	2.997	0.039	0.608	1.066	1.782	2.688	3.599	4.341	4.772	0.048	0.612	
T (°C)	170	*t (ks)*	0.000	0.010	0.020	0.040	0.080	0.160	0.320	0.640	1.280	2.560	5.120	10.000
Ḋ (Gy/s)	0.119	*L$_x$/T$_x$*	0.901	0.904	0.901	0.902	0.898	0.902	0.893	0.893	0.888	0.886	0.881	0.869
T (°C)	190	*t (ks)*	0.000	0.010	0.020	0.040	0.080	0.160	0.320	0.640	1.280	2.560	5.120	10.000
Ḋ (Gy/s)	0.119	*L$_x$/T$_x$*	0.893	0.898	0.9	0.891	0.899	0.904	0.889	0.887	0.883	0.872	0.843	0.83
T (°C)	210	*t (ks)*	0.000	0.010	0.020	0.040	0.080	0.160	0.320	0.640	1.280	2.560	5.120	10.000
Ḋ (Gy/s)	0.119	*L$_x$/T$_x$*	0.904	0.902	0.901	0.903	0.905	0.892	0.876	0.868	0.856	0.832	0.802	0.773
T (°C)	230	*t (ks)*	0.000	0.010	0.020	0.040	0.080	0.160	0.320	0.64	1.280	2.560	5.120	10.000
Ḋ (Gy/s)	0.119	*L$_x$/T$_x$*	0.893	0.906	0.899	0.906	0.895	0.884	0.871	0.838	0.816	0.768	0.714	0.637
T (°C)	250	*t (ks)*	0.000	0.010	0.020	0.040	0.080	0.160	0.320	0.64	1.280	2.560	5.120	10.000
Ḋ (Gy/s)	0.119	*L$_x$/T$_x$*	0.893	0.89	0.894	0.889	0.874	0.857	0.818	0.787	0.713	0.649	0.558	0.463
T (°C)	300	*t (ks)*	0.000	0.010	0.020	0.040	0.080	0.160	0.320	0.64	1.280	2.560	5.120	10.000
Ḋ (Gy/s)	0.119	*L$_x$/T$_x$*	0.848	0.833	0.813	0.776	0.719	0.641	0.542	0.426	0.321	0.222	0.14	0.077
T (°C)	350	*t (ks)*	0.000	0.010	0.020	0.040	0.080	0.160	0.320	0.64				
Ḋ (Gy/s)	0.119	*L$_x$/T$_x$*	0.699	0.608	0.524	0.44	0.336	0.232	0.14	0.072				
T (°C)	15	*t (ks)*	0.9828	14.879	20.88	32.879	56.873	0.9828						
Ḋ (Gy/s)	0.119	*L$_x$/T$_x$*	0.931	0.905	0.897	0.904	0.903	0.92						
T (°C)	15	*t (ks)*	0.9792	16.571	22.572	34.574	58.565	0.9828						
Ḋ (Gy/s)	0.119	*L$_x$/T$_x$*	0.921	0.906	0.904	0.902	0.912	0.917						
T (°C)	15	*t (ks)*	0.9792	18.263	24.264	36.263	60.26	0.9828						
Ḋ (Gy/s)	0.119	*L$_x$/T$_x$*	0.93	0.913	0.903	0.903	0.891	0.919						

Table C.5 Raw data of all IRSL$_{50}$ measurements for fault gouge sample Bt1BTY2, including fading and isothermal holding measurements.

Sample Bt1BTY2
Natural T (°C)
Natural Ḋ (Gy/ka)   3.94   0.25
Lab calibration:

T (°C)	15	*t (ks)*	Nat	0.000	0.250	0.500	1.000	2.000	4.000	8.000	16.000	0.000	0.250
Ḋ (Gy/s)	0.240	*Lx/Tx*	1.193	0.003	0.645	1.201	1.943	3.037	4.222	4.829	5.106	0.007	0.662
T (°C)	15	*t (ks)*	Nat	0.000	0.250	0.500	1.000	2.000	4.000	8.000	16.000	0.000	0.250
Ḋ (Gy/s)	0.240	*Lx/Tx*	1.143	0.003	0.633	1.150	1.916	2.963	3.946	4.696	4.876	0.006	0.644
T (°C)	15	*t (ks)*	Nat	0.000	0.250	0.500	1.000	2.000	4.000	8.000	16.000	0.000	0.250
Ḋ (Gy/s)	0.240	*Lx/Tx*	1.284	0.004	0.627	1.166	2.04	3.215	4.49	5.387	5.752	0.005	0.635
T (°C)	170	*t (ks)*	0.500	0.500	0.500	0.500	0.500	0.500	0.500	0.500	0.500	0.500	0.500	0.500
Ḋ (Gy/s)	0.119	*Lx/Tx*	0.95	0.975	0.957	0.966	0.950	0.954	0.949	0.94	0.935	0.89	0.878	0.831
T (°C)	190	*t (ks)*	0.500	0.500	0.500	0.500	0.500	0.500	0.500	0.500	0.500	0.500	0.500	0.500
Ḋ (Gy/s)	0.119	*Lx/Tx*	0.949	0.955	0.957	0.966	0.955	0.955	0.943	0.917	0.879	0.835	0.781	0.683
T (°C)	210	*t (ks)*	0.500	0.500	0.500	0.500	0.500	0.500	0.500	0.500	0.500	0.500	0.500	0.500
Ḋ (Gy/s)	0.119	*Lx/Tx*	0.956	0.954	0.956	0.947	0.94	0.916	0.897	0.853	0.779	0.687	0.597	0.481
T (°C)	230	*t (ks)*	0.500	0.500	0.500	0.500	0.500	0.500	0.500	0.500	0.500	0.500	0.500	0.500
Ḋ (Gy/s)	0.119	*Lx/Tx*	0.953	0.947	0.931	0.922	0.901	0.854	0.778	0.689	0.577	0.459	0.35	0.243
T (°C)	250	*t (ks)*	0.500	0.500	0.500	0.500	0.500	0.500	0.500	0.500	0.500	0.500	0.500	0.500
Ḋ (Gy/s)	0.119	*Lx/Tx*	0.943	0.919	0.892	0.85	0.782	0.694	0.582	0.463	0.36	0.252	0.171	0.101
T (°C)	300	*t (ks)*	0.500	0.500	0.500	0.500	0.500	0.500	0.500	0.500	0.500	0.500	0.500	0.500
Ḋ (Gy/s)	0.119	*Lx/Tx*	0.761	0.617	0.513	0.408	0.316	0.2	0.127	0.071	0.032	0.016	0.006	0.002
T (°C)	350	*t (ks)*	0.500	0.500	0.500	0.500	0.500	0.500	0.500	0.500				
Ḋ (Gy/s)	0.119	*Lx/Tx*	0.313	0.171	0.111	0.064	0.031	0.012	0.005	0.001				
T (°C)	15	*t (ks)*	0.414	9.2556	15.253	27.248	51.242	0.414						
Ḋ (Gy/s)	0.119	*Lx/Tx*	0.977	0.931	0.916	0.912	0.908	0.97						
T (°C)	15	*t (ks)*	0.414	10.944	16.942	28.937	52.931	0.414						
Ḋ (Gy/s)	0.119	*Lx/Tx*	0.961	0.929	0.925	0.925	0.898	0.967						
T (°C)	15	*t (ks)*	0.414	12.632	18.63	30.629	54.623	0.414						
Ḋ (Gy/s)	0.119	*Lx/Tx*	0.981	0.937	0.919	0.915	0.908	0.96						

Table C.6 Raw data of all IRSL$_{100}$ measurements for fault gouge sample Bt1BTY2, including fading and isothermal holding measurements.

Sample Bt1BTY2
Natural T (°C)
Natural $\dot{D}$ (Gy/ka)   3.94   0.25
Lab calibration:

T (°C)	15	*t (ks)*	Nat	0.000	0.250	0.500	1.000	2.000	4.000	8.000	16.000	0.000	0.250	
$\dot{D}$ (Gy/s)	0.240	*L_x/T_x*	2.996	0.015	0.635	1.116	1.877	2.975	4.18	5.035	5.325	0.017	0.632	
T (°C)	15	*t (ks)*	Nat	0.000	0.250	0.500	1.000	2.000	4.000	8.000	16.000	0.000	0.250	
$\dot{D}$ (Gy/s)	0.240	*L_x/T_x*	3.164	0.015	0.625	1.131	1.915	3.044	4.144	5.104	5.431	0.022	0.62	
T (°C)	15	*t (ks)*	Nat	0.000	0.250	0.500	1.000	2.000	4.000	8.000	16.000	0.000	0.250	
$\dot{D}$ (Gy/s)	0.240	*L_x/T_x*	3.151	0.013	0.605	1.132	1.934	3.074	4.291	5.246	5.565	0.019	0.609	
T (°C)	170	*t (ks)*	0.500	0.500	0.500	0.500	0.500	0.500	0.500	0.500	0.500	0.500	0.500	0.500
$\dot{D}$ (Gy/s)	0.119	*L_x/T_x*	0.944	0.94	0.958	0.896	0.949	0.965	0.94	0.962	0.944	0.915	0.906	0.864
T (°C)	190	*t (ks)*	0.500	0.500	0.500	0.500	0.500	0.500	0.500	0.500	0.500	0.500	0.500	0.500
$\dot{D}$ (Gy/s)	0.119	*L_x/T_x*	0.944	0.927	0.951	0.954	0.965	0.937	0.937	0.945	0.917	0.853	0.854	0.787
T (°C)	210	*t (ks)*	0.500	0.500	0.500	0.500	0.500	0.500	0.500	0.500	0.500	0.500	0.500	0.500
$\dot{D}$ (Gy/s)	0.119	*L_x/T_x*	0.914	0.96	0.938	0.948	0.922	0.937	0.939	0.882	0.858	0.779	0.713	0.634
T (°C)	230	*t (ks)*	0.500	0.500	0.500	0.500	0.500	0.500	0.500	0.500	0.500	0.500	0.500	0.500
$\dot{D}$ (Gy/s)	0.119	*L_x/T_x*	0.927	0.955	0.965	0.91	0.912	0.908	0.855	0.8	0.711	0.616	0.526	0.405
T (°C)	250	*t (ks)*	0.500	0.500	0.500	0.500	0.500	0.500	0.500	0.500	0.500	0.500	0.500	0.500
$\dot{D}$ (Gy/s)	0.119	*L_x/T_x*	0.957	0.947	0.908	0.904	0.852	0.809	0.742	0.633	0.517	0.383	0.286	0.178
T (°C)	300	*t (ks)*	0.500	0.500	0.500	0.500	0.500	0.500	0.500	0.500	0.500	0.500	0.500	0.500
$\dot{D}$ (Gy/s)	0.119	*L_x/T_x*	0.838	0.768	0.699	0.584	0.472	0.347	0.22	0.135	0.075	0.042	0.017	0.001
T (°C)	350	*t (ks)*	0.500	0.500	0.500	0.500	0.500	0.500	0.500	0.500				
$\dot{D}$ (Gy/s)	0.119	*L_x/T_x*	0.445	0.296	0.216	0.136	0.074	0.038	0.015	-0.004				
T (°C)	15	*t (ks)*	0.5832	9.4176	15.415	27.414	51.404	0.5832						
$\dot{D}$ (Gy/s)	0.119	*L_x/T_x*	0.933	0.922	0.94	0.92	0.921	0.958						
T (°C)	15	*t (ks)*	0.5832	11.106	17.104	29.102	53.096	0.5832						
$\dot{D}$ (Gy/s)	0.119	*L_x/T_x*	0.924	0.936	0.939	0.912	0.904	0.953						
T (°C)	15	*t (ks)*	0.5832	12.798	18.796	30.794	54.788	0.5832						
$\dot{D}$ (Gy/s)	0.119	*L_x/T_x*	0.956	0.93	0.922	0.928	0.918	0.947						

Table C.7 Raw data of all IRSL$_{150}$ measurements for fault gouge sample Bt1BTY2, including fading and isothermal holding measurements.

Sample Bt1BTY2
Natural T (°C)
Natural Ḋ (Gy/ka)   3.94   0.25
Lab calibration:

T (°C)	15	*t (ks)*	Nat	0.000	0.250	0.500	1.000	2.000	4.000	8.000	16.000	0.000	0.250	
Ḋ (Gy/s)	0.240	*Lₓ/Tₓ*	3.497	0.017	0.625	1.155	1.88	2.997	4.174	5.088	5.532	0.025	0.64	
T (°C)	15	*t (ks)*	Nat	0.000	0.250	0.500	1.000	2.000	4.000	8.000	16.000	0.000	0.250	
Ḋ (Gy/s)	0.240	*Lₓ/Tₓ*	3.764	0.018	0.596	1.113	1.899	3.001	4.201	5.167	5.645	0.024	0.617	
T (°C)	15	*t (ks)*	Nat	0.000	0.250	0.500	1.000	2.000	4.000	8.000	16.000	0.000	0.250	
Ḋ (Gy/s)	0.240	*Lₓ/Tₓ*	3.742	0.018	0.621	1.121	1.907	3.049	4.229	5.294	5.777	0.024	0.593	
T (°C)	170	*t (ks)*	0.500	0.500	0.500	0.500	0.500	0.500	0.500	0.500	0.500	0.500	0.500	0.500
Ḋ (Gy/s)	0.119	*Lₓ/Tₓ*	0.926	0.942	0.962	0.963	0.932	0.941	0.942	0.926	0.881	0.934	0.938	0.903
T (°C)	190	*t (ks)*	0.500	0.500	0.500	0.500	0.500	0.500	0.500	0.500	0.500	0.500	0.500	0.500
Ḋ (Gy/s)	0.119	*Lₓ/Tₓ*	0.975	0.945	0.946	0.966	0.949	0.937	0.94	0.92	0.932	0.898	0.869	0.874
T (°C)	210	*t (ks)*	0.500	0.500	0.500	0.500	0.500	0.500	0.500	0.500	0.500	0.500	0.500	0.500
Ḋ (Gy/s)	0.119	*Lₓ/Tₓ*	0.946	0.931	0.965	0.947	0.924	0.937	0.945	0.905	0.885	0.863	0.803	0.726
T (°C)	230	*t (ks)*	0.500	0.500	0.500	0.500	0.500	0.500	0.500	0.500	0.500	0.500	0.500	0.500
Ḋ (Gy/s)	0.119	*Lₓ/Tₓ*	0.937	0.934	0.939	0.937	0.919	0.908	0.874	0.845	0.78	0.742	0.676	0.552
T (°C)	250	*t (ks)*	0.500	0.500	0.500	0.500	0.500	0.500	0.500	0.500	0.500	0.500	0.500	0.500
Ḋ (Gy/s)	0.119	*Lₓ/Tₓ*	0.947	0.92	0.957	0.907	0.867	0.878	0.811	0.747	0.647	0.553	0.452	0.342
T (°C)	300	*t (ks)*	0.500	0.500	0.500	0.500	0.500	0.500	0.500	0.500	0.500	0.500	0.500	0.500
Ḋ (Gy/s)	0.119	*Lₓ/Tₓ*	0.861	0.806	0.78	0.718	0.611	0.521	0.409	0.265	0.181	0.097	0.058	0.03
T (°C)	350	*t (ks)*	0.500	0.500	0.500	0.500	0.500	0.500	0.500	0.500				
Ḋ (Gy/s)	0.119	*Lₓ/Tₓ*	0.602	0.454	0.354	0.256	0.183	0.109	0.057	-0.002				
T (°C)	15	*t (ks)*	0.7704	9.6048	15.602	27.598	51.592	0.7704						
Ḋ (Gy/s)	0.119	*Lₓ/Tₓ*	0.942	0.935	0.937	0.935	0.928	0.957						
T (°C)	15	*t (ks)*	0.774	11.293	17.291	29.286	53.28	0.7704						
Ḋ (Gy/s)	0.119	*Lₓ/Tₓ*	0.935	0.931	0.914	0.919	0.907	0.941						
T (°C)	15	*t (ks)*	0.7704	12.982	18.979	30.978	54.972	0.7704						
Ḋ (Gy/s)	0.119	*Lₓ/Tₓ*	0.925	0.935	0.932	0.916	0.911	0.946						

Table C.8 Raw data of all IRSL$_{225}$ measurements for fault gouge sample Bt1BTY2, including fading and isothermal holding measurements.

Sample Bt1BTY2
Natural T (°C)
Natural Ḋ (Gy/ka)   3.94   0.25
Lab calibration:

T (°C)	15	*t (ks)*	Nat	0.000	0.250	0.500	1.000	2.000	4.000	8.000	16.000	0.000	0.250	
Ḋ (Gy/s)	0.240	*Lx/Tx*	3.337	0.028	0.614	1.087	1.762	2.628	3.415	3.885	4.36	0.033	0.614	
T (°C)	15	*t (ks)*	Nat	0.000	0.250	0.500	1.000	2.000	4.000	8.000	16.000	0.000	0.250	
Ḋ (Gy/s)	0.240	*Lx/Tx*	3.379	0.029	0.6	1.067	1.74	2.571	3.404	4.021	4.296	0.037	0.6	
T (°C)	15	*t (ks)*	Nat	0.000	0.250	0.500	1.000	2.000	4.000	8.000	16.000	0.000	0.250	
Ḋ (Gy/s)	0.240	*Lx/Tx*	3.37	0.028	0.604	1.061	1.749	2.608	3.492	4.142	4.477	0.037	0.611	
T (°C)	170	*t (ks)*	0.500	0.500	0.500	0.500	0.500	0.500	0.500	0.500	0.500	0.500	0.500	0.500
Ḋ (Gy/s)	0.119	*Lx/Tx*	0.91	0.914	0.898	0.902	0.904	0.898	0.909	0.893	0.881	0.886	0.903	0.851
T (°C)	190	*t (ks)*	0.500	0.500	0.500	0.500	0.500	0.500	0.500	0.500	0.500	0.500	0.500	0.500
Ḋ (Gy/s)	0.119	*Lx/Tx*	0.908	0.885	0.902	0.901	0.915	0.886	0.878	0.887	0.869	0.852	0.836	0.833
T (°C)	210	*t (ks)*	0.500	0.500	0.500	0.500	0.500	0.500	0.500	0.500	0.500	0.500	0.500	0.500
Ḋ (Gy/s)	0.119	*Lx/Tx*	0.885	0.92	0.917	0.891	0.888	0.903	0.887	0.882	0.842	0.829	0.787	0.762
T (°C)	230	*t (ks)*	0.500	0.500	0.500	0.500	0.500	0.500	0.500	0.500	0.500	0.500	0.500	0.500
Ḋ (Gy/s)	0.119	*Lx/Tx*	0.912	0.902	0.885	0.905	0.893	0.856	0.859	0.82	0.801	0.77	0.73	0.666
T (°C)	250	*t (ks)*	0.500	0.500	0.500	0.500	0.500	0.500	0.500	0.500	0.500	0.500	0.500	0.500
Ḋ (Gy/s)	0.119	*Lx/Tx*	0.906	0.917	0.885	0.873	0.858	0.847	0.817	0.787	0.744	0.677	0.606	0.515
T (°C)	300	*t (ks)*	0.500	0.500	0.500	0.500	0.500	0.500	0.500	0.500	0.500	0.500	0.500	0.500
Ḋ (Gy/s)	0.119	*Lx/Tx*	0.819	0.834	0.82	0.779	0.734	0.67	0.573	0.477	0.354	0.274	0.185	0.106
T (°C)	350	*t (ks)*	0.500	0.500	0.500	0.500	0.500	0.500	0.500	0.500				
Ḋ (Gy/s)	0.119	*Lx/Tx*	0.669	0.612	0.543	0.449	0.368	0.256	0.172	0.001				
T (°C)	15	*t (ks)*	0.9828	9.8136	15.811	27.806	51.8	0.9828						
Ḋ (Gy/s)	0.119	*Lx/Tx*	0.874	0.894	0.873	0.862	0.898	0.908						
T (°C)	15	*t (ks)*	0.9864	11.502	17.5	29.498	53.489	0.9828						
Ḋ (Gy/s)	0.119	*Lx/Tx*	0.887	0.894	0.879	0.892	0.876	0.903						
T (°C)	15	*t (ks)*	0.9828	13.19	19.188	31.187	55.181	0.9828						
Ḋ (Gy/s)	0.119	*Lx/Tx*	0.901	0.899	0.876	0.89	0.883	0.905						

Table C.9 Raw data of all IRSL$_{50}$ measurements for fault gouge sample BT19FG, including fading and isothermal holding measurements.

Sample BT19FG
Natural T (°C)
Natural $\dot{D}$ (Gy/ka)   3.42   0.15
Lab calibration:

T (°C)	15	*t (ks)*	Nat	0.000	0.500	1.000	2.000	4.000	8.000	16.000	32.000	0.000	0.500	
$\dot{D}$ (Gy/s)	0.119	*L_x/T_x*	4.724	0.007	1.19	2.16	3.785	5.929	8.31	10.15	10.828	0.015	1.219	
T (°C)	15	*t (ks)*	Nat	0.000	0.500	1.000	2.000	4.000	8.000	16.000	32.000	0.000	0.500	
$\dot{D}$ (Gy/s)	0.119	*L_x/T_x*	4.68	0.011	1.202	2.27	3.814	5.939	8.308	10.196	10.833	0.018	1.206	
T (°C)	15	*t (ks)*	Nat	0.000	0.500	1.000	2.000	4.000	8.000	16.000	32.000	0.000	0.500	
$\dot{D}$ (Gy/s)	0.119	*L_x/T_x*	4.33	0.008	1.200	2.199	3.736	5.96	8.182	10.135	10.577	0.012	1.208	
T (°C)	170	*t (ks)*	0.500	0.500	0.500	0.500	0.500	0.500	0.500	0.500	0.500	0.500	0.500	0.500
$\dot{D}$ (Gy/s)	0.119	*L_x/T_x*	0.958	0.965	0.94	0.963	0.953	0.961	0.952	0.927	0.912	0.893	0.86	0.804
T (°C)	190	*t (ks)*	0.500	0.500	0.500	0.500	0.500	0.500	0.500	0.500	0.500	0.500	0.500	0.500
$\dot{D}$ (Gy/s)	0.119	*L_x/T_x*	0.967	0.945	0.96	0.965	0.94	0.949	0.932	0.903	0.876	0.821	0.739	0.655
T (°C)	210	*t (ks)*	0.500	0.500	0.500	0.500	0.500	0.500	0.500	0.500	0.500	0.500	0.500	0.500
$\dot{D}$ (Gy/s)	0.119	*L_x/T_x*	0.968	0.953	0.939	0.938	0.934	0.9	0.876	0.819	0.744	0.638	0.535	0.421
T (°C)	230	*t (ks)*	0.500	0.500	0.500	0.500	0.500	0.500	0.500	0.500	0.500	0.500	0.500	0.500
$\dot{D}$ (Gy/s)	0.119	*L_x/T_x*	0.955	0.95	0.944	0.907	0.877	0.821	0.735	0.629	0.529	0.402	0.308	0.215
T (°C)	250	*t (ks)*	0.500	0.500	0.500	0.500	0.500	0.500	0.500	0.500	0.500	0.500	0.500	0.500
$\dot{D}$ (Gy/s)	0.119	*L_x/T_x*	0.951	0.926	0.873	0.831	0.763	0.646	0.542	0.417	0.321	0.241	0.16	0.105
T (°C)	300	*t (ks)*	0.500	0.500	0.500	0.500	0.500	0.500	0.500	0.500	0.500	0.500	0.500	0.500
$\dot{D}$ (Gy/s)	0.119	*L_x/T_x*	0.745	0.585	0.496	0.386	0.285	0.2	0.133	0.082	0.049	0.022	0.011	0.004
T (°C)	350	*t (ks)*	0.500	0.500	0.500	0.500	0.500	0.500	0.500	0.500				
$\dot{D}$ (Gy/s)	0.119	*L_x/T_x*	0.307	0.162	0.123	0.079	0.042	0.02	0.007	0.001				
T (°C)	15	*t (ks)*	0.414	9.2592	15.253	27.252	51.242	0.414						
$\dot{D}$ (Gy/s)	0.119	*L_x/T_x*	0.963	0.941	0.916	0.9	0.896	0.964						
T (°C)	15	*t (ks)*	0.414	10.955	16.942	28.94	52.931	0.414						
$\dot{D}$ (Gy/s)	0.119	*L_x/T_x*	0.966	0.934	0.912	0.912	0.907	0.961						
T (°C)	15	*t (ks)*	0.414	12.647	18.634	30.632	54.623	0.414						
$\dot{D}$ (Gy/s)	0.119	*L_x/T_x*	0.97	0.922	0.912	0.906	0.878	0.966						

Table C.10 Raw data of all IRSL$_{100}$ measurements for fault gouge sample BT19FG, including fading and isothermal holding measurements.

Sample BT19FG
Natural T (°C)
Natural Ḋ (Gy/ka)   3.42   0.15
Lab calibration:

T (°C)	15	*t (ks)*	Nat	0.000	0.500	1.000	2.000	4.000	8.000	16.000	32.000	0.000	0.500	
Ḋ (Gy/s)	0.119	*Lx/Tx*	5.401	0.039	1.173	2.115	3.522	5.767	7.834	9.291	10.144	0.045	1.202	
T (°C)	15	*t (ks)*	Nat	0.000	0.500	1.000	2.000	4.000	8.000	16.000	32.000	0.000	0.500	
Ḋ (Gy/s)	0.119	*Lx/Tx*	5.454	0.043	1.152	2.125	3.607	5.517	7.929	9.755	10.477	0.059	1.176	
T (°C)	15	*t (ks)*	Nat	0.000	0.500	1.000	2.000	4.000	8.000	16.000	32.000	0.000	0.500	
Ḋ (Gy/s)	0.119	*Lx/Tx*	5.407	0.038	1.205	2.137	3.646	5.702	7.865	9.432	9.751	0.048	1.212	
T (°C)	170	*t (ks)*	0.500	0.500	0.500	0.500	0.500	0.500	0.500	0.500	0.500	0.500	0.500	0.500
Ḋ (Gy/s)	0.119	*Lx/Tx*	0.98	0.965	0.945	1.003	0.941	0.985	0.954	0.943	0.916	0.931	0.924	0.881
T (°C)	190	*t (ks)*	0.500	0.500	0.500	0.500	0.500	0.500	0.500	0.500	0.500	0.500	0.500	0.500
Ḋ (Gy/s)	0.119	*Lx/Tx*	0.957	0.96	0.957	0.969	0.965	0.949	0.944	0.923	0.91	0.827	0.823	0.758
T (°C)	210	*t (ks)*	0.500	0.500	0.500	0.500	0.500	0.500	0.500	0.500	0.500	0.500	0.500	0.500
Ḋ (Gy/s)	0.119	*Lx/Tx*	0.96	0.972	0.96	0.961	0.922	0.905	0.894	0.895	0.801	0.755	0.667	0.556
T (°C)	230	*t (ks)*	0.500	0.500	0.500	0.500	0.500	0.500	0.500	0.500	0.500	0.500	0.500	0.500
Ḋ (Gy/s)	0.119	*Lx/Tx*	0.962	0.973	0.956	0.918	0.892	0.87	0.835	0.762	0.664	0.576	0.466	0.311
T (°C)	250	*t (ks)*	0.500	0.500	0.500	0.500	0.500	0.500	0.500	0.500	0.500	0.500	0.500	0.500
Ḋ (Gy/s)	0.119	*Lx/Tx*	0.922	0.939	0.898	0.885	0.817	0.763	0.689	0.559	0.456	0.372	0.258	0.173
T (°C)	300	*t (ks)*	0.500	0.500	0.500	0.500	0.500	0.500	0.500	0.500	0.500	0.500	0.500	0.500
Ḋ (Gy/s)	0.119	*Lx/Tx*	0.859	0.736	0.655	0.555	0.439	0.311	0.228	0.132	0.097	0.036	0.022	0.004
T (°C)	350	*t (ks)*	0.500	0.500	0.500	0.500	0.500	0.500	0.500	0.500				
Ḋ (Gy/s)	0.119	*Lx/Tx*	0.459	0.282	0.205	0.128	0.085	0.024	0.019	0.003				
T (°C)	15	*t (ks)*	0.5832	9.4212	15.415	27.414	51.404	0.5832						
Ḋ (Gy/s)	0.119	*Lx/Tx*	0.939	0.943	0.956	0.938	0.928	0.948						
T (°C)	15	*t (ks)*	0.5832	11.117	17.107	29.102	53.093	0.5832						
Ḋ (Gy/s)	0.119	*Lx/Tx*	0.939	0.939	0.934	0.914	0.918	0.935						
T (°C)	15	*t (ks)*	0.5832	12.809	18.796	30.794	54.785	0.5832						
Ḋ (Gy/s)	0.119	*Lx/Tx*	0.961	0.947	0.935	0.917	0.93	0.963						

Table C.11 Raw data of all IRSL$_{150}$ measurements for fault gouge sample BT19FG, including fading and isothermal holding measurements.

Sample BT19FG
Natural T (°C)
Natural Ḋ (Gy/ka)   3.42   0.15
Lab calibration:

T (°C)	15	*t (ks)*	Nat	0.000	0.500	1.000	2.000	4.000	8.000	16.000	32.000	0.000	0.500	
Ḋ (Gy/s)	0.119	*Lx/Tx*	6.253	0.046	1.129	2.1	3.539	5.703	7.77	9.325	10.262	0.066	1.184	
T (°C)	15	*t (ks)*	Nat	0.000	0.500	1.000	2.000	4.000	8.000	16.000	32.000	0.000	0.500	
Ḋ (Gy/s)	0.119	*Lx/Tx*	6.493	0.056	1.145	2.134	3.579	5.59	7.714	9.54	10.478	0.075	1.138	
T (°C)	15	*t (ks)*	Nat	0.000	0.500	1.000	2.000	4.000	8.000	16.000	32.000	0.000	0.500	
Ḋ (Gy/s)	0.119	*Lx/Tx*	6.269	0.049	1.189	2.160	3.559	5.605	7.793	9.443	10.114	0.065	1.245	
T (°C)	170	*t (ks)*	0.500	0.500	0.500	0.500	0.500	0.500	0.500	0.500	0.500	0.500	0.500	0.500
Ḋ (Gy/s)	0.119	*Lx/Tx*	0.952	0.929	0.997	0.954	0.946	0.938	0.956	0.940	0.958	0.942	0.947	0.888
T (°C)	190	*t (ks)*	0.500	0.500	0.500	0.500	0.500	0.500	0.500	0.500	0.500	0.500	0.500	0.500
Ḋ (Gy/s)	0.119	*Lx/Tx*	0.936	0.948	0.946	0.949	0.934	0.928	0.936	0.956	0.909	0.908	0.86	0.826
T (°C)	210	*t (ks)*	0.500	0.500	0.500	0.500	0.500	0.500	0.500	0.500	0.500	0.500	0.500	0.500
Ḋ (Gy/s)	0.119	*Lx/Tx*	0.954	0.942	0.941	0.965	0.927	0.939	0.96	0.936	0.873	0.84	0.771	0.677
T (°C)	230	*t (ks)*	0.500	0.500	0.500	0.500	0.500	0.500	0.500	0.500	0.500	0.500	0.500	0.500
Ḋ (Gy/s)	0.119	*Lx/Tx*	0.935	0.942	0.987	0.93	0.912	0.903	0.876	0.844	0.782	0.695	0.601	0.484
T (°C)	250	*t (ks)*	0.500	0.500	0.500	0.500	0.500	0.500	0.500	0.500	0.500	0.500	0.500	0.500
Ḋ (Gy/s)	0.119	*Lx/Tx*	0.948	0.938	0.929	0.903	0.867	0.815	0.766	0.683	0.64	0.51	0.415	0.285
T (°C)	300	*t (ks)*	0.500	0.500	0.500	0.500	0.500	0.500	0.500	0.500	0.500	0.500	0.500	0.500
Ḋ (Gy/s)	0.119	*Lx/Tx*	0.86	0.804	0.779	0.676	0.606	0.504	0.376	0.253	0.157	0.086	0.045	0.014
T (°C)	350	*t (ks)*	0.500	0.500	0.500	0.500	0.500	0.500	0.500	0.500				
Ḋ (Gy/s)	0.119	*Lx/Tx*	0.564	0.423	0.326	0.255	0.15	0.077	0.034	0.005				
T (°C)	15	*t (ks)*	0.7704	9.6084	15.602	27.601	51.592	0.7704						
Ḋ (Gy/s)	0.119	*Lx/Tx*	0.934	0.965	0.958	0.938	0.94	0.972						
T (°C)	15	*t (ks)*	0.7704	11.304	17.291	29.29	53.28	0.7704						
Ḋ (Gy/s)	0.119	*Lx/Tx*	0.95	0.932	0.929	0.917	0.916	0.942						
T (°C)	15	*t (ks)*	0.7704	12.996	18.983	30.978	54.972	0.7704						
Ḋ (Gy/s)	0.119	*Lx/Tx*	0.956	0.936	0.934	0.942	0.915	0.958						

Table C.12 Raw data of all IRSL$_{225}$ measurements for fault gouge sample BT19FG, including fading and isothermal holding measurements.

Sample BT19FG
Natural T (°C)
Natural Ḋ (Gy/ka)   3.42   0.15
Lab calibration:

T (°C)	15	*t (ks)*	Nat	0.000	0.500	1.000	2.000	4.000	8.000	16.000	32.000	0.000	0.500	
Ḋ (Gy/s)	0.119	*Lx/Tx*	5.587	0.068	1.175	1.949	3.139	4.616	6.032	7.087	7.371	0.096	1.135	
T (°C)	15	*t (ks)*	Nat	0.000	0.500	1.000	2.000	4.000	8.000	16.000	32.000	0.000	0.500	
Ḋ (Gy/s)	0.119	*Lx/Tx*	5.619	0.078	1.111	1.968	3.101	4.436	5.749	6.686	7.064	0.108	1.128	
T (°C)	15	*t (ks)*	Nat	0.000	0.500	1.000	2.000	4.000	8.000	16.000	32.000	0.000	0.500	
Ḋ (Gy/s)	0.119	*Lx/Tx*	5.879	0.067	1.166	1.963	3.208	4.675	6.079	7.107	7.475	0.084	1.23	
T (°C)	170	*t (ks)*	0.500	0.500	0.500	0.500	0.500	0.500	0.500	0.500	0.500	0.500	0.500	0.500
Ḋ (Gy/s)	0.119	*Lx/Tx*	0.92	0.932	0.947	0.934	0.918	0.924	0.919	0.893	0.888	0.919	0.887	0.865
T (°C)	190	*t (ks)*	0.500	0.500	0.500	0.500	0.500	0.500	0.500	0.500	0.500	0.500	0.500	0.500
Ḋ (Gy/s)	0.119	*Lx/Tx*	0.938	0.924	0.926	0.933	0.907	0.93	0.929	0.895	0.886	0.906	0.847	0.843
T (°C)	210	*t (ks)*	0.500	0.500	0.500	0.500	0.500	0.500	0.500	0.500	0.500	0.500	0.500	0.500
Ḋ (Gy/s)	0.119	*Lx/Tx*	0.937	0.926	0.913	0.935	0.911	0.926	0.907	0.887	0.856	0.837	0.811	0.769
T (°C)	230	*t (ks)*	0.500	0.500	0.500	0.500	0.500	0.500	0.500	0.500	0.500	0.500	0.500	0.500
Ḋ (Gy/s)	0.119	*Lx/Tx*	0.907	0.923	0.915	0.91	0.914	0.891	0.87	0.875	0.821	0.761	0.74	0.661
T (°C)	250	*t (ks)*	0.500	0.500	0.500	0.500	0.500	0.500	0.500	0.500	0.500	0.500	0.500	0.500
Ḋ (Gy/s)	0.119	*Lx/Tx*	0.925	0.937	0.89	0.878	0.882	0.853	0.817	0.783	0.747	0.7	0.592	0.497
T (°C)	300	*t (ks)*	0.500	0.500	0.500	0.500	0.500	0.500	0.500	0.500	0.500	0.500	0.500	0.500
Ḋ (Gy/s)	0.119	*Lx/Tx*	0.87	0.847	0.832	0.804	0.732	0.679	0.571	0.473	0.37	0.236	0.159	0.089
T (°C)	350	*t (ks)*	0.500	0.500	0.500	0.500	0.500	0.500	0.500	0.500				
Ḋ (Gy/s)	0.119	*Lx/Tx*	0.734	0.596	0.554	0.458	0.347	0.234	0.147	0.003				
T (°C)	15	*t (ks)*	0.9792	9.8172	15.811	27.81	51.8	0.9828						
Ḋ (Gy/s)	0.119	*Lx/Tx*	0.925	0.946	0.911	0.916	0.91	0.921						
T (°C)	15	*t (ks)*	0.9828	11.509	17.5	29.498	53.489	0.9828						
Ḋ (Gy/s)	0.119	*Lx/Tx*	0.912	0.899	0.911	0.893	0.879	0.923						
T (°C)	15	*t (ks)*	0.9828	13.205	19.192	31.19	55.181	0.9828						
Ḋ (Gy/s)	0.119	*Lx/Tx*	0.94	0.932	0.922	0.921	0.914	0.923						

APPENDIX D. Rock Surface Dating Analysis
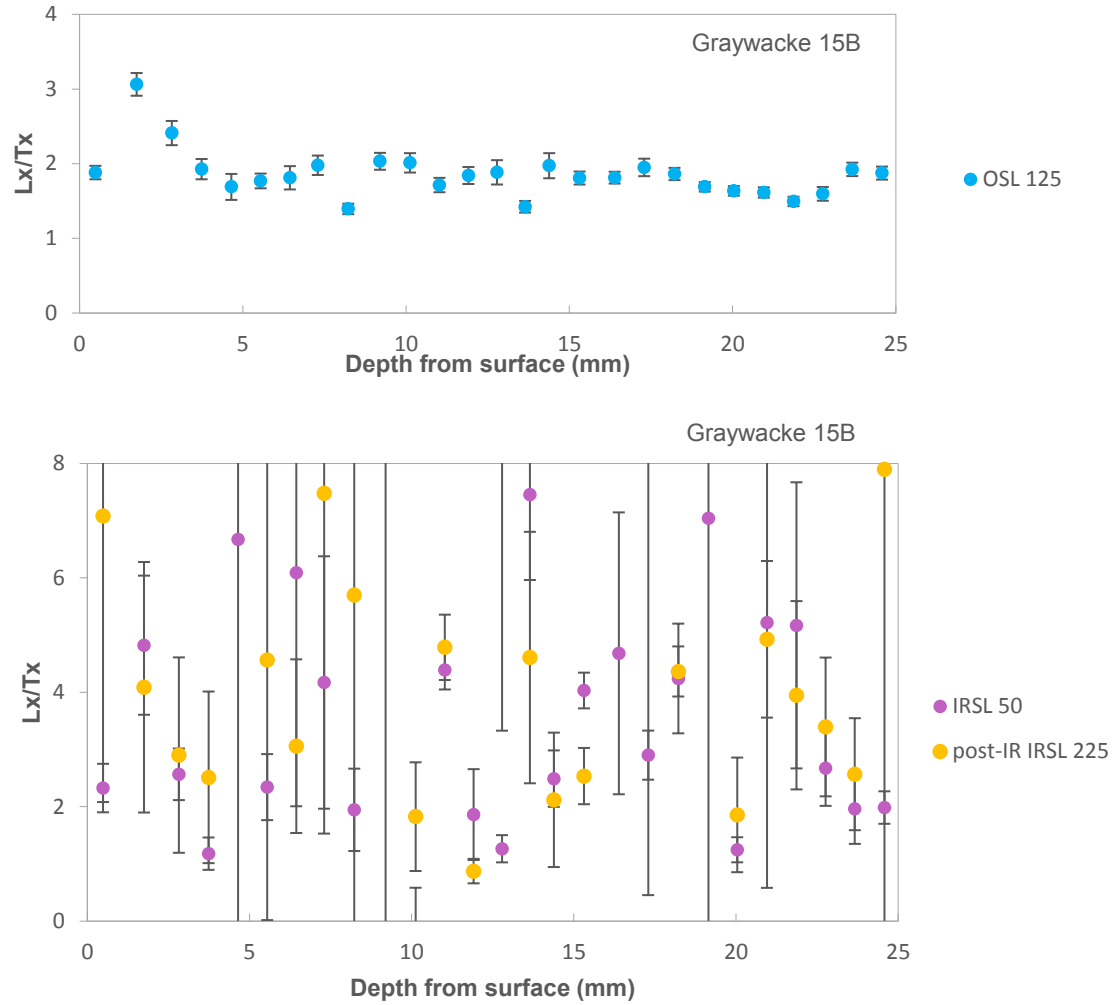
Figure D.1 L_x/T_x ratios with depth into cobbles for OSL_{125}, $IRSL_{50}$, and post-IR $IRSL_{225}$ signals, shown for initial investigations using the first sliced core of graywacke cobble 15B.
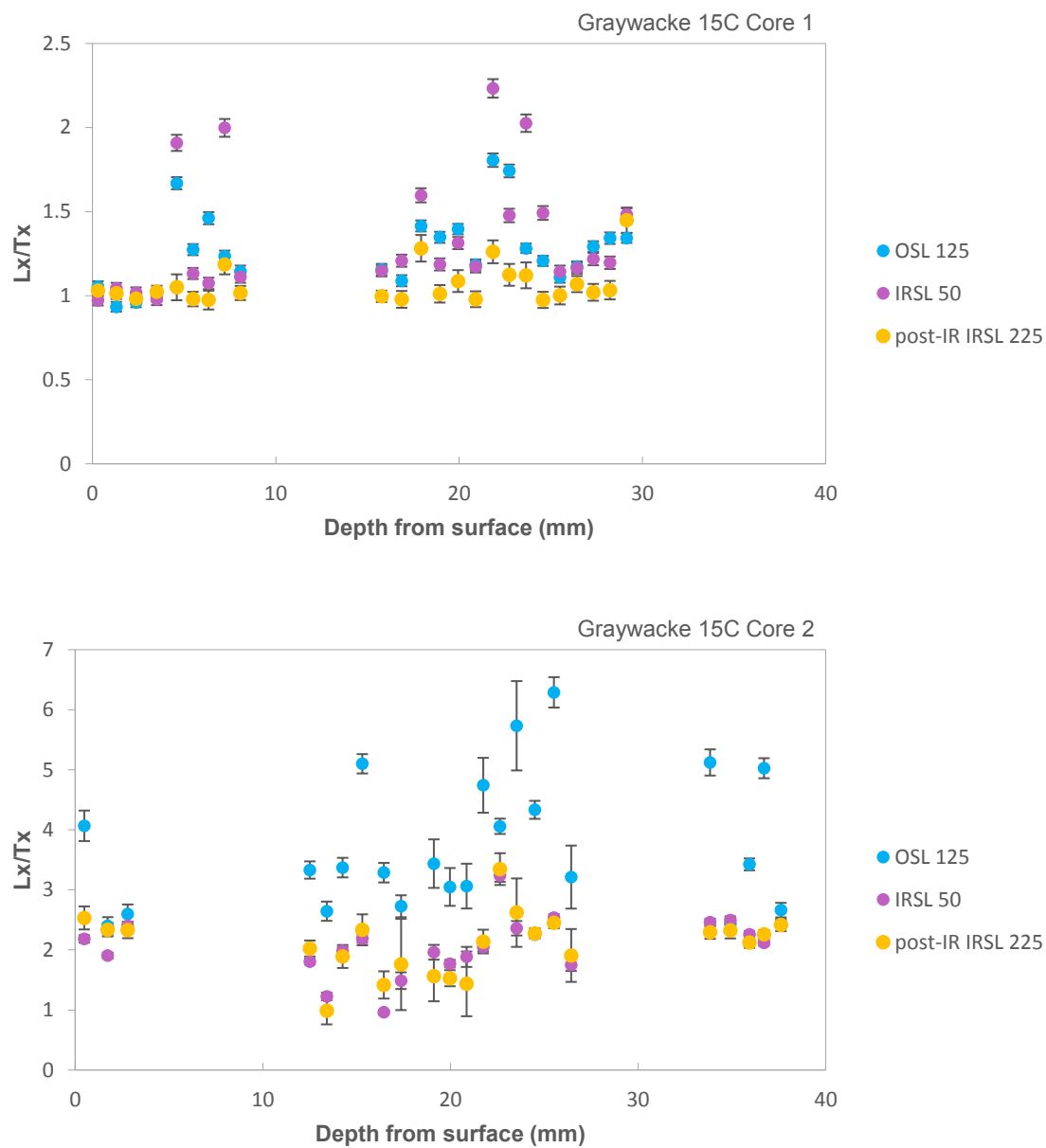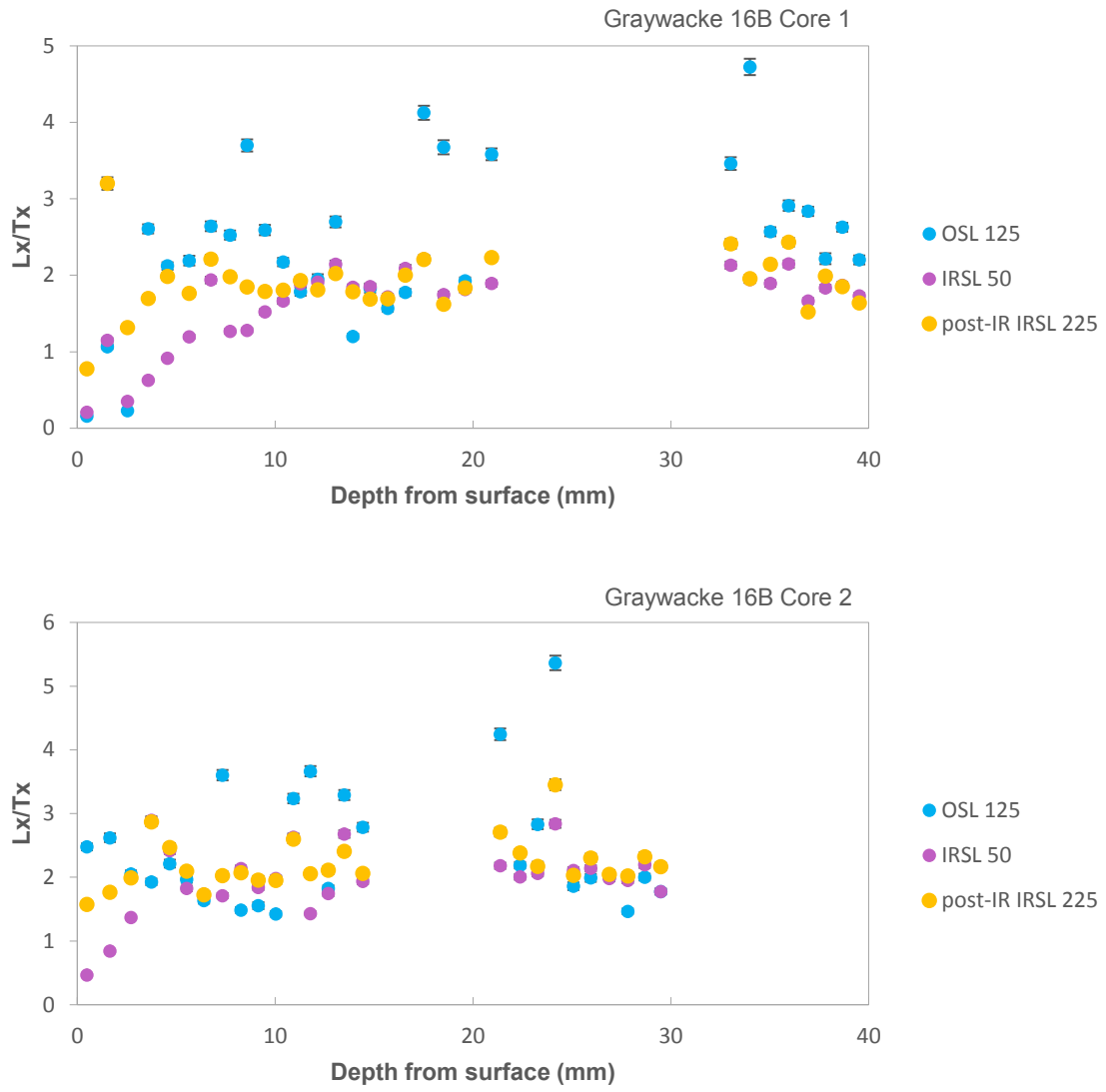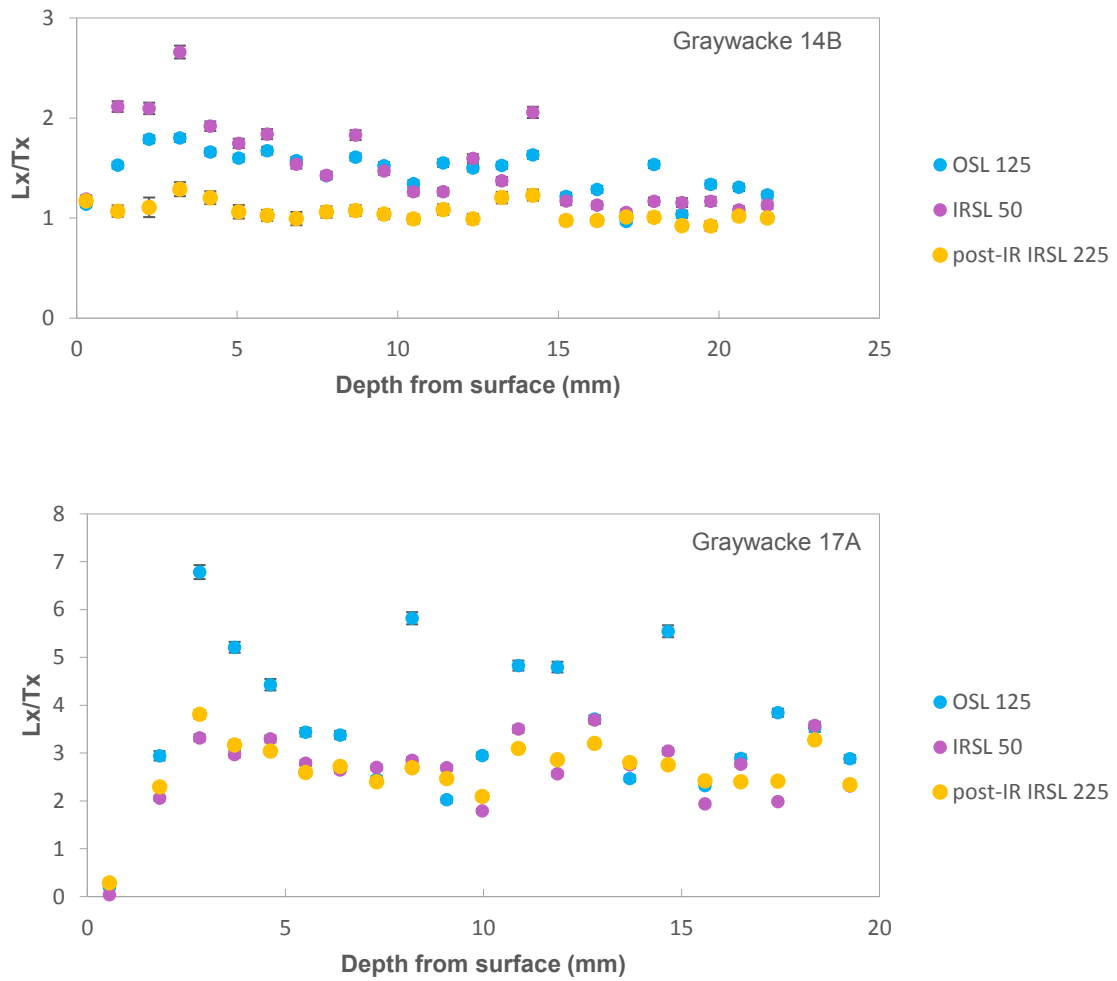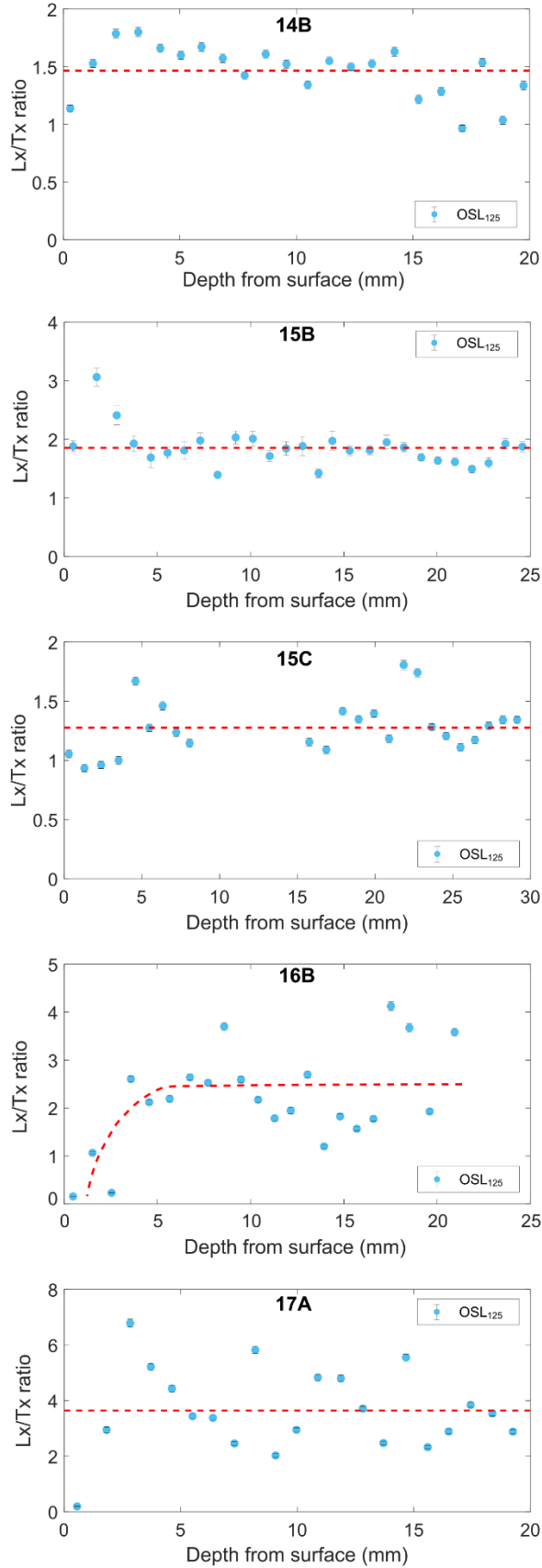
Figure D.2 L_x/T_x ratios with depth into cobbles for OSL_{125}, $IRSL_{50}$, and post-IR $IRSL_{225}$ signals, shown for initial investigations using the first sliced core of graywacke cobble 15C. Since this cobble is fragile, its two cobble cores were measured to compare the L_x/T_x ratio changes in each signal with depth.

Figure D.3 L_x/T_x ratios with depth into cobbles for OSL_{125}, $IRSL_{50}$, and post-IR $IRSL_{225}$ signals, shown for initial investigations using the first sliced core of graywacke cobble 16B. Since this cobble is fragile, its two cobble cores were measured to compare the L_x/T_x ratio changes in each signal with depth.

Figure D.4 L_x/T_x ratios with depth into cobbles for OSL_{125}, $IRSL_{50}$, and post-IR $IRSL_{225}$ signals, shown for initial investigations using the first sliced core of graywacke cobbles 14B and 17A.

Figure D.5 Luminescence-depth profile generated for the OSL_{125} signal from each graywacke cobble (14B, 15B, 15C, 16B, and 17A) and for initial investigations. Each profile is constructed using the first sliced core and illustrated as the red dashed line.
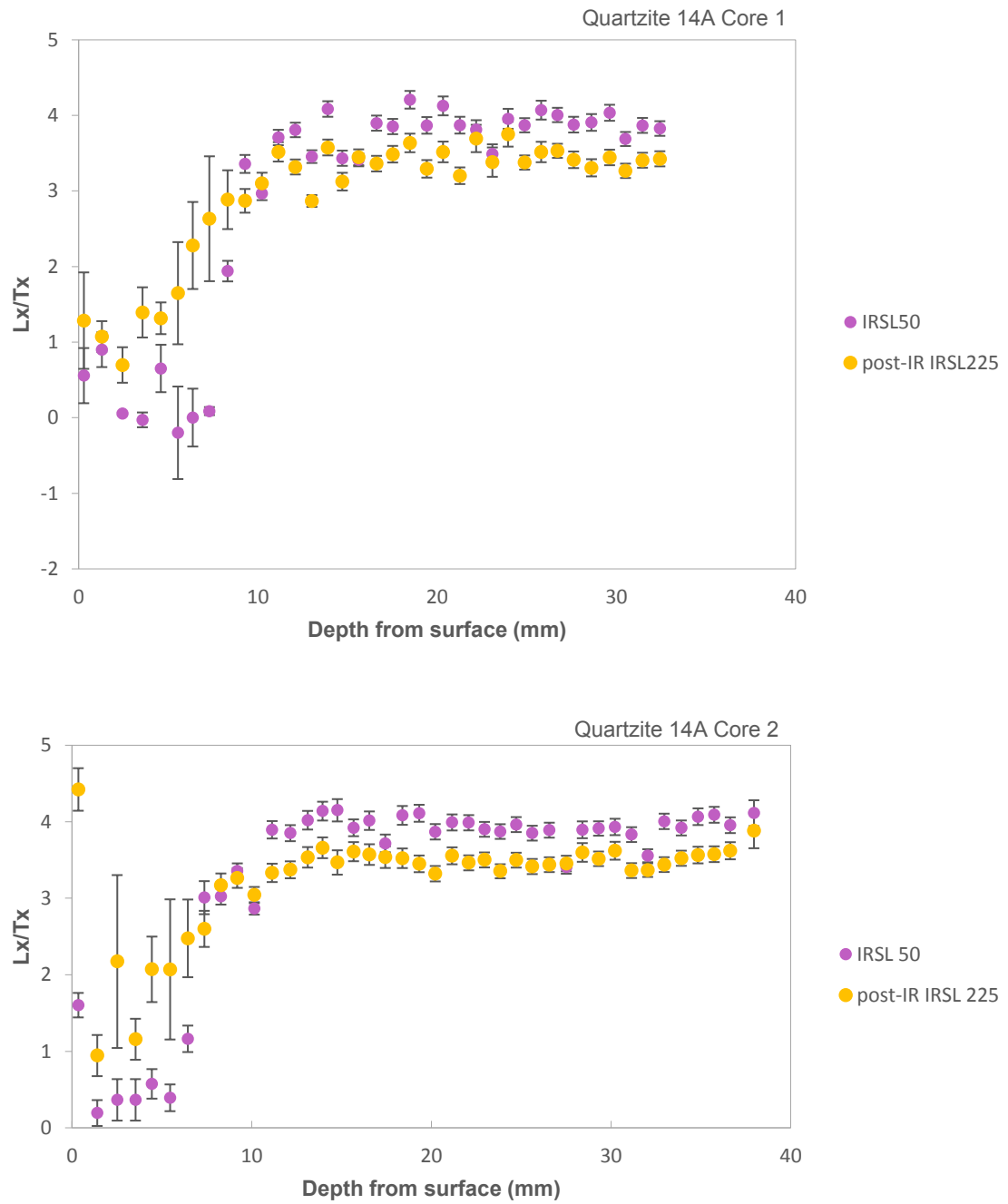
Figure D.6 L_x/T_x ratios with depth into cobbles for $IRSL_{50}$ and post-IR $IRSL_{225}$ signals, shown with large errors, for quartzite cobble 14A.
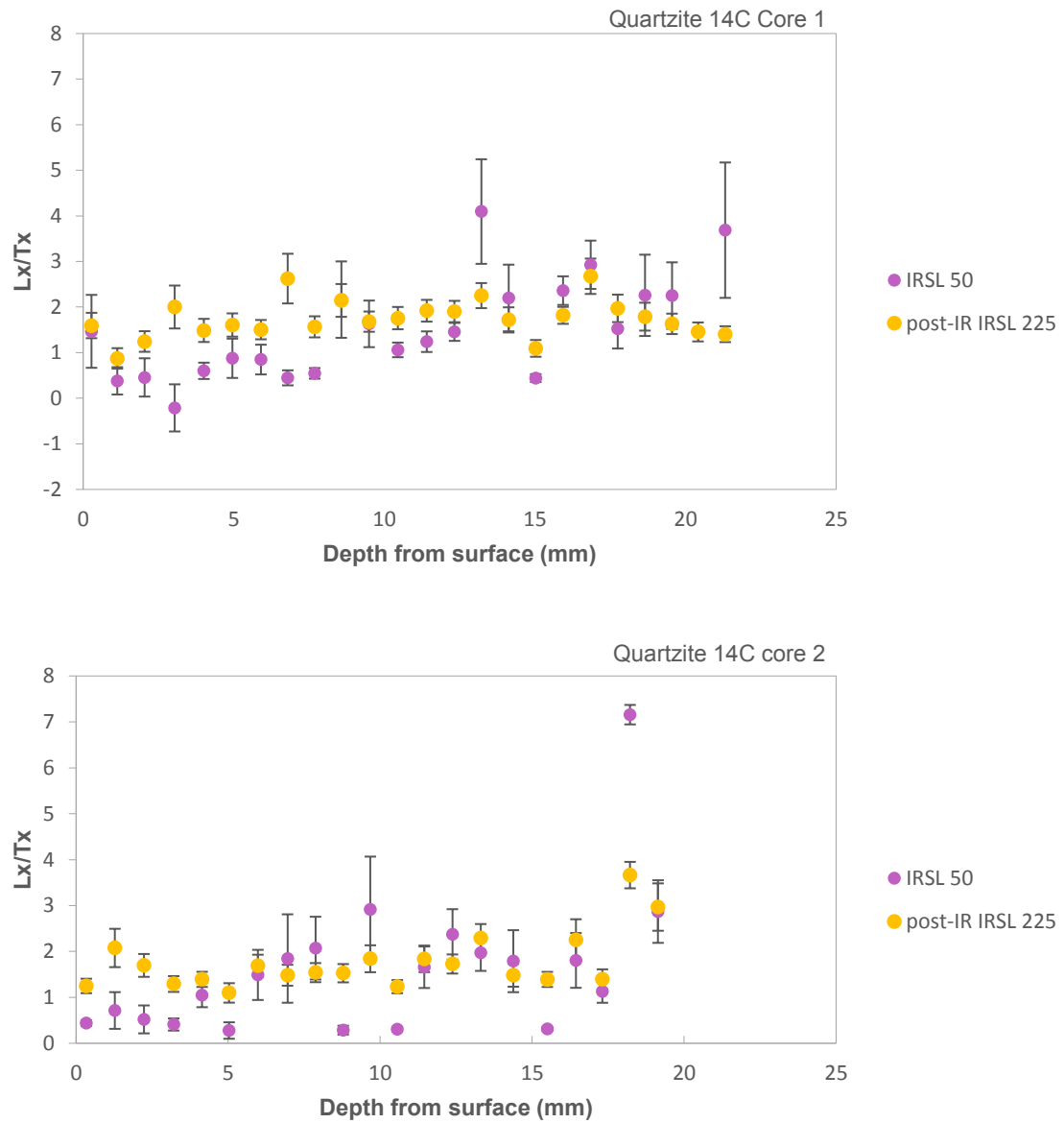
Figure D.7 L_x/T_x ratios with depth into cobbles for IRSL$_{50}$ and post-IR IRSL$_{225}$ signals, shown with large errors, for quartzite cobble 14C.
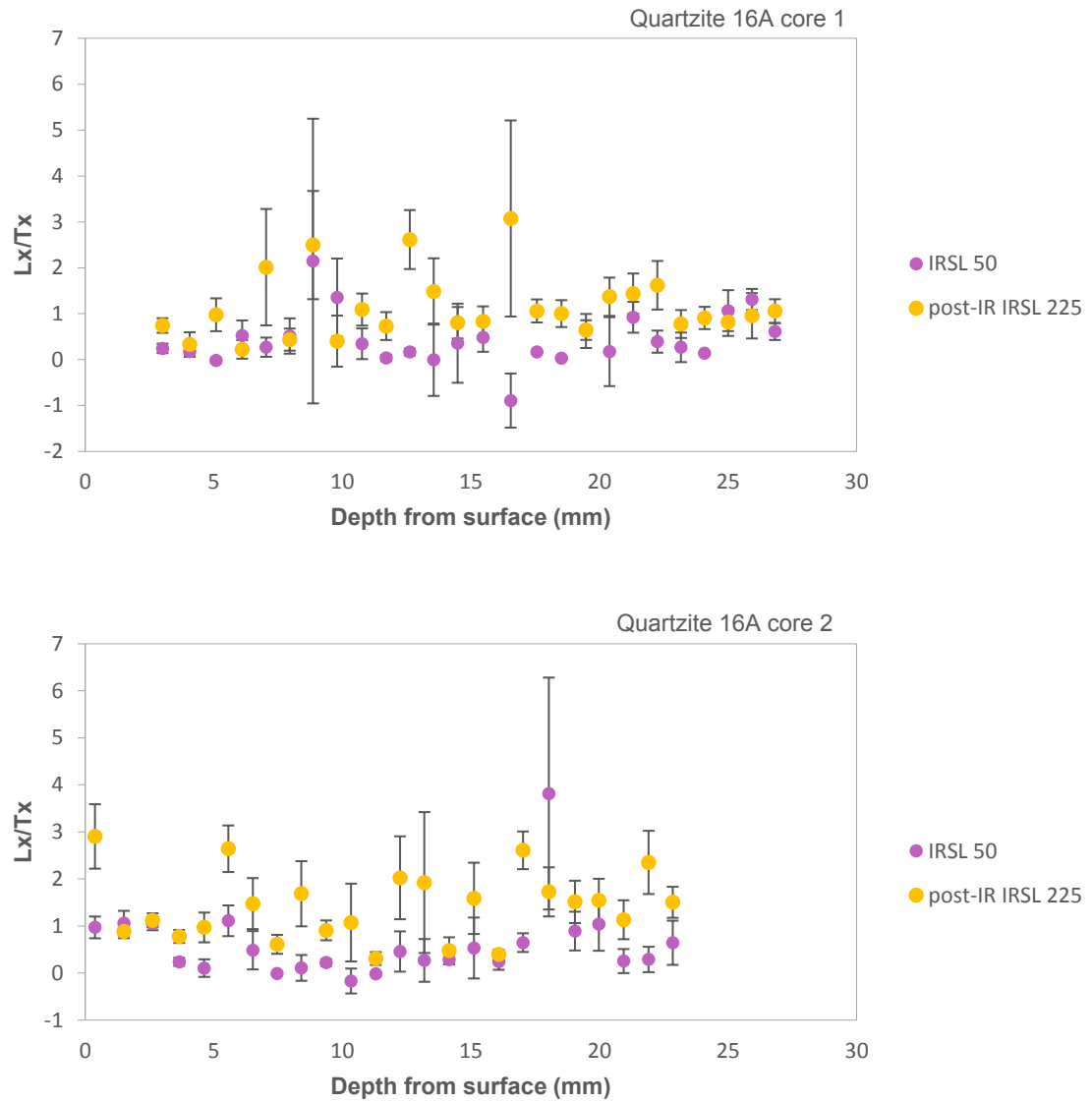
Figure D.8 L_x/T_x ratios with depth into cobbles for IRSL$_{50}$ and post-IR IRSL$_{225}$ signals, shown with large errors, for quartzite cobble 16A.

Table D.1 Luminescence OSL$_{125}$ age calculation for each slice of each cobble core.

Core-slice	x (mm)	h (mm)	DR-β	ErrDR-β	DR-γ	ErrDR-γ	DR-α	ErrDR-α	Int.-β	Err Int.-β	DR-c	ErrDR-c	Total DR	Err Total DR	De (Gy)	err De (Gy)	Age (ka)	errAge (ka)
14A-1-1	0.285	37.74	0.80383	0.03320	1.18449	0.04893	0.00536	0.00252	0.263	0.09	0.068	0.007	2.325	0.108	51.415	8.800	22.117	3.922
14A-1-2	1.295	37.74	0.71694	0.00523	1.18351	0.04884	0.00541	0.00255	0.263	0.09	0.068	0.007	2.237	0.103	59.518	10.187	26.608	4.716
14A-1-3	2.443	37.74	0.70369	0.00206	1.18247	0.04875	0.00547	0.00257	0.263	0.09	0.068	0.007	2.223	0.103	77.436	11.811	34.840	5.552
14A-2-1	0.350	43.67	0.79200	0.02935	1.17167	0.04780	0.00604	0.00284	0.263	0.09	0.068	0.007	2.301	0.106	47.734	6.106	20.747	2.822
14A-2-2	1.403	43.67	0.71418	0.00441	1.17052	0.04770	0.00610	0.00287	0.263	0.09	0.068	0.007	2.222	0.102	111.154	12.950	50.029	6.267
14A-2-3	2.515	43.67	0.70347	0.00205	1.16937	0.04760	0.00616	0.00290	0.263	0.09	0.068	0.007	2.210	0.102	74.626	6.614	33.767	3.375
14C-1-3	2.040	34.64	0.21477	0.00120	1.12218	0.04935	0.00164	0.00075	0.078	0.025	0.068	0.007	1.485	0.056	73.207	7.161	49.311	5.167
14C-1-4	3.040	34.64	0.20731	0.00027	1.12082	0.04928	0.00165	0.00075	0.078	0.025	0.068	0.007	1.476	0.056	79.932	11.234	54.162	7.882
14C-1-5	4.010	34.64	0.20621	0.00020	1.11958	0.04921	0.00167	0.00076	0.078	0.025	0.068	0.007	1.473	0.056	79.027	11.310	53.634	7.939
14C-2-3	2.233	32.435	0.21208	0.00084	1.13077	0.04981	0.00156	0.00071	0.078	0.025	0.068	0.007	1.490	0.056	70.138	7.094	47.059	5.080
14C-2-4	3.210	32.435	0.20695	0.00024	1.12953	0.04974	0.00157	0.00071	0.078	0.025	0.068	0.007	1.484	0.056	102.247	8.814	68.898	6.485
14C-2-5	4.145	32.435	0.20616	0.00020	1.12843	0.04968	0.00158	0.00072	0.078	0.025	0.068	0.007	1.482	0.056	93.334	6.973	62.971	5.273
16A-1-3	3.008	35.105	0.10508	0.00037	1.12849	0.07631	0.00106	0.00046	0.04	0.011	0.106	0.011	1.381	0.078	25.366	3.882	18.372	2.997
16A-1-4	4.065	35.105	0.10328	0.00020	1.12699	0.07620	0.00107	0.00046	0.04	0.011	0.106	0.011	1.377	0.078	19.051	2.941	13.832	2.274
16A-1-5	5.090	35.105	0.10304	0.00020	1.12565	0.07610	0.00108	0.00046	0.04	0.011	0.106	0.011	1.376	0.078	30.281	2.719	22.010	2.335
16A-1-6	6.105	35.105	0.10301	0.00020	1.12442	0.07601	0.00109	0.00047	0.04	0.011	0.106	0.011	1.375	0.078	12.649	1.727	9.203	1.359
16A-1-7	7.040	35.105	0.10300	0.00020	1.12339	0.07593	0.00109	0.00047	0.04	0.011	0.106	0.011	1.373	0.078	34.660	7.217	25.235	5.444
16A-2-1	0.383	33.17	0.40735	0.04496	1.14098	0.07725	0.00099	0.00043	0.04	0.011	0.106	0.011	1.695	0.091	17.866	2.408	10.538	1.528
16A-2-2	1.505	33.17	0.13907	0.00533	1.13919	0.07712	0.00100	0.00043	0.04	0.011	0.106	0.011	1.425	0.079	14.801	1.779	10.385	1.374
16A-2-3	2.623	33.17	0.10732	0.00067	1.13753	0.07699	0.00101	0.00043	0.04	0.011	0.106	0.011	1.392	0.079	18.185	2.277	13.065	1.794
16A-2-4	3.655	33.17	0.10361	0.00022	1.13612	0.07689	0.00102	0.00044	0.04	0.011	0.106	0.011	1.387	0.078	10.817	3.039	7.801	2.236
16A-2-6	5.568	33.17	0.10302	0.00020	1.13378	0.07671	0.00103	0.00044	0.04	0.011	0.106	0.011	1.384	0.078	15.124	3.532	10.929	2.626
16A-2-7	6.515	33.17	0.10300	0.00020	1.13277	0.07663	0.00104	0.00045	0.04	0.011	0.106	0.011	1.383	0.078	13.037	2.390	9.428	1.809

Equation 3.12 is used for the dose rate calculation at a certain slice.

x – depth into cobble in mm; h – thickness of cobble in mm.

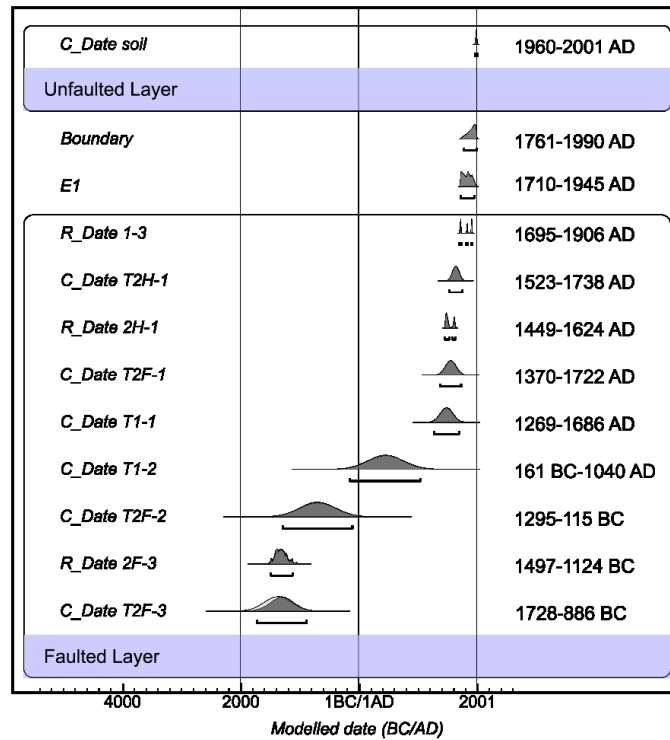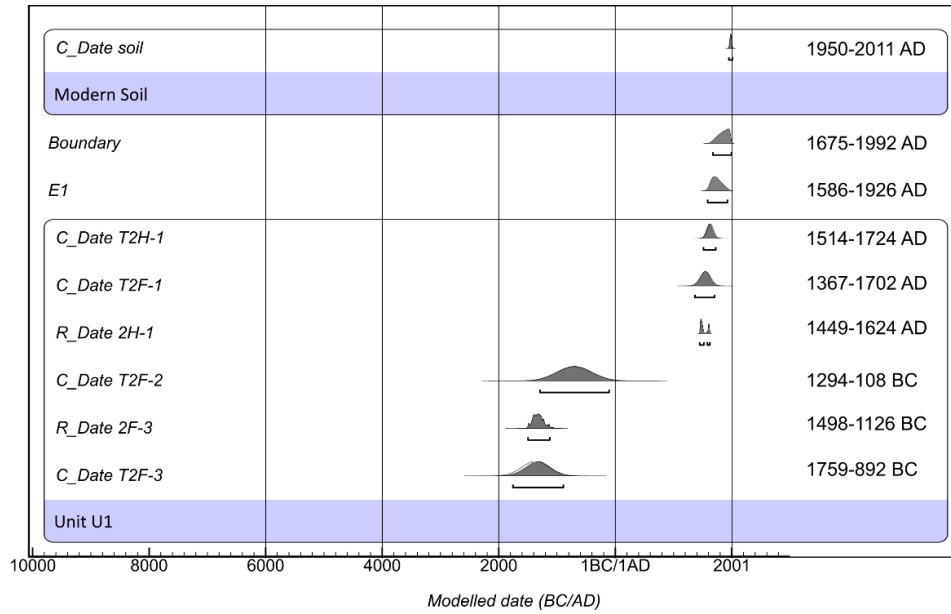# APPENDIX E. OxCal Chronostratigraphic Model Scenarios

Figure E.1 Two scenarios of OxCal chronostratigraphic model built to constrain the surface-rupturing event E1 at the Dungsam Chu exposure. The top model is constrained by two detrital charcoal samples and four OSL samples in the faulted unit U1 and one inferred age corresponding to the undisturbed modern soil unit. The bottom model additionally includes all samples (one detrital charcoal sample and two OSL samples) in the terrace T1 probably deformed during E1. The OSL data were input by converting the laboratory OSL ages with the laboratory uncertainties to calendar dates (Lienkaemper and Ramsey, 2009).

APPENDIX F. Magnitude Calculation and Interpretation
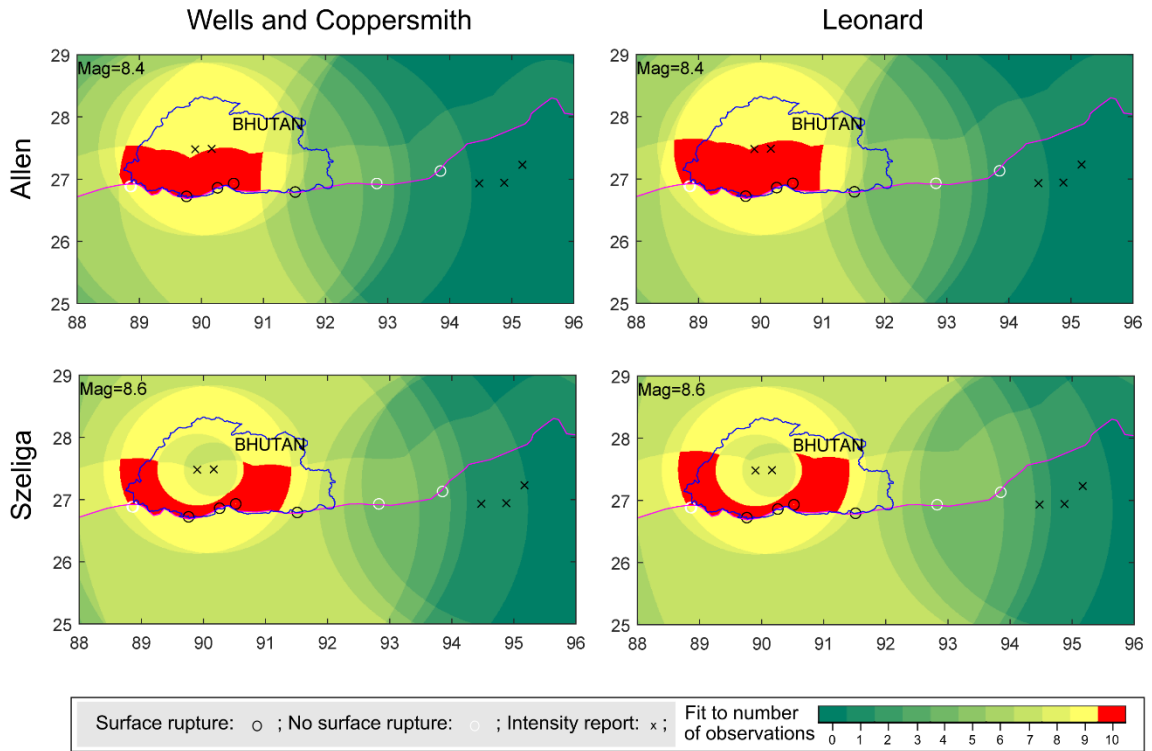
Figure F.1 Scenarios of earthquake magnitude beyond the maximum solutions that were yielded using the combination of each intensity prediction equation (of Allen et al. (2012) or Szeliga et al. (2010)) and each scaling equation (of Leonard (2010) or Wells and Coppersmith (1994)). The possible hypocenter locations fitting all the observed data points are shown as the red area.

APPENDIX G. Coulomb Stress Transfer Calculations
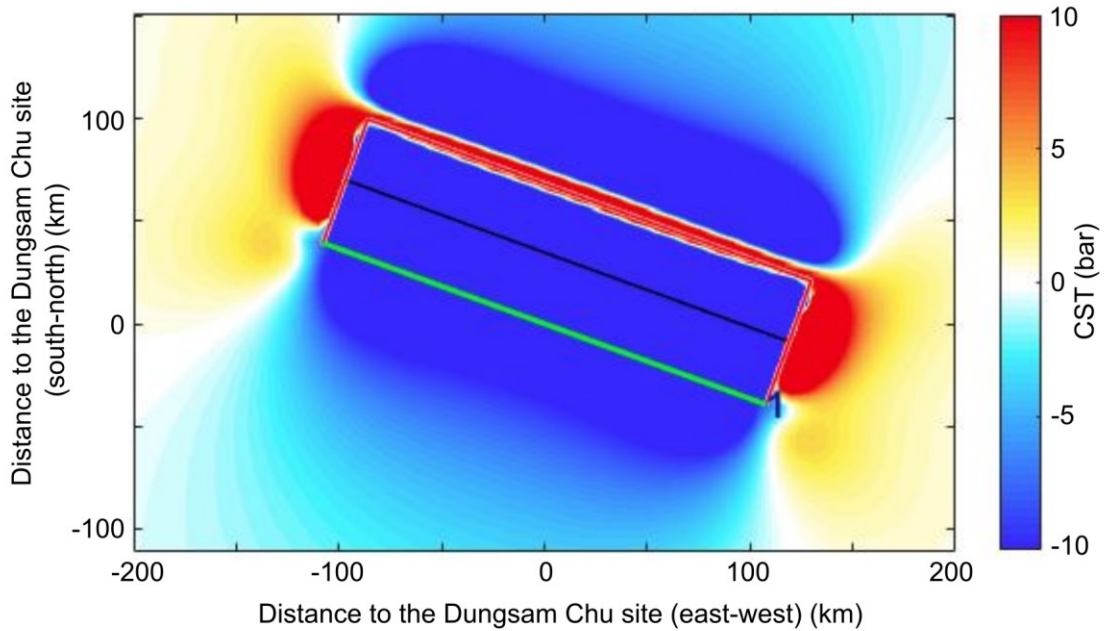
Figure G.1 Coulomb stress changes caused by the 1714 M8.1 earthquake along the MHT in eastern Bhutan. Without considering any Coulomb stress transfer from the neighboring faults, a coseismic slip of 10.5 m on the rupture fault with an approximate slip area of 230 km × 70 km estimated by using the scaling relationships in Wells and Coppersmith (1994) yields a mean stress drop of ~17 bar. Friction coefficient μ = 0.4, and Young's modulus E = 80 GPa. The green line denotes the fault trace at the surface with 290/24/90 of strike/dip/rake. The red rectangular marks the surface projection. The black line indicates the fault line at the target depth of ~14.5 km. Point (0, 0) is the Dungsam Chu site (26.79201°N, 91.51116°E) (this study).

APPENDIX H. Contributions of Authors

Yuqiu Zhao was mainly responsible for the paleoseismic study at the Dungsam Chu site in eastern Bhutan under the supervision of Dr. Djordje Grujic, including fieldwork, data acquisition and interpretation (regarding all the dating samples, the retro-deformation analysis, magnitude calculations, and return time estimate), and writing. Djordje Grujic supervised the entire study, participated in all data analysis and discussion, supported final data interpretation, and edited the manuscript. Santanu Baruah, Dawchu Drukpa, and Nityam Nepal contributed to fieldwork and data acquisition, most as to geomorphic analyses. Joanne Elkadi and Georgina E. King helped with data acquisition and interpretation, all related to luminescence dating techniques. György Hetényi directed the application of the model of the 1714 earthquake and participated in, supported, and edited the interpretation of associated data. Zoë K. Mildon contributed to Coulomb stress transfer modeling and related data interpretation. Caroline Welte helped with data acquisition and interpretation regarding organic material dating. All the co-authors reviewed the final version of the manuscript and approved the manuscript for submission.

APPENDIX I. Copyright Agreement